Automatic Ultrasound Scanning

Moshavegh, Ramin; Jensen, Jørgen Arendt; Hemmsen, Martin Christian; Martins, Bo

Publication date:
2016

Document Version
Early version, also known as pre-print

Ph.D. Thesis

Automatic Ultrasound Scanning

Ramin Moshavegh

Supervised by: Prof. Jørgen Arendt Jensen, Ph.D., Dr. Techn.

Co-supervised by: Martin Christian Hemmsen, Ph.D.
Bo Martins, Ph.D.

Technical University of Denmark
Kgs. Lyngby, Denmark 2016

Technical University of Denmark

Department of Electrical Engineering

Center for Fast Ultrasound Imaging (CFU)

Ørsteds Plads 349

2800 Kgs. Lyngby

DENMARK

Tel: (+45) 4525 3898

Web: www.cfu.elektro.dtu.dk

Author e-mail: ramosh@elektro.dtu.dk

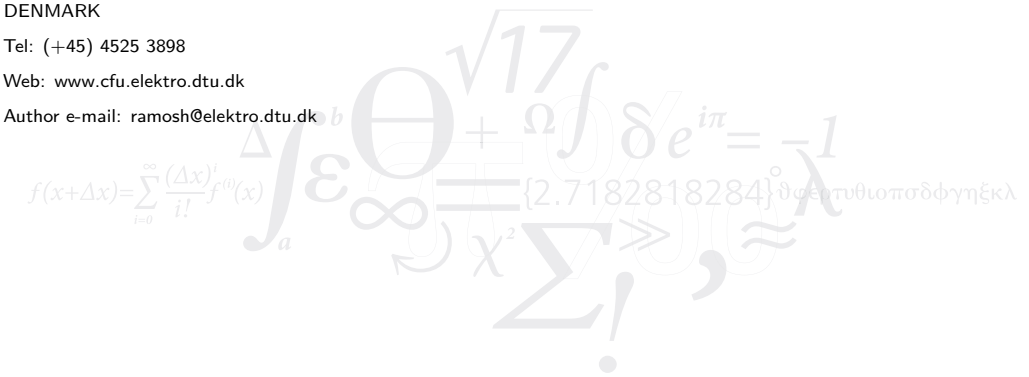

Contents

Preface

This PhD thesis has been submitted to the Department of Electrical Engineering at the Technical University of Denmark in partial fulfillment of the requirements for acquiring the PhD degree. The research and development underlying the thesis have been conducted over a period of three years from December 15th, 2013, to Dec 14th, 2016 at the Center for Fast Ultrasound Imaging (CFU), Department of Electrical Engineering. This project has been supervised by Prof. Jørgen Arendt Jensen, PhD, Dr. Techn, and co-supervised by Bo Martins, PhD. The project was financially supported by grant 82-2012-4 from the Danish National Advanced Technology Foundation and by BK Ultrasound Aps, Denmark.

During these three years of research, I have had the opportunity to participate and present my latest research at many internationally recognized conferences in Orlando, Helsingborg, Taipei, San Diego, and Tours. These premier forums enabled me to have fruitful discussions with fellow researchers from other esteemed groups and built professional connections with some of the experts. It has always been quite educational to learn from others' different perspective to the same problems I might also have had. Traveling to these conferences has been a huge experience as it has broadened my technical and clinical knowledge of ultrasound. During My PhD, I have had the opportunity of co-supervising an engineering student in a master project and one bachelor project. I have also enjoyed the experience of teaching and tutoring students for three semesters on a biomedical engineering programming course.

Ramin Moshavegh
Copenhagen, Denmark
December 2016

x

Summary

Medical ultrasound has been a widely used imaging modality in healthcare platforms for examination, diagnostic purposes, and for real-time guidance during surgery. However, despite the recent advances, medical ultrasound remains the most operator-dependent imaging modality, as it heavily relies on the user adjustments on the scanner interface to optimize the scan settings. This explains the huge interest in the subject of this PhD project entitled "AUTOMATIC ULTRASOUND SCANNING". The key goals of the project have been to develop automated techniques to minimize the unnecessary settings on the scanners, and to improve the computer-aided diagnosis (CAD) in ultrasound by introducing new quantitative measures. Thus, four major issues concerning automation of the medical ultrasound are addressed in this PhD project. They touch upon gain adjustments in ultrasound, automatic synthetic aperture image quality optimization, automated vessel segmentation in ultrasound, and lack of CAD in point-of-care lung ultrasound.

The goals of this PhD are achieved for each of the subjects. First, a new automated time gain compensation technique is proposed that compensates for gains of the scans in 2-D. The proposed model outperforms the current 1-D curve compensation in commercial scanners, as the 2-D topology of the scans are not fully integrated in those techniques. Second, an automated generic technique is proposed for optimization of synthetic aperture image quality. This generic model can be used for any imaging regime using any transducer geometry. Third, a hybrid vessel segmentation technique is proposed that combines both vector velocity estimates (VFI) and B-mode images. The technique enables the wall-to-wall visualization of VFI, as well as provides a firm ground for quantitative quantification of VFI in state-of-the-art US scanners. Finally, a new technique is introduced to detect disease-related reverberation artifacts in lung ultrasound, thereby exploiting the full potential of this imaging modality.

Resumé

(Summary in Danish)

Medicinsk ultralyd er en udbredt realtids billedmodalitet, der benyttes i klinikken til både diagnostisering og under operationer. På trods af den konstante udvikling er medicinsk ultralyd stadig meget brugerafhængigt, da mange parametre skal justeres og optimeres manuelt for at opnå det bedst mulige resultat af en undersøgelse. Motivationen i dette PhD projekt har derfor været at automatisere en række af disse processer, således at brugerafhængigheden kunne minimeres. Ydermere har fokus været på at udvikle algoritmer, der kunne assistere brugeren i det daglige arbejde ved brug af et computer-automatiseret diagnosticeringsværktøj (CAD). Denne afhandling gennemgår fire større problemstillinger relateret til automatisering af medicinsk ultralyd. Disse emner er automatiseret kontrol af "gain", automatisk syntetisk apertur billedkvalitets-optimering, automatiseret segmentering af blodkar samt manglen på automatiserede diagnostiseringsværktøjer til lungepatienter.

Denne PhD afhandling forsøger at løse hver af de fire opstillede problemstillinger. Således foreslås en automatiseret "gain" kompenseringsteknik, der kan justere "gainen" for 2-D ultralydsbilleder. Den foreslåede metode udkonkurrerer de nuværende 1-D kompenseringskurver i kommercielle scannere, da 2-D topologien ikke er fuldt integreret i disse teknikker. Den anden problemstilling foreslår en automatisk generisk metode til optimering af billeder genereret med syntetisk apertur teknikker. Den generiske model er kompatibel med en hvilken som helst billeddannelsesmetode og kan benyttes af alle transducergeometrier. Den tredje problemstilling løses ved at kombinere information om blodets bevægelse i 2-D og et B-mode billede. En metode baseret på disse input kan producere en forbedret og automatiseret segmentering af blodkarrene, hvilket giver et bedre udgangspunkt for at estimere kvantitative værdier i "state-of-the-art" ultralydsscannere. slutteligt præsenteres en ny teknik, der automatisk kan identificere artefakter relateret til lungesygdomme.

Acknowledgements

First and foremost I would like to express my deepest appreciation to my principal adviser Prof. Jørgen Arendt Jensen. Thank you for your guidance, support, everlasting enthusiasm, and your faith in my ability to complete this thesis. I extent my sincere thanks to my co-supervisors Martin Christian Hemmsen (during the first two years of the project) and Bo Martins for their commitment and guidance throughout the project. I am indebted to Kristoffer Lindskov Hansen for his tenacity in collaboration and adapting new techniques in clinics, and for reading and commenting on my various writings. Thanks also to all of my colleagues at the Center for Fast Ultrasound Imaging (CFU) and at Copenhagen University Hospital Rigshospitalet for their comradeship, intellectual input, and the many intellectual and earthy discussions over weekly meetings. A special thank to my office mates Jonas Jensen and Tommaso Di Ianni for providing a pleasant atmosphere in the office. Further, I would like to thank Nina Kjærgaard for proof-reading parts of the thesis.

The hardest thing has been the separation from my family. I have missed them all very much. I thank them, and especially my parents –my father Fazlallah and my mother Mahin– for their unflagging love and support throughout my life, My siblings Mitra and Zhoubin for their encouragement, love, and support.

Last, but by no means least, I thank the love of my life Atieh Zahmatkesh. Thank you for your unwavering belief in me. Through your eyes I have seen myself as a capable, intelligent man who could do anything once I made up my mind. There are no words that can express my gratitude and appreciation for all you have done and been for me.

Thank you all!

List of Figures

List of Tables

Abbreviations

1-D	One-Dimensional
2-D	Two-Dimensional
3-D	Three-Dimensional
α_{max}	Maximum steering angle
ATGC	Automatic Time Gain Compensation
CA	Carotid Artery
CAD	Computer Aided Diagnosis
CFM	Color Flow Map
CT	Computed Tomography
DTU	Danmarks Tekniske Universitet (Technical University of Denmark)
$F_{\#}$	f-number, equal to the focal length divided by the aperture diameter
LUS	Lung Ultrasound
MRI	Magnetic Resonance Imaging
PRF	Pulse Repetition Frequency
PSV	Peak Systolic Velocity
RF	Radio Frequency
ROI	Region of Interest
Rx	Receive
SA	Synthetic Aperture Imaging
SAFI	Synthetic Aperture Flow Imaging
SARUS	Synthetic Aperture Real-time Ultrasound System
SDU	Spectral Doppler Ultrasound
SNR	Signal to Noise Ratio
SSA	Singular Spectrum Analysis
Std	Standard deviation
SVD	Singular Value Decomposition
TGC	Time Gain Compensation
TO	Transverse Oscillation

Tx	Transmit
US	Ultrasound
VFI	Vector Flow Imaging
VFM	Vector Flow Map

CHAPTER 1

Introduction

Medical ultrasound (US) is a widely used imaging modality to assist medical doctors for examination, diagnostic purposes, and for real-time guidance during surgery (Harvey et al. 2002; OBrien and Holmes 2007). Today, US is used for a great variety of imaging applications, such as cardiac imaging (Willadsen 2004; Tong et al. 2013), abdominal imaging (Meire et al. 2001; Moore, Holliday, et al. 2008), fetal imaging (Thompson, Trudinger, and Cook 1985), and recently also for lung imaging (Volpicelli, Cardinale, et al. 2008; Gargani 2011; Lichtenstein 2014). Ultrasound scanners are often the preferred modality of choice as they

- provide a real-time and non-invasive imaging with a high quality of soft tissue (Wardlaw et al. 2006); and
- are inexpensive compared with other imaging modalities (OBrien and Holmes 2007); and
- are mobile, and thus can be used at point-of-care (Moore and Copel 2011), while remaining safe for the patients.

These factors can be compared with other medical imaging modalities such as computed tomography (CT) and magnetic resonance imaging (MRI), whose comprising large and relatively expensive systems cannot easily be transported to the patient (Harvey et al. 2002; Terkawi et al. 2013). Medical US is progressing continuously with a rapid pace, and new imaging methods are constantly being exploited (OBrien and Holmes 2007). Many of the new techniques aim to extend the application field of US into new areas, and to improve the quality of the images and thereby making the diagnostic process more reliable.

Many new technological features have been added to the modern diagnostic US systems. However, despite the recent advances, medical US remains the most operator-dependent imaging modality, as it heavily relies on the actions of medical doctor to optimize the scan settings (Baker, J. Jensen, and Behrens 2013). These for instance, include the overall image gain, the gain as a function of depth (Pye, Wild, and McDicken 1992; Lee, Kim, and Ra 2006; Tang, Luo, and Liu 2009), Doppler sensitivity (Stewart

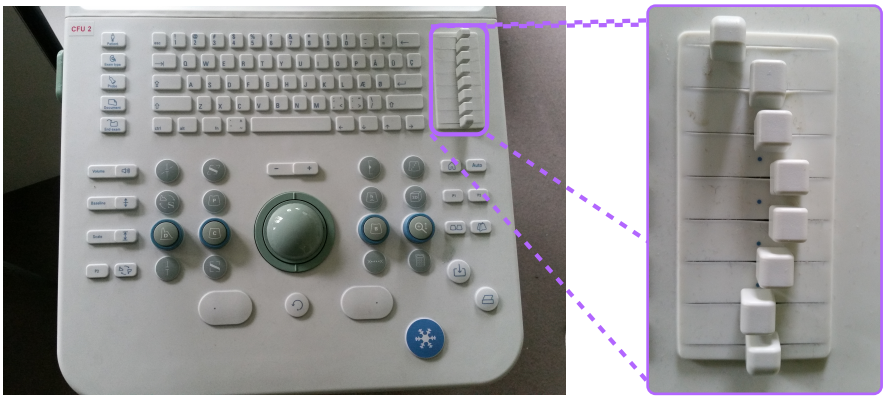

Figure 1.1: The keyboard of a commercial ultrasound scanner. The zoom-in shows the TGC gain sliders.

2001), pulse repetition time (Stewart 2001), echo canceling filter (Schlaikjer, Torp-Pedersen, and J. A. Jensen 2003), focusing (J. N. Tjøtta, S. Tjøtta, and Verfring 1991), and many more. This is also reflected by the keyboard, which most modern scanners have (see Fig. 1.1). Here, a plethora of buttons are present and they have slightly different functions and placement for each new scanner and manufacturer. This introduces sources of errors, prolongs the education time, and also slows down the work-flow for the clinical users. In such systems, operator's skill in obtaining the images plays a critical role in the radiologist's ability to confidently provide a correct diagnosis. However, operator skill varies as a result of experience, education, and knowledge of the ultrasound system capabilities. This variability can lead to significant differences in the diagnostic images provided, even in same type of study or on the same patient.

Another major problem with current US is that many parameters are measured manually on the images, and often have to be corrected to be useful. This again, introduces the possibility for error and slows down the clinical process.

Prior to discussing the objectives of this PhD project, the state-of-the-art of medical US has to be studied.

1.1 State-of-the-art ultrasound and the need for automation

Four major issues concerning the medical US are addressed in this PhD project. They touch upon gain adjustments in US, synthetic aperture image quality, segmentation of major vessels in US, and point-of-care lung ultrasound. For each of them, the state-of-the-

art, the challenges, and the suggestions to reduce the engineering adjustments performed by the user are introduced.

1.1.1 Automated Gain adjustments

Ultrasound waves propagating in tissue encounter losses in scanned media. Two main mechanisms contribute to the acoustic attenuation: absorption and scattering. Time gain compensation (TGC) is usually used to compensate for the acoustic attenuation. TGC offsets the attenuation of ultrasound echo signals along the depth, so that echoes belonging to deep structures are more amplified compared with echoes of superficial structures. This provides more uniform signals to be displayed on the scanner (Lee, Kim, and Ra 2006).

Modern US scanners use a 1-D curve for time gain compensation (TGC). The user adjusts the shape by manually using TGC sliders for different depths, and the image quality is dependent on the adjustments. An automatic adjustment of the TGC (ATGC) without user intervention can address the shortcomings of the manual TGC (Pye, Wild, and McDicken 1992). To date, several designs of ATGC are proposed in the literature (Pye, Wild, and McDicken 1992; Lee, Kim, and Ra 2006; Tang, Luo, and Liu 2009). However, the majority of these algorithms rely on the presence of sufficiently large homogeneous soft tissues with uniform distribution of attenuation in other tissues is ignored in these algorithms (Klesenski 1996; Lee, Kim, and Ra 2006; Tang, Luo, and Liu 2009). These methods fail to compensate the overall gain when large fluid collections such as the urine bladder and gallbladder are present that change the uniform distribution of the attenuation drastically. Large anechoic segments, surrounded by soft tissue, present a large variation in attenuation. A new automated gain compensation that considers the 2-D topology of the scanned media is then essential.

1.1.2 Optimization of synthetic aperture image quality

When it comes to US imaging techniques, Synthetic Aperture (SA) has shown that it highly improves the frame rate in comparison with conventional US imaging, where one line at a time is beamformed for generating the final ultrasound image (Gammelmark and J. A. Jensen 2003). In SA, emissions with large areas of sonification can be used and a complete resolution image can be beamformed for each emission. By adding a series of low resolution images (LRI) a high resolution image (HRI) is generated (Nikolov 2001). However, several different interdependent parameters effecting the image quality in SA such as number of successive emissions, $F_{\#}$, aperture size, and α_{max}. Achieving optimal image quality using SA sequence is then highly dependent to optimizing the parameters involved in image acquisition. An automated optimization procedure of the

interdependent parameters is then required for ensuring the optimal image quality in SA sequence designs.

1.1.3 Automated segmentation of major vessels

Current vessel segmentation techniques in US use only B-mode images as the input to their algorithm (Mao et al. 2000; Golemati et al. 2007; Santhiyakumari et al. 2011; Loizou 2014). The information about the flow moving inside the vessel is therefore not considered. Flow data adds invaluable information by locating the regions inside the vessels, and strengthen the segmentation of the vessels. One study used a combination of B-mode and contrast enhanced images for segmentation (Carvalho et al. 2015). The technique segments the border of the carotid artery which can hardly be detected in standard B-mode images. Nonetheless, it requires special micrometer-sized gas bubbles to be injected into the blood stream, which is not achievable in everyday use in a normal scan session.

The challenge remains in devising an accurate vessel segmentation technique that incorporates both B-mode image and flow data non-invasively, to better identify the vessels. Vector Flow Imaging (VFI) (J. A. Jensen et al. 2016a,b) can be used for this purpose, as it enables reliable, robust, and non-invasive estimation of blood flow. A new segmentation technique, using a combination of B-mode and VFI data, can be an alternative. This is mainly because the VFI is robust, reliable, and can be acquired in real-time along with the B-mode. Thus, the technique has the potential for automated quantification of flow in state-of-the-art US scanners.

1.1.4 Automated point-of-care lung ultrasound

In daily clinical practice, patients suspected for pulmonary disease such as pulmonary edema or pneumothorax are imaged with X-ray, and often repeatedly imaged with short intervals to monitor the effect of the applied treatment (Volpicelli, Mussa, et al. 2006; Gargani 2011). Lung ultrasound (LUS) is a well-established modality but is often bypassed as the medical staff handling these patients is not familiar with the method (Lichtenstein 2014). The bed-side LUS is an emerging technique, and the standard pathological routine for diagnosing pulmonary disease is to analyze a single scan or frame by a doctor (Gargani 2011). However, a major factor affects the accuracy of the examination. That factor is interpretation error for reasons including inexperience and habituation. Computer-assisted interpretation can potentially address the issue related to interpretation error. Despite the recent developments of LUS, there are no computerized and automated models for detecting pulmonary diseases in the literature. Therefore, an automated technique for detecting pulmonary disease based on physical understanding of ultrasonic specific features such as reverberation artifacts related to diseases in LUS is needed.

1.2 Objective

The overall objective of this project is to develop algorithms to reduce the engineering adjustments done by the medical doctors on the scanners to optimize the quality of the scans. A second goal is to automate the diagnostic process by developing automatic methods for yielding quantitative measures.

The first part of this dissertation investigates algorithms for optimizing the gain settings employed in acquiring the data. Algorithms for adjusting the gain to optimize both the acquisition process and the display. A large database of clinical images acquired at University Hospital of Copenhagen, Rigshospitalet, is used to validate the algorithm.

The second part of the project seeks to develop automated and generic techniques to optimize the SA image quality.

The third part of the project seeks to develop methods for assisting the diagnostic process. This comprises methods for automatically segmenting vessels and from this , to automatically determine quantitative flow measures, such as volume flow.

Finally, the last part of the dissertation focuses on implementing automated techniques for detecting pulmonary diseases in point-of-care lung ultrasound.

1.3 Scope

As noted in previous sections, this PhD project addressed four different topics. First, the TGC is addressed and a new automated method is introduced that compensates the images in 2-D compared with 1-D curve compensation. Second, SA image quality is addressed, when SA is used for image acquisition and a novel and automated method for optimization of SA image quality is proposed. Third, the segmentation of major vessels in US is addressed. This is performed to assist vector flow images VFI (wall-to-wall visualization of VFI), and to automate the quantification of VFI in state-of-the-art US scanners.

Finally, this project addressed the lack of an automated tool for identifying pulmonary disease in point-of-care LUS, and thus introduced a new technique to quantify disease-related reverberation artifacts.

Therefore, the scope of this PhD entitled ”Automated Ultrasound Scanning” has the following steps:

1. Automatic gain adjustments in medical US and clinical validation of the proposed method.

2. Proposing an automated optimization procedure for optimizing interdependent parameters effecting SA image quality.

3. Proposing a novel vessel segmentation technique in US that uses the combination of B-mode and VFI flow data. The proposed method implements automated VFI quantitative flow measures, such as peak systolic velocity (PSV) and volume flow.

4. Proposing an automated method for detecting disease-correlated reverberation artifacts in LUS, more specifically B-lines.

1.4 Scientific contributions

The thesis compiles the research presented in two manuscripts that have been submitted for publication in ISI journals, and a patent application taken up by Analogic. Additionally, five conference proceedings are included in the project. Besides the included papers, the author has contributed to publications on segmentation of vessels and validation of VFI quantitative measures, both experimentally and during clinical settings. A full publication list is given below.

1.4.1 Journal papers

Paper A: **Ramin Moshavegh**, C. Ewertsen, K. L. Hansen, A. H. Brandt, T. Bechsgaard, M. C. Hemmsen, B. Martins, M. B. Nielsen, and J. A. Jensen. Advanced Gain Adjustments for Ultrasound Imaging. Submitted to *Journal of Ultrasound in Medicine and Biology (UMB)*.

Paper B: **Ramin Moshavegh**, C. A. Villagomez-Hoyos, M. B. Stuart, B. Martins, and J. A. Jensen. Advanced Multi-objective Synthetic Aperture Image Quality Optimization. Submitted to *IEEE Trans. Ultrasons., Ferroelec., Freq. Contr.*.

1.4.2 Conference papers

Paper C: **Ramin Moshavegh**, K. L. Hansen, H. M. S. M. C. Hemmsen, C. Ewertsen, M. B. Nielsen, and J. A. Jensen. "Novel automatic detection of pleura and B-lines (comet-tail artifacts) on in vivo lung ultrasound scans". In: *Proc. SPIE Med. Imag.* Vol. 9790, pp. 97900K-97900K-7, 2016.

Paper D: **Ramin Moshavegh**, M. C. Hemmsen, B. Martins, K. L. Hansen, C. Ewertsen, A. H. Brandt, T. Bechsgaard, M. B. Nielsen, and J. A. Jensen. "Advanced automated gain adjustments for in-vivo ultrasound imaging". In: *Proc. IEEE Ultrason. Symp.*, pp. 1–4, 2015.

Paper E: **Ramin Moshavegh**, M. Hemmsen, B. Martins, A. Brandt, K. Hansen, M. Nielsen, and J. A. Jensen. "Automated hierarchical time gain compensation for in-vivo

ultrasound imaging". In:*Proc. SPIE Med. Imag.*, Vol. 9419, pp. 941904-941904-9, 2015.

Paper F: **Ramin Moshavegh**, J. Jensen, C. A. Villagomez-Hoyos, M. B. Stuart, M. C. Hemmsen, and J. A. Jensen. "Optimization of synthetic aperture image quality". In: *Proc. SPIE Med. Imag.*, Vol. 9790, pp. 97900Z-97900Z-9, 2016.

Paper G: **Ramin Moshavegh**, B. Martins, K. L. Hansen, T. Bechsgaard, M. B. Nielsen, and J. A. Jensen., "Hybrid Segmentation of Vessels and Automated Flow Measures in In-Vivo Ultrasound Imaging". In: *Proc. IEEE Ultrason. Symp.*, 2016 IEEE International, pp. 1–4, 2016.

1.4.3 Patent application

Patent A: **Ramin Moshavegh**, B. Martins, and J. A. Jensen.Wall-to-wall vessel segmentation in US imaging using a combination of VFI data and US imaging data, Patent Application, filed on September 09, 2016, number: ANA1311-US; PD08509.

1.4.4 Second-author journal paper

SA A: A. H. Brandt, **R. Moshavegh**, K. L. Hansen, T. Bechsgaard, J. A. Jensen, L. Lönn, and M. B. Nielsen. Ultrasound Vector Flow makes Insonation Angle irrelevant in Portal Vein Velocity Measurements. Submitted to *American Journal of Roentgenology (AJR)*, Dec 2016.

1.4.5 Additional papers

- P. T. Sarnikowski, A. B. Kjær, **R. Moshavegh**, and J. A. Jensen. "Automatic segmentation of vessels in in-vivo ultrasound scans". Accepted To be published: *Proc. SPIE Med. Imag.*, 2017.

1.5 Other contributions

Besides the conducted research and the published papers, several software projects were developed for the benefit of the colleagues at the center for fast ultrasound imaging (CFU). A collection of scripts was programmed in Python for acquiring beamformed RF-data from the BK3000 scanner.

A MATLAB interface was programmed to visualize The US data (B-mode and flow data), and to perform quantitative measures such as PSV and volume flow is on the US data. The visualization tool entitled "CFUvisualization" consists of a collection of MATLAB and C++ scripts. Excluding all external scripts, CFUvisualization consists of

more than 10,000 lines of code. The tool can be used for visualizing US B-mode and VFI data with multiple options for renderization of the flow. The tool can also be used for performing quantitative flow measurements such as measuring PSV and volume flow using the VFI data. The tool enables exporting high quality plots from MATLAB, PDF conversion, creation of high quality video from MATLAB figures for publications.

1.6 Outline of the thesis

The structure of the thesis is four-fold. The first chapter introduces the technical background related to the conducted research. The subsequent chapters concern the scientific contributions and are structured to demonstrate the progress of project. This thesis is presented as a whole, and the chapters are intended to be read in succession. The thesis is designed to enforce logical and scientific rigor and make it easy to read.

This chapter has:

- Provided an overview of the state-of-the-art medical US in TGC, SA imaging, vessel segmentation and finally, point-of-care LUS. The shortcomings of each are also reviewed. The rationale for introducing new automated techniques For TGC, SA image optimization, segmentation of vessels in US, and pulmonary disease detection in LUS is discussed.
- Defined the aim, objectives, and scope of this research.
- Highlighted the main scientific contributions in this PhD project.

The remainder of the thesis is organized as follows:

Chapter 2 deals specifically with the problem of automatically, accurately and robustly adjusting the gains in ultrasound imaging. The chapter acquaints the reader with the acoustic attenuation and discusses the shortcomings of the recent implementations of TGC, specially in regard to gain compensation in scans with large anechoic regions. It then presents an ATGC algorithm that adapts to the large attenuation variation between different types of tissues and structures. The technique relies on decay of the power spectral density of the received signal with respect to depth, as well as estimates of scattering strength, and noise level to gain a more quantitative understanding of the underlying tissue.

Chapter 3 deals specifically with the optimization of SA image quality. The task of automatically selecting optimal parameters for acquisition of the SA images. The chapter introduces the principles of the synthetic aperture (SA), reviews the literature on

SA, and highlights the need to automatically optimize the parameters affecting the SA image quality. It then presents a pilot study of image quality optimization for SA based on the performance measures of full-width at half maximum (FWHM) and the contrast resolution (CTR). The multi-objective optimization technique used in this chapter is based on theory of Pareto optimality.

Chapter 4 introduces the transverse oscillation (TO) and synthetic aperture flow imaging (SAFI) –the two techniques used for acquisition of velocity data in this project.The velocity data is combined with the optimized B-mode from Chapter 3, and used in Chapter 5 to segment vessel lumen in ultrasound images.

Chapter 5 deals specifically with the segmentation of major vessels, particularly carotid artery, and automating quantitative flow measures in ultrasound using VFI. The chapter thus, proposes and discusses a novel hybrid technique for accurate vessel segmentation that fuses VFI data and B-mode for robustly detecting and delineating vessels. The proposed method delineates the vessels in ultrasound scans and enables a better visualization of flow inside the vessel, as well as providing a firm ground for quantitative flow measures for VFI, such as PSV and volume flow.

Chapter 6 introduces a technique for automated detection of disease correlated reverberation artifacts, more specifically B-lines, in ultrasound lung scans. The proposed technique also enables quantitative measures in bed-side lung ultrasound, thereby exploiting the full potential of this imaging technique.

Chapter 7 reviews the work that is presented in this PhD project and summarizes the major contributions and findings. In addition, it proposes an avenue of future research.

References from Chapter 1

Thompson, R. S., B. J. Trudinger, and C. M. Cook (1985). "Doppler ultrasound waveforms in the fetal umbilical artery; Quantitative analysis technique". In: *Ultrasound Med. Biol.* 11, pp. 707–718 (cit. on p. 1).

Tjøtta, J. N., S. Tjøtta, and E. H. Verfring (1991). "Effects of focusing on the nonlinear interaction between two collinear finite amplitude sound beams". In: *J. Acoust. Soc. Am.* 89, pp. 1017–1027 (cit. on p. 2).

Pye, S., S. Wild, and W. McDicken (1992). "Adaptive time gain compensation for ultrasonic imaging". In: *Ultrasound Med. Biol.* 18.2, pp. 205–212 (cit. on pp. 1, 3).

Klesenski, K. (1996). "Automatic gain compensation in an ultrasound imaging system". In: *US Patent*, pp. 5, 579, 768. URL: http://www.google.com/patents/US5579768 (cit. on p. 3).

Mao, F., J. Gill, D. Downey, and A. Fenster (2000). "Segmentation of carotid artery in ultrasound images: Method development and evaluation technique". In: *Medical physics* 27.8, pp. 1961–1970 (cit. on p. 4).

Meire, H. B., D. O. Cosgrove, K. C. Dewbury, and P. Farrant (2001). *Abdominal and General Ultrasound*. Vol. 2. Churchill Livingstone (cit. on p. 1).

Nikolov, S. I. (2001). "Synthetic Aperture Tissue and Flow Ultrasound Imaging". PhD thesis. 2800, Lyngby, Denmark: Ørsted•DTU, Technical University of Denmark (cit. on p. 3).

Stewart, S. F. C. (2001). "Effects of transducer, velocity, Doppler angle, and instrument settings on the accuracy of color Doppler ultrasound". In: *Ultrasound Med. Biol.* 27.4, pp. 551–564. DOI: 10.1016/s0301-5629(01)00357-x (cit. on pp. 1, 2).

Harvey, C. J., J. M. Pilcher, R. J. Eckersley, M. J. Blomley, and D. O. Cosgrove (2002). "Advances in Ultrasound". In: *Clinical Radiology* 57.3, pp. 157–177 (cit. on p. 1).

Gammelmark, K. L. and J. A. Jensen (2003). "Multielement Synthetic Transmit Aperture Imaging using Temporal Encoding". In: *IEEE Trans. Med. Imag.* 22.4, pp. 552–563 (cit. on p. 3).

Schlaikjer, M., S. Torp-Pedersen, and J. A. Jensen (2003). "Simulation of RF data with tissue motion for optimizing stationary echo canceling filters". In: *Ultrasonics* 41, pp. 415–419 (cit. on p. 2).

Willadsen, J. (2004). "Investigation of Synthetic Aperture Ultrasound Cardiac Imaging". MA thesis. Lyngby, Denmark: Ørsted•DTU, Technical University of Denmark (cit. on p. 1).

Lee, D., Y. Kim, and J. Ra (2006). "Automatic time gain compensation and dynamic range control in ultrasound imaging systems". In: *Proc. SPIE Med. Imag.* 6147, pages (cit. on pp. 1, 3).

Volpicelli, G., A. Mussa, G. Garofalo, L. Cardinale, G. Casoli, F. Perotto, C. Fava, and M. Frascisco (2006). "Bedside lung ultrasound in the assessment of alveolar-interstitial syndrome". In: *Am. J. Emerg. Med.* 24.6, pp. 689–696 (cit. on p. 4).

Wardlaw, J. M., F. M. Chappell, J. J. K. Best, K. Wartolowska, and E. Berry (2006). "Non-invasive imaging compared with intra-arterial angiography in the diagnosis of symptomatic carotid stenosis: a meta-analysis". In: *Lancet* 367.9521, pp. 1503–1512 (cit. on p. 1).

Golemati, S., J. Stoitsis, E. G. Sifakis, T. Balkizas, and K. S. Nikita (2007). "Using the Hough transform to segment ultrasound images of longitudinal and transverse sections of the carotid artery". In: *Ultrasound Med. Biol.* 33.12, pp. 1918–1932 (cit. on p. 4).

OBrien, R. T. and S. P. Holmes (2007). "Recent Advances in Ultrasound Technology". In: *Clinical Techniques in Small Animal Practice* 22.3, pp. 93–103 (cit. on p. 1).

Moore, C. L., R. S. Holliday, J. Q. Hwang, and M. R. Osborne (2008). "Screening for abdominal aortic aneurysm in asymptomatic at-risk patients using emergency ultrasound". In: *The American Journal of Emergency Medicine* 26.8, pp. 883–887 (cit. on p. 1).

Volpicelli, G., L. Cardinale, G. Garofalo, and A. Veltri (2008). "Usefulness of lung ultrasound in the bedside distinction between pulmonary edema and exacerbation of COPD". In: *Am. Soc. Emerg. Radiol.* 15.3, pp. 145–151 (cit. on p. 1).

Tang, M., F. Luo, and D. Liu (2009). "Automatic Time Gain Compensation in Ultrasound Imaging System". In: *Proc. IEEE Int. Conf. Bioinfo. Biomed. Eng.* Pp. 1–4. DOI: 10.1109/ICBBE.2009.5162432 (cit. on pp. 1, 3).

Gargani, L. (2011). "Lung ultrasound: A new tool for the cardiologist". In: *Cardiovascular ultrasound* 9.1 (cit. on pp. 1, 4).

Moore, C. L. and J. A. Copel (2011). "Point-of-Care Ultrasonography". In: *New England Journal of Medicine* 364.8, pp. 749–757 (cit. on p. 1).

Santhiyakumari, N., P. Rajendran, M. Madheswaran, and S. Suresh (2011). "Detection of the intima and media layer thickness of ultrasound common carotid artery image using efficient active contour segmentation technique". In: *Med. Biol. Eng. Comp.* 49.11, pp. 1299–1310 (cit. on p. 4).

Baker, M., J. Jensen, and C. Behrens (2013). "Inter-operator variability in defining uterine position using three-dimensional ultrasound imaging". In: *2013 IEEE Int. Ultrason. Symp.* Pp. 848–851 (cit. on p. 1).

Terkawi, A. S., D. Karakitsos, M. Elbarbary, M. Blaivas, and M. E. Durieux (2013). "Ultrasound for the anesthesiologists: present and future". In: *The scientific world journal* 2013, pp. 1–15 (cit. on p. 1).

Tong, L., A. Ortega, H. Gao, and J. D'hooge (2013). "Fast Three-Dimensional Ultrasound Cardiac Imaging Using Multi-Transmit Beam Forming: A Simulation Study". In: *Proc.*

IEEE Ultrason. Symp. Pp. 1448–1451. DOI: 10.1109/ULTSYM.2013.0369 (cit. on p. 1).

Lichtenstein, D. A. (2014). "Lung ultrasound in the critically ill". In: *Ann Intensive Care* 4.1 (cit. on pp. 1, 4).

Loizou, C. P. (2014). "A review of ultrasound common carotid artery image and video segmentation techniques". In: *Med. Biol. Eng. Comp.* 52.12, pp. 1073–1093 (cit. on p. 4).

Carvalho, D. D. B., Z. Akkus, S. C. H. van den Oord, A. F. L. Schinkel, A. F. W. van der Steen, W. J. Niessen, J. G. Bosch, and S. Klein (2015). "Lumen Segmentation and Motion Estimation in B-Mode and Contrast-Enhanced Ultrasound Images of the Carotid Artery in Patients With Atherosclerotic Plaque". In: *IEEE Trans. Med. Imag.* 34.4, pp. 983–993 (cit. on p. 4).

Jensen, J. A., S. I. Nikolov, A. Yu, and D. Garcia (2016a). "Ultrasound Vector Flow Imaging I: Sequential Systems". In: *IEEE Trans. Ultrason., Ferroelec., Freq. Contr.* 63.11, pp. 1704–1721. DOI: 10.1109/TUFFC.2016.2600763 (cit. on p. 4).

— (2016b). "Ultrasound Vector Flow Imaging II: Parallel Systems". In: *IEEE Trans. Ultrason., Ferroelec., Freq. Contr.* 63.11, pp. 1722–1732. DOI: 10.1109/TUFFC.2016.2598180 (cit. on p. 4).

CHAPTER 2

Advanced Hierarchical Gain Adjustments

The present chapter deals specifically with the problem of automatically, accurately and robustly adjusting the gains in ultrasound imaging. The chapter acquaints the reader with acoustic attenuation and time gain compensation (TGC), reviews the recent implementations of TGC in commercial scanners, and discusses their shortcomings. The chapter then presents an automated hierarchical TGC (AHTGC) algorithm that adapts to the large attenuation variation between different types of tissues and structures. The technique relies on decay of the power spectral density of the received signal with respect to depth, as well as estimates of scattering strength, and noise level to obtain a more quantitative understanding of the underlying tissue. The proposed algorithm is applied to *in-vivo* ultrasound scans and the image quality is evaluated.

The remainder of this chapter is organized as follows. Sections 2.1 discusses the acoustic attenuation. Section 2.2 introduces the time gain compensation (TGC) and reviews the current implementations of TGC. Section 2.3 presents a high level description of the proposed technique. Sections 2.4 to 2.8 introduce the different steps of the algorithm. Section 2.9 describes the scan protocol of the study, and introduces the images acquired. Sections 2.10 and 2.11 empirically evaluate the results. Finally, Section 2.12 summarizes the chapter.

2.1 Attenuation

Ultrasound waves propagating in tissue encounter energy loss in scanned media. Two main mechanisms contribute to the acoustic attenuation: absorption and scattering. Real tissue data suggest that attenuation has a power-law dependency on frequency. As a consequence of the frequency dependency of attenuation, ultrasound waves become smaller in amplitude as they propagate in media, and change shape (Jensen 1996; Szabo 2014). A linear dependency is often considered between the attenuation and the distance traveled, and the frequency. The most commonly used unit for attenuation in ultrasound is $\mathrm{dB/cm} \times \mathrm{MHz}$. Attenuation values for different human tissues are depicted in Table 2.1.

Tissue	Attenuation $\mathrm{dB/cm} \times \mathrm{MHz}$
Liver	0.6 – 0.9
Kidney	0.8 – 1.0
Spleen	0.5 – 1.0
Fat	1.0 – 2.0
Plasma	0.01
Bone	16.0 – 23.0
Blood	0.17 – 0.24

Table 2.1: Attenuation values for human tissue (taken from (Jensen 1996))

The acoustic attenuation is due to different phenomena. A strong factor is scattering, which spreads the acoustic energy in all directions. Another important factor is absorption of the energy. This is mainly due to viscous loss, heat conduction, and losses associated with molecular exchanges of energy. Absorption mechanism accounts for roughly 75% to 95% of the total attenuation (Jensen 1996). Complex nature of the tissue structures in the human body complicates the formulation of frequency dependence of the attenuation. Thus, literature often, reports a basic phenomenological model for attenuation. The amplitude attenuation transfer for a plane wave propagating through tissue is given by:

$$|H(f;z)| = \exp(-(\beta_0 z + \beta_1 f z)), \tag{2.1}$$

where z is depth in tissue, f is frequency, β_0 is assumed to be the frequency-independent attenuation, and β_1 is the frequency-dependent attenuation term. The major part of the attenuation is the frequency-dependent term, and frequency-independent attenuation is usually disregarded from the model. The frequency-dependent attenuation causes a larger attenuation of higher frequencies than lower frequencies. This reduces the mean frequency of the spectrum of the received signal, as it propagates in the tissue, and changes the shapes of the spectrum of the signal. Assume a Gaussian pulse given by:

$$p(t) = \exp(2(B_r f_0 \pi)^2 t^2) \cos(2\pi f_0 t), \tag{2.2}$$

where f_0 is the center frequency, and B_r is the relative bandwidth. The linear decrease in mean frequency with depth can be explained by taking the Fourier transform of (2.2) and multiplying by the attenuation function(2.1):

$$P_a(f) = \frac{1}{2B_r f_0\sqrt{2\pi}} \left(\exp\left(-\frac{(f_0 - f)^2}{2(B_r f_0)^2} \right) + \exp\left(-\frac{(f_0 + f)^2}{2(B_r f_0)^2} \right) \right) \times \exp(-(\beta_0 z + \beta_1 f z)). \tag{2.3}$$

Condidering only the term for positive frequencies yields

$$P_{ap}(f) = \frac{1}{2B_r f_0\sqrt{2\pi}} \left(\exp\left(-\frac{f_0^2 + f^2 - 2f_0(1 - \beta_1 z B_r^2 f_0) f}{2(B_r f_0)^2} \right) \right) \times \exp(-\beta_0 z). \tag{2.4}$$

The maximum value of the spectrum, coinciding with its mean value, is attained when the argument of the exponential is zero, since the spectrum is symmetric. The first derivative with respect to frequency will also be zero due to symmetry, so

$$2f_{mean} - 2f_0(1 - \beta_1 z B_r^2 f_0) = 0 \longleftrightarrow f_{mean} = f_0 - (\beta_1 z B_r^2 f_0^2) z. \tag{2.5}$$

The mean frequency will, thus, decrease linearly with depth and it is dependent on attenuation, transducer center frequency, and bandwidth. Eq. (2.5) also holds approximately for other pulse shapes, where a nearly linear decrease in center frequency is seen with depth, and the downshift is dependent on attenuation, frequency, bandwidth, and spectral shape. Thus, RF echoes are strongly attenuated by the tissues scanned (Lee, Kim, and Ra 2006). For a tissue with attenuation of 0.7 $\mathrm{dB/cm} \times \mathrm{MHz}$, The acoustic wave would be attenuated $2\times12\times3.5\times0.7$ = 58.8 dB for a received signal using a 3.5 MHz transducer with an imaging depth of 12 cm (as the sound penetrates the tissue twice). Therefore, the received signals span a wide dynamic range, and are not suitable to be visualized before the gains are compensated for the attenuation.

2.2 Time-Gain-Compensation (TGC)

TGC is usually used to compensate for the acoustic attenuation. TGC offsets the attenuation of ultrasound echo signals along the depth, so that echoes belonging to deep structures are more amplified compared to echoes of superficial structures. This provides more uniform signals to be displayed on the scanner (Lee, Kim, and Ra 2006).

Current ultrasound scanners use a TGC curve for time gain compensation. The user adjusts the shape by manually using TGC sliders for different depths, and the image

quality is dependent on the adjustments. An automatic adjustment of the TGC (ATGC) without user intervention can address the shortcomings of the manual TGC (Pye, Wild, and McDicken 1992). To date, several designs of ATGC are proposed in the literature (Inbar and Delevy 1989; Pye, Wild, and McDicken 1992; Lee, Kim, and Ra 2006; Tang, Luo, and Liu 2009). Pye. et. al. (Pye, Wild, and McDicken 1992) proposed a technique, in which the gain applied to each location in the image is determined by using echo information averaged over a large part of the image.

Lee. et. al. (Lee, Kim, and Ra 2006) proposed an algorithm, which consisted of both TGC and dynamic range (DR) optimization. The algorithm used log-compressed digital echo data as input. The gains along the depth are first compensated and then an optimization procedure is performed to find the optimal dynamic range. The paper used a single TGC curve for compensating all the scan lines. An attenuation curve is computed and used for the purpose of compensation. However, the curve is computed from the log-compressed data and the complex nature of the RF data is already lost.

The majority of these algorithms rely on the presence of sufficiently large homogeneous soft tissues with uniform distribution of attenuation (Klesenski 1996; Lee, Kim, and Ra 2006; Tang, Luo, and Liu 2009). Thus, the dependency of the attenuation for several different tissues is ignored in these algorithms. These methods fail to compensate the overall gain when large fluid collections such as the urine bladder or gallbladder are present that change the uniform distribution of the attenuation drastically. Large anechoic segments, surrounded by soft tissue, present a large variation in attenuation. Also, at present, TGC is performed manually or automatically on the commercial scanners, using a 1-D curve, in which the 2-D topology of the scan plane is ignored. The main challenge remains to devise an effective ATGC that considers the 2-D topology, and potential drastic changes in the attenuation distributions, of the scanned media.

2.3 High-level description of the proposed algorithm

The novelty of the proposed technique comes from incorporating several physical estimates of the scanned media as constituents of the compensation strategy. Fig. 2.1 shows the diagram of the the proposed algorithm, which contains five distinct steps as follows.

1. First, the shadow regions on the scans are detected and excluded from the gain compensation procedure.

2. Second, the received signal by the transducer is calibrated for the shape of the beam profile to ensure that all the scanned media receives the same amount of energy.

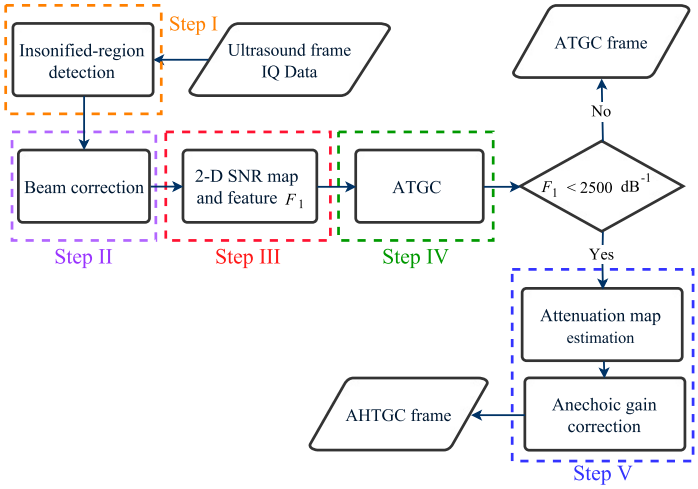

Figure 2.1: Diagram of the proposed AHTHC algorithm.

3. Third, a 2-D SNR map is computed for each frame, and a feature (F_1) is computed to decide whether the frame contains large anechoic regions (Type 1) or not (Type 2).

4. In the fourth step, a TGC curve is computed dynamically for each frame and used to compensate for the gains in that frame.

5. Finally, a 2-D normalized map highlighting the anechoic regions is generated for the frame and used to correct the adjusted gains inside the anechoic regions after applying the TGC curve. This correction is performed only on the scans including large fluid collections (Type 1).

2.4 Insonified-region detection

The main purpose of this step is to determine the insonified region on the ultrasound scans. Often, during normal scan sessions, the transducer is not perfectly attached to the body surface, generating long dark shadows in the image. The Imperfect connections are expected to be seen more on scans acquired using convex arrays, where sides of the array are not always touching the body. These generate shadows appearing on one or both sides of ultrasound images. Therefore, identifying the insonified regions and excluding the

Algorithm 1 Shadow detection

Input: Env envelope of RF-data,
Output: B_{shdw} binary mask outlining the shadow regions.

procedure SHDW
  Let B_{shdw} be a binary mask with the same size as Env.
  Let min_env be the minimum intensity of Env in dB and N be the size of the Env.
  for each $i \in N$ **do**
    if $Env(i) \leq min\_env + 0.1 \times |min\_env|$ **then**
      $B_{shdw}(i) = 1$ # Creating the binary mask by including very dark regions
    end if
  end for
  Let M be the number of columns of the Env.
  for each $i \in M$ **do**
    if $sum(B_{shdw}(i).col) \leq 0.9 \times length(B_{shdw}(i).col)$ **then**
      $B_{shdw}(i).col = 0$ # Excluding scan-lines shorter then 90% of scan depth.
    end if
  end for
  $B_{shdw} = rmv\_obj(B_{shdw})$ # function removing objects that are not attached at least to one side of the B_{shdw}.
end procedure

shadow regions from the gain adjustment process are essential to reduce the unnecessary gain adjustments and increase the speed of the algorithm.

The RF-data is used in this step to identify the insonified regions. For this purpose, the envelope of the RF data is computed. A binary mask, including intensity values lower than 10% of the dynamic range of the envelope data is generated. Each scan-line in the binary mask is then treated independently. Scan-lines longer than 90% of the maximum scan depth are kept on the binary mask and shorter ones are excluded. Parts of the mask that are not attached to one of the right or left borders are also excluded from the mask. This ensured that only elongated and very dark regions on one side or both sides of the scan remained. Those regions are considered as non-insonified areas and are excluded from the gain adjustments. Alg. 1 details the procedure. Fig. 2.2 shows a detected dark shadow, which is overlaid with brown color on top of the B-mode image.

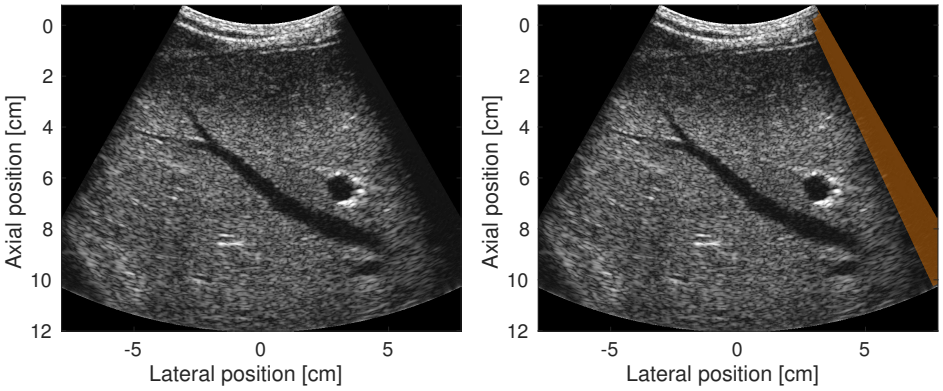

(a) Original scan.

(b) Shadow regions overlaid with color on the B-mode image.

Figure 2.2: Figure shows a *in-vivo* scan of human liver, for which shadow regions extracted using Alg. 1, and overlaid with brown color on the B-mode image. Only insonified-regions are used in gain adjustment.

2.5 Energy equalization

Another essential step in the gain adjustment is to compensate for the focusing effects and beam profile, and to homogenize the energy distribution in the scan plane. For this purpose, an experiment is conducted, in which a tissue mimicking speckle phantom is scanned and 50 frames are acquired. The mean of all 50 frames computed yielded a mean frame. The lateral median of the 50 scan lines bracketing the center-line on the mean frame is computed to yield an energy curve as a function of depth, which is shown in Fig. 2.3(a). The curve, in a sense, describes the energy distribution in the scan. The curve is then inverted, normalized to a maximum of one, and used to scale the energy levels of all the scan-lines in the image (see Fig. 2.3(b)). This is performed to ensure that the energy is equally distributed throughout the scanned media.

2.6 SNR map

This section computes 2-D SNR maps and uses them as a rough indication of whether the images contain large fluid regions or not. Complex IQ data are used to compute the SNR for all the frames. The acquired frame from the transducer, is contaminated with noise and can be written as $\mathbf{Y}_i = \mathbf{S}_i + \mathbf{E}_i$, where matrix $\mathbf{S}_i$ is the desired frame signal,

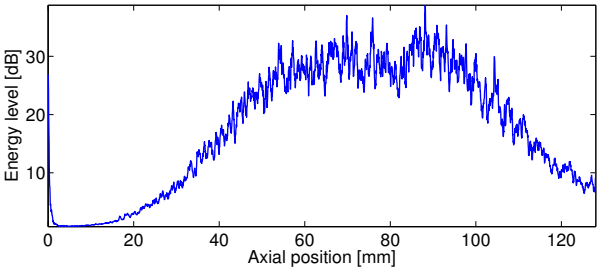

(a) Median of the energy levels of 50 scan lines on the mean frame.

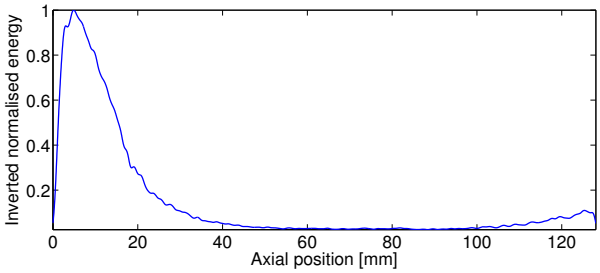

(b) Inverted and normalized energy curve in *(a)* which is applied to all scan lines for energy equalization.

Figure 2.3: Illustration of energy equalization procedure using tissue mimicking phantom measurements. 50 frames of a tissue mimicking phantom is acquired. 50 frames are averaged and a mean-frame is generated. (a) This curve shows the lateral Median of the energy levels of 50 scan lines bracketing the center-line of the mean-frame. (b) The curve in *(a)* is inverted, scaled to a maximum of one and applied to all scan-lines.

$\mathbf{E}_i$ is the noise contribution, and i is the frame number. The measurement is performed on a tissue mimicking phantom with an attenuation of $0.5\ \mathrm{dB/cm} \times \mathrm{MHz}$ and N frames acquired, the mean acquired signal is given by

$$\mathbf{M} = \hat{\mathbf{Y}} = E\left\{\mathbf{Y}_i\right\} = E\left\{\mathbf{S}_i + \mathbf{E}_i\right\} = \frac{1}{N}\sum_{i=1}^{N}(\mathbf{S}_i + \mathbf{E}_i) \tag{2.6}$$

in which matrix $\mathbf{M}$ represents the mean of acquired frames. Given the assumption that $E\left\{\mathbf{E}_i\right\} = 0$, the mean acquired signal by averaging all the frames will be equivalent to the mean desired signal and can be written as $\mathbf{M} = \hat{\mathbf{Y}} = \hat{\mathbf{S}}$. The noise contribution for each frame is estimated by subtracting the mean of the all frames from a single frame $\mathbf{E}_i = \mathbf{Y}_i - \hat{\mathbf{Y}}$. Therefore, the noise power for the ultrasound system is expressed as follows:

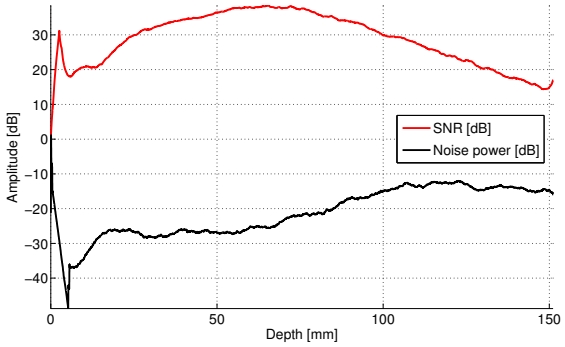

Figure 2.4: SNR and noise contribution along the center-line of a scan of a tissue mimicking phantom with an attenuation of $0.5\ \mathrm{dB/cm} \times \mathrm{MHz}$.

$$\mathbf{P}_{noise} = \left| \frac{1}{N} \sum_{i=1}^{N} \mathbf{E}_i^2 \right| \tag{2.7}$$

Finally, the SNR map for an acquired *in vivo* frame is determined by dividing the signal power of that frame by the system noise power $\mathbf{P}_{noise}$ computed in (2.7)

$$\mathbf{P}_{signal}(i) = |\mathbf{Y}_i|^2 \tag{2.8}$$

$$\mathbf{SNR}_{dB}(i) = 10 \log_{10} \left(\frac{\mathbf{P}_{signal}(i)}{\mathbf{P}_{noise}} \right) \tag{2.9}$$

where $\mathbf{Y}_i$ in (2.8) is the signal acquired from frame number i in a sequence of *in_vivo* scans. The power of signal changes from frame to frame, while the noise power is unchanged. The variation of noise and SNR with depth for a scan of tissue mimicking phantom along its center-line is depicted in Fig. 2.4. Also, two examples of the 2-D SNR maps computed from scans of the human bladder and liver are shown in Figs. 2.5(a) and 2.5(c) respectively.

The essential first step in the proposed time gain compensation algorithm is to determine whether the scans included large fluid collections or not. As it is anticipated, fluid collections appear as very low SNR regions on the SNR maps. Two features are specifically designed to characterize this property on SNR maps. First, a cumulative histogram of the values inside the SNR map is computed. Then, a curve is fitted to the counts, and the slopes of the fitted curve at 25th and 80th percentiles of the curve are used to characterize the amount of fluid in the scans.

The idea behind using these two features is to benefit from changes in distribution of SNR values in SNR maps to distinguish between different scans. The number of counts of low SNR values in scans with large fluid collections is higher compared to that of scans with small or no fluid collections. This yield a steeper slope of the cumulative histogram at low SNR values (i.e. 25th percentile) for scans with large anechoic regions compared to that of scans with no anechoic regions. The same effect decreased the slope of the cumulative histogram at high SNR values (i.e. 80th percentile) for scans with large anechoic regions compared to that of scans with no anechoic regions. The rate of decrease in the slope at the 80th percentile is much larger than the increase in the slope at the 25 percentile. Therefore, it is decided to use the slope at the 80th percentile (F_1) to distinguish between the two different scans with large fluid collections and small or no fluid collections. The value of F_1 is determined empirically using 4 scans additional to the 44 scans used for evaluation of the AHTGC algorithm. $F_1 < 2500\ \mathrm{dB}^{-1}$ characterized a scan with large fluid collection, otherwise, the scan is considered to contain small or no collections of fluid.

Figs. 2.5(b) and 2.5(d) illustrate how this feature is calculated for two scans of the human bladder and liver. These two figures show the cumulative histogram of the SNR images over 100 bins. 100 bins are used to ensure that a high variation of SNR values in each map is captured in the histogram and also that the precision of the density estimation is not jeopardized. In the next step of the algorithm, each scan is dynamically compensated for the attenuated gain using a TGC curve.

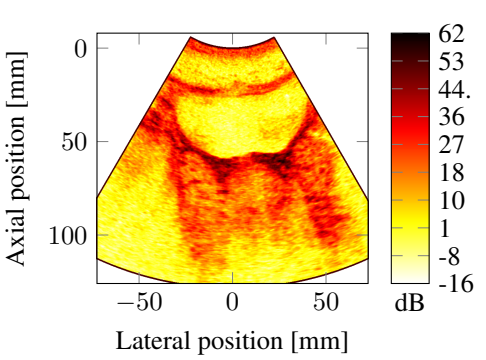

(a) 2-D SNR map of a scan of human bladder.

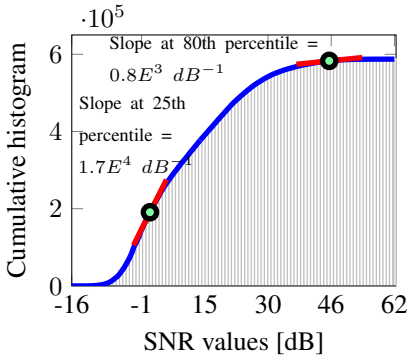

(b) Cumulative histogram of SNR values in *(a)*.

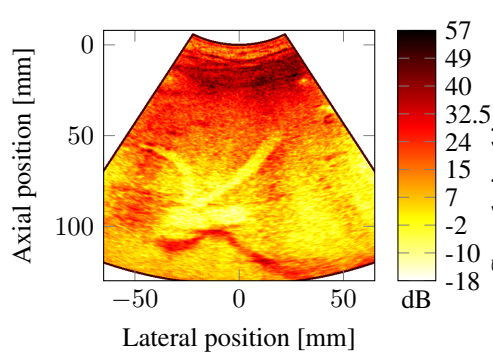

(c) 2-D SNR map of a scan of human liver.

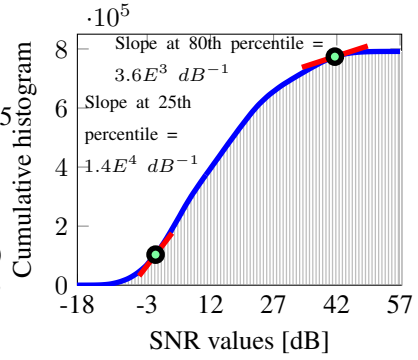

(d) Cumulative histogram of SNR values in *(c)*.

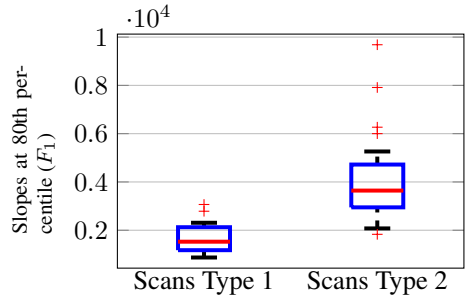

Type 1: Scans with large fluid regions.

Type 2: Scans with small or no fluid regions.

(e) Distribution of 80th percentile slopes (feature F_1)for two types of scans.

Figure 2.5: Two examples of 2-D SNR maps computed for scans of human bladder and liver with illustration of how their corresponding slope feature is calculated. (a) 2-D SNR map of the human bladder. (b) Cumulative histogram of all SNR values in map *(a)* and slopes calculated at 25th and 80th percentiles of the fitted curve. (c) 2-D SNR map of the human liver. (d) Cumulative histogram of the values in map *(c)* and slopes calculated at 25th and 80th percentiles of the fitted curve. (e) Boxplots of 80th percentile slopes for two types of scans.

2.7 Dynamic TGC

A TGC curve is dynamically computed for each frame and used to compensate for the gains. For this purpose, the envelope of the acquired scan is first computed. A cumulative histogram of the intensity values is then generated. The intensity values less than half of the maximum intensities in the envelope are disregarded and a mask of strong signal regions is generated. The mask is applied to the envelope, and the lateral median of the intensities lying inside the mask is computed. The computed curve presents drastic fluctuations and cannot be used directly to analyze the axial intensity changes in the envelope. To address this, the curve is smoothed using a Sovitsky-Golay filter. This technique fits a low-degree polynomial to a subset of adjacent data points by the linear least-squared method. If data points are equally spaced, an analytical solution to the least-squared method can be reached by expressing it as a generic set of convolution coefficients. Applying the convolution coefficients onto the subset of data points produces an estimate of the smoothed signal together with its derivatives at the central point of the subset. Smoothing a data set using convolution coefficients was first introduced by Savitzky and Golay in 1964 (Savitzky and Golay 1964). The values of the convolution coefficients depend solely on the size of the subset and the order of the polynomial that is fitted to the subset. For instance, fitting a second-order polynomial to a subset of five data points gives the following equations for approximating the zero, first, and second-order derivatives (Orfanidis 1996):

$$y_n = \frac{1}{35}(-3x_{n-2} + 12x_{n-1} + 17x_n + 12x_{n+1} - 3x_{n+2}), \tag{2.10}$$

$$\dot{y}_n = \frac{1}{35}(-7x_{n-2} - 3.5x_{n-1} + 3.5x_{n+1} + 7x_{n+2}), \tag{2.11}$$

$$\ddot{y}_n = \frac{1}{35}(10x_{n-2} - 5x_{n-1} - 10x_n - 5x_{n+1} + 10x_{n+2}). \tag{2.12}$$

Eqs. (2.11)–(2.12) find the first and second-order derivatives of y_n at x_n, where n is the central data point of the subset. Each window of five data points is weighted by the Savitzky-Golay convolution coefficients, B_k, which for the two derivatives are $B_1 = \frac{1}{35}[-7, -3.5, 0, 3.5, 7]$ and $B_2 = \frac{1}{35}[10, -5, -10, -5, 10]$, respectively.

Then the general trend of the curve is extracted by applying the singular-spectrum analysis (SSA). SSA does not require a model of time series, and extracts the trend of time series in the presence of noise and oscillations (Golyandina, Nekrutkin, and Zhigljavsky 2001).

The basic algorithm of SSA has two parts: decomposition of a time series, and then reconstruction of a desired additive component, such as a trend. For decomposition, a window with length of $L(1 < L < N)$ is chosen and a trajectory matrix $X \in \mathbb{R}^{L \times K}$,

$K = N - L + 1$ is constructed, with step-wise portions of the time series x_n taken as columns:

$$(x_0, ..., x_{N-1}) \rightarrow \mathbf{X} = \begin{pmatrix} x_0 & x_1 & \dots & x_{N-L} \\ x_1 & x_2 & \dots & x_{N-L+1} \\ \vdots & \vdots & \ddots & \vdots \\ x_{L-1} & x_L & \dots & x_{N-1} \end{pmatrix} \tag{2.13}$$

Then the Singular Value Decomposition (SVD) of $\mathbf{X}$ is performed, where the j'th SVD component is represented by an eigenvalue j and a real-value eigenvector U_j of $\mathbf{X}\mathbf{X}^T$:

$$\mathbf{X} = \sum_{j=1}^{L} \sqrt{\lambda_j} U_j V_j^T, \qquad Vj = \frac{\mathbf{X}^T U_j}{\sqrt{\lambda_j}}. \tag{2.14}$$

The SVD components are sorted in the descending order of their eigenvalues. The reconstruction has three steps. First, a sub-group ($\xi \subset 1, \dots, L$) of several SVD components are chosen. The second step is performed by hankelization (averaging along entries with indices $i + j = const$) of the $L \times K$ matrix from the selected ξ components of the SVD. Finally, reconstruction of a time series component of length N from the Hankel matrix by the one-to-one correspondence but in the reverse direction, see below the exact formulae.

The result of the reconstruction stage is a time series additive component:

$$\mathbf{X}_\xi = \sum_{\xi} \sqrt{\lambda_j} U_j V_j^T \rightarrow G = (g_0, \dots, g_{N-1}) \tag{2.15}$$

For a complete description of the SSA algorithm, see ((Golyandina, Nekrutkin, and Zhigljavsky 2001), Chapter 1) and (Alexandrov 2008). Trend extraction in SSA requires choosing a window length L, and selecting a group of SVD components used for trend reconstruction. The L is assumed to be 5% of the maximum penetration depth.

The reconstructed trend curve depicts the trend of intensity change within the envelope and harbors no sudden fluctuations. The curve is finally normalized to its maximum, inverted and applied as a TGC to the envelope to compensate for the gradual changes in the intensities (see Fig. 2.6). Alg. 2 details the dynamic TGC curve computation for a frame. The dynamic adjustment of intensities using this curve might over-gain inside the fluid regions. The next step computes normalized attenuation maps that can be used to

correct the possible miss-adjusted gains inside the fluid regions after applying the TGC curve.

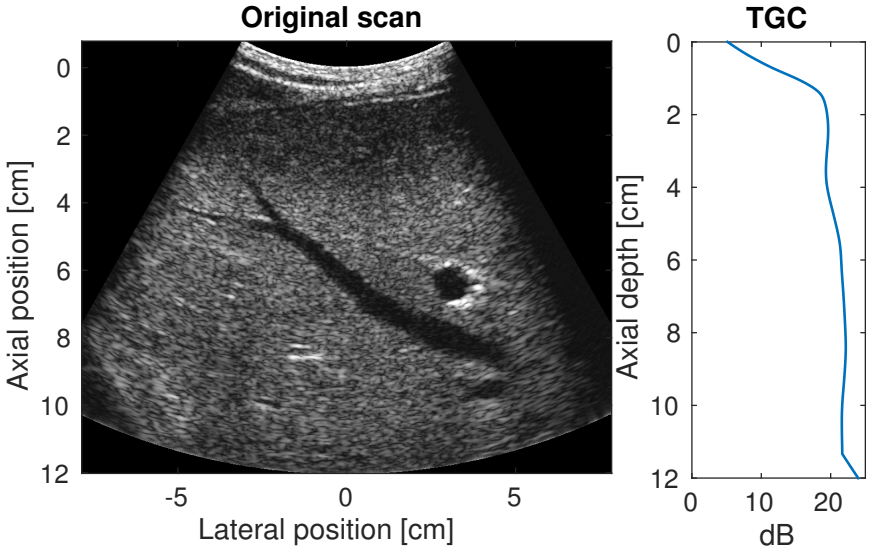

(a) Scan for which the TGC curve is computed.

(b) TGC curve computed for *(a)*.

Figure 2.6: Illustration of a TGC curve dynamically computed for an *in vivo* scan of the human liver using ALg 2. TGC curve does not harbor any sudden fluctuations.

2.8 Tissue characterization map

A log spectral difference method adapted from Kuc (Kuc, Schwartz, and Micsky 1976; Kuc 1984) is used to compute tissue characterization maps highlighting less attenuating regions. The beamformed RF data is used to compute the characterization maps. Each RF line is partitioned into several overlapping segments, in which each RF segment is gated axially by a Tukey function to alleviate the spectral leakage at both boundaries. Each two overlapping segments in the RF line are paired together, where the upper segment is considered as the proximal and the underlying segment is considered as the distal segment. For each pair, the difference between the logarithm of power spectra is computed, a line is fitted to the power spectral difference, and the slope of the resulting line is considered

Algorithm 2 Dynamic TGC calculation

Input: Env envelope of RF-data,
Output: TGC Time-gain compensation curve dynamically computed for each frame.

procedure DYNATGC
Let Env be a discrete gray scale image and let n_i be the number of occurrences of gray level i.
$p_{_{Env}(i)} = p\,(Env = i) = \frac{n_i}{N}, 0 < i < L$ # probability of an occurrence of a pixel of level i in the Env.
Let L be the total number of gray levels in the Env (in our case 256), N being the total number of pixels in the image, and $p_{_{Env}(i)}$ be the image's histogram for pixel value i, and normalized to $[0, 1]$.
for each $i \in L$ **do**
$cdf_{_{Env}(i)} = \sum_{j=0}^{i} p_{_{Env}(j)}$ # define the cumulative distribution function corresponding to $p_{_{Env}}$.
end for
Let th_l be the gray value for which $cdf_{_{Env}=0.5}$ and th_h be the gray value in which $cdf_{_{Env}=1}$.
Let I_{bright} be a zero gray scale image with the same size as image Env
for each $ii \in N$ **do** # N is the total number of pixels in the image Env.
if $th_l \leq Env(ii) \leq th_h$ **then**
$I_{bright}(ii) = Env(ii)$ # I_{bright} contains parts of the Env lying between the two thresholds of th_l and th_h.
end if
end for
$TGC = lat\_med(I_{bright})$ # computes the lateral median of I_{bright}.
$TGC = Sovitsky\_Golay(TGC)$ # smoothes the TGC curve using Sovitsky-Golay filter.
$TGC = SSA(TGC)$ # performing single-spectrum-analysis and extracting the trend of TGC.
$TGC = \frac{TGC}{max(TGC)}$ # normalizes the TGC curve to its maximum.
$TGC = \frac{1}{TGC}$ # inverts the curve to be multiplied to each scan line.
end procedure

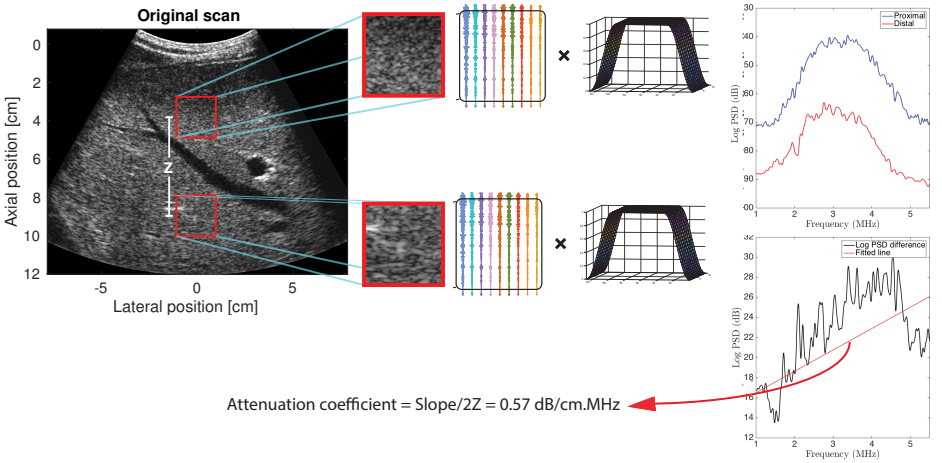

Figure 2.7: Illustration of how attenuation coefficients are computed. The scanned plane is subdivided to several overlapping proximal and distal segments. Each RF segment is gated axially by a Tukey function to alleviate the spectral leakage at both boundaries. The the slop of the line fitted to the curve created from subtracting the log spectra of the two segments identifies the attenuation coefficient.

as an attenuation value for the proximal segment (see Fig. 2.7). Both proximal and distal segments are moved down on the RF line and several attenuation values are calculated along the RF line by pairing the proximal and distal segments. Blocks are overlapped 50% to increase axial resolution of the characterization maps. The resulted values for RF lines are laterally averaged over scan lines to reduce the high variability of the characterization values in the map. Fig. 2.8 shows an example of a normalised tissue characterization map computed for a scan of human bladder, overlaid on the B-mode image. The length of the RF segments and the number of averaging scan lines determined the axial and lateral resolution of the estimated profiles, respectively. The literature suggests the axial RF segment lengths to be between 1 to 2 cm, and that the number of the averaging lines should be between 8 to 25 RF lines (Klimonda, Litniewski, and Nowicki 2009). In this study, anechoic regions adjacent to soft tissue presented a large attenuation variation. To capture this variation, the length of axial segments is set to 1 cm, and the number of averaging RF lines is set to 10 lines. The generated characterization maps are then normalized and multiplied to the compensated images using the dynamic TGC curve (Section 2.7) to correct the gains inside the fluid collections.

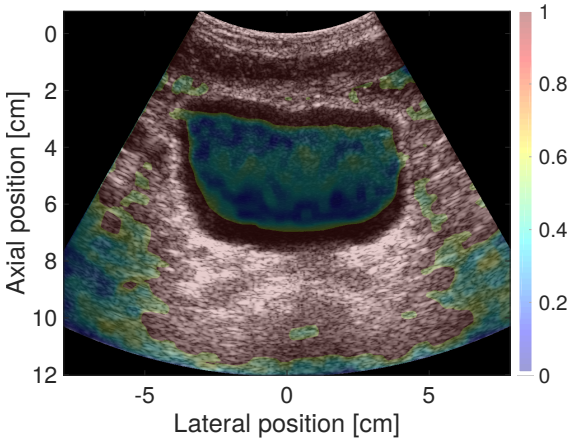

Figure 2.8: Normalized tissue characterization map computed for a scan of human bladder. Values close to zero indicate structures attenuating less, and regions with values close one identify the structures attenuating more.

2.9 Scan protocol and image data

Fifteen subjects are recruited and scanned after informed consent, and a total of 45 abdominal sequences each containing 50 frames are acquired. In addition to the urine bladder and gallbladder scans with large anechoic regions, other anatomical locations such as the liver and kidney are also included in the dataset. This is done to evaluate the performance of the algorithm on images with less-variable attenuation distribution. The beamformed RF data are acquired using a BK3000 ultrasound scanner (BK Ultrasound, Denmark) connected to a 192-element 3.5 MHz convex array transducer (9040, BK Ultrasound). The dynamic received focus technique with factory preset TGC is employed to generate the sequences.

2.10 Evaluation of image quality

The proposed algorithm is applied to all 45 *in-vivo* movie sequences each containing 50 frames. To empirically evaluate the performance of the AHTGC algorithm, matching pairs of *in vivo* sequences, one adjusted by the factory preset TGC with no default gains and the other processed with AHTGC, are evaluated side by side by four experienced radiologists. The evaluation is double blinded, and each pair is shown twice by randomizing the left and right positioning. This resulted in a total of 360 ($45_{image\ pairs} \times 4_{evaluators} \times 2_{random\ displays}$) independent visual evaluations. The radiologists are asked to score the

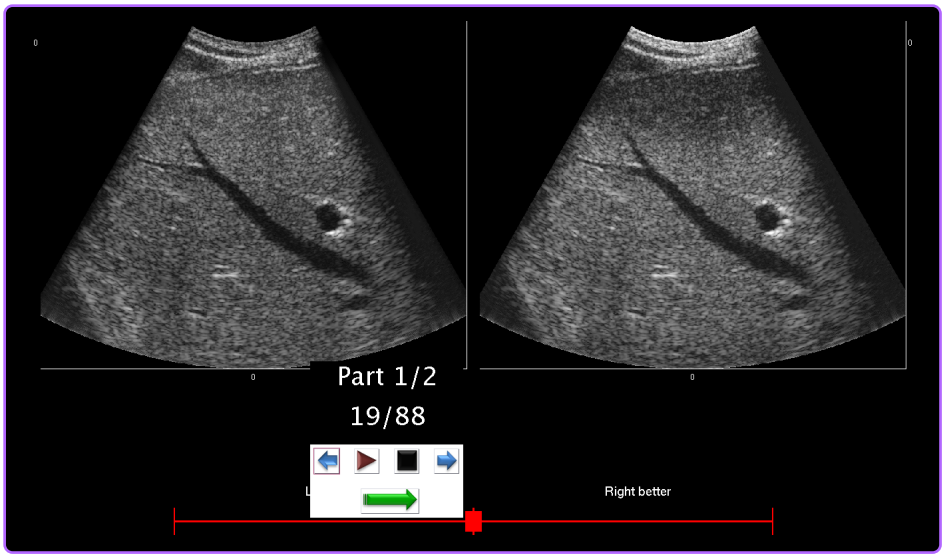

Figure 2.9: Evaluation of the image quality performed by randomizing the position of matching pairs of processed and unprocessed data. The image on the left is a AHTGC processed scan of human liver, and the image on the right is right is the scan adjusted by the factory preset TGC with no default gains.

image quality of each pair on a visual analogue scale (VAS) ranging between -50 and +50. This is performed by dragging a slider towards their favored cine loop, where a positive scale favors the processed sequence with the AHTGC algorithm (see Fig. 2.9). The distribution of ratings from the individual doctors are shown in Fig. 2.10. Visualization and assessment are handled using the program IQap (Hemmsen et al. 2010). Figs. 2.11 to 2.14 show eight examples of the experimental results of the AHTGC algorithm applied to scans of a human bladder, gallbladder, liver and carotid artery.

2.11 Evaluation criteria

The Wilcoxon signed-rank test, a non-parametric statistical hypothesis test, is applied to the provided ratings by the radiologists to examine whether radiologists preferred the processed sequences or the unprocessed data. This test is often used when comparing repeated measurements on a single sample to assess whether their population mean ranks differ.

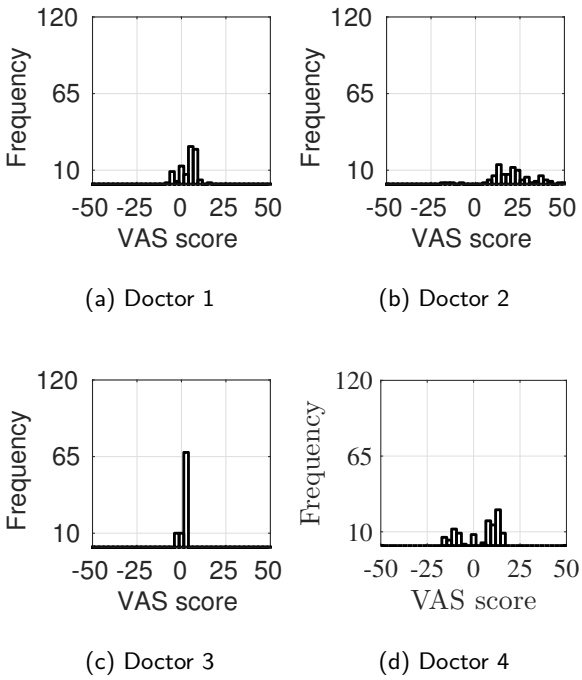

Figure 2.10: Distribution of visual analogue scale (VAS) scores from assessment of overall image quality by four expert radiologists using the tool shown in Fig. 2.9. Positive values favor AHTGC algorithm.

2.12 Summary

The average VAS score computed is highly positive 11.1 (p-value: 1.09×10^{-13}), explicitly indicating that the Proposed AHTGC technique is preferred by the doctors. The Wilcoxon signed-rank test is also applied to scores provided by doctors only for scans with large anechoic regions (type 1). The p-value: 3×10^{-5} indicated that in a subset of cine-loops with large fluid collections, the proposed AHTGC is preferred.

This chapter presented an automatic hierarchical TGC that uses estimates such as focus gain and energy level, scatterer strength, and decay of the spectrum of the received signal for gain adjustments. 2-D SNR maps are used for distinguishing between the different scans. 2-D tissue characterization profiles are used to correct the gains after scaling the gains by TGC curves. The proposed technique is automatic, robust, and has a more

flexible control over the gains, specially for the anechoic regions. The technique alleviates the problems with 1-D manual and automated TGC methods, reduces the unnecessary and manual gain adjustments on the scanners keyboards, and has the potential to facilitate the use of scanners in point-of-care ultrasound.

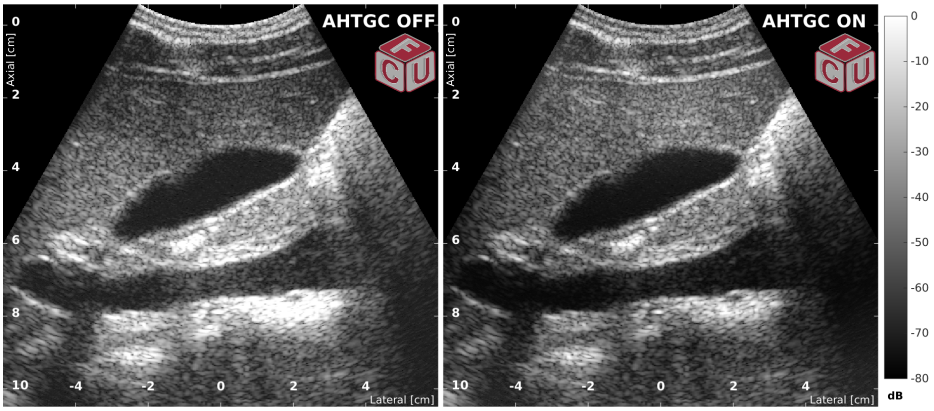

(a) Result of AHTGC applied to a sagittal view of a human gallbladder and inferior vena cava. The Image on the left is adjusted by the factory preset TGC with no default gains, and The image on the right is processed with AHTGC.

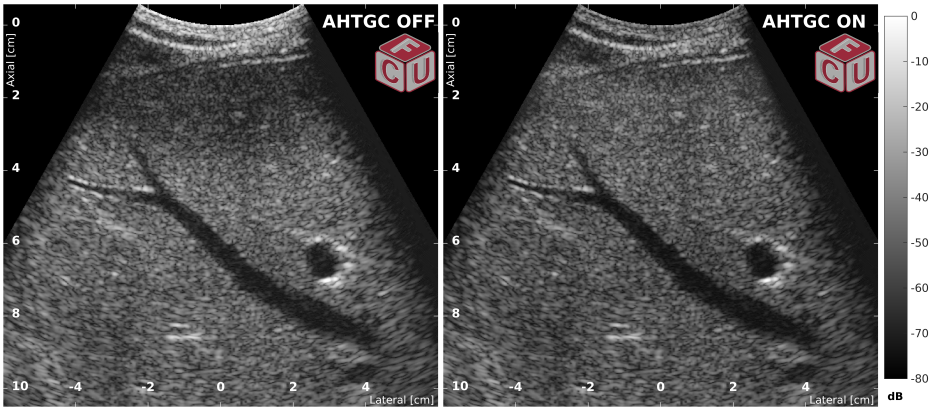

(b) Result of AHTGC applied to a axial view of a human liver. The Image on the left is adjusted by the factory preset TGC with no default gains, and The image on the right is processed with AHTGC.

Figure 2.11: *In-vivo* scans adjusted by the factory preset TGC with no default gains "AHTGC OFF" are compared with the identical scans processed with AHTGC algorithm "AHTGC ON".

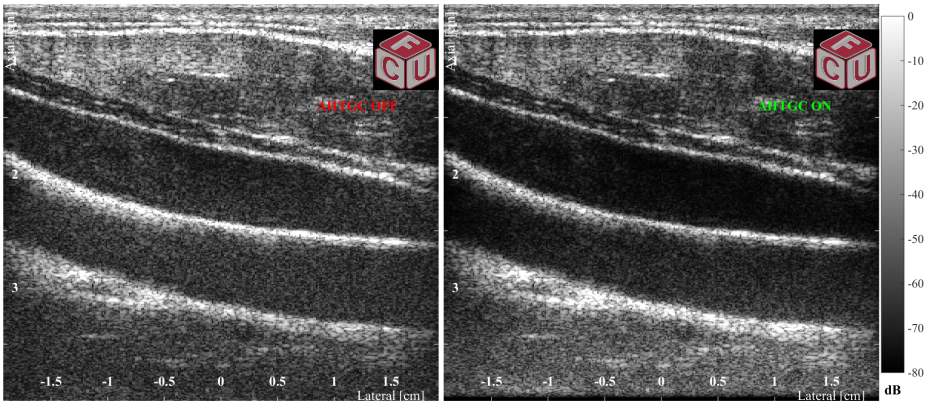

(a) Result of AHTGC applied to a sagittal view of a human carotid and jugular vein. The Image on the left is adjusted by the factory preset TGC with no default gains, and The image on the right is processed with AHTGC.

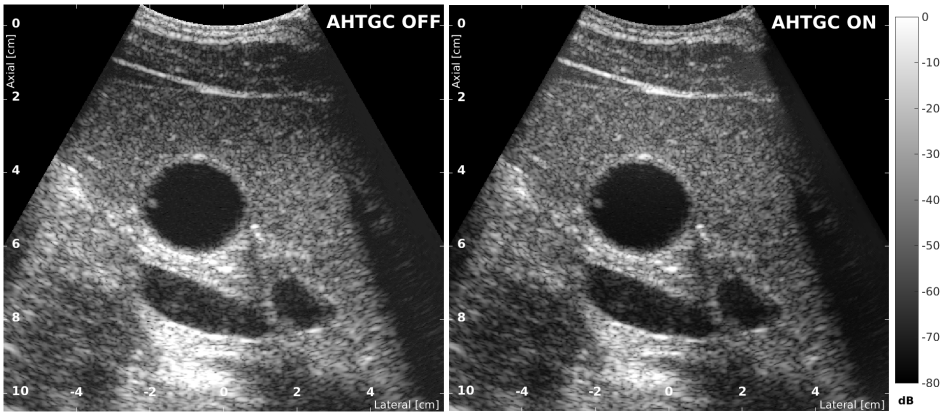

(a) Result of AHTGC applied to an axial view of a human gallbladder. The Image on the left is adjusted by the factory preset TGC with no default gains, and The image on the right is processed with AHTGC.

Figure 2.12: *In-vivo* scans adjusted by the factory preset TGC with no default gains "AHTGC OFF" are compared with the identical scans processed with AHTGC algorithm "AHTGC ON".

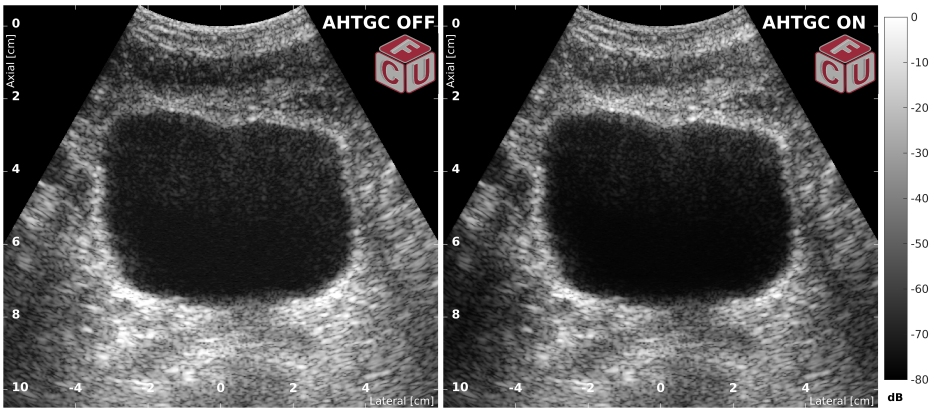

(a) Result of AHTGC applied to an axial view of a human bladder. The Image on the left is adjusted by the factory preset TGC with no default gains, and The image on the right is processed with AHTGC.

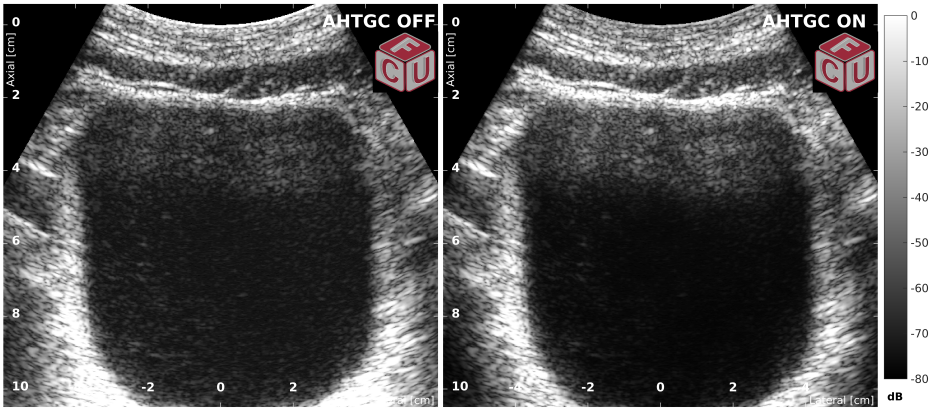

(b) Result of AHTGC applied to an axial view of a human bladder. The Image on the left is adjusted by the factory preset TGC with no default gains, and The image on the right is processed with AHTGC.

Figure 2.13: *In-vivo* scans adjusted by the factory preset TGC with no default gains "AHTGC OFF" are compared with the identical scans processed with AHTGC algorithm "AHTGC ON".

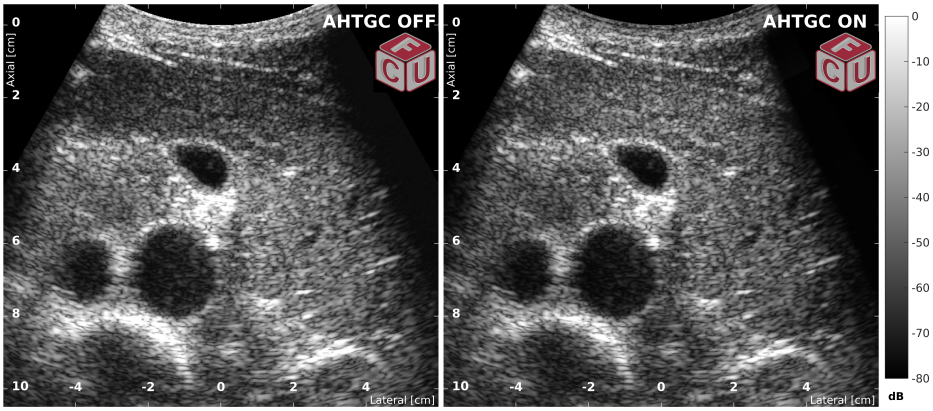

(a) Result of AHTGC applied to an axial view of a human gallbladder. The Image on the left is adjusted by the factory preset TGC with no default gains, and The image on the right is processed with AHTGC.

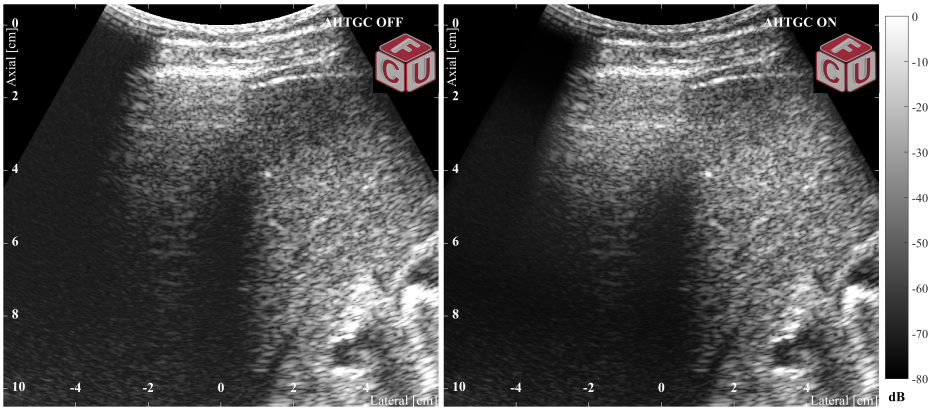

(b) Result of AHTGC applied to a scan of human kidney. The Image on the left is adjusted by the factory preset TGC with no default gains, and The image on the right is processed with AHTGC.

Figure 2.14: *In-vivo* scans adjusted by the factory preset TGC with no default gains "AHTGC OFF" are compared with the identical scans processed with AHTGC algorithm "AHTGC ON".

References from Chapter 2

Savitzky, A. and M. J. E. Golay (1964). "Smoothing and differentiation of data by simplified least squares procedures". In: *Anal. Chem.* 36.8, pp. 1627–1639 (cit. on p. 24).

Kuc, R., M. Schwartz, and L. Micsky (1976). "Parametric Estimation of the Acoustic Attenuation Coefficient Slope for Soft Tissue". In: *Proc. IEEE Ultrason. Symp.* Pp. 44–47 (cit. on p. 26).

Kuc, R. (1984). "Estimating acoustic attenuation from reflected ultrasound signals: Comparison of spectral-shift and spectral-difference approaches". In: *IEEE Trans. Acous., Speech, Sig. Pro.* 32.1, pp. 1–6 (cit. on p. 26).

Inbar, D. and M. Delevy (1989). *Time gain compensation for ultrasonic medical imaging systems*. US Patent 4,852,576 (cit. on p. 16).

Pye, S., S. Wild, and W. McDicken (1992). "Adaptive time gain compensation for ultrasonic imaging". In: *Ultrasound Med. Biol.* 18.2, pp. 205–212 (cit. on p. 16).

Jensen, J. A. (1996). *Estimation of Blood Velocities Using Ultrasound: A Signal Processing Approach*. New York: Cambridge University Press (cit. on pp. 13, 14).

Klesenski, K. (1996). *Automatic gain compensation in an ultrasound imaging system*. US Patent 5,579,768 (cit. on p. 16).

Orfanidis, S. J. (1996). *Introduction to signal processing*. Pearson Education, Inc. (cit. on p. 24).

Golyandina, N., V. Nekrutkin, and A. A. Zhigljavsky (2001). *Analysis of time series structure: SSA and related techniques*. CRC press (cit. on pp. 24, 25).

Lee, D., Y. Kim, and J. Ra (2006). "Automatic time gain compensation and dynamic range control in ultrasound imaging systems". In: *Proc. SPIE Med. Imag.* 6147, pages (cit. on pp. 15, 16).

Alexandrov, T. (2008). *A method of trend extraction using singular spectrum analysis*. Tech. rep. arXiv preprint arXiv:0804.3367 (cit. on p. 25).

Klimonda, Z., J. Litniewski, and A. Nowicki (2009). "Spatial Resolution of Attenuation Imaging". In: *Archives of Acoustics* 34.4, pp. 461–470 (cit. on p. 28).

Tang, M., F. Luo, and D. Liu (2009). "Automatic Time Gain Compensation in Ultrasound Imaging System". In: *Proc. IEEE Int. Conf. Bioinfo. Biomed. Eng.* Pp. 1–4. DOI: 10.1109/ICBBE.2009.5162432 (cit. on p. 16).

Hemmsen, M. C., M. M. Petersen, S. I. Nikolov, M. B., Nielsen, and J. A. Jensen (2010). "Ultrasound image quality assessment: A framework for evaluation of clinical image quality". In: *Proc. SPIE Med. Imag.* Vol. 76291. Medical Imaging 2010: Ultrasonic Imaging, Tomography, and Therapy, pp. 76290C–12 (cit. on p. 30).

Szabo, T. L. (2014). *Diagnostic ultrasound imaging: Inside out*. 2nd ed. Elsevier (Oxford, UK) (cit. on p. 13).

CHAPTER 3

Synthetic Aperture Image Quality Optimization

The present chapter deals specifically with the optimization of SA image quality, the task of automatically selecting optimal parameters for acquisition of the SA images. The chapter discusses the principles behind the SA, reviews the literature on SA, and highlights the needs for SA image quality optimization. This chapter consequently, proposes a method for SA image quality optimization using a multi-objective optimization technique based on theory of Pareto optimality.

The remainder of this chapter is organized as follows. Section 3.1 introduces the SA, Section 3.2 reviews the literature on SA, and Section 3.3 discusses the need for optimization in SA. Sections 3.4 and 3.5 introduce the steering of the SA emissions, and the concept of grating lobes, respectively. Section 3.6 introduces the quality metrics used in this chapter for either optimization, or the assessment of the image quality. Section 3.7 introduces the analogy of the multi-objective Pareto optimality, and Section 3.8 uses the optimization procedure to optimize the SA image quality in simulation. Section 3.9 details the measurements cunducted in the study. Section 3.10 presents the results and Section 3.11 discusses the findings. Finally, Section 3.12 summarizes the chapter.

3.1 Principle of synthetic aperture

The basic principle in synthetic aperture (SA) imaging is to transmit a spherical wave using a single element or a transducer sub-aperture, which propagates in all directions in the medium simultaneously. The echoes recorded by the transducer elements used for reception contain information about every scatterer in the insonified region. Thus, the received signals can be steered and focused at all image points to form a complete image after one emission. This process is repeated by emitting a series of spherical waves one by one, and the reconstructed low resolution images (LRIs) are finally summed to produce a high resolution image (HRI). Fig. 3.1 illustrates the approach. Conceptually, the reconstruction of each point or pixel in the displayed SA image is performed by

coherently summing for all transmissions the echoes received from a point target located at the center of each pixel.

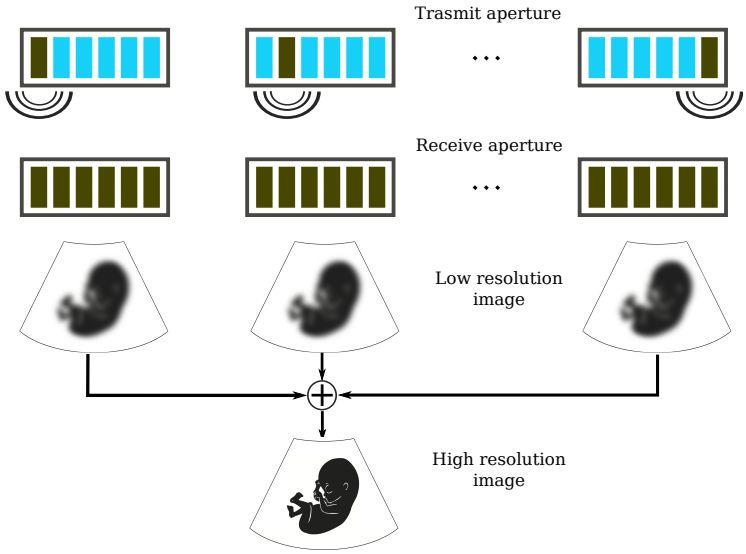

Figure 3.1: Illustration of the SA imaging principle. At each transmit event a single element or a sub-aperture is used to generate a spherical wave. The ultrasound pulse propagates in all directions in the medium simultaneously, and, thus, the recorded echoes contain information about every scatterer within the interrogated region. By steering and focusing these signals at every image point, a complete image is reconstructed after one emission. This procedure is repeated for all aperture element, and the resulting images are finally summed to produce the displayed ultrasound image.

3.2 Review of the synthetic aperture techniques

The modality was first introduced in radar systems in 1950s. In 1974, Burckhardt (Burckhardt, Grandchamp, and Hoffmann 1974) was the first in the literature to mention about application of the SA in medical imaging. He used the principles of the SA sonar and translated them for the use in ultrasound B-mode imaging. His investigations indicated that the lateral resolution using SA was improved in compare with that of conventional B-mode imaging. His paper also showed that SA was able to break the conventional paradigm between the frame rate and spatial resolution, and that object motion would

have deteriorating effects on resolution. Finally, Burckhardt (Burckhardt, Grandchamp, and Hoffmann 1974) suggested that the problem could be addressed by developing a fast parallel SA imaging system.

Conventional ultrasound imaging techniques acquired an image by sequentially beamforming one image line at a time. The acquisition time is, thus, limited by the speed of sound c. The maximum frame rate f_{max} for a frame with N lines with a depth of D is given by

$$f_{max} = \frac{c}{2DN}. \tag{3.1}$$

Therefore, by increasing depth and number of lines, the frame rate gets progressively lower. Another issue to be addressed in conventional techniques is the single transmit focus, for the situation which imaging is only optimally focused in one depth. This is usually addressed by performing compound imaging of number of transmit foci, which also decreased the frame rate. These issues opened new horizons for developing alternative imaging techniques in which the problem with the frame rate and the single transmit focusing.

SA has shown that can highly improve the frame rate and focus problems of traditional techniques (J. A. Jensen 2006). In standard SA approach, spherical waves are emitted in transmit that covers the full region of intereset. The received signals for all or part of the elements in the aperture are sampled for each transmission. The data are used to generate low resolution images (LRI), which are only focused in the receive (due to the un-focused transmission). The LRIs are then combined to generate a high resolution image (HRI) to synthesize the transmit focusing. The focus is both dynamic in transmit and receive, and the highest possible resolution for delay-sum beamforming is obtained everywhere in the image. Therefore, SA addressed the problems with low frame rate; when emissions with large areas of sonification can be used, and a complete LRI can be beamformed for each emission. By combining all the LRIs the final HRI is generated (J. A. Jensen, S. Nikolov, et al. 2006). SA also decouples the pulse repetition time and number of lines. This is possible as only a few set of emissions can create a full image, thus, very fast imaging can be performed.

Since the first introduction in 1974 (Burckhardt, Grandchamp, and Hoffmann 1974), different reconstruction algorithms have been introduced, in time and frequency doamin for SA. The frequency domain reconstruction algorithms became interesting in early synthetic aperture radar (SAR) (Goodman 1996). Given the limitations of available computational power at the time, they were very suitable for signal processing tasks. Other frequency based reconstruction was implemented by Mayer et al. (Mayer et al. 1990) and Busse (Busse 1992). Time domain SA reconstruction algorithms were also

introduced, which were computationally more expensive (Soumekh 1999). A mono-static SA focusing was introduced by (Bennett et al. 1982), and the performance of the system was discussed. O'Donnell in early 1990s used SA for intra-vascular imaging (O'Donnell and Thomas 1992). Ylitalo investigated several transducer geometries in SA and studied the signal-to-noise ratio (Ylitalo 1994; Ylitalo and Ermert 1994; Ylitalo 1995, 1996a,b). He also developed a real-time SA system.

In SA there is a trade-off between image quality and frame rate. However, the relationship is not straightforward, and many parameters must be considered such as signal to noise ratio (SNR). Given that SA uses expanding spherical waves, The signal energy might drop. To address the issue, SA using spherical waves has been studied for multi-element excitation using subapertures by O'Donnell and Thomas (O'Donnell and Thomas 1992), Karaman et al. (Karaman, Li, and O'Donnell 1995), (Karaman and O'Donnell 1998), Nikolov et al. (S. I. Nikolov, K. Gammelmark, and J. A. Jensen 1999), and for sparse synthetic aperture systems by Lockwood et al. (Lockwood, Talman, and Brunke 1998). Compared to conventional imaging, SA imaging has shown to improve anatomical imaging (K. L. Gammelmark and J. A. Jensen 2003), flow estimation (S. I. Nikolov and J. A. Jensen 2003; J. A. Jensen and S. I. Nikolov 2004; Yiu, Lai, and Yu 2014). All these applications required study of the number of emissions to preserve the frame rate and obtain optimal image quantity, useful for anatomic imaging, for fast flow estimation, and for image segmentation. Therefore, optimization of the SA imaging and transducer parameters should be performed to obtain the best trade-off between frame rate and image quality.

For the case of B-mode SA imaging, the number of emissions can be kept relatively high, whereas when flow estimates are needed, less emissions and consequently higher frame rates are interesting (O'Donnell and Thomas 1992; Karaman, Li, and O'Donnell 1995; Karaman and O'Donnell 1998; S. I. Nikolov, K. Gammelmark, and J. A. Jensen 1999). Few studies have investigated the application of synthetic aperture focusing for affordable ultrasound systems (Karaman, Li, and O'Donnell 1995). Other Studies have also applied SA focusing in ultrasound imaging (Vray et al. 1997).

3.3 Synthetic aperture and the need for optimization

Synthetic Aperture (SA) imaging produces high-quality images and velocity estimates of both slow and fast flow at high frame rates. However, the use of broader beams can generate higher side lobes, which degrades the image quality. This demands more emissions for a higher quality image, and as a consequence, lowers the frame rate. The trade-off between the image quality and frame rate must then be taken into account. This is why, optimization of parameters effecting the SA image quality is of great importance.

According to the literature review of SA in Section 3.2, currently, There are no automated and generic techniques in the literature for selecting optimal parameters in SA for different scenarios, such as B-mode imaging or flow imaging. The main challenge in devising such technique is to consider a multi-objective optimization regime that can accommodate several interdependent imaging parameters.

3.4 synthetic aperture steered emissions

In addition to subdividing the aperture in small portions during transmit in SA, each emission can also be steered to provide a better insonification of the interesting regions (see Fig. 3.2). However, every transducer element has a directivity pattern that determines the element's acceptance angle. This angle is related to how much an emission can be steered, and to the minimum receive F-number used for beamforming. The first essential step in designing steered emissions prior to image quality optimization, is to investigate the angular response of the transducer elements used in this study. Jensen et al. (J. Jensen, Stuart, and J. A. Jensen 2016) used the same transducer as this study and employed a model proposed by Oddershede and Jensen (Oddershede and J. A. Jensen 2007) based on SNR considerations to determine the opening angle of a virtual source. It is done to determine the element acceptance angle. The study showed that the acceptance angle for the transducer elements is $\pm 38^\circ$ giving a F-number of 0.64. Therefore, minimum and maximum thresholds of $\pm 30^\circ$ is used in this study as the maximum possible steering angle of the SA emissions during optimization. This is performed by considering that in imaging setups the maximum steering angle ranges between -30°:0.25°:+30°.

3.5 Grating Lobes and $\lambda/2$-pitch requirement

In linear array transducers, owing to regular spacing of the array elements, grating lobes exist in transmission and reception, if the inter-element pitch is wider than a half wavelength (Barthez, Léveillé, and Scrivani 1997; Szabo 2014).

For a linear array transducer, the location (angle θ_g) of receive grating lobes is obtained as (Huang, Que, and Jin 2004; Szabo 2014):

$$\theta_g = \sin^{-1}\left(\sin(\theta_s) - \frac{m\lambda}{p}\right), \quad (m = \pm 1, \pm 2, \pm 3, ...) \tag{3.2}$$

where p is the transducer pitch, λ is the receive-signal wavelength, θ_s is the steering angle of the main receiving lobe and m is a signed integer that is the order of the grating lobes. The location of the main receiving lobe corresponds to the value of $m = 0$. Considering the first order grating lobe ($m = \pm 1$),

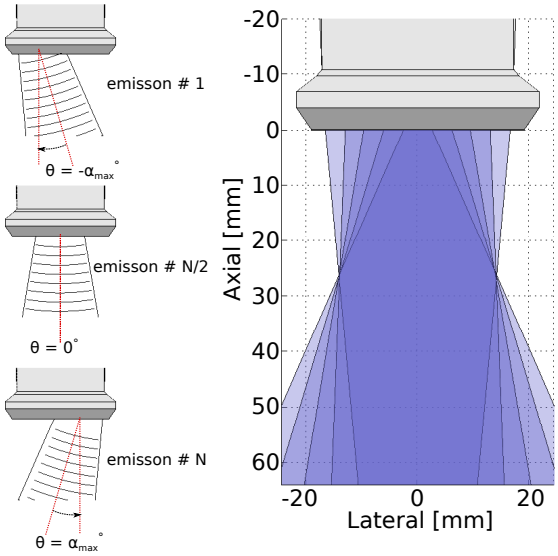

Figure 3.2: Illustration of the steered SA emissions principle. At each transmit event a sub-aperture is used. The maximum steering angle is α_{max}, and N is the number of emissions. The figure on the right shows the HRI created by combining all N emissions.

$$\theta_g = \sin^{-1}\left(\sin(\theta_s) - \frac{\lambda}{p}\right). \tag{3.3}$$

With a pitch of λ as for most commercial linear transducers, a steered wave of 15° generates a grating lobe at -48°. This is illustrated in Fig. 3.3, where the top and middle images show the emitted fields for a fixed time using a 1.5λ-pitch array and a λ-pitch array with Hamming transmit apodization. There is energy behind the wave front that travels in a direction -48° off axis. The grating lobe amplitude is around -25 dB relative to the main lobe, and the large spatial extend of the grating lobe in the near field results in artifacts in the final image. A pitch of $\lambda/2$ moves grating lobes outside the imaging plane even for steered wave fronts as shown in Fig. 3.3 (bottom image). The spherical edge waves emanate from the transducer edges. They can be suppressed in the emitted field by the use of apodization in transmit, and a Hamming apodization (weight 0.5) is efficient for this as shown in all three arrays.

(a) 1.5λ-pitch array with Hamming apodization.

(b) λ-pitch array with Hamming apodization.

(c) λ/2-pitch array with Hamming apodization.

Figure 3.3: Illustration of grating lobes, when a SA emission is emitted at 15°. For a 1.5λ-pitch array (top image), λ-pitch array (middle), and λ/2-pitch array(bottom). A Hamming (0.5) window was applied as apodization for the three arrays.

3.6 Imaging performance measures

Three metrics used in the literature for evaluating the performance of the ultrasound imaging quality are contrast resolution (CTR) (Ranganathan and Walker 2007; Guenther and Walker 2009), detail resolution or full-width at half maximum (FWHM) (Szabo 2014), and the contrast-to-noise ratio (CNR) (Lediju et al. 2011). Given the fact that CTR and FWHM are commonly used features to describe the quality of images in ultrasound imaging, this paper uses these two features for optimization. Optimization is performed based on the rate of changes in these features, while considering all the possible setups.

The CNR is not used in the optimization procedure. However, it is used as an alternative and independent measure for quantifying anechoic regions in measurements. This was done to evaluate, whether the optimal setup achieved by optimization, actually

yielded the optimal image quality.

3.6.1 Contrast resolution (CTR)

The CTR measures the contrast resolution and determines the ability of the imaging system to differentiate between an anechoic region bracketed within a uniform scattering medium. Ranganathan and Walker (Ranganathan and Walker 2007) quantified CTR as the ratio between the energy outside of a circular area surrounding the point spread function (PSF) with radius of r to the total energy of the PSF. Therefore it gives a measure of clutter energy outside the main lobe of the PSF. The CTR is then related to the radius r and is given as

$$CTR(r) = \sqrt{\frac{E_{out}(r)}{E_{total}}}, \tag{3.4}$$

where $E_{out}(r)$ is the PSF energy outside a circular region with radius r centered at the peak of the PSF and E_{total} is the total energy. CTR can be calculated for either a fixed radius to get a contrast measure, or by fixing the CTR to determine resolution as the required radius for a fixed relative energy. In this study the radius r is kept fixed, and CTR is determined as the relative energy for a fixed radius of 2.5λ ($r_{2.5\lambda}$).

3.6.2 Contrast-to-Noise Ratio (CNR)

The Contrast-to-Noise Ratio (CNR) is also used to quantify cyst contrast as (Lediju et al. 2011):

$$CNR = \frac{\mu_s - \mu_c}{\sqrt{\delta_s^2 + \delta_c^2}}, \tag{3.5}$$

where μ_c and μ_s are the mean intensities of envelope-detected signals from a region inside a cyst and a region of image speckle, and δ_c^2 and δ_s^2 are the corresponding variances. The cyst and speckle regions are of the same size and at the same depth.

3.6.3 Detail resolution

The detail resolution is the -6 dB width of the main lobe of the point-spread-function (PSF), i.e., the full width at half maximum (FWHM) (Szabo 2014). The FWHM is usually measured both axially and laterally, and those are both influenced by the bandwidth of the imaging system. The lateral FWHM is also dependent on the pulse wavelength, size of the aperture (F number), and the maximum steering angle of the emissions.

3.7 Method of optimization

This section describes the multi-objective optimization used in this study for optimizing the SA image quality based on the theory of Pareto optimality (Deb 2005).

In many circumstances, solutions in the presence of conflicting objectives are needed. In such cases, solutions are chosen such that sensible trade-offs exist among different objectives. Pareto optimization is used for finding these solutions. In multi-objective optimality theory, many solutions are found that satisfy the Pareto optimality criterion (Coello, Lamont, and Veldhuizen 2007). Consider an imaging system , in which two parameters of x_1 and x_2 are required to be optimized with respect to two interdependent objectives of f_1 and f_2 (i.e. performance metrics). vector $\mathbf{x} = \{x_1, x_2\}$ represents a possible solution or setup of the imaging system, which is a combination of x_1 and x_2. Notice, F is the objective function. A point $\mathbf{P} = F(\mathbf{x})$ is a set of interdependent objectives and can be shown by $\mathbf{P} = \{f_1, f_2\}$.

Pareto optimality criterion considers a solution to be optimum, only if there are no other solutions better than that with respect to all the objectives. A solution $\mathbf{x}' = \{x_1, x_2\}$ is a Pareto optimal solution if there exists no other solutions like $\mathbf{x}$ for which $\mathbf{P} = F(\mathbf{x})$ dominates $\mathbf{P}' = F(\mathbf{x}')$. A point $\mathbf{P}$ (a set of parameters in objective space) is dominating another point $\mathbf{P}'$ (mathematically given by $\mathbf{P} \preceq \mathbf{P}'$), when $\mathbf{P}$ is no worse than $\mathbf{P}'$ in all objectives, and $\mathbf{P}$ is strictly better than $\mathbf{P}'$ in at least one objective. Therefore, a Pareto optimal solution is given by

$$\mathcal{P}^* := \left\{ \mathbf{x}' \middle| \nexists\, \mathbf{x} : \ \mathbf{P} \preceq \mathbf{P}' \right\}. \tag{3.6}$$

The set of all optimal solutions is called the Pareto front or curve or surface (see red curve in Fig. 3.4). The shape of the Pareto front manifests the nature of trade-off between different parameters in the objective space. In this study the Pareto optimization is applied to a two-objective problem, in which two interdependent metrics of CTR and FWHM are used. The Pareto front is particularly interesting, because it contains the solutions where improvement in one variable is not possible without jeopardizing the other. Hence, in this study only the Pareto optimal solutions are considered.

The optimization proposed in this paper, aims to optimize SA image quality for superficial and small parts ultrasound imaging, such as carotid artery imaging for areas bracketed under the surface of the transducer. The interesting imaging area in this study, corresponded to the scanned region in a traditional line-by-line technique without steering of emissions.

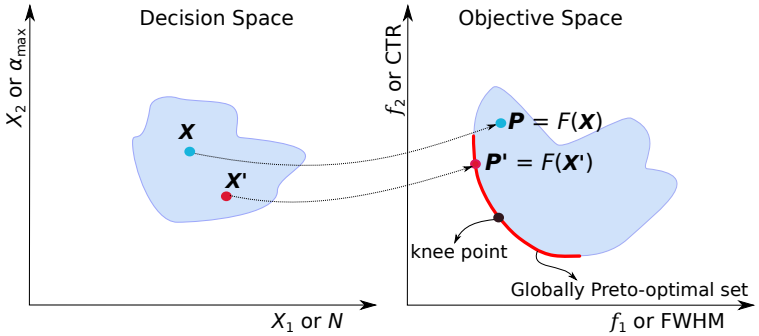

Figure 3.4: Illustration of how the Pareto optimization is performed. The axes of decision space include independent variables (imaging parameters that can be independently changed), whereas the axes of objective space contain the dependent variables (the interdependent features such as CTR and FWHM). The set of all Pareto optimal solutions or the Pareto front is shown with the red curve. The knee point of this curve represents the best trade-off between the dependent variables, and the best solution to the optimization.

3.8 Optimization of the SA sequence

This section explains how the optimization technique is performed using simulations.

3.8.1 Simulations

As described in Section 3.5, a λ/2-pitch transducer is more suitable in image formation in terms of producing much less grating lobes. Based on this, a λ/2-pitch array was modeled and six different point scatterers are simulated independently along the center-line of the transducer located at depths of 10, 20, 30, 40, 50, and 60 mm. Simulations are performed using the Field II program (J. A. Jensen and Svendsen 1992; J. A. Jensen 1996, 2014) (see Table 3.1 for details of the parameters used). A Hamming apodization on the active transmit aperture is used to reduce the edge waves.

The independent variables are number of emissions N and the maximum steering angle α_{max}. The evaluation of the image quality is performed with respect to the CTR and FWHM, which are thus, the dependent variables or objectives. The dependency means that improvement in one metrics jeopardizes the other. The objective function F maps the independent variables (N and α_{max}) to the dependent objectives (FWHM and CTR) (see Fig. 3.4). An automated technique is developed in MATLAB to generate a Pareto plot and it's Pareto front, for each of the six point targets. Several combinations of N and α_{max} ($\mathbf{x}$ in the decision space) are used for generating a HRI of each of point scatterers, and calculating the corresponding FWHM and CTR.

Table 3.1: Parameters used for simulation and measurements.

Parameters	λ/2-pitch transducer
Number of elements	192
Trans. center frequency f_0	4.1 MHz
Wavelength λ	0.376 mm
Element pitch	0.2 mm (0.56λ)
Element height	6 mm
Elevation focus	38 mm
Cycles in emitted pulse	1
Transmit apodization	Hamming
Receive apodization	Hamming
Transmit F-number	0.8
Receive F-number	1
Emission steering angles	-30°:0.25°:+30°
trans. sub aperture size (elements)	48

Based on Section 3.4, α_{max} are set to vary from -30° to +30° with 0.25° separation between emissions. This is performed to ensure that emissions are not outside the transducer element's acceptance angle. Number of emissions set to vary between 1 to 256. Received signals from all elements are stored for each emission and beamformation are performed using the BFT3 toolbox (Hansen, Hemmsen, and J. A. Jensen 2011). The beamformed LRIs are subsequently combined to HRIs. Several HRIs are generated by considering several combinations of maximum beam steered angle (α_{max}) and the number of emissions (N). The image quality of the HRIs are then evaluated by computing both CTR and the lateral FWHM for simulated point scatterers. Section 3.8.2 details how exactly the Pareto optimization is applied in simulation.

3.8.2 Optimization of the setup

For each simulated scatterer, two plots are generated. First one, quantifying the CTR as a function of α_{max} and N, and the second, quantifying the FWHM as a function of α_{max}

and N. Each of these plots represented a decision space for the simulated point scatterer (see the decision space in Fig. 3.4).

Two constraints based on the rate of improvement in CTR and FWHM, when increasing the α_{max} and N, is put on the number of required HRIs. First, at least an improvement of 1% is required in FWHM, when steering 2° more and using 2 more emissions. Second, at least an improvement of 2.5% is required in CTR, when steering 2° more and using 2 more emissions. The two constrains must be both satisfied, and those combinations, for which the constraints are no longer satisfied, are excluded from the possible optimal solutions. The remaining of the decision spaces are merged in a Pareto plot(see objective space in Fig. 3.4). It must be pointed out that several other constraints could have been used, such as weighting either CTR or FWHM and cut-off at a specified CTR or FWHM, yielding specified HRI quality. As mentioned in Section 3.7, the Pareto front is particularly interesting, but special attention must be paid to the knee-point solution on the Pareto front. It represents the best (among other points in the Pareto front) trade-off between CTR and FWHM for each point scatterer (see knee-point in Fig. 3.4). The center of gravity of all the knee-point solutions, belonging to all six point scatterers, is used as an optimal solution for the SA imaging system. This is done to include depth-dependency and to achieve a setup that yields good quality images for depths less than 60 mm.

3.9 Measurements

Phantom measurements are made using the SARUS experimental ultrasound scanner (J. A. Jensen, Holten-Lund, et al. 2013) driving a 192-element 4.1 MHz λ/2-pitch linear transducer (BK Ultrasound). A SA B-mode imaging sequence using the virtual sources behind the transducer is used to perform the imaging. Parameters used in the imaging sequence are depicted in the Table 3.1. First, a geometry wire phantom including two wires is scanned. A multi-purpose, multi-tissue phantom containing three anechoic cysts located at 17 mm, 48 mm, and 75 mm (Model 040GSE, CIRS inc., Virginia, USA) with acoustic attenuation of 0.5 dB/(cm$\times$MHz) is also scanned.

The *in-vivo* measurements are also performed using the SARUS scanner, driving a 192-element 4.1 MHz λ/2-pitch linear transducer (BK Ultrasound). The same imaging sequence as for the phantom measurements is used, but with the optimal values of the maximum steering angle α_{max} and the number of emissions N (computed in Section 3.10.1). Longitudinal scans of the right common carotid artery, and common carotid with bulbous are acquired from a 29 year-old male volunteer.

3.10 Results

This section presents the results of the simulations performed for the optimization procedure, phantom measurements and *in-vivo* measurements performed with the optimized sequence.

3.10.1 Simulation results

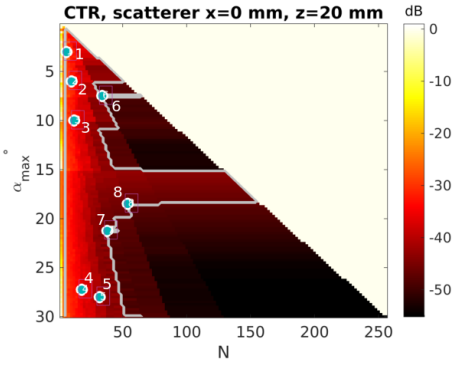

(a) CTR decision space, computed as a function of α_{max} and N for scatterer at 20 mm.

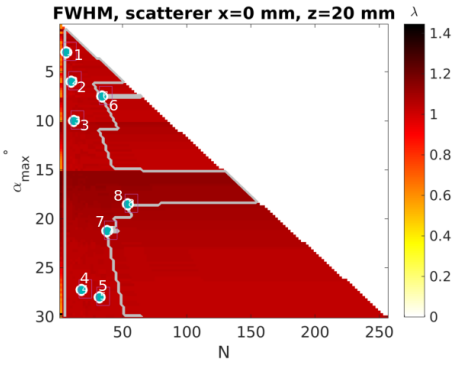

(b) FWHM decision space as a function of α_{max} and N for scatterer at 20 mm.

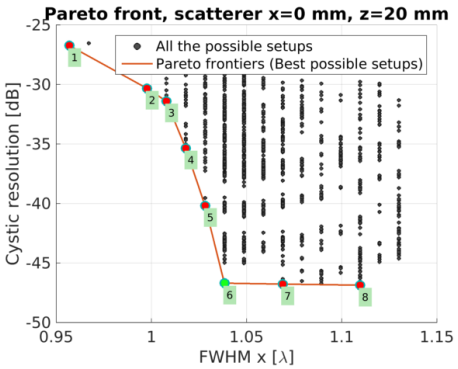

(c) Pareto plot (Objective space) created by merging the CTR and FWHM decision spaces for scatterer at 20 mm.

Figure 3.5: Optimization procedure demonstrated for the scatterer at 20 mm. (a) shows the CTR decision space. (b) shows the FWHM decision space. White lines on *(a)* and *(b)* are the border lines. the enumerated points are the Pareto front optimal solutions. The green point (number 6) is the knee-point solution shown in *(c)*.

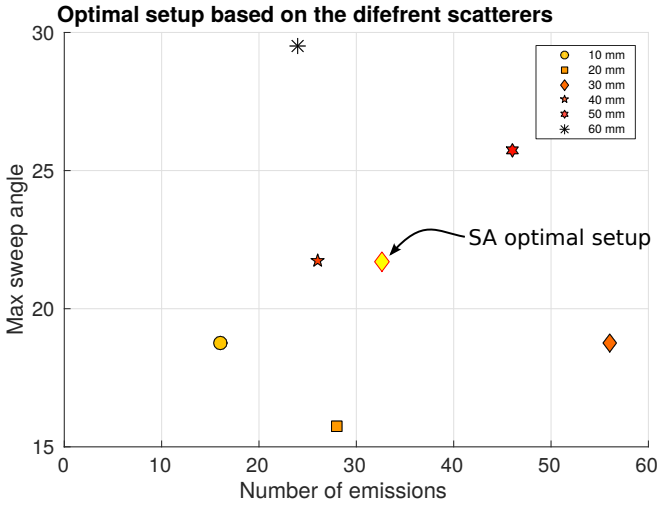

Figure 3.6: Illustrates the α_{max} and N corresponding to the knee-points computed for six scatterers. The yellow diamond ($\alpha_{max} = 22^{\circ}$ and $N = 32$) is the center of the gravity of all points and considered to be the optimal setup for SA imaging.

The automated optimization technique is applied to six scatterers. The simulation results shown in this paper, belong to one of the six scatterers (located at 20 mm), which exemplifies the optimization performed. The CTR and Lateral FWHM of HRIs for the scatterer 20 mm, for all combinations of α_{max} and N, is shown in the Figs. 3.5(a) and 3.5(b). The white lines on figures show the areas of the plots satisfying the two constraints put on rates of changes of CTR and FWHM (mentioned in Section 3.8.2). The axial FWHM is not considered, as the simulations showed that it is very close to λ, for all the combinations. The areas satisfying the two constraints merged into a Pareto plot shown in Fig. 3.5(c). It represented the objective space of dependent variables (CTR and FWHM) for the point scatterer located at 20 mm.

The Pareto plots, alone, do not yield the optimal setup for the SA imaging sequence. That is why, Pareto fronts are more interesting, because they decrease the number of optimal solutions to be considered for imaging. The Pareto fronts for all six scatterers are computed. Fig. 3.5(c) shows the Pareto plot belonging to the scatterer at 20 mm. The enumerated points on the Pareto front, show the optimal solutions (set of α_{max} and N) that yield the optimal solutions for the 20 mm scatterer. The eight frontier points in Fig. 3.5(c) are shown with blue points on the CTR and FWHM decision spaces in Figs. 3.5(a) and 3.5(b). The knee-point of the pareto-front is also shown with green circle

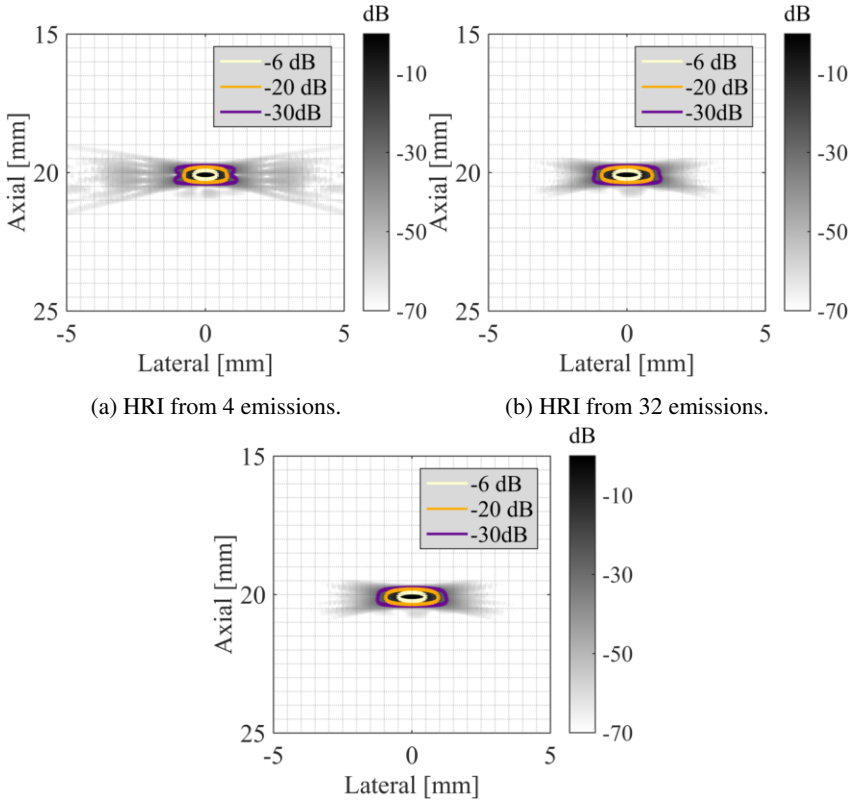

(a) HRI from 4 emissions.

(b) HRI from 32 emissions.

(c) HRI from 256 emissions.

Figure 3.7: Simulation results of a point scatterer located at 20 mm. HRIs reconstructed from low, optimal and high number of emissions.

on the Pareto front in Fig. 3.5(c). The α_{max} and N corresponding to the knee-points computed for six scatterers are shown in Fig. 3.6. The yellow diamond ($\alpha_{max} = 22°$ and $N = 32$) is the center of the gravity of all points and the optimal setup for SA imaging. This optimal setup requires 32 emissions and 22° maximum sweeping angle. Fig. 3.7 shows the point scatterer simulated at 20 mm. HRIs of the scatterer are reconstructed using three different number of emissions (N = 4, 32, 256). The FWHM and CTRs are depicted in the Table 3.2.

Table 3.2: Simulated scatterer at 20 mm quality metrics.

Scatterers	20 mm
N = 4	FWHM = 1.40λ CTR = -25.41 dB
N = 32 (optimal)	FWHM = 1.49λ CTR = -30.25 dB
N = 256	FWHM = 1.50λ CTR = -30.31 dB

3.10.2 Phantom measurement results

3.10.2.1 Wire phantom results

An experiment is conducted, where a phantom containing two wires located at 32.5 mm, and 57.5 mm are imaged using a SA sequence using varying number of emissions. Fig. 3.8 shows the HRIs belonging to two wires located at 32.5 mm (left column), and 57.5 mm (right column). Each HRI is reconstructed with 4, 32 and 256 emissions, where the 32 emissions is the optimized sequence. The FWHM and CTR corresponding to each of the reconstructions is depicted in the Table 3.3.

The results show that the FWHM increases 0.41λ from 4 emissions to 32 emissions for the wire at 32.5 mm, but it only changes 0.07λ from 32 emissions to 256 emissions. for the same wire, the CTR improves 3.63 dB from 4 emissions to 32 emissions for the wire at 32.5 mm, while it does not change from 32 emissions to 256 emissions. For the wire at 57.5 mm, the FWHM increases 0.04λ from 4 emissions to 32 emissions for the wire at 32.5 mm, but it only changes 0.02λ from 32 emissions to 256 emissions. The CTR changes are not noticeable for this wire. The point wires reconstructed with 32 emissions represent similar CTR and FWHM compared with wires reconstructed with 256 emissions. This suggests that for the same image quality, number of emissions can be lowered from 256 to 32.

3.10.2.2 Cyst phantom results

A multi-purpose phantom, containing three anechoic cysts located at 17 mm, 48 mm, and 75 mm (Model 040GSE, CIRS inc., Virginia, USA) with acoustic attenuation of 0.5 dB/(cm$\times$MHz) is scanned, and the HRIs reconstructed with different number of emissions. Fig. 3.10 shows the phantom measured and HRIs reconstructed with $N = 4$, the optimized sequence ($\alpha_{max} = 22^{\circ}$ and $N = 32$), and also $N = 256$. To evaluate the quality of the HRIs, the CNR is used to quantify cysts contrast. The mean CNRs of the two cysts located at 17 mm and 48 mm, are computed for the HRIs reconstructed with increasing number of emissions. This is done to evaluate the performance of the sequence for small parts imaging, and scanning superficial tissues located not beyond 60 mm in

depth. Fig. 3.10 shows that the CNR increases from 1.475 to 1.82 by reaching to 32 emissions, and plateaus after 32 emissions. This coincides with the simulation and wire phantom measurement results, and indicates that for achieving a specific image quality, the number of emissions does not have to be increased to more than the optimal value computed for the SA.

3.10.2.3 *In-vivo* RESULTS

A healthy 28 male is scanned using the optimized SA sequence with ($\alpha_{max} = 22^{\circ}$ and $N = 32$), in two longitudinal views of the common carotid, and carotid with bulbous. The results are shown in Fig. 3.11.

3.11 Discussion

High-quality SA imaging demands fast beamformation, fast and precise interpolation, choosing the appropriate receive F-number, number of emissions, and in case of using steering emissions, choosing the correct steering angles. These considerations, all together, increase the contrast and lower the side-lobes in HRI. As discussed in the Section 3.5, having a good control over the emissions wave front is crucial, and a $\lambda/2$-pitch transducer ensures avoiding the grating lobes behind the wave front.

A multi-objective optimization technique is used to optimize the SA image quality, by automatically selecting the optimal number of emissions, and the steering angles. The optimization performed on $\lambda/2$-pitch transducer. However, the method is a generic optimization technique and can be applied for any kind of transducer and imaging regime.

The optimization performed in this study is a 2-objective optimization, in which two SA imaging parameters of α_{max} and N was optimized only. The technique can be more advanced and the number of parameters to be optimized can be increased. For SA, the optimization can be 4-objective, by optimizing the α_{max}, N, F-number, and aperture size (the transmit sub-aperture). If the number of dependent variables does not change (only CTR and FWHM are considered), then the technique yields two 4-D decision spaces (one for the CTR, and one for the FWHM). The final objective space would still be 2-D, because of considering CTR and FWHM only.

A higher dimension decision space requires a higher dimension objective space. For a 4-objective optimization (4-D decision spaces), a 3-D objective space can be a good alternative (Using CTR, FWHM, and CNR), since the solutions in 4-D decision spaces can be distributed in 3-D objective space, and do not squeeze in a 2-D space that might not be quantitatively representative. The only trade-off is that the volume of the space increases so fast that the available data become sparse. This sparsity is

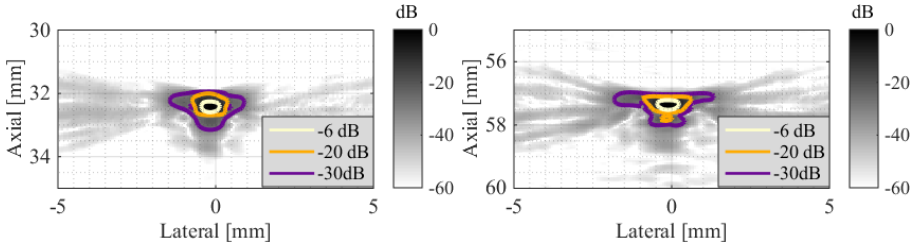

(a) HRI from 4 emissions.

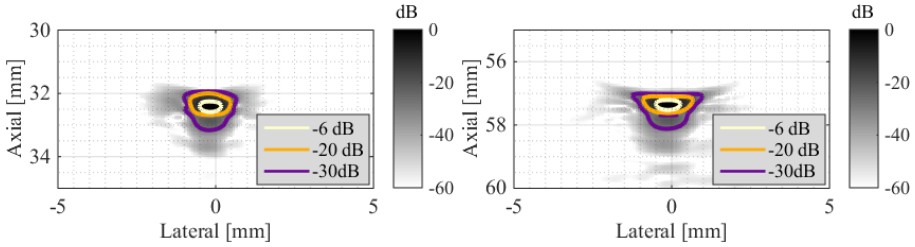

(b) HRI from 32 emissions (optimal).

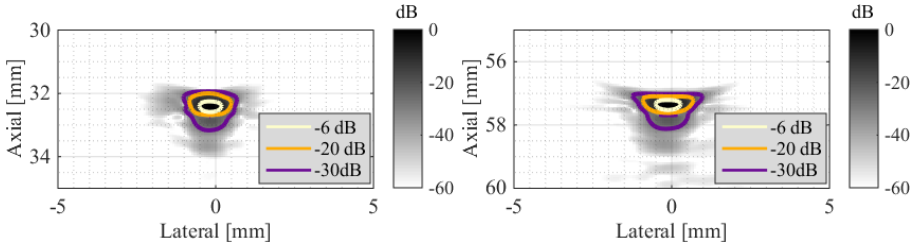

(c) HRI from 256 emissions.

Figure 3.8: Phantom measurement results of wires located at 32.5 mm and 57.5 mm. HRIs reconstructed from low, optimal and high number of emissions.

Table 3.3: Wire phantom measurements quality metrics.

Scatterers	32.5 mm	57.5 mm
$N = 4$	FWHM = 1.09λ CTR = -19.62 dB	FWHM = 1.38λ CTR = -10.19 dB
$N = 32$ (optimal)	FWHM = 1.5λ CTR = -23.25 dB	FWHM = 1.44λ CTR = -10.39 dB
$N = 256$	FWHM = 1.43λ CTR = -23.2 dB	FWHM = 1.46λ CTR = -10.3 dB

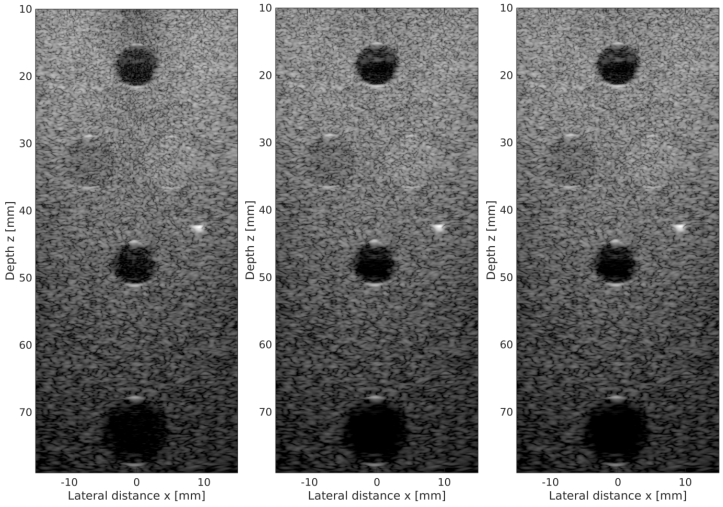

(a) HRI from 8 emissions.

(b) HRI from 32 emissions.

(c) HRI from 256 emissions.

Figure 3.9: Measured cyst phantom and reconstructed from low, optimal, and high number of emissions. All three images are shown using a 60 dB dynamic range.

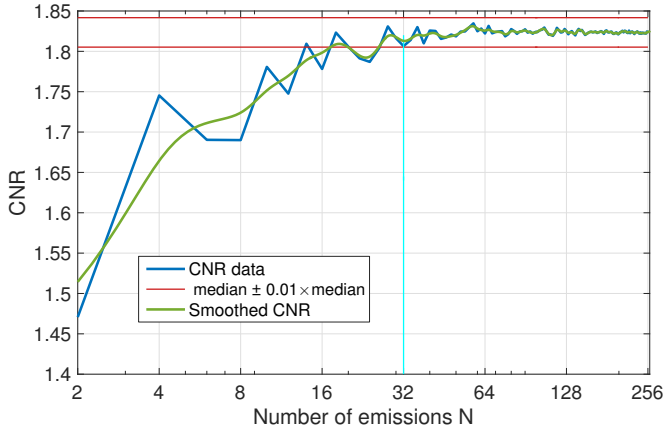

Figure 3.10: CNR computed for measured phantom images and reconstructed with increasing number of emissions.

problematic for any optimization technique that requires statistical significance. The

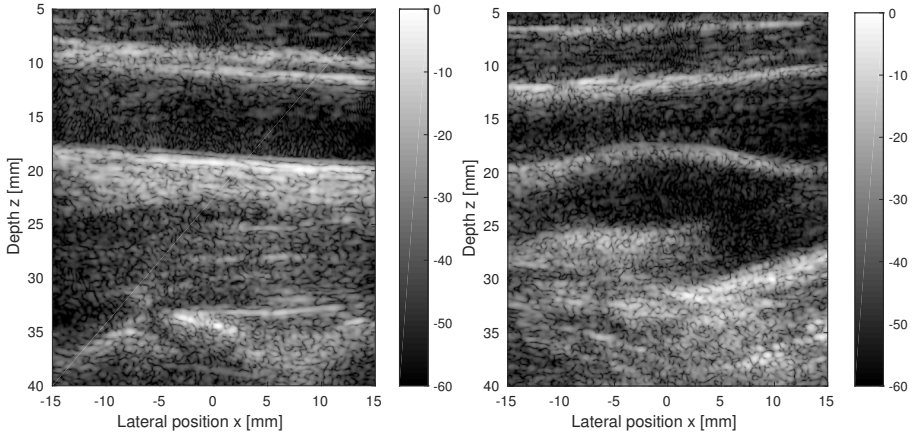

(a) Measured Common carotid on a healthy subject and reconstructed from 32 emissions.

(b) Measured Common carotid with bulbous on a healthy subject and reconstructed from 32 emissions.

Figure 3.11: Measurements performed on a 28 years old healthy male using the optimized sequence.

"curse of dimensionality" has to be considered, when increasing the number of parameters to be optimized (see Chapter 2 of (Hastie, Tibshirani, and Friedman 2009)). This refers to how certain optimization techniques or machine learning algorithms may perform poorly in high-dimensional data. Increasing the number of parameters will not necessarily yield a correct optimization.

Another challenge in high quality SA, is the inter-emission tissue motions. They are more obvious, when number of emissions used for recunstructing HRI is very high. The issue is addressed by (Denarie et al. 2013; K. L. Gammelmark and J. A. Jensen 2014), and can be compensated for. The clutter behind the wire in Fig. 3.8 can be due to a long impulse response of the transducer. It can also be related to artifacts arising from quantization of the transmit delay profile at 70 MHz (Stuart et al. 2015).

SA image quality is investigated using a $\lambda/2$-pitch transducer, and slightly improved contrast is obtained for the same number of emissions when using $\lambda/2$-pitch rather than λ-pitch (Hasegawa and Korte 2016). Other techniques exist for lowering the grating lobes in SA and plane wave, which are mainly based on sparse-aperture methods (Lockwood, Talman, and Brunke 1998), special apodizations of the array (Cooley and Robinson 1994), or modulating receive beams (Ponnle, Hasegawa, and Kanai 2013). The common problem with these techniques is mainly the reduced transmitted energy. The other problem with

these methods is that transmit grating lobes are not always avoided. However, the grating lobes can be completely avoided by using a $\lambda/2$-pitch transducer, as suggested in this paper.

3.12 Summary

This paper presented a hierarchical and automated optimization technique for characterizing the optimal setup in SA imaging. The optimization technique is performed using simulation. The results of the simulation showed that with only $\alpha_{max} = \pm 22^{\circ}$ and $N = 32$, the image quality is comparable with a high number of emissions. Phantom measurement results, also indicated that CNR increases from 1.475 to 1.82 by reaching to 32 emissions, and plateaus after 32 emissions. Wire phantom measurement results indicated that for achieving a specific image quality, the number of emissions does not have to be increased to more than the optimal value. Improvements in frame rate is also achievable by using less number of emissions. This can be highlighted when high frame rate is needed for velocity estimation, and when the standard deviation of the velocity estimates are related to the frame rate. The technique is applied for a $\lambda/2$-pitch transducer, and image quality is compared for simulations, phantom measurements and *in-vivo* scans. The grating lobes are avoided by using a $\lambda/2$-pitch transducer, and therefore fewer emissions are needed to obtain the same image quality. Thus, with a pulse repetition frequency of 5 kHz, more than 156 fps are obtained. The proposed generic technique in this study can be applied to any ultrasound imaging modality, using any transducer geometry.

References from Chapter 3

Burckhardt, C. B., P.-A. Grandchamp, and H. Hoffmann (1974). "An Experimental 2 MHz Synthetic Aperture Sonar System Intended for Medical Use". In: *IEEE Trans. Son. Ultrason.* 21.1, pp. 1–6 (cit. on pp. 40, 41).

Bennett, S., D. K. Peterson, D. Corl, and G. S. Kino (1982). "A real-time synthetic aperture digital acoustic imaging system". In: *Acoust. Imaging*. Ed. by P. Alais and A. F. Metherell. Vol. 10, pp. 669–692 (cit. on p. 42).

Mayer, K., R. Marklein, K. J. Langenberg, and T. Kreutter (1990). "Three-dimensional imaging system based on Fourier transform synthetic aperture focusing technique". In: *Ultrasonics* 28, pp. 241–255 (cit. on p. 41).

Busse, L. J. (1992). "Three-dimensional imaging using a frequency-domain synthetic aperture focusing technique". In: *IEEE Trans. Ultrason., Ferroelec., Freq. Contr.* 39, pp. 174–179 (cit. on p. 41).

Jensen, J. A. and N. B. Svendsen (1992). "Calculation of Pressure Fields from Arbitrarily Shaped, Apodized, and Excited Ultrasound Transducers". In: *IEEE Trans. Ultrason., Ferroelec., Freq. Contr.* 39, pp. 262–267 (cit. on p. 48).

O'Donnell, M. and L. J. Thomas (1992). "Efficient synthetic aperture imaging from a circular aperture with possible application to catheter-based imaging". In: *IEEE Trans. Ultrason., Ferroelec., Freq. Contr.* 39, pp. 366–380 (cit. on p. 42).

Cooley, C. R. and B. S. Robinson (1994). "Synthetic aperture imaging using partial datasets". In: *Proc. IEEE Ultrason. Symp.* Pp. 1539–1542. DOI: 10.1109/ULTSYM.1994.401884 (cit. on p. 58).

Ylitalo, J. T. (1994). "In-vitro study of computed ultrasound imaging method". In: *Proc. IEEE Ultrason. Symp.* Pp. 1577–1580 (cit. on p. 42).

Ylitalo, J. T. and H. Ermert (1994). "Ultrasound synthetic aperture imaging: Monostatic approach". In: *IEEE Trans. Ultrason., Ferroelec., Freq. Contr.* 41, pp. 333–339 (cit. on p. 42).

Karaman, M., P. C. Li, and M. O'Donnell (1995). "Synthetic aperture imaging for small scale systems". In: *IEEE Trans. Ultrason., Ferroelec., Freq. Contr.* 42, pp. 429–442 (cit. on p. 42).

Ylitalo, J. T. (1995). "Synthetic aperture ultrasound imaging using a convex array". In: *Proc. IEEE Ultrason. Symp.* Pp. 1337–1340 (cit. on p. 42).

Goodman, J. W. (1996). *Introduction to Fourier optics*. Second. New York: McGraw Hill Inc. (cit. on p. 41).

Jensen, J. A. (1996). "Field: A Program for Simulating Ultrasound Systems". In: *Med. Biol. Eng. Comp.* 10th Nordic-Baltic Conference on Biomedical Imaging, Vol. 4, Supplement 1, Part 1, pp. 351–353 (cit. on p. 48).

Ylitalo, J. T. (1996a). “A fast ultrasonic synthetic aperture imaging method: application to NDT”. In: *Ultrasonics*, pp. 331–333 (cit. on p. 42).

— (1996b). “On the signal-to-noise ratio of a synthetic aperture ultrasound imaging method”. In: *Eur. J. Ultrasound* 3, pp. 277–281 (cit. on p. 42).

Barthez, P. Y., R. Léveillé, and P. V. Scrivani (1997). “Side lobes and grating lobes artifacts in ultrasound imaging”. In: *Veterinary Radiology & Ultrasound* 38.5, pp. 387–393 (cit. on p. 43).

Vray, D., T. Rastello, F. Schoofs, and P. Delachartre (1997). “Improving the spatial resolution of intravascular ultrasound imaging with synthetic aperture Fourier-based methods”. In: *Proc. IEEE Ultrason. Symp.* Pp. 1531–1534 (cit. on p. 42).

Karaman, M. and M. O’Donnell (1998). “Subaperture processing for ultrasonic imaging”. In: *IEEE Trans. Ultrason., Ferroelec., Freq. Contr.* 45, pp. 126–135 (cit. on p. 42).

Lockwood, G. R., J. R. Talman, and S. S. Brunke (1998). “Real-time 3-D ultrasound imaging using sparse synthetic aperture beamforming”. In: *IEEE Trans. Ultrason., Ferroelec., Freq. Contr.* 45, pp. 980–988 (cit. on pp. 42, 58).

Nikolov, S. I., K. Gammelmark, and J. A. Jensen (1999). “Recursive ultrasound imaging”. In: *Proc. IEEE Ultrason. Symp.* Vol. 2, pp. 1621–1625 (cit. on p. 42).

Soumekh, M. (1999). *Synthetic aperture radar. Signal processing with MATLAB algorithms*. New York: John Wiley & Sons, Inc. (cit. on p. 42).

Gammelmark, K. L. and J. A. Jensen (2003). “Multielement Synthetic Transmit Aperture Imaging using Temporal Encoding”. In: *IEEE Trans. Med. Imag.* 22.4, pp. 552–563 (cit. on p. 42).

Nikolov, S. I. and J. A. Jensen (2003). “In-vivo Synthetic Aperture Flow Imaging in Medical Ultrasound”. In: *IEEE Trans. Ultrason., Ferroelec., Freq. Contr.* 50.7, pp. 848–856 (cit. on p. 42).

Huang, J., P. W. Que, and J. H. Jin (2004). “A Parametric Study of Beam Steering for Ultrasonic Linear Phased Array Transducer”. In: *Russ. J. Nondestr. Test.* 40.4, pp. 254–259 (cit. on p. 43).

Jensen, J. A. and S. I. Nikolov (2004). “Directional Synthetic Aperture Flow Imaging”. In: *IEEE Trans. Ultrason., Ferroelec., Freq. Contr.* 51, pp. 1107–1118 (cit. on p. 42).

Deb, K. (2005). “Multi-objective optimization”. In: *Search methodologies*. Springer (cit. on p. 47).

Jensen, J. A. (2006). “Spectral velocity estimation in ultrasound using sparse data sets”. In: *J. Acoust. Soc. Am.* vol 120(1), pp. 211–220 (cit. on p. 41).

Jensen, J. A., S. Nikolov, K. L. Gammelmark, and M. H. Pedersen (2006). “Synthetic Aperture Ultrasound Imaging”. In: *Ultrasonics* 44, e5–e15 (cit. on p. 41).

Coello, C. A. C., G. B. Lamont, and D. A. V. Veldhuizen (2007). "Basic Concepts". In: *Evolutionary Algorithms for Solving Multi-Objective Problems*. Springer (cit. on p. 47).

Oddershede, N. and J. A. Jensen (2007). "Effects influencing focusing in synthetic aperture vector flow imaging". In: *IEEE Trans. Ultrason., Ferroelec., Freq. Contr.* 54.9, pp. 1811–1825 (cit. on p. 43).

Ranganathan, K. and W. F. Walker (2007). "Cystic Resolution: A Performance Metric for Ultrasound Imaging Systems". In: *IEEE Trans. Ultrason., Ferroelec., Freq. Contr.* 54.4, pp. 782–792. DOI: 10.1109/TUFFC.2007.311 (cit. on pp. 45, 46).

Guenther, D. A. and W. F. Walker (2009). "Generalized cystic resolution: a metric for assessing the fundamental limits on beamformer performance". In: *IEEE Trans. Ultrason., Ferroelec., Freq. Contr.* 56.1, pp. 77–90 (cit. on p. 45).

Hastie, T., R. Tibshirani, and J. Friedman (2009). *The Elements of Statistical Learning Data Mining, Inference, and Prediction*. Second edition. Springer Series in Statistics (cit. on p. 58).

Hansen, J. M., M. C. Hemmsen, and J. A. Jensen (2011). "An object-oriented multi-threaded software beamformation toolbox". In: *Proc. SPIE Med. Imag.* Vol. 7968, pages. DOI: 10.1117/12.878178 (cit. on p. 49).

Lediju, M. A., G. E. Trahey, B. C. Byram, and J. J. Dahl (2011). "Short-lag spatial coherence of backscattered echoes: imaging characteristics". In: *IEEE Trans. Ultrason., Ferroelec., Freq. Contr.* 58.7, pp. 1377–1388. DOI: 10.1109/TUFFC.2011.1957 (cit. on pp. 45, 46).

Denarie, B., T. A. Tangen, I. K. Ekroll, N. Rolim, H. H. Torp, T. Bjastad, and L. Løvstakken (2013). "Coherent Plane Wave Compounding for Very High Frame Rate Ultrasonography of Rapidly Moving Targets". In: *IEEE Trans. Ultrason., Ferroelec., Freq. Contr.* 32.7, pp. 1265–1276 (cit. on p. 58).

Jensen, J. A., H. Holten-Lund, R. T. Nilsson, M. Hansen, U. D. Larsen, R. P. Domsten, B. G. Tomov, M. B. Stuart, S. I. Nikolov, M. J. Pihl, Y. Du, J. H. Rasmussen, and M. F. Rasmussen (2013). "SARUS: A Synthetic Aperture Real-time Ultrasound System". In: *IEEE Trans. Ultrason., Ferroelec., Freq. Contr.* 60.9, pp. 1838–1852 (cit. on p. 50).

Ponnle, A., H. Hasegawa, and H. Kanai (2013). "Suppression of grating lobe artifacts in ultrasound images formed from diverging transmitting beams by modulation of receiving beams". In: *Ultrasound Med. Biol.* 39.4, pp. 681–691. DOI: 10.1016/j.ultrasmedbio.2012.10.019 (cit. on p. 58).

Gammelmark, K. L. and J. A. Jensen (2014). "2-D Tissue Motion Compensation of Synthetic Transmit Aperture Images". In: *IEEE Trans. Ultrason., Ferroelec., Freq. Contr.* Pp. 594–610. DOI: http://dx.doi.org/10.1109/TUFFC.2014.2948 (cit. on p. 58).

Jensen, J. A. (2014). “A Multi-threaded Version of Field II”. In: *Proc. IEEE Ultrason. Symp.* IEEE, pp. 2229–2232 (cit. on p. 48).

Szabo, T. L. (2014). *Diagnostic ultrasound imaging: Inside out*. 2nd ed. Elsevier (Oxford, UK) (cit. on pp. 43, 45, 46).

Yiu, B. Y., S. S. Lai, and A. C. Yu (2014). “Vector projectile imaging: time-resolved dynamic visualization of complex flow patterns.” In: *Ultrasound Med. Biol.* 40.9, pp. 2295–2309 (cit. on p. 42).

Stuart, M. B., J. Jensen, T. Di Ianni, and J. A. Jensen (2015). “Image quality degradation from transmit delay profile quantization”. In: *Proc. IEEE Ultrason. Symp.* Pp. 1–4. DOI: 10.1109/ULTSYM.2015.0126 (cit. on p. 58).

Hasegawa, H. and C. L. de Korte (2016). “Impact of element pitch on synthetic aperture ultrasound imaging”. In: *J. Med. Ultrason.* Pp. 1–9. DOI: 10.1007/s10396-016-0700-6 (cit. on p. 58).

Jensen, J., M. B. Stuart, and J. A. Jensen (2016). “Optimized Plane Wave Imaging for Fast and High-Quality Ultrasound Imaging”. In: *IEEE Trans. Ultrason., Ferroelec., Freq. Contr.* 63.11, pp. 1922–1934. DOI: 10.1109/TUFFC.2016.2591980 (cit. on p. 43).

CHAPTER 4

Vector Velocity Estimation

Abnormal blood flow is considered a diagnostic marker in determining the physiological state of a diseased vessel. Measuring flow velocities is therefore of great importance in medical ultrasound, as it provides a non-invasive tool for monitoring blood flow.

The present chapter introduces the transverse oscillation (TO) and synthetic aperture flow imaging, the techniques used for acquisition of velocity data in this project. The velocity data is used in Chapter 5 in combination with the optimized B-mode from Chapter 3 to segment vessel lumen in ultrasound images.

Blood flow measurement using ultrasound is considered as a quantitative diagnostic bio-marker to determine the physiological state of a vessel. Ultrasound provides a non-invasive tool for measuring blood flow, in which abnormal velocities measured can be signs of abnormal flow due to a diseased vessel.

Two commonly used flow techniques for velocity measurement are color flow mapping (CFM) and the spectral Doppler (SDU). In both techniques, ultrasound pulses are emitted to the scanned media with a specific pulse repetition frequency (PRF). The returned echoes from the scanned media is then recorded by the transducer. Given the fact that the back scattering tissue moves in between successive emissions, a time-shift will be generated between the received signals. The velocity of the moving scatterer can then be found from the time shift. However, there is a limitation inherent in these techniques. They can only detect the movements in parallel to the ultrasound beam (the axial velocity component v_z), given by $v_z = |\mathbf{v}|\cos\alpha$, where $|\mathbf{v}|$ is the in-plane velocity magnitude and α is the beam-to-flow angle. For situations, where blood moves at an angle relative to the beam, the measured flow needs to be compensated for that angle. This compensation is performed manually, by dividing the measured velocity to the cosine of the angle α, which is the angle between the insonifying beam and the the vessel wall. This means that finding the correct blood velocity highly depends on the user's skills that exact angle. The dependency is related to the inverse of the cosine $\frac{1}{\cos(\alpha)}$ and increases with the angle, as illustrated in Fig. 4.1.

The angle-dependency hinders the possibility of measuring blood flow in vessels oriented at an angle close to $90°$, which is quite unfortunate, as superficial vessels lie mostly perpendicular to the skin surface,and therefore, also to the insonation beam. It

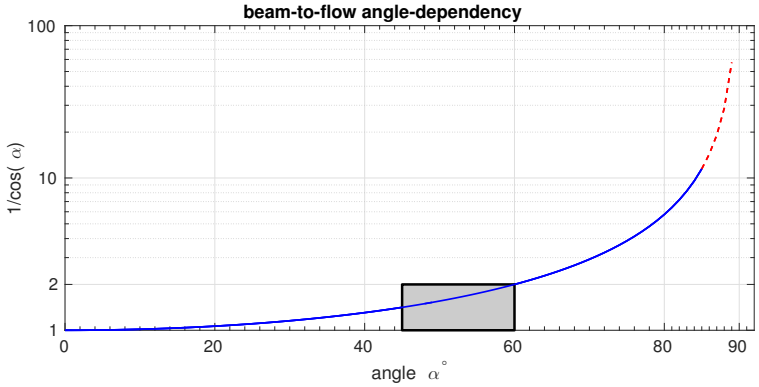

Figure 4.1: Blood velocity estimated in a vessel oriented at the angle α to the insonifying beam has to be compensated by a factor of $\frac{1}{\cos(\alpha)}$. It is illustrated that this factor increases exponentially with increasing angle, thus, the task of compensation gets progressively harder as angle increases.

is therefore, suggested by the literature that the insonation angle should be between $45°$ and $60°$ to obtain the must reliable flow estimates (Picot and Embree 1994; Kruskal et al. 2004).

The angle-dependency can be addressed by using velocity vector flow imaging (VFI) techniques for velocity data for conventional sequential data acquisition (Jensen et al. 2016a) or parallel acquisition (Jensen et al. 2016b). These include speckle tracking (Trahey, Allison, and Ramm 1987), transverse oscillation (TO) (Jensen 1996a; Jensen and Munk 1998; Jensen 2000; Udesen and Jensen 2006), directional beamforming (S. I. Nikolov and Jensen 2001; Jensen and S. I. Nikolov 2004; Jensen, S. Nikolov, et al. 2006; Villagomez-Hoyos et al. 2016) , and synthetic aperture flow imaging (Jensen and S. I. Nikolov 2002).

Given the fact that TO and synthetic aperture flow imaging are used for acquiring the velocity data in this project, only these two methods are explained in this chapter. Therefore, the technical background of these two velocity estimators are detailed only.

The TO approach is the only vector velocity estimator implemented on a commercially available ultrasound scanner (Hansen et al. 2011). Fig. 4.2 shows an example of the TO on a commercial scanner, where blood flow in a vessel perpendicular to the beam angle is measured by conventional color flow mapping, and the TO approach.

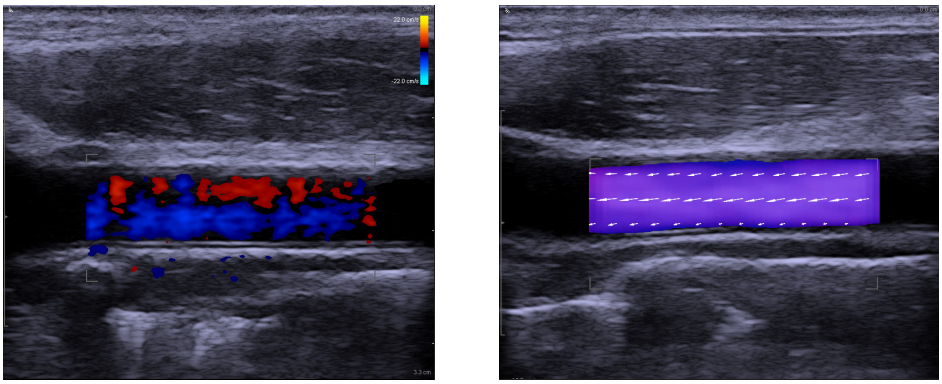

(a) (b)

Figure 4.2: (a) and (b) show blood flow inside a vessel lying perpendicular to the insonifying beam, using conventional CFM, and TO, respectively. (a) shows that the conventional method is incapable of detecting the actual flow, as the movement of the blood generates no shift between successive received echoes by the transducer. The same measurement is performed in (b), but now using the TO. The image depicts a map of the flow with vector velocities indicating both directions and magnitudes of the flow. The figure is taken from (BK Medical 2015).

4.1 Transverse Oscillation

Conventional Doppler techniques consisted of generating the oscillating field along the propagating pulse, from which the axial velocity component v_z can be estimated. The underlying idea of TO was introduced by Jensen, Munk and Anderson (Anderson 1998; Jensen and Munk 1998) consisted of a transverse oscillation, introduced perpendicular to the propagation of the pulse, which enables detection of the lateral velocity component v_x. The transverse oscillation can be explained by considering a interference pattern generated, when two point sources emit pulses simultaneously. The interference pattern introduced, generates a double-oscillating field, which varies spatially with respect to both axial oscillation (along the direction of the pulse), and lateral oscillation (areas where the two waves meeting each other).

The double oscillating field can be visually perceived by considering the pattern formed when two point sources (i.e. two fingers, or two droplets) pounding in into still water. An oscillating wave front propagates in all directions around each point source.

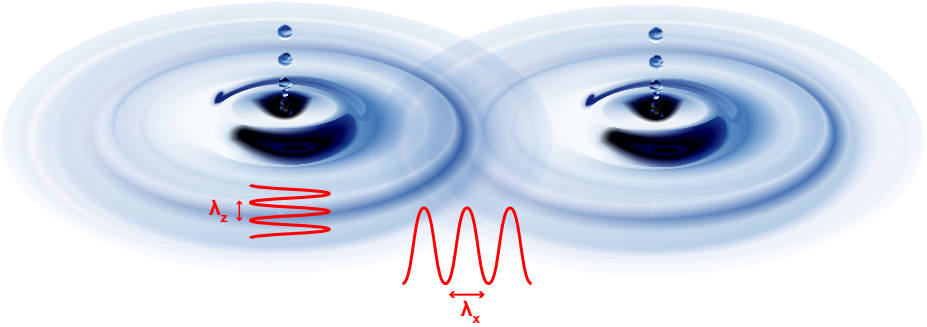

Figure 4.3: Two droplets pounding still water surface, generating oscillations that travel out in all directions. In regions where the two oscillation patterns interfere, a double-oscillating field is created.

The two oscillating wave fronts will eventually meet and create an interference pattern, as shown in Fig. 4.3. In some areas, the interference pattern creates a double oscillating field characterized by the two wavelengths λ_z and λ_x.

Center frequency of the emitted pulse determines the axial wavelength λ_z. However, the latteral oscillation is more complex and depends on the distance between the two point sources, depth, and also the axial wavelength.The spatial wavelength of the transverse oscillation $\lambda_x(z)$ can be approximated by (Udesen and Jensen 2006),

$$\lambda_x(z) = 2\lambda_z \frac{z}{d} \,. \tag{4.1}$$

where d is the distance between the two point sources, z is the axial depth, and λ_z is the wavelengths of the emitted pulse.

The analogy of generating a double-oscillating field using two point sources can be translated to ultrasound systems, when two transducer elements act as point sources and generate ultrasonic waves. The transducer transmits pulses from two distinct positions and create an oscillating presure field. Fig. 4.4(b) depicts an example of the oscillating field generated by using two apodization functions. This approach is first introduced by Jensen (Jensen and Munk 1998). The apodization function shows two sets of active elements or sub-apertures (see the two apodizing windows onthe surface of the transducer in Fig. 4.4(a)). This double-apodization function can be either implemenetd in transmit, or in receive. Either of the implementations results in the same pressure map observed by the transducer. Therefore, any apodization function containing the two distinct windows, will generate a double-oscillating pattern, from which the axial and lateral velocity components can be determined.

To estimate the axial velocity, Hilbert transform is performed to yield the in-phase and the quadrature signal. The two signals are essentially characterized by being 90° phase shifted to each other. This phase shift enables the calculation of the instantaneous phase of the received signal. Phase calculation is also essential, as it illustrates the changes across multiple emissions, when the tissue movement exists between successive pulses. The direction of the movement, is also identified by sign of the phase change. Changes in the in-phase and the quadrature signals across several emissions, determines the flow direction.

Essentially these two signals are obtained by sampling the received signal with a frequency, at least four times greater than the center frequency of the emitted pulse, which automatically results in 90° phase shift between two samples. Sampling the signal with four-times the center frequency corresponds to sampling at instances which are $\lambda_z/4$ separated in axial direction. To yield the same in the lateral direction, two lines, which are $\lambda_x/4$ separated are required to be beamformed. Fig. 4.4(a) shows the two beamformed lines in the receive.

The calculated axial and lateral quadrature signals, are then used to determine the phase change in axial and lateral directions. The size of the phase change is proportional to the velocity of the moving scatterer. The details for how exactly the velocity components derived is explained by Jensen (Jensen 1996b, 2001). The idea is that an ultrasound pulse is emitted, from the received signal by the transducer with a double-windowed apodization, the two in-plane velocity components are measured. The velocity components are then overlaid on the B-mode, which illustrates the 2-D vector velocity field. Fig. 4.2 shows a screen-shot of the visualization of the vector velocities in a human carotid artery, using a BK3000 ultrasound scanner (BK Ultrasound, Denmark).

4.2 Velocity estimation using synthetic aperture (SAFI) and directional beamforming

The current implementation of TO on ultrasound scanners, sequentially probes the scanned media in different directions to create vector flow images (VFI). The frame rates of scanners using this technique are limited to $15\,\text{Hz} - 30\,\text{Hz}$, depending on the size of the image and the desired penetration depth. Normally, such frame rates are not sufficient for capturing complex flow characteristics during a cardiac cycle. As an alternative to The TO, The use of broader beams or SA was proposed. The advantages of using the SA in compare with the conventional line-by-line scanning is discussed in detail in Chapter 3. This section details how SA can be used with directional beamforming for estimating vector velocities.

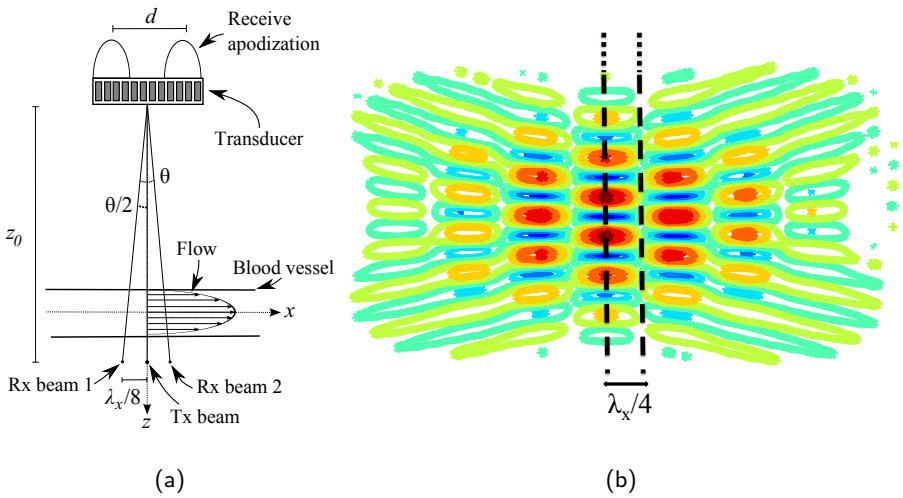

Figure 4.4: (a) shows the transducer with the two apodizations windows for creating the double-oscillating field. The two lines (R_x beam 1 and R_x beam 2) are the required lines to be beamformed in receive to determine the in-phase, and the quadrature signal in the lateral direction. (b) shows an example of a double-oscillating field created by using the apodizations. The distance between the two lines is expanded due to the lateral wavelength increasing as a function of depth, see (4.1). Two figures are taken from (Jensen and Munk 1998).

SA insonifies a broad region of Interest (ROI), which enables focusing in any direction in media to estimate the velocity components. Fig. 4.5 introduces the concept, in which only four emissions are used. Four signals from a single moving scatterer measured at two different aperture configurations. The aperture configuration for first and thrid emissions is the same, as well as aperture configuration for second and fourth emissions. combination of the pairwise emissions, create two identical but slightly shifted point spread functions between emissions (see third row in Fig. 4.5).

A directional beamforming can be used to determine the velocity and direction of the moving target. The directional beamforming has two main steps. First a set of velocity components are computed for each emission pair. second, the velocity components from two emission pairs are compared. The comparison reveals a crossing between the estimated velocities, which determines the actual velocity and direction of the moving target. Cross-correlation of directional lines beamformed in several directions inside the low resolution image determines the set of velocities. A velocity is estimated for each

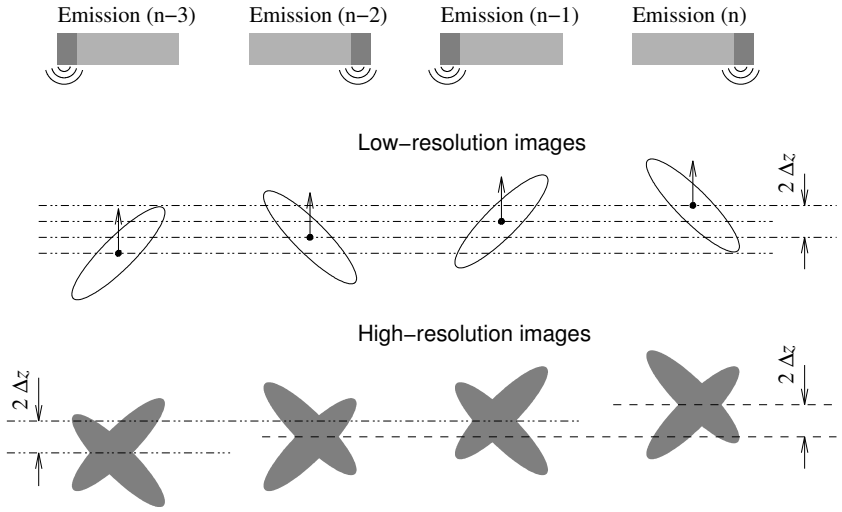

Figure 4.5: The figure depicts four signals measured from a moving target. They are measured with two different aperture configurations. Assume that first and third emissions are combined in one emission, and second and fourth emissions are combined in another(taken from (S. I. Nikolov 2001)).

directional line. The process is repeated for many directional lines, and a velocity-to-angle map is generated (see Fig. 4.6). The intersection of the profiles in the velocity-to-angle map depicts the actual velocity with the corresponding flow angle.

Therefore, flow estimation using SA and directional beamforming benefits from the fact that velocities can be accurately found in any direction, and independent to the beam-to-flow angle. This technique is able to generate VFI images from only few emissions, compared to the commercial scanners that need several hundred emissions to complete a vector flow map (VFM).

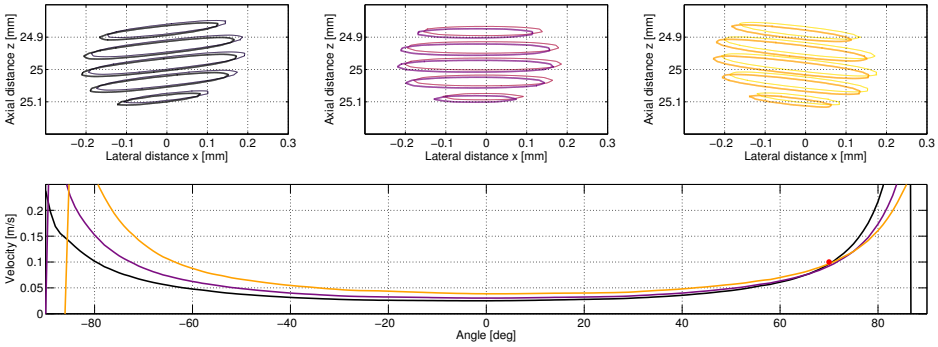

Figure 4.6: Several signals measured from a point target moving with speed of $0.1\,\mathrm{m\,s^{-1}}$ an angle of 70°.Top row shows that three different aperture configurations are used and three emission pairs are measured. Bottom row illustrates the velocity-to-angle profiles generated from the three emissions pairs. The intersection of the three profiles (red dot), determines the correct velocity of the moving target. The figure is from (Villagomez-Hoyos et al. 2016)

References from Chapter 4

Trahey, G. E., J. W. Allison, and O. T. von Ramm (1987). "Angle independent ultrasonic detection of blood flow". In: *IEEE Trans. Biomed. Eng.* BME-34, pp. 965–967 (cit. on p. 66).

Picot, P. A. and P. M. Embree (1994). "Quantitative volume flow estimation using velocity profiles". In: *IEEE Trans. Ultrason., Ferroelec., Freq. Contr.* 41, pp. 340–345 (cit. on p. 66).

Jensen, J. A. (1996a). *Apparatus and method for determining movements and velocities of moving objects*. International patent PCT/DK97/00287 (cit. on p. 66).

— (1996b). *Estimation of Blood Velocities Using Ultrasound: A Signal Processing Approach*. New York: Cambridge University Press (cit. on p. 69).

Anderson, M. E. (1998). "Multi-dimensional velocity estimation with ultrasound using spatial quadrature". In: *IEEE Trans. Ultrason., Ferroelec., Freq. Contr.* 45, pp. 852–861 (cit. on p. 67).

Jensen, J. A. and P. Munk (1998). "A New Method for Estimation of Velocity Vectors". In: *IEEE Trans. Ultrason., Ferroelec., Freq. Contr.* 45, pp. 837–851 (cit. on pp. 66–68, 70).

Jensen, J. A. (2000). *Estimation of vector velocity*. International patent PCT/DK00/00243 (cit. on p. 66).

— (2001). "A New Estimator for Vector Velocity Estimation". In: *IEEE Trans. Ultrason., Ferroelec., Freq. Contr.* 48.4, pp. 886–894 (cit. on p. 69).

Nikolov, S. I. (2001). “Synthetic Aperture Tissue and Flow Ultrasound Imaging”. PhD thesis. 2800, Lyngby, Denmark: Ørsted•DTU, Technical University of Denmark (cit. on p. 71).

Nikolov, S. I. and J. A. Jensen (2001). “Velocity estimation using synthetic aperture imaging”. In: *Proc. IEEE Ultrason. Symp.* Pp. 1409–1412 (cit. on p. 66).

Jensen, J. A. and S. I. Nikolov (2002). “Transverse flow imaging using synthetic aperture directional beamforming”. In: *Proc. IEEE Ultrason. Symp.* Pp. 1488–1492 (cit. on p. 66).

— (2004). “Directional Synthetic Aperture Flow Imaging”. In: *IEEE Trans. Ultrason., Ferroelec., Freq. Contr.* 51, pp. 1107–1118 (cit. on p. 66).

Kruskal, J. B., P. A. Newman, L. G. Sammons, and R. A. Kane (2004). “Optimizing Doppler and Color Flow US: Application to Hepatic Sonography”. In: *Radiographics* 24.3, pp. 657–675 (cit. on p. 66).

Jensen, J. A., S. Nikolov, K. L. Gammelmark, and M. H. Pedersen (2006). “Synthetic Aperture Ultrasound Imaging”. In: *Ultrasonics* 44, e5–e15 (cit. on p. 66).

Udesen, J. and J. A. Jensen (2006). “Investigation of Transverse Oscillation Method”. In: *IEEE Trans. Ultrason., Ferroelec., Freq. Contr.* 53, pp. 959–971 (cit. on pp. 66, 68).

Hansen, P. M., M. M. Pedersen, K. L. Hansen, M. B. Nielsen, and J. A. Jensen (2011). “Demonstration of a vector velocity technique”. In: *Ultraschall in Med.* 32, pp. 213–215 (cit. on p. 66).

BK Medical (2015). *http://bkultrasound.com/bk-medical/VectorFlow* (cit. on p. 67).

Jensen, J. A., S. I. Nikolov, A. Yu, and D. Garcia (2016a). “Ultrasound Vector Flow Imaging I: Sequential Systems”. In: *IEEE Trans. Ultrason., Ferroelec., Freq. Contr.* 63.11, pp. 1704–1721. DOI: 10.1109/TUFFC.2016.2600763 (cit. on p. 66).

— (2016b). “Ultrasound Vector Flow Imaging II: Parallel Systems”. In: *IEEE Trans. Ultrason., Ferroelec., Freq. Contr.* 63.11, pp. 1722–1732. DOI: 10.1109/TUFFC.2016.2598180 (cit. on p. 66).

Villagomez-Hoyos, C. A., M. B. Stuart, K. L. Hansen, M. B. Nielsen, and J. A. Jensen (2016). “Accurate Angle Estimator for High Frame Rate 2-D Vector Flow Imaging”. In: *IEEE Trans. Ultrason., Ferroelec., Freq. Contr.* 63.6, pp. 842–853 (cit. on pp. 66, 72).

CHAPTER 5

Hybrid segmentation of vessels in ultrasound

The following chapter deals with the segmentation of major vessels, in particular carotid artery (CA), and automating quantitative flow measures in ultrasound. The chapter presents a literature review of CA segmentation techniques in US. It also, acquaints the reader with the importance of automated quantitative flow measures. The chapter thus proposes and discusses a hybrid technique for accurate vessel segmentation that fuses VFI data and B-mode for robustly detecting and delineating vessels. The proposed method delineates the vessels in ultrasound scans and enables a better visualization of flow inside the vessel, as well as providing the firm ground for quantitative flow measures for VFI such as Peak systolic velocity (PSV) and volume flow.

The remainder of this chapter is organized as follows. Section 5.1 Reviews the state-of-the-art CA segmentation techniques and highlights the need for a new automated hybrid technique. Section 5.2 present a high-level description of the proposed segmentation technique. Sections 5.3 to 5.6 introduce the different steps of the segmentation method. Section 5.7 introduces the quantitative flow measures, such as PSV and volume flow. Section 5.8 implements the automated quantitative flow measures. Sections 5.9 and 5.10 present the evaluations carried out for assessment of the segmentation, and the automated measures. Section 5.11 discusses the results for segmentation and automated flow measures. Finally, section 5.12 summarizes the chapter.

5.1 Review of the state-of-the-art carotid artery segmentation techniques in ultrasound

A chronological overview of the segmentation methods proposed in the literature for segmenting the carotid artery is presented in Table 5.1. This review is pertinent to the hybrid segmentation technique proposed in this chapter.

Table 5.1: Carotid artery segmentation approaches found in the literature.

Author	Segmentation Method	Images	Year
Wendelhag et al. (Wendelhag et al. 1997)	Dynamic programming	USC	1997
Mojsilovic et al. (Mojsilovic et al. 1997)	Texture based	IVUS	1997
Mao et al. (Mao et al. 2000)	Discrete dynamic contour	USC	2000
Selzer et al. (Selzer et al. 2001)	Edge tracking	USC	2001
Cheng et al. (Cheng et al. 2002)	Snakes	USC	2002
Gutierrez et al. (Gutierrez et al. 2002)	Active contour and baloon	USC	2002
Xiao et al. (Xiao et al. 2002)	Inhomogeneity correction	USC	2002
Stein et al. (Stein et al. 2005)	Gradient based	USC	2005
Delsanto et al. (Delsanto et al. 2007)	Fuzzy C means and Snakes	USC	2007
Loizou et al. (Loizou et al. 2007)	Snakes	USC	2007
Golemati et al. (Golemati et al. 2007)	Hough transform	USC	2007
Faita et al. (Faita et al. 2008)	First-order edge operator	USC	2008
Destrempes et al. (Destrempes et al. 2009)	Nakagami distributions	USC	2009
Rossi et al. (Rossi, Brands, and Hoeks 2010)	Anisotropic barycenter	USC	2010
Santhiyakumari et al. (Santhiyakumari et al. 2011)	Active contours	USC	2011
Molinari et al.(Molinari et al. 2012)	Multi-resolution edge snapper	USc	2012
Xu et al. (Xu et al. 2012)	Hough and dual Snake	USC	2012
Petroudi et al. (Petroudi et al. 2012)	Active contours and level sets	USC	2012
Lara et al. (Menchon-Lara et al. 2014)	Neural networks	USC	2013
Yang et al. (Yang et al. 2013)	Active shape model	USC	2013
Carvalho et al. (Carvalho et al. 2015)	Graph based dynamic programming	USC + CEUS	2015

Note: USC is ultrasound B-mode carotid images, IVUS is intravescular ultrasound images, and CEUS is contrast enhanced ultrasound images.

According to the literature, basically, all segmentation techniques, but one, use only B-mode images as the input to the segmentation procedure. The flow data corresponding to the B-mode images are then not considered in these techniques. The flow data add invaluable information to the segmentation, and can locate the regions inside the vessels. Carvalho et al. (Carvalho et al. 2015) used contrast enhanced ultrasound images (CEUS) in addition to the B-mode images. The CEUS images are used to extract the center-line of vessels, as an indication of regions inside the vessel. For generating these images *in-vivo*, contrast agents must be used for the subjects, which are micrometer-sized gas bubbles that flow inside the blood stream. However, This is not achievable for everyday use in a normal scan session. Thus, the challenge remains in devising an accurate vessel segmentation procedure that incorporates both B-mode image and flow data non-invasively, to better identify the vessels.

As dicussed in Chapter 4, VFI enables angle independent visualization of blood

flow, and allows doctors to see and estimate the direction and velocity of blood flow in all directions and at any angle. This provides an angle independent and non-invasive visualization of blood hemodynamics of the cardiovascular system in real time (Pedersen et al. 2012). These advantages make VFI estimates a reliable alternative marker for identification of vessels, and for being incorporated in the segmentation of vessels. This chapter thus presents a hybrid segmentation algorithm that fuses B-mode and vector velocity estimations (VFI) for robustly detecting and segmenting vessels in ultrasound images.

5.2 High-level description of the proposed segmentation algorithm

The novelty of the proposed technique comes from combining VFI estimations and B-mode as input to the segmentation procedure. The proposed algorithm contains five distinct steps.

1. First, the shadow regions on the scans are detected and excluded from the segmentation procedure. The technique proposed in Section 2.4 of Chapter 2 is used for this purpose.

2. Second, a marker image is generated from both VFI data and B-mode.

   - Binary mask of the VFI data is generated.
   - A skeletonization procedure is employed , and center-line of the VFI data is extracted. The center-line indicated to the locations inside the vessel boundary. This center-line is called the inner-marker of the vessel.
   - A binary mask containing the strong specular regions in B-mode is generated, and multiplied to a dilated version of the VFI mask. This mask indicated to regions ouside the vessel boundaries. The mask is called the outer-marker.
   - The combination, union, of the inner-marker and outer-marker yielded the marker image. The marker image is used in a region growing procedure to delineate the vessel boundary.

3. Third, a marker-controlled watershed is applied to the median filtered B-mode image, with respect to the marker image. The result of watershed includes the vessel structures and also the artifacts.

4. In the fourth step, Artifacts are rejected and the vessel structure is retained.

5. Finally, a rigid co-registration of the segmentations of successive frames is performed to deform the segmentations towards the actual vessel boundaries.

5.3 Generating the marker image

5.3.1 Detection of inner-markers

The main purpose of this section is to find markers that indicate to the areas inside the vessel boundaries. The VFI data can be used to address this, since it can be obtained in real-time non-invasively, along with the B-mode, and is independent of the insonation angle.

Detection of inner-markers are achieved by skeletonization of the VFI data. The absolute value of VFI estimates is first computed and a binary mask of the VFI data generated (see Fig. 5.1(b). The skeletonization process started by computing the Euclidean distance transform of the inverted binary mask of VFI data (see Fig. 5.1(c)). The ridge lines on the distance transform are considered as the center-line of the flow data (see Fig. 5.1(d)). The center-line of the flow data, in a sense, serves as the inner-markers indicating to the locations inside the vessel boundary.

5.3.2 Detection of outer-markers

Information regarding non-vessel regions are also required to fully equip the segmentation process. The detection of outer-markers are achieved by using both the VFI mask and the B-mode image. Strong specular regions are extracted from the B-mode and used as an indication of regions outside the vessels.

For this purpose, the envelope of the acquired scan is first computed. A cumulative histogram of the intensity values is then generated. The intensity values less than half of the maximum intensities in the envelope are disregarded, and a mask of strong signal regions is generated. The mask is then multiplied to a dilated version of the VFI mask and yielded the outer-marker mask as shown in Fig. 5.2(a).

The inner- and outer-markers are combined in one binary mask, so called ”marker image” (see Fig. 5.2(b)). The marker image fully equips the segmentation algorithm with information regarding regions corresponding to the inside and outside of the vessel. The marker image is used to initialize and narrow the region of interest for a region growing algorithm applied to the B-mode image.

5.4 Marker-controlled watershed

Region growing algorithms start from a set of initialization points (seeds) characterizing the desired regions and use specific similarity criteria to append neighboring pixels. The procedure is continued until the entire image is partitioned. Many variations of the region growing algorithms have been introduced in the literature. Smeulders et al. (Smeulders et al. 1978) and Kondo et al. (Kondo and Taniguchi 1986) initiated the region growing

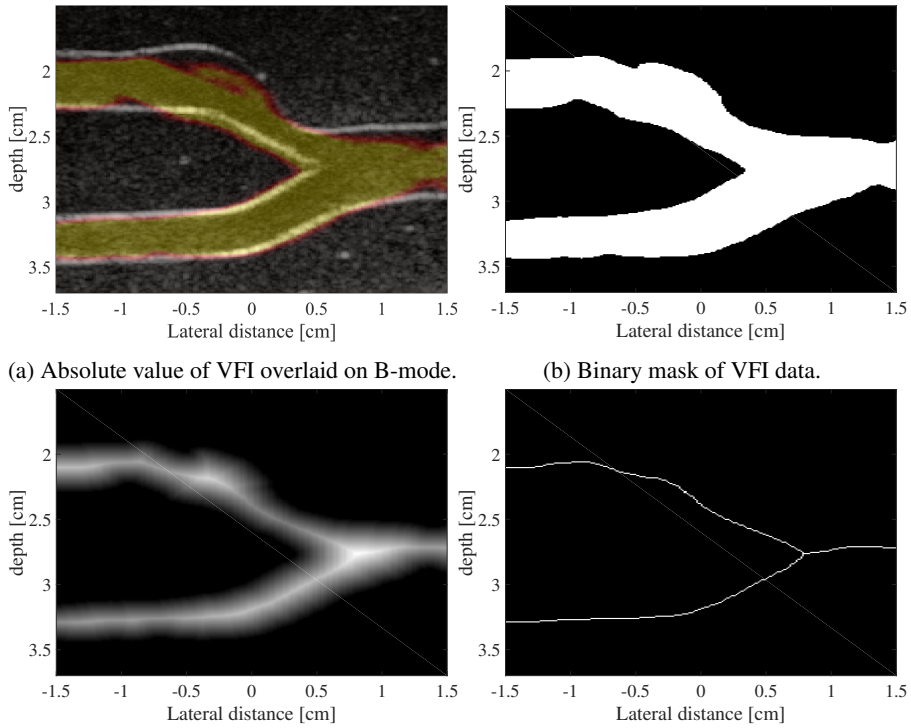

(a) Absolute value of VFI overlaid on B-mode.

(b) Binary mask of VFI data.

(c) Distance transform of inverted mask in *(b)*.

(d) Center-line of image in *(c)* (inner-markers).

Figure 5.1: Illustration of how inner-markers are detected for a scan of CA phantom.

algorithm from local maxima on the image. Adams et al. (Adams and Bischof 1994), on the other hand, proposed a seeded region growing algorithm. However, generating the initialization seeds is not straightforward. In fact, seeding is the most difficult part of the segmentation. The seeding procedure must provide markers that are accurately correspond to the desired objects. To address this issue, Adams (Adams and Bischof 1994) suggested to put manual seeds corresponding to the desired objects. This limits the final segmentation, so that the result has the same number of objects as the seeds. Therefore, this is not achievable in real-time imaging as the seeds are required to be detected automatically. The watershed trasnform is a special case of seeded region growing, and has been a major segmentation tool in mathematical morphology (Beucher and Lantuejoul 1979). The analogy of watershed originates from geography. Consider a landscape with holes pierced in local minima. When the landscape is flooded, basins would fill up with water from those local minima, and if the merging of waters of different

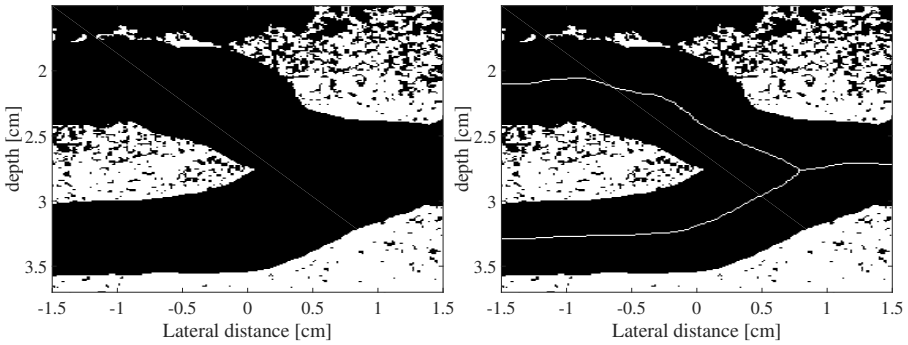

(a) Outer markers generated from B-mode and VFI.

(b) Marker image –combination of *(d)* and *(e)*.

Figure 5.2: Outer-markers and marker image generated for a scan of CA phantom.

basins are stopped by dams, the landscape is therefore partitioned in catchment basins separated by dams (watershed lines). The process is exemplified in the Fig. 5.3. A B-mode image can be regarded as a topographic landscape by considering gray levels as altitude. Watershed transform can be appllied to the B-mode images for segmentation

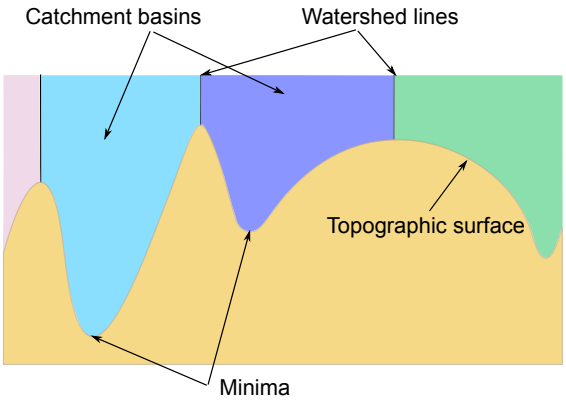

Figure 5.3: Analogy of the watershed by simulating the flooding of a topographic surface from its regional minima.

of vessel structures. However, specular pattern of the B-mode images might lead to over-segmentation of non-desired structures. The marker-controlled watershed introduced by Beucher and Meyer (Meyer and Beucher 1990) can address this issue. To avoid over-segmentation due to numerous sources of flooding, Mayer (Meyer and Beucher 1990)

suggetsed that a priori set of markers should be defined and flooding are only allowed from those markers (instead of flooding from all the minima in the image). Thus, the essential step in marker-controlled watershed is the extraction of object markers. This means that if the extracted markers fails to mark an object, the segmentation fails to segment the object too. Since the first introduction in 1990 (Meyer and Beucher 1990), several studies developed fully automated algorithms for the extraction of desired markers. Thresholding methods introduced by Kamgar-Parsi (Kamgar-Parsi and Kamgar-Parsi 2001) is sensitive to noise. Techniques using the distance transform (Borgefors 1986) results in multiple markers for one object. Marker extraction techniques based on mathematical morphology such as h-minima, top hat transforms and the skeleton of the gradient image are also proposed (Bengtsson, Wahlby, and Lindblad 2004).

In this study, a marker-controlled watershed is used to delineate the boundaries of the vessel-like structures bracketed by the marker image generated in Section 5.3. The B-mode image is median filtered, and a watershed segmentation of this filtered image with respect to the Marker image yielded the segmentation of the vessel-like structures (see Fig. 5.4(a)). However, segmentation results contain non-vessel structures that should be excluded.

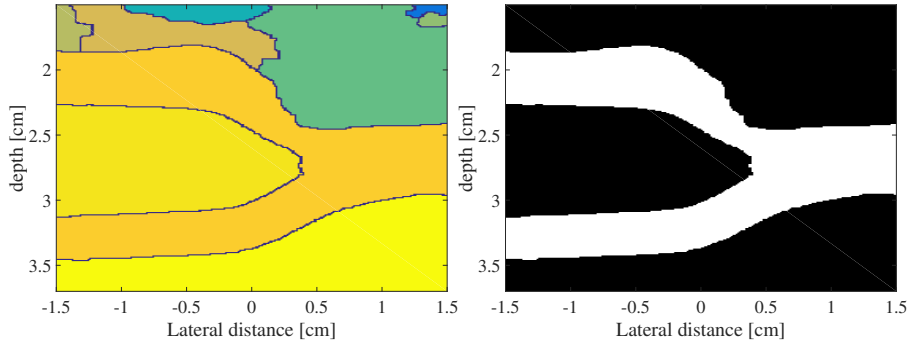

(a) Result of watershed segmentation.

(b) Artifacts rejected from image *(g)*.

Figure 5.4: Marker-controlled watershed applied to the B-mode image with respect to the marker image.

5.5 Artifact rejection

The marker-controlled watershed resulted in over-segmented regions, which are not vessels. This step implements artifact rejection based on size, shape and amount of flow to ensure that only the vessels are retained (see Fig.5.4(b)). Basically, elongated objects

containing the inner-marker (center-line of VFI data) are kept in segmentation results and the rest are excluded. Even though, the retained structures in this step are vessel-like objects, the boundaries of the vessels might present some discrepancies with respect to the actual vessel boundaries.

5.6 Inter-frame co-registration of segmentations

To refine the segmentation, so that it follows the exact vessel boundaries, an inter-frame co-registration of segmentations is performed. To deform parts of the segmentation that does not follow the actual vessel boundaries, 10 to 25 frames (depending on the frame rate) neighboring in time are considered. Segmentations performed on all the neighboring frames are co-registered and regions matching in at least 80% of the frames are considered to be the actual vessels (See Fig. 5.5).

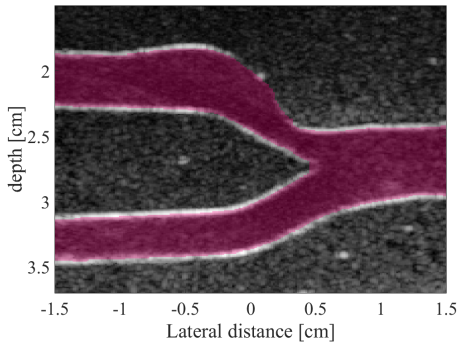

Figure 5.5: Inter-frame co-registration and refinement.

5.7 Quantitaive flow measures and the need for automation

Today's commercial ultrasound scanners are not able to present a perfect wall-to-wall delineation of vessels, while displaying the VFI images. Of particular interest is the extraction of new features that can express several desired properties of a vessel (i.e. constriction in carotid artery) in a single feature such as peak systolic velocity (PSV) (Grant et al. 2003; Reutern et al. 2012) using VFI. The volume flow is also a very interesting measure when inspecting the VFI, which quantifies the flow and characterizes the vessel (Hansen, Heerwagen, et al. 2013; Hansen, Olesen, et al. 2014; J. Jensen, Olesen, Hansen, et al. 2014; Brandt et al. 2016). However, this measure is very susceptible to the vessel diame-

ter, which makes the accurate delineation of the vessel very essential (J. Jensen, Olesen, Hansen, et al. 2014; J. Jensen, Olesen, Stuart, et al. 2016).

The proposed method delineates the vessel walls and enables the correct estimation of the volume flow. In the current implementation of VFI in ultrasound scanners, the correct volume flow estimation is not possible. The reason is that the VFI does not perfectly attach to the vessel walls, and therefore the VFI data is not available for regions very close to the vessel walls.

5.8 Enabling VFI automated measures

In this section the possibility of automating two crucial flow measures such as PSV and volume flow using VFI are introduced.

Spectral Doppler ultrasound (SDU) is the most commonly used tool for quantitative flow measures, such as peak velocities, resistive index, turbulence, and also the degree of stenosis. However, all of these measurements performed by spectral Doppler have to be corrected for the insonation angle. As discussed in Chapter 4, the angle correction is relatively impossible for complex and pulsating flow through constrictions, where flow angles fluctuate drastically over time and space (J. A. Jensen 2016). Quantitative measures acquired using this technique are then susceptible to angle correction, and can result in mis-diagnosis. Today's ultrasound devices use power Doppler or color flow mapping (CFM) to determine the flow and compute flow measures using the spectral velocity estimation (J. A. Jensen 1996; Evans and McDicken 2000). Transverse Oscillation (TO) vector flow imaging (J. A. Jensen and Munk 1998) and using synthetic aperture (SA) and directional beamforming introduced in Section 4.2 can be used to remedy the problems. Therefore, accurate and reliable quantitative flow measures can be calculated from the vector velocities estimated using these techniques. The remaining of the chapter implements automatic flow measures from VFI, and evaluate the performance of the implementations.

5.8.1 Automated Peak systolic velocity (PSV) measurement using VFI

The importance of the PSV, as a crucial flow meaure, to identify the stenosis is discussed in Section 5.7. PSV is also an important constituent of the clinical protocol, when examining a patient suspected of having carotid artery disease. In such meaurements, automatic PSV and automaic velocity angle estimations would be invaluable. This is because, the automatic meaurements reduces both the intera- and inter-observer variability (Steel et al. 2003)

Vector velocities acquired using the TO or SAFI can be used for PSV estimator. Consider a vector flow image (VFI) at time t acquired from a longitudinal section of a vessel (see Fig. 5.6). The image contains all the velocity estimates inside the vessel. A 2-D vector velocity $\mathbf{v}(r, m, t)$ identifies velocity magnitude and direction located on a perpendicular line to the vessel boundaries denoted by m and at distance r from the center-line of the vessel. Several vector velocities along the line m are used for computing the PSV as shown in Fig. 5.6. The PSV along line m in a cardiac cycle can be calculated by

$$PSV(m,t) := \left\{ max\left(\mathbf{v}(r,m,t)\right) | \forall r : 0 \leq r \leq R \right\}, \tag{5.1}$$

where R is the radius of the vessel, **e** is a unit vector normal to the surface S. Flow can be in any direction within the VFI image.

5.8.2 Automated volume flow measurement using VFI

The same VFI image used for PSV, is used for volume flow estimator. Given the fact that the acquired VFI is 2-D, three assumptions have been made to be able to estimate the volume flow. The first assumption is that flow is axisymmetric. The second is that cross-section of vessel is circular. Finally the third is that the velocity is sampled along a diameter of the vessel. The volume flow Q of a fluid passing through a circular surface S at time t is given by

$$Q(t) = \int_S \mathbf{v}(\mathbf{x}, t) \cdot \mathbf{e} \, \mathrm{d}S, \tag{5.2}$$

where **v** is a velocity vector positioned at **x** with respect to a random origin, **e** is a unit vector normal to the surface S, and $\cdot$ denotes the dot product operator.

Several vector velocities $\mathbf{v}(r, m, t)$ along the line m are used for estimating the volume flow as shown in Fig. 5.6. The volume flow is implemented using the method proposed in (J. Jensen, Olesen, Stuart, et al. 2016). The volume flow passing through the line m can be given by

$$Q(m,t) = \pi \int_{-R}^{R} \mathbf{v}(r,m,t) \cdot \mathbf{e} \, |r| \, \mathrm{d}r, \tag{5.3}$$

in which the rotation of the 2-D velocity profile around the axis of the vessel is due to the fact that the velocity vectors are assumed to be axisymmetrical.

The projection of **v** onto **e** ensures a flow, normal to the cross-section of the vessel. A discrete version of the integral in (5.3), considering a finite number N of velocity vectors sampled along the line m can be given by

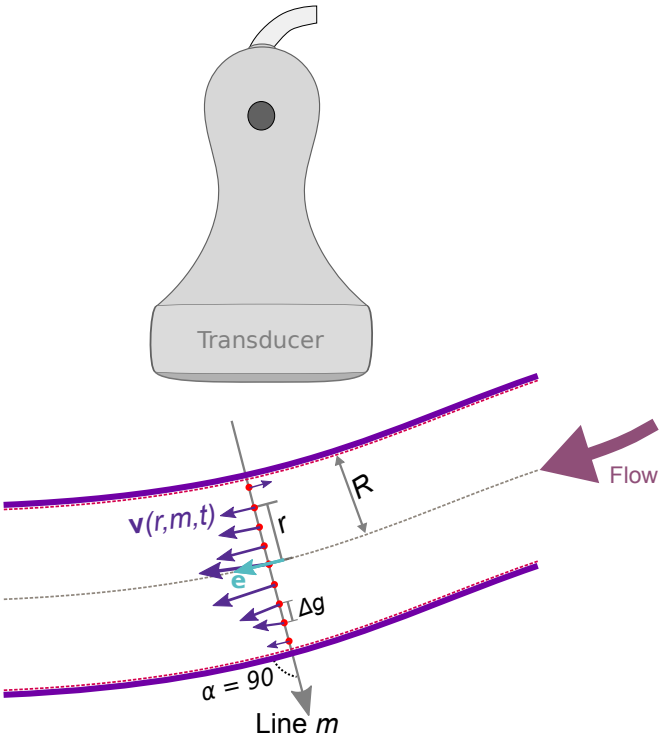

Figure 5.6: Longitudinal view of a vessel, and velocities estimated along line m. The vector velocity sample $\mathbf{v}(r, m, t)$ is at a radial and perpendicular distance r from the center axis. The radius of the vessel is R, and the radial distance between velocity estimation points is Δg. The line-to-flow angle is $\alpha = 90°$, and vector **e** is a unit vector normal to the cross-sectional vessel area.

$$Q(m,t) = \pi \Delta g^2 \sum_{n=-N/2}^{N/2} \mathbf{v}(n,m,t) \cdot \mathbf{e}\, |n|. \tag{5.4}$$

where Δg is the distance between two velocity samples and substitutes dr so that $r = n\Delta g$. This is, in a sense, the sum of volume flows in semi-annular rings with area of $\pi \Delta g^2 |n|$, each corresponding to a velocity component $\mathbf{v}(n, m, t) \cdot \mathbf{e}$. The angle between the line m and the normal vector **e** is $\alpha = 90°$, which is used to calculate Δg. Also, a mean volume flow for a cine-loop can be computed by averaging several volume flows from different

perpendicular lines to the vessel, over a number of frames N_f in the cine-loop as follows

$$Q = \frac{1}{MN_f} \sum_{t=1}^{N_f} \sum_{m=1}^{M} Q(m,t), \tag{5.5}$$

where M is the number of perpendicular lines chosen on the VFI. In pulsatile flow, N_f frames usually cover the whole number of cardiac cycles.

5.9 Evaluation of the segmentation algorithm

The proposed segmentation algorithm is applied to sequences acquired from carotid artery of five healthy volunteers. Each measurement contained 500 frames. Also a phantom mimicking a carotid artery at its bifurcation is scanned and used in this study. The beamformed RF data are acquired using a BK3000 scanner (BK Ultrasound, Denmark) connected to a 192-element 4.1 MHz linear array transducer (9032, BK Ultrasound). The beamformed RF data are simultaneously recorded by a research interface on the scanner, and processed with the proposed algorithm off-line. Automated segmentation results are compared with manual segmentations performed by an experienced user on 60 frames (10 frame randomly chosen from each sequence). Dice coefficient denoting the similarity between segmentations is then computed. The coefficient ranges between 0 and 1. A value of 1 indicates perfect agreement and a value of 0 indicates no agreement.

5.10 Empirical evaluation of the quantitative flow measures measured from VFI

Section 5.8 argued that TO VFI (J. A. Jensen and Munk 1998), and SA with directional beamforming introduced in Section 4.2 can be used to address the inherent problems of the SDU. It is consequently, expected to achieve more accurate and reliable quantitative flow measures from the VFI compare to SDU. However, prior to implementing the VFI measures in a commercial scanner, it must be investigated whether it performs better than the already used SDU. Therefore, PSVs measured from VFI and SDU are compared *in-vitro* and *in-vivo*.

5.10.1 *in-vitro* measurement setup

A Bk3000 ultrasound scanner equipped with VFI (BK3000, BK Ultrasound, Herlev, Denmark) was used to obtain VFI data. The *in-vitro* evaluation of the VFI was performed with both, a linear (4.1 MHz) and a convex (3.5 MHz) transducer (BK ultrasound, Herlev,

Denmark). This was done to validate the PSVs measured from superficial structures using the linear array, and from deep structures using the convex array.

For in-vitro flowrig validation of VFI, a flow system (CompuFlow 1000, Shelley Medical Imaging Technologies, Toronto, Canada) circulating a blood-mimicking fluid (BMF-US, Shelley Medical Imaging Technologies, Toronto, Canada) in a closed loop was used.

The linear transducer was fixed at a distance of 1.5 cm from the vessel of 12 mm in diameter with a beam-to-flow angle of 60 degrees. For increasing constant flowrig peak velocities of 5-60 cm/s, SDU and VFI data were recorded. For precision analysis, each velocity setting was recorded twice.

The convex transducer was positioned at 7 cm from the vessel. SDU and VFI data were recorded for increasing constant flowrig peak velocities of 5-50 cm/s. For precision analysis, each velocity setting was recorded twice. VFI was measured 10 times for the peak velocity of 25 cm/s, and the STD of VFI peak velocities was then calculated.

5.10.2 *in-vivo* measurement setup

Thirty two healthy volunteers were recruited after informed consent, and approval obtained from the National Committee on Biomedical Research Ethics (journal no. 15000104). Each volunteer was fasted for 4 to 6 hours prior to the examination. The convex transducers (3.5 MHz 6C2, BK ultrasound, Herlev, Denmark) was used for this study. All the Scans were performed in supine position, at intercostal and subcostal views. Two cine-loops with both SDU and VFI were recorded at each scan view for precision analyses.

For intera- and inter- observer study, Three radiologists were asked to re-scan a subset of 10 subjects from the 32 subjects –while blinded to the peak velocity estimates provided by SDU on the scanner.

5.11 Results and discussion

5.11.1 Segmentation results

Automated segmentation results were compared with manual segmentations performed by an experienced user on 60 frames (10 frame randomly chosen from each sequence). Dice coefficient denoting the similarity between segmentations was then computed. The coefficient ranges between 0 and 1. A value of 1 indicates perfect agreement and a value of 0 indicates no agreement. The Dice coefficient was 0.91, indicating that vessel boundaries obtained using the algorithm are highly accurate and consistent with the experts' visual perception of vessel boundaries. Two examples of segmentations performed by the

proposed hybrid method on scans acquired from a carotid phantom with a bifurcation and carotid of a normal male subject are shown in Figs. 5.7(a) and 5.7(b) respectively.

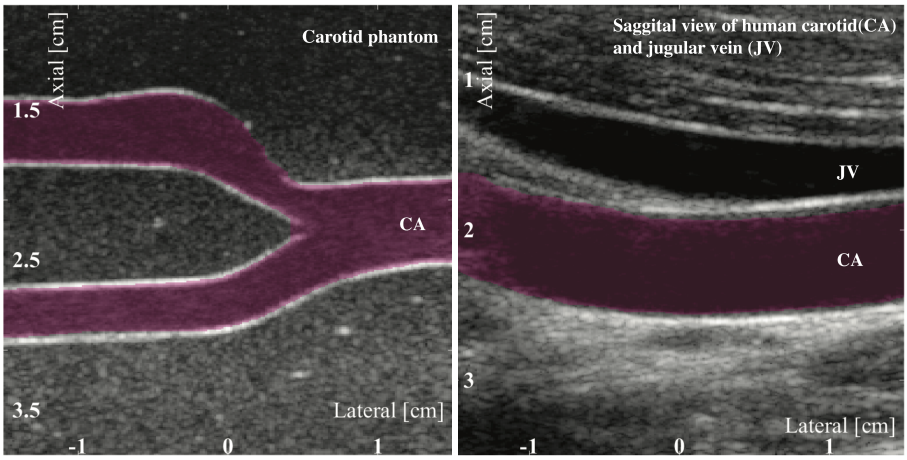

(a) Carotid artery segmented on carotid phantom.

(b) Carotid artery segmentation *in-vivo*.

Figure 5.7: Results of carotid segmentations performed on phantom and *in-vivo* scans.

5.11.2 VFI validation results

5.11.2.1 *In-vitro* RESULTS

Fig. 5.8 shows the results of in-vitro flowrig validation of VFI for measuring PSV. Relative errors of the PSVs measured from VFI and spectral Doppler comparing to the actual PSVs were 14.5% and 29.5% respectively (see Fig. 5.9). The figure shows that VFI offers a more precise and reliable alternative for velocity estimation of PSV in comparison with the current clinical standard using spectral Doppler, for the linear array.

5.11.2.2 *In-vivo* RESULTS

Precisions of VFI and SDU for the intercostal view were 18.1% and 28.3%, and those of the subcostal view were 23.2% and 76.8%, respectively.

Bias between VFI and SDU was 0.57 cm/s (p=0.38) intercostal and 9.89 cm/s ($p < 0.001$) subcostal. Intra- and interobserver agreement was highest for VFI (interobserver ICC: VFI 0.80, SDU 0.37; intraobserver ICC: VFI 0.90, SDU 0.86).

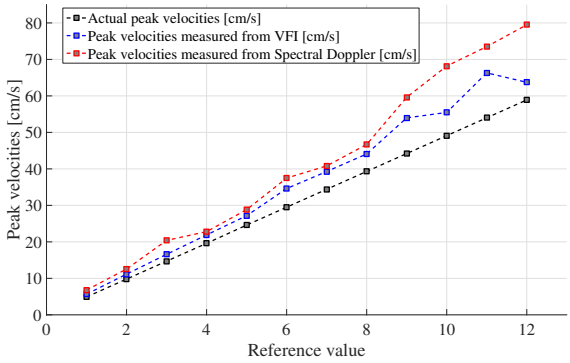

Figure 5.8: Comparison of flowrig PSV measured by VFI and spectral Doppler.

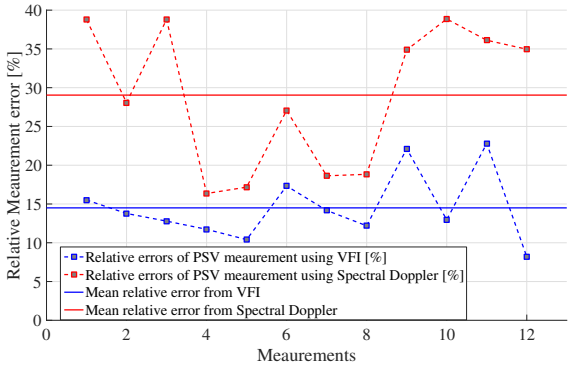

Figure 5.9: Relative errors of measurements with VFI and spectral Doppler.

5.11.3 Automated VFI measures results

PSV and volume flow, are implemented in an in-house tool specialized for VFI visualization and quantitative flow measures. All the PSV and volume flow measurements are performed using this application. Fig. 5.10(a) shows a screen shot of the visualization tool, in which a carotid artery belonging to a 29 years old healthy male subject is segmented and VFI is visualized. The PSV and volume flow are also measured using the application and reported across three cardiac cycles. PSV was 52.66 cm/s and the volume flow was 9 cm^3/s. The distribution of angle during one cardiac cycle was 89.54 ± 1.46 degrees.

5.11.3.1 Automated PSV

Using the proposed segmentation method, the vessel walls are accurately delineated. Fig. 5.10(a) shows an example of segmentation of a human carotid. The red lines indicate the location of the vessel walls delineated by the proposed method. user located a point on either side of the vessel boundaries. A perpendicular line to the vessel boundaries is automatically created across the vessel. Then, PSV along the perpendicular line, through the vessel, across a specified number of cardiac cycles is calculated. The red horizontal line indicates the position as well as the mean-angle of the peak velocity throughout the cycle. The green horizontal line indicates the center and the circular cross-section found inside the vessel for measuring the volume flow discussed in the next section. Fig. 5.10(b) shows the velocity profile measured at the PSV point across three cardiac cycles.

5.11.3.2 Automated volume flow

For Volume flow measurements *in-vivo*, first, the vessel walls are automatically delineated, and VFI is refined so that it covers the whole vessel region. This enables the correct estimation of volume flow. Second, the volume flow can be computed with minimal user actions. This is performed by selecting a point on either of the vessel walls. A vessel cross-section between the segmented walls is automatically generated for computing the volume flow in VFI (see yellow circular cross-section in Fig. 5.10(a)). The volume flow is then estimated using the formula in 5.4.

5.12 Summary

This chapter presented a novel hybrid segmentation algorithm that combines VFI and B-mode to delineate the vessel boundaries. The algorithm also implemented PSV and volume flow for VFI. The empirical results showed a dice coefficient of 0.91, indicating a good match between segmentation performed by the algorithm and the expert. The results of the flowrig measurements also showed that VFI was 15% more precise than spectral Doppler for PSV measurement.

The results indicated that regardless of the beam-to-flow angle, VFI is more precise in compare with SDU for PSV estimation in the portal vein. Furthermore, VFI can estimate the same peak velocity in the main portal vein with an insonation angle inapplicable for spectral Doppler. Therefore, the proposed method enables a better visualization of VFI, as well as the automatic quantitative flow measures using vector velocities. The algorithm can also be used in daily clinical practice as an alternative tool for making a quantitative flow measures.

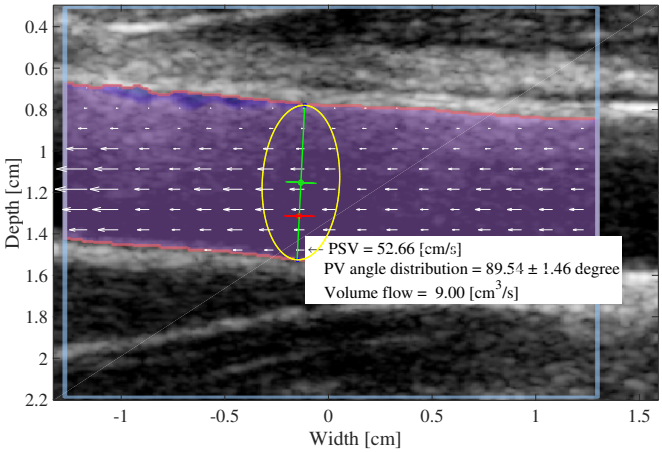

(a) Carotid artery of a 29 years old male subject is segmented and VFI is visualized. PSV and volume flow are measured automatically across three cardiac cycles.

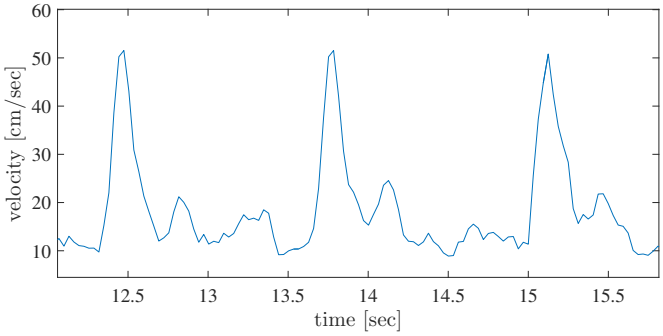

(b) Velocity profile measured at the PSV point shown with red on *(a)* in the vessel, across three cardiac cycles.

Figure 5.10: Automated segmentation and quantitative flow measurements performed on a carotid artery of a 29 years old male subject.

All the flow measures introduced in this chapter, are implemented in an in-house application specialized for VFI visualization and quantitative flow measures. All the PSV and volume flow measurements are performed using this application. Also, the distribution of peak velocity amplitudes and angles across specified number of cardiac cycles can be automatically computed and reported.

References from Chapter 5

Smeulders, A., C. Cornelisse, A. Vossepoel, and J. Ploem (1978). “An image segmentation approach to the analysis of nuclear texture of cervical cells”. In: *Acta histochemica. Supplement band* 20, pp. 217–222 (cit. on p. 78).

Beucher, S. and C. Lantuejoul (1979). “Use of watersheds in contour detection”. In: (cit. on p. 79).

Borgefors, G. (1986). “Distance Transformations in Digital Images”. In: *Comput. Vision Graph. Image Process.* 34.3, pp. 344–371 (cit. on p. 81).

Kondo, A. and K. Taniguchi (1986). “Evaluation of the chromatin for cell images”. In: *Systems and Computers in Japan* 17.9, pp. 11–19 (cit. on p. 78).

Meyer, F. and S. Beucher (1990). “Morphological segmentation”. In: *Journal of Visual Communication and Image Representation* 1.1, pp. 21–46 (cit. on pp. 80, 81).

Adams, R. and L. Bischof (1994). “Seeded Region Growing”. In: *IEEE Trans. Pattern Anal. Mach. Intell.* 16.6, pp. 641–647 (cit. on p. 79).

Jensen, J. A. (1996). *Estimation of Blood Velocities Using Ultrasound: A Signal Processing Approach*. New York: Cambridge University Press (cit. on p. 83).

Mojsilovic, A., M. Popovic, N. Amodaj, R. Babic, and M. Ostojic (1997). “Automatic segmentation of intravascular ultrasound images: a texture-based approach”. In: *Annals of biomedical engineering* 25.6, pp. 1059–1071 (cit. on p. 76).

Wendelhag, I., Q. Liang, T. Gustavsson, and J. Wikstrand (1997). “A new automated computerized analyzing system simplifies readings and reduces the variability in ultrasound measurement of intima-media thickness”. In: *Stroke* 28.11, pp. 2195–2200 (cit. on p. 76).

Jensen, J. A. and P. Munk (1998). “A New Method for Estimation of Velocity Vectors”. In: *IEEE Trans. Ultrason., Ferroelec., Freq. Contr.* 45, pp. 837–851 (cit. on pp. 83, 86).

Evans, D. H. and W. N. McDicken (2000). *Doppler Ultrasound, Physics, Instrumentation, and Signal Processing*. New York: John Wiley & Sons (cit. on p. 83).

Mao, F., J. Gill, D. Downey, and A. Fenster (2000). “Segmentation of carotid artery in ultrasound images: Method development and evaluation technique”. In: *Medical physics* 27.8, pp. 1961–1970 (cit. on p. 76).

Kamgar-Parsi, B. and B. Kamgar-Parsi (2001). “Improved image thresholding for object extraction in IR images”. In: *Int. Conf. Image Processing*. Vol. 1, pp. 758–761 (cit. on p. 81).

Selzer, R. H., W. J. Mack, P. L. Lee, H. Kwong-Fu, and H. N. Hodis (2001). “Improved common carotid elasticity and intima-media thickness measurements from computer

analysis of sequential ultrasound frames". In: *Atherosclerosis* 154.1, pp. 185–193 (cit. on p. 76).

Cheng, D., A. Schmidt-Trucksaess, K. Cheng, and H. Burkhardt (2002). "Using snakes to detect the intimal and adventitial layers of the common carotid artery wall in sonographic images". In: *Computer methods and programs in biomedicine* 67.1, pp. 27–37 (cit. on p. 76).

Gutierrez, M., P. Pilon, S. Lage, L. Kopel, R. Carvalho, and S. Furuie (2002). "Automatic measurement of carotid diameter and wall thickness in ultrasound images". In: *Computers in Cardiology*. IEEE, pp. 359–362 (cit. on p. 76).

Xiao, G., M. Brady, J. A. Noble, and Y. Zhang (2002). "Segmentation of ultrasound B-mode images with intensity inhomogeneity correction". In: *IEEE Trans. Med. Imag.* 21.1, pp. 48–57 (cit. on p. 76).

Grant, E. G., C. B. Benson, G. L. Moneta, A. V. Alexandrov, J. D. Baker, E. I. Bluth, B. A. Carroll, and et al. (2003). "Carotid artery stenosis: gray-scale and Doppler US diagnosis - Society of radiologists in ultrasound consensus conference". In: *Radiology* 229.2. M. Eliasziw and J. Gocke and B. S. Hertzberg, pp. 340–346. DOI: 10.1148/radiol.2292030516 (cit. on p. 82).

Steel, R., K. V. Ramnarine, F. Davidson, P. J. Fish, and P. R. Hoskins (2003). "Angle-independent estimation of maximum velocity through stenoses using vector Doppler ultrasound". In: *Ultrasound Med. Biol.* 29.4, pp. 575–584. DOI: http://dx.doi.org/10.1016/S0301-5629(02)00736-6 (cit. on p. 83).

Bengtsson, E., C. Wahlby, and J. Lindblad (2004). "Robust cell image segmentation methods". In: *Patt. Recog. Im. anal.* 14.2, pp. 157–167 (cit. on p. 81).

Stein, J. H., C. E. Korcarz, M. E. Mays, P. S. Douglas, M. Palta, H. Zhang, T. LeCaire, D. Paine, D. Gustafson, and L. Fan (2005). "A semiautomated ultrasound border detection program that facilitates clinical measurement of ultrasound carotid intima-media thickness". In: *J. Am. Soc. Echocardiog.* 18.3, pp. 244–251 (cit. on p. 76).

Delsanto, S., F. Molinari, P. Giustetto, W. Liboni, S. Badalamenti, and J. S. Suri (2007). "Characterization of a completely user-independent algorithm for carotid artery segmentation in 2-D ultrasound images". In: *IEEE Transactions on Instrumentation and Measurement* 56.4, pp. 1265–1274 (cit. on p. 76).

Golemati, S., J. Stoitsis, E. G. Sifakis, T. Balkizas, and K. S. Nikita (2007). "Using the Hough transform to segment ultrasound images of longitudinal and transverse sections of the carotid artery". In: *Ultrasound Med. Biol.* 33.12, pp. 1918–1932 (cit. on p. 76).

Loizou, C., C. Pattichis, M. Pantziaris, T. Tyllis, and A. Nicolaides (2007). "Snakes based segmentation of the common carotid artery intima media". In: *Medical & Biological Engineering & Computing* 45.1, pp. 35–49. DOI: 10.1007/s11517-006-0140-

3. URL: http://dx.doi.org/10.1007/s11517-006-0140-3 (cit. on p. 76).

Faita, F., V. Gemignani, E. Bianchini, C. Giannarelli, L. Ghiadoni, and M. Demi (2008). "Real-time measurement system for evaluation of the carotid intima-media thickness with a robust edge operator". In: *Journal of Ultrasound in Medicine* 27.9, pp. 1353–1361 (cit. on p. 76).

Destrempes, F., J. Meunier, M. Giroux, G. Soulez, and G. Cloutier (2009). "Segmentation in ultrasonic B-mode images of healthy carotid arteries using mixtures of Nakagami distributions and stochastic optimization". In: *IEEE Trans. Med. Imag.* 28.2, pp. 215–229 (cit. on p. 76).

Rossi, A. C., P. J. Brands, and A. P. Hoeks (2010). "Automatic localization of intimal and adventitial carotid artery layers with noninvasive ultrasound: a novel algorithm providing scan quality control". In: *Ultrasound Med. Biol.* 36.3, pp. 467–479 (cit. on p. 76).

Santhiyakumari, N., P. Rajendran, M. Madheswaran, and S. Suresh (2011). "Detection of the intima and media layer thickness of ultrasound common carotid artery image using efficient active contour segmentation technique". In: *Med. Biol. Eng. Comp.* 49.11, pp. 1299–1310 (cit. on p. 76).

Molinari, F., C. S. Pattichis, G. Zeng, L. Saba, U. R. Acharya, R. Sanfilippo, A. Nicolaides, and J. S. Suri (2012). "Completely automated multiresolution edge snappera new technique for an accurate carotid ultrasound IMT measurement: clinical validation and benchmarking on a multi-institutional database". In: *IEEE Transactions on Image Processing* 21.3, pp. 1211–1222 (cit. on p. 76).

Pedersen, M. M., M. J. Pihl, P. Haugaard, J. M. Hansen, K. L. Hansen, M. B. Nielsen, and J. A. Jensen (2012). "Comparison of Real-Time In Vivo Spectral and Vector Velocity Estimation". In: *Ultrasound Med. Biol.* 38.1, pp. 145–151 (cit. on p. 77).

Petroudi, S., C. Loizou, M. Pantziaris, and C. Pattichis (2012). "Segmentation of the common carotid intima-media complex in ultrasound images using active contours". In: *IEEE Trans. Biomed. Eng.* 59.11, pp. 3060–3069 (cit. on p. 76).

Reutern, G. M. von, M. W. Goertler, N. M. Bornstein, M. D. Sette, D. H. Evans, A. Hetzel, M. Kaps, F. Perren, and et al. (2012). "Grading Carotid Stenosis Using Ultrasonic Methods". In: *Stroke* 43.3, pp. 916–921. DOI: 10.1161/STROKEAHA.111.636084 (cit. on p. 82).

Xu, X., Y. Zhou, X. Cheng, E. Song, and G. Li (2012). "Ultrasound intima–media segmentation using Hough transform and dual snake model". In: *Computerized Medical Imaging and Graphics* 36.3, pp. 248–258 (cit. on p. 76).

Hansen, P. M., S. Heerwagen, M. M. Pedersen, M. Rix, L. Lønn, M. B. Nielsen, J. B. Olesen, M. J. Pihl, and J. A. Jensen (2013). "Vector Volume Flow in Arteriovenous Fistulas". In: *Proc. IEEE Ultrason. Symp.* Pp. 2026–2029 (cit. on p. 82).

Yang, X., W. He, K. Li, J. Jin, X. Zhang, M. Yuchi, and M. Ding (2013). "Ultrasound common carotid artery segmentation based on active shape model". In: *Computational and mathematical methods in medicine*, pp. 1–11 (cit. on p. 76).

Hansen, P. M., J. B. Olesen, M. J. Pihl, T. Lange, S. Heerwagen, M. M. Pedersen, M. Rix, L. Lønn, J. A. Jensen, and M. B. Nielsen (2014). "Volume Flow in Arteriovenous Fistulas using Vector Velocity Ultrasound". In: *Ultrasound Med. Biol.* 40.11, pp. 2707–2714 (cit. on p. 82).

Jensen, J., J. B. Olesen, P. M. Hansen, M. B. Nielsen, and J. A. Jensen (2014). "Accuracy and Sources of Error for an Angle Independent Volume Flow Estimator". In: *Proc. IEEE Ultrason. Symp.* Pp. 1714–1717 (cit. on pp. 82, 83).

Menchon-Lara, R., M. C. Bastida-Jumilla, J. Morales-Sanchez, and J. Sancho-Gomez (2014). "Automatic detection of the intima-media thickness in ultrasound images of the common carotid artery using neural networks". In: *Medical biological engineering computing* 52.2, pp. 169–181 (cit. on p. 76).

Carvalho, D. D. B., Z. Akkus, S. C. H. van den Oord, A. F. L. Schinkel, A. F. W. van der Steen, W. J. Niessen, J. G. Bosch, and S. Klein (2015). "Lumen Segmentation and Motion Estimation in B-Mode and Contrast-Enhanced Ultrasound Images of the Carotid Artery in Patients With Atherosclerotic Plaque". In: *IEEE Trans. Med. Imag.* 34.4, pp. 983–993 (cit. on p. 76).

Brandt, A. H., J. Jensen, K. L. Hansen, P. M. Hansen, T. Lange, M. Rix, J. A. Jensen, L. Lönn, and M. B. Nielsen (2016). "Surveillance for Hemodialysis Access Stenosis: Usefulness of Ultrasound Vector Volume Flow". In: *J. Vascul. Access.* Accepted for publication (cit. on p. 82).

Jensen, J. A. (2016). "Quantitative Measurements using Ultrasound Vector Flow Imaging". In: *Proc. IEEE Ultrason. Symp.* Pp. 1–4 (cit. on p. 83).

Jensen, J., J. B. Olesen, M. B. Stuart, P. M. Hansen, M. B. Nielsen, and J. A. Jensen (2016). "Vector velocity volume flow estimation: Sources of error and corrections applied for arteriovenous fistulas". In: *Ultrasonics* 70, pp. 136–146. DOI: http://dx.doi.org/10.1016/j.ultras.2016.04.023 (cit. on pp. 83, 84).

CHAPTER 6

Automated Detection and Visualization of B-line Artifacts in Lung Ultrasound Imaging

The present chapter aims to present a automated technique for diagnosing pulmonary diseases using lung ultrasound. The chapter thus, presents a technique for automated detection of disease correlated reverberation artifacts, more specifically B-lines, in ultrasound lung scans. B-lines are the most commonly used artifacts for diagnosing pulmonary diseases in lung ultrasound. They are reverberation artifacts, which arise from the pleura and spread down without fading to the edge of the screen. Apart from the recent advances in application of lung ultrasound, there are no computerized and automated techniques for characterizing the B-line artifacts and pulmonary disease in the literature. This chapter proposes an automatic method for accurate detection of B-lines in ultrasound lung scans. The proposed method also enables quantitative measures in bed-side lung ultrasound, thereby exploiting the full potential of this imaging technique.

The remainder of this chapter is organized as follows. Section 6.1 reviews the literature in lung ultrasound and B-line artifacts. Section 6.2 introduces the B-line artifacts, and section 6.3 gives high-level describtion of the proposed method. Sections 6.4 to 6.9 discuss the proposed technique. Section 6.10 is the scan protocol of the study, and section 6.11 introduces the images acquired. Section 6.12 presents the results and discuss the findings. Finally, section 6.13 summarizes the chapter.

6.1 Review of the state-of-the-art lung ultrasound imaging

Lung ultrasound has received increasing attention in recent years, as it enables a quick visual analysis of lung, as well as diagnosis of pulmonary diseases without imposing radiation. In lung ultrasound imaging, An intimate mixture of air and water characterizes the lung state. Change in their balance can be a sign of pulmonary disease. Interactions of water and air in ultrasound lung scans generate a variety of artifacts, and a lung ultrasound

image of pulmonary disease is therefore based on analyzing these artifacts rather than pure visualization of the structures (D. Lichtenstein, Meziere, et al. 1999; E.Agricola et al. 2005; Volpicelli, Mussa, et al. 2006; Gargani, Frassi, et al. 2008). B-lines are reverberation artifacts generated by multiple reflections of the ultrasound beam trapped between air- and water-rich structures. They originate from the visceral pleura (serous membrane covering the surface of the lungs) and spread down to the edge of the screen. B-line detection is essential in the assessment of lung-edema in lung ultrasound imaging, which is often present in patients with heart and lung diseases as well as patients having undergone major surgery (Volpicelli, Mussa, et al. 2006; Gargani 2011; D. A. Lichtenstein 2014). B-lines are also used to detect pneumothorax as B-lines disappear, when a pneumothorax is present.

The condition where air is found within the pleural cavity can result in a collapsed lung, and if untreated be fatal. In daily clinical practice, patients suspected for pulmonary edema or pneumothorax are imaged with X-ray, and often repeatedly imaged with short intervals to monitor the effect of the applied treatment. Lung ultrasound is a well-established modality, but it is often bypassed, as the medical staff handling these patients are not familiar with the method.

In 1997, Lichtenstein (D. Lichtenstein, Mézière, et al. 1997) showed a correlation between B-lines in ultrasound and chest computed tomography (CT). Even though lung ultrasound already had been used for evaluation of pleural effusion, it was the first time that the diagnostic value of B-line artifacts was shown. In 2004, Picano (Jambrik et al. 2004) showed the correlation between the number of B-lines detected by lung ultrasound and X-ray findings for assessing the presence of extra-vascular lung water (EVLW). Since then, multiple studies have shown the methodological validation and clinical application of B-lines for diagnosing pulmonary diseases (E.Agricola et al. 2005; Volpicelli, Mussa, et al. 2006; Gargani, Lionetti, et al. 2007; Gargani, Frassi, et al. 2008). The common practice for diagnosing pulmonary edema with ultrasound is based on visual analysis and interpretation of B-lines on still lung ultrasound images.

For the detection of pneumothorax, the detection of a single B-line excludes pneumothorax in the imaged lung segment. Several B-lines on an ultrasound scan are called ”lung rockets” or B+ lines. This pattern distributed in more scans on each lung defines diffuse alveolar-interstitial syndrome (in some cases caused by pulmonary edema) (Volpicelli, Mussa, et al. 2006). The standard pathological routine for diagnosing this disease is to detect B+ pattern in a single scan or frame. A study performed by intensivists (D. Lichtenstein, Meziere, et al. 1999) showed that the mean distance between two adjacent B-lines at lung surface is never more than 7 mm, and this should be the widest distance between B-lines to be significant. Another study used the criteria of counting at least three artifacts with a distance between adjacent lines of no more than 7 mm for identifying a

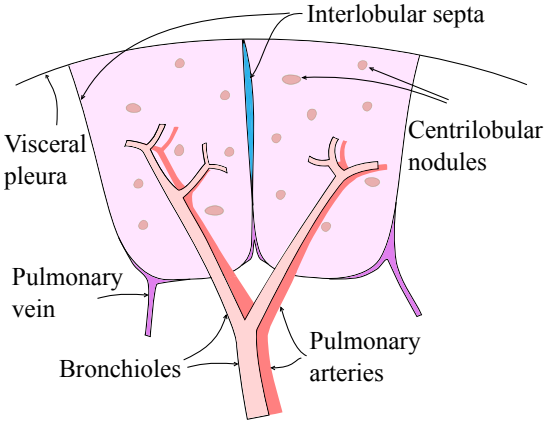

Figure 6.1: Anatomy of the secondary lobule and its components. The interlobular septum is thickened due to the existence of fluid.

B+ pattern (Volpicelli, Cardinale, et al. 2008). On the other hand, visualization of isolated B-lines, or visualization of multiple B-lines of more than 7 mm apart in a single scan, was considered a normal finding (Volpicelli, Cardinale, et al. 2008). However, a major factor affects the accuracy of the examination. That factor is interpretation error for reasons including, inexperience, and habituation. Computer-assisted interpretation can potentially address the issue of interpretation error, and facilitates the adoption by users . Based on the authors' knowledge, apart from recent advances in application of B-lines, there are no computerized and automated models for characterizing the B-line artifacts in the literature.

6.2 B-lines artifacts

B-lines are the most commonly used artifacts for diagnosing pulmonary diseases. They are reverberation artifacts that originate from water-thickened pulmonary interlobular septa (Gargani 2011), and spread down without fading to the edge of the screen. Fig. 6.1 shows the anatomy of secondary lobule, in which the interlobular septum is thickened due to the existence of fluid. In ultrasound images of lung, B-lines originate from the visceral pleural line and extend to the edge of the display. Fig. 6.2 illustrates how B-lines are generated in ultrasound.

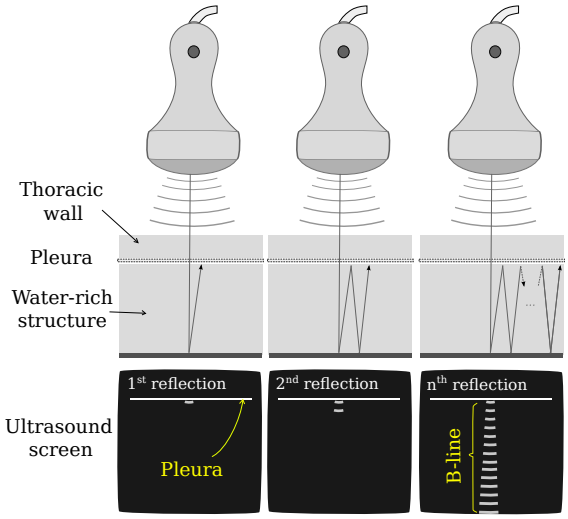

Figure 6.2: Illustration of how B-line artifacts are generated. They are hyper-echoic reverberation artifacts arising from the pleural line and spreading down towards the lower edge of the screen.

6.3 High-level description of the proposed algorithm

The proposed method contains six distinct steps.

1. First, the pleural line is delineated using a random walks method (Grady 2006; Karamalis et al. 2012).
2. Second, the upper-pleural region is excluded from the scan and the B-line artifacts are identified on the scan plane.
3. Third, an alternate sequential filtration is applied to the results of step 2 to better highlight the B-lines.
4. Fourth, the result of step 4 is top-hat filtered to make sure that B-lines are laterally detached.
5. Fifth, a Gaussian model is fitted to each detected B-line.
6. Finally, the center or peak point of the fitted Gaussian models corresponding to the B-lines are calculated and used to determine the position of the B-lines. B-lines are then overlaid on the B-mode image.

6.4 Pleural line delineation

The first essential step in detection of B-lines is to delineate the pleural line on the lung scans. For this purpose, a graph based approach that computes a per-pixel uncertainty map based on the information depicted by an ultrasound image is used (Karamalis et al. 2012). This method rather specifically measures the uncertainty in attenuated and/or shadow regions. To identify the map for each ultrasound frame, a random walks framework is used that takes into account ultrasound specific constraints (Karamalis et al. 2012). The solution of the random walks equilibrium problem is global and takes the entire content of the RF data into account. The required starting points are automatically placed at the beginning of each scan-line to represent the transducer elements. Thus, a problem is formulated by computing the probability of a random walk starting from a pixel to reach the transducer elements. The domain specific knowledge for ultrasound is integrated with a simple modeling of the ultrasound image formation process. The ultrasound specific constraints obtained from physics of acquired RF data by the transducer must be integrated to ensure the accuracy of the confidence map. One of the fundamental properties of ultrasound is the attenuation of the signal by increasing depth. The Beer–Lambert Law is used to express the depth dependent attenuation, and the attenuated signal I could be given by $I = I_0 \exp(-\alpha d)$, where I_0 is the initial intensity, α the attenuation coefficient, and d the distance from the source. This property is included into the confidence map in a way that the further away a random walk starts from the transducer is, the more unlikely it will be able to reach one of the transducer elements. The computed confidence map is used to determine the upper-pleural region and exclude that from the RF-data prior to detecting the B-lines (see Fig. 6.3(b) on page 105). The pleural line is delineated on the confidence map by globally thresholding the confidence map to be higher than the global threshold of the entire map. The region with values higher than the threshold is considered the upper pleura, and the rest is lower pleural region. In the next step the B-lines starting from the pleura and appearing inside the lower pleural region are detected.

6.5 B-lines detection

B-line detection contains four steps. First, The area on the scan corresponding to the upper-pleura is excluded from the data (Fig. 6.3(c) on page 105), and the B-lines are characterized from the remaining of the RF-data. This is done because B-lines originate from the pleura and extend downwards to the end of the screen. Second, to extract the vertical edges in the RF-data, a normalized cumulative histogram the remained RF-data is computed axially. This yielded an axial-cumulative image, in which each column is the cumulative sum of the corresponding scan-line in the RF-data (Fig. 6.3(d) on page 105).

Each column of the axial-cumulative image is normalized to the maximum brightness of the same column. Third, this image is inverted and an adaptive histogram equalization is performed to increase the contrast (Fig. 6.3(e) on page 105). Finally, a binary mask including the strong specular regions inside the histogram-equalized image is generated (Fig. 6.3(f) on page 105). This binary mask, outlines the most prominent B-lines in the envelope data . The procedure is detailed in Algorithm 3. This mask is further manipulated in Sections 6.6 and 6.7 to better characterize and visualize the B-lines.

6.6 B-lines axial improvement

The binary mask generated in the previous section and shown in Fig. 6.3(f) on page 105, provides a very crude characterization of B-lines. An alternate sequential filtering (ASF) procedure using a repeated sequential morphological opening and closing is applied to the mask. ASF closes small gaps axially and isolates the objects laterally. The procedure is depicted in Algorithm. 5. ASF highlights the vertical B-lines and isolate them from each other laterally. Fig. 6.3(g) on page 105 is the result of ASF, in which the B-lines are better identified in comparison with those in Fig. 6.3(f) on page 105. An axial line-structuring element, along the ultrasound beam, is used for ASF filtering. This is used to ensure that only elongated and axial information (B-line artifacts) in the compressed data are preserved and highlighted.

6.7 B-lines latteral separation

The generated mask in the previous step contains prominent axially elongated and adjacent tails locating the B-lines. However, the tails can be laterally connected that deteriorate the clean separation of them (B-lines). To separate and extract the B-lines automatically, a top-hat transformation is used. The top-hat transformation originally proposed by Mayer (Meyer 1977) is a mathematical morphology operator that uses morphological opening or closing for extracting bright (respectively dark) objects from an uneven background in a 2D grey-scale image. Top-hat transformation can be formulated in two ways: white top-hat (WTH) and black top-hat (BTH). WTH can also be used to identify prominent peaks in a 1D signal, and the BTH as the dual of the WTH can be used to identify the prominent minima in a 1D signal. In this study a (WTH) with a flat disk structuring element is used to extract the B-lines. The WTH transformation of a 1D signal f with a flat structuring element B is defined as $T_{white}(f) = f - (f \circ B)$.

To identify the actual B-lines, the top-hat transform is applied using a line structuring element (B) that is somewhat longer than the size of the connected regions. The $\circ$ is the opening operator and is basically a min operation that removes the regions smaller than

Algorithm 3 B-line detection

Input: RF, which is the RF-data acquired from the scanner.
Output: Binary mask (B_{bl}) in which the strong axial B-lines are highlighted.

procedure B-LINE DETECTION
    $Env = \log_{10}\left(|\mathcal{H}\{RF\}|\right)$ # performing the Hilbert transformation, and computing the envelope of RF data.
    Let $Ax\_cdf(M, N)$ be a discrete gray scale image denoting the axial cumulative image of the envelope data with M rows and N columns.
    for each $i \in M$ **do**
        for each $ii \in N$ **do**
            $Ax\_cdf(i, ii) = \frac{\sum_{j=0}^{i} Env(j,ii)}{max(Env(ii).col)}$ # computing the axial cumulative sum and normalizing to the maximum intensity of that column.
        end for
    end for
    $B_c = max(Ax\_cdf) - Ax\_cdf$ # inverting the axial cumulative image.
    $B_c = adapthisteq(B_c)$ # function performing the adaptive histogram equalization.
    Let B_c be a discrete gray scale image and let n_i be the number of occurrences of gray level i.
    $p_{B_c(i)} = p\left(B_c = i\right) = \frac{n_i}{n}, 0 < i < L$ # probability of an occurrence of a pixel of level i in the image.
    Let L be the total number of gray levels in the image (in our case 256), n being the total number of pixels in the image, and $p_{B_c(i)}$ be the image's histogram for pixel value i, and normalized to $[0, 1]$.
    for each $i \in L$ **do**
        $cdf_{B_c(i)} = \sum_{j=0}^{i} p_{B_c(j)}$ # define the cumulative distribution function corresponding to p_{B_c}.
    end for
    Let th_l be the gray value for which $cdf_{B_c=0.5}$ and th_h be the gray value in which $cdf_{B_c=1}$.
    Let B_{bl} be a zero binary mask with the same size as image B_c
    for each $ii \in N$ **do** # N is the total number of pixels in the image B_{bl}.
        if $th_l < B_c(ii) < th_h$ **then**
            $B_{bl}(ii) = 1$
        end if
    end for
end procedure

Algorithm 4 Alternate sequential filtering

Input: B_{in} Binary mask outlining most prominent edges in RF-data, and N maximum size of the structuring element in ASF.
Output: B_{ASF} Binary mask in which the strong axial B-lines are highlighted.

procedure ASF
    $B_{ASF} = B_{in}$
    for each $i \in N$ **do**
        Let S_{lin} be a line structuring element of length N.
        $B_{ASF} = (B_{ASF} \ominus S_{lin}) \oplus S_{lin}$ # performing the morphological opening.
        $B_{ASF} = (B_{ASF} \oplus S_{lin}) \ominus S_{lin}$ # performing the morphological closing.
    end for
end procedure

Note: $\oplus$ and $\ominus$ denote morphological dilation and erosion respectively.

the size of structuring element. Subtracting this signal from the original signal produces a signal that only contains the desired strong peaks. Fig. 6.3(h) on the facing page shows B-lines detected after top-hat filtering for a lung scan of a healthy subject.

6.8 Gaussian model fitting

The B-lines curve after top-hat filtering is quite rough and the peak points of the B-lines are not well-defined. A Gaussian model is fitted to each B-line (Fig. 6.3(i) on the next page). The peak points of the Gaussian models were calculated and considered to be the position of the B-lines along the pleura. The final Gaussian-fitted B-line mask is then overlaid on the B-mode.

6.9 Enabling automated quantification of B-lines

The essential first step to automate the characterization of B-lines is to implement measures that can quantify the distribution of these lines in ultrasound lung sequences. The average number of B-lines across the acquired frames in each sequence is computed automatically, and used as an indication of whether the scans acquired from the subject was normal or not.

6.10 Scanning protocol

The proposed algorithm was applied to in-vivo ultrasound lung scans acquired from healthy subjects and patients after informed consent. An eight-zone scanning proto-

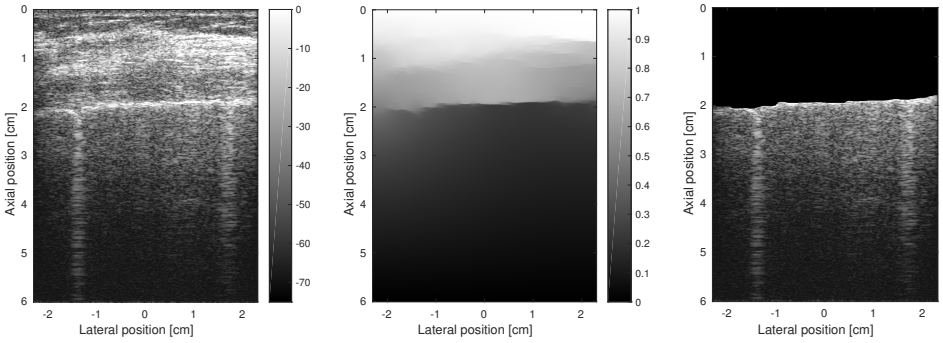

(a) LUS image.

(b) Confidence map of image in *(a)*.

(c) Upper pleura excluded from image in *(a)*.

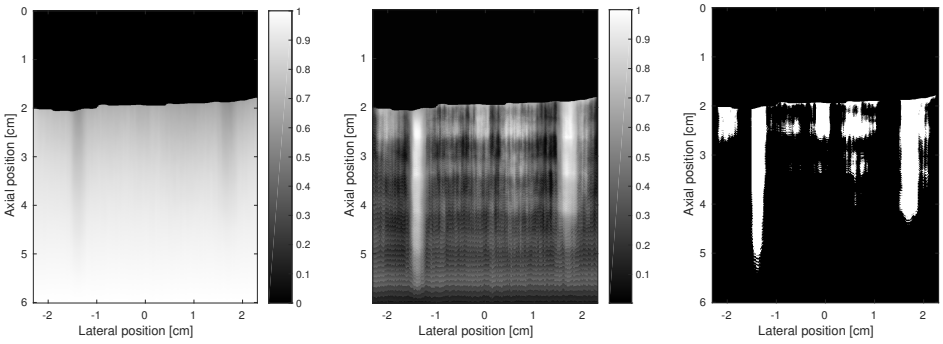

(d) Axial-cumulative image of *(c)*.

(e) Image *(d)* inverted and the histogram equalized.

(f) Strong specular regions detected on *(e)*.

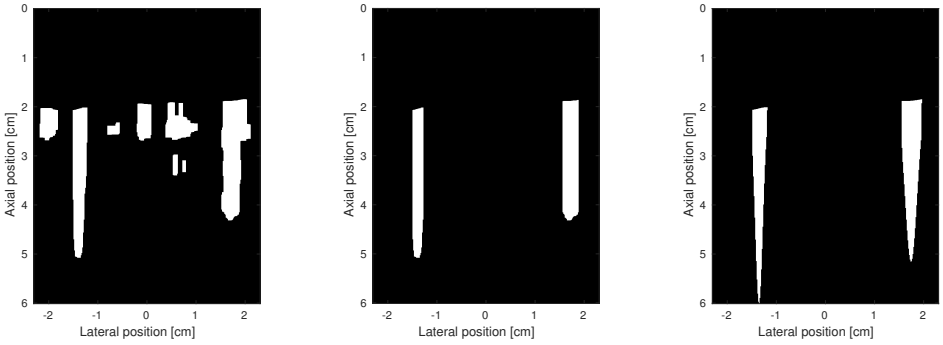

(g) Result of ASF.

(h) Result of top-hat.

(i) Result of Gaussian fitting.

Figure 6.3: B-line detection performed on a LUS scan of a patient with pulmonary edema.

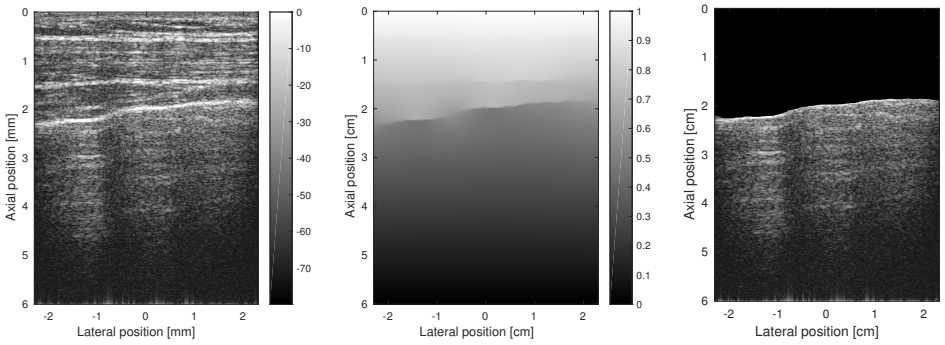

(a) LUS image.

(b) Confidence map of image in *(a)*.

(c) Upper pleura excluded from image in *(a)*.

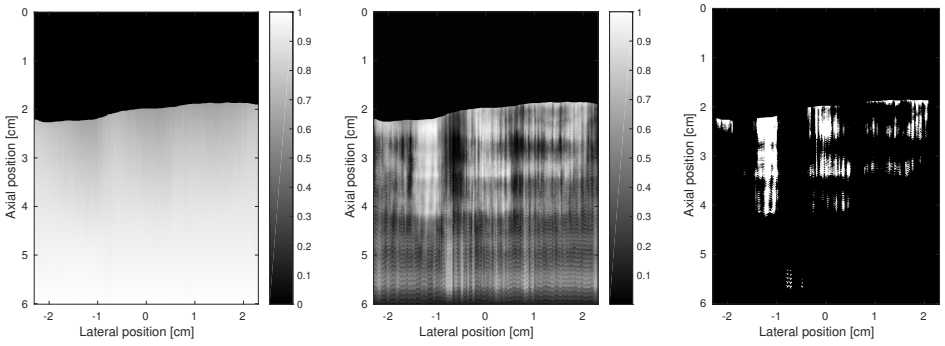

(d) Axial-cumulative image of *(c)*.

(e) Image *(d)* inverted and the histogram equalized.

(f) Strong specular regions detected one *(e)*.

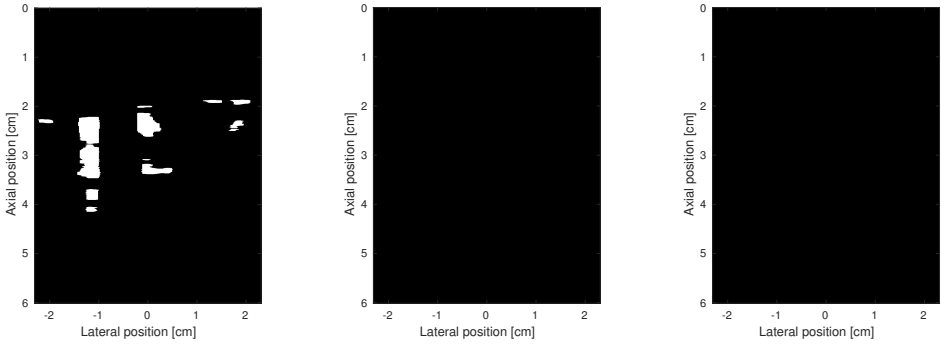

(g) Result of ASF.

(h) Result of top-hat.

(i) Result of Gaussian fitting.

Figure 6.4: B-line detection performed on a LUS scan of a healthy subject.

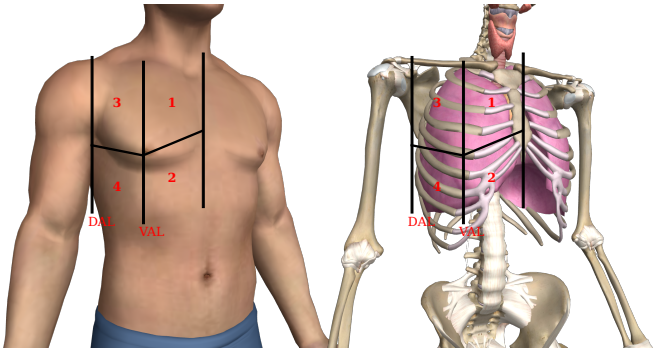

Figure 6.5: 8-zone scanning protocol. Chest was divided into 8 zones (4 per hemithorax), for each of which the intercostal spaces were examined for B-lines and the best scan is recorded (one scan per zone).

col (Volpicelli, Cardinale, et al. 2008) was used for acquiring ultrasound lung scans. The ultrasound examination consisted of bilateral scanning of the ventral and dorsal chest walls performed on subjects in cranial and caudal positions. This standardized acquisition is employed to ensure that the lung is thoroughly examined. Chest was divided into 8 zones (4 per hemithorax), for each of which the intercostal spaces were examined for B-lines and the best scan was recorded (one scan per zone). Fig. 6.5 shows where on the subjects examination was performed.

6.11 Ultrasound dataset

Four healthy subjects and four patients with different degrees of pulmonary edema were scanned. The patients had undergone major open-chest surgery. The healthy subjects were four males of 32, 42, 31 and 28 -year-old. The first patient was a 67-year-old male, who have had coronary artery bypass grafting (CABG) for stenotic coronary arteries (abnormal narrowing in 3 vessels). The second patient was a 44-year-old female, who have had surgery for myxoma (benign tumor) in the left atrium. The third patient was a 83-year-old male, who have had CABG surgery for stenotic coronary arteries (abnormal narrowing in 3 vessels). Finally, the fourth patient was a 68 years old male, with heart-mate (mechanical heart) because of cardiomyopathy ; a chronic disease of the heart muscle in which the heart muscle becomes enlarged, thick, or rigid.

A coarse method to predict the level of edema is to measure the need of extra O_2 to the patient. The normal required O_2 concentration is around 21%. The higher supply of O_2

increases the probability of presence of pulmonary edema in patients. The oxygen supply for the patients is depicted in Table 6.1. A total of 64 lung sequences each containing 50 frames were acquired. The study was approved by the Danish National Committee on Biomedical Research Ethics and the local Ethics Committee, and the volunteers were included into the study after informed consent. The beamformed RF data were acquired using a BK3000 ultrasound scanner (BK Ultrasound, Denmark).

6.12 Results and discussion

Figs. 6.3 on page 105 and 6.4 on page 106 show two examples of the B-lines detection procedure performed on LUS scan of a patient and healthy volenteer, respectively.

Figs. 6.6 on page 110 and 6.7 on page 111 show two examples of the B-lines overlaid on the B-mode image.

The algorithm was applied to all 64 acquired lung sequences (3200 frames). The proposed algorithm used all data in a sequence and not single frames, as in conventional lung ultrasound, for B-line detection. Fig. 6.6 shows two examples of the detected pleura and B-lines on lung scans of a patient and a healthy subject. Average number of B-lines was calculated for each subject across 8 scans recorded from a subject. The can potentially be used as an indication of whether the scans acquired from the subject was normal or not. The results are shown in Table 6.1.

The average number of B-lines values were more than 0.2 in scans belonging to the patients. On the other hand, in the healthy subjects, Average number of B-lines were lower than 0.2. The results of the study showed that the proposed algorithm was able to detect the B-lines on ultrasound scans. The proposed method can potentially be used as an automated tool to differentiate between scans belonging to patients and healthy subjects.

6.13 summary

This chapter presented a novel automatic B-line detection algorithm. It automatically finds B-lines (comet tail artifacts) using sequences of B-mode ultrasound for diagnosing pulmonary diseases. The empirical results showed that the proposed technique was able to detect the B-lines and was able to differentiate the ultrasound scans acquired from the patients with sever edema and those acquired from healthy subjects. Chest x-ray doesn't provide a quantification for pulmonary edema and is not the best modality for detection of pulmonary edema even though it is modality most often chosen due to availability. Chest x-ray is a ionizing modality, which is harmful for cellular DNA, while ultrasound is harmless. Also, Chest x-ray imaging is a service offered by the radiology department, while lung ultrasound is performed bedside by staff of the home department of patient.

Table 6.1: Number of B-lines detected for all subjects.

Measures / Subjects	Age / Gender	Health issue / Healthy	Operation	O_2 needed [%]	Views in which B-lines observed and # of B-lines	Average # of B-lines
Patient 1	67 / male	Stenotic coronary arteries (3 vessels)	By-pass surgery (CABG)	40%	View 8 (2 B-lines)	0.25
patient 2	44 / female	Myxoma (benign tumor) in the left atrium	Operated for myxoma	70%	View 3 (1 B-line) and View 6 (1 B-line)	0.25
patient 3	83 / male	Stenotic coronary arteries (3 vessels)	By-pass surgery (CABG)	50%	View 5 (1 B-line) and View 6 (1 B-line)	0.25
patient 4	68 / male	Cardiomyopati (cardiac muscle disease)	Heart-mate (mechanical heart)	63%	View 3 (2 B-lines) and View 6 (1 B-line)	0.375
Volenteer 1	32 / male	Healthy	–	–	–	0
Volenteer 2	42 / male	Healthy	–	–	–	0
Volenteer 3	31 / male	Healthy	–	–	–	0
Volenteer 4	28 / male	Healthy	–	–	View 7 (1 B-line)	0.125

The proposed automated algorithm will ease the use of lung ultrasound and may be used by e.g. nurses without profound knowledge of ultrasound. The algorithm can potentially be used in daily clinical practice as a tool for making a quantitative estimation of pulmonary edema and detection of pneumothorax. Furthermore, the algorithm can be an aid for the untrained personnel performing the ultrasound scan, as well as providing a quantitative measure for B-lines presence.

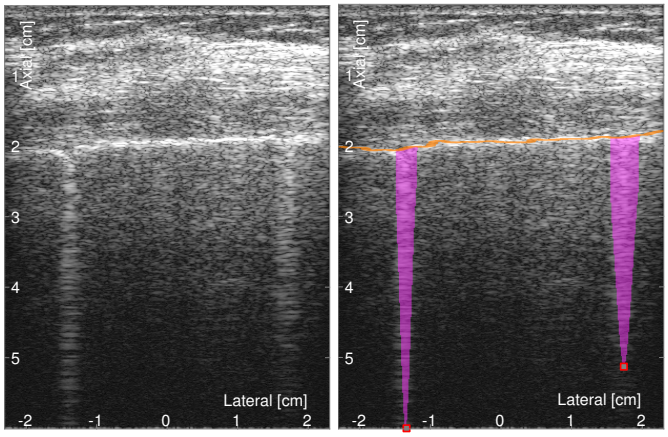

(a) LUS scan containing two B-lines.

(b) Pleural line is outlined and B-lines are detected in *(a)* and overlaid.

Figure 6.6: lung scan of a patient after surgery, for which the pleural line is outlined, and two B-lines are detected.

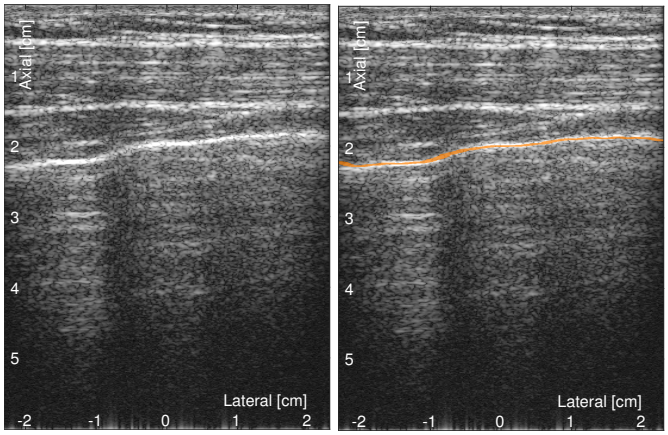

(a) LUS scan containing no B-lines.

(b) Pleural line is outlined and no B-lines are detected in *(a)*.

Figure 6.7: lung scan of a healthy subject, for which the pleural line is outlined, and no B-lines are detected.

References from Chapter 6

Meyer, F. (1977). "Contrast features extraction, Special Issues of Practical Metallography". In: *Quant. Anal. Microstruct. Mat. Sc. Bio. Med.* Vol. 8 (cit. on p. 102).

Lichtenstein, D., G. Mézière, P. Biderman, A. Gepner, and O. Barré (1997). "The Comet-tail Artifact. An ultrasound sign of alveolar-interstitial syndrome". In: *Am. J. Respir. Crit. Care. Med.* 156.5, pp. 1640–1646 (cit. on p. 98).

Lichtenstein, D., G. Meziere, P. Biderman, and A. Gepner (1999). "The comet-tail artifact: An ultrasound sign ruling out pneumothorax". In: *Intensive Care Medicine* 25.4, pp. 383–388 (cit. on p. 98).

Jambrik, Z., S. Monti, V. Coppola, E. Agricola, G. Mottola, M. Miniati, and E. Picano (2004). "Usefulness of ultrasound lung comets as a nonradiologic sign of extravascular lung water". In: *Am. J. Cardiology* 93.10, pp. 1265–1270 (cit. on p. 98).

E.Agricola, T. Bove, M. Oppizzi, G. Marino, A. Zangrillo, A. Margonato, and E. Picano (2005). "Ultrasound Comet-Tail Images: A Marker Of Pulmonary Edema: A Comparative Study With Wedge Pressure And Extravascular Lung Water". In: *Chest* 127.5, pp. 1690–1695 (cit. on p. 98).

Grady, L. (2006). "Random Walks for Image Segmentation". In: *IEEE. Trans Patt. Ana. Mach. Int.* 28.11, pp. 1768–1783 (cit. on p. 100).

Volpicelli, G., A. Mussa, G. Garofalo, L. Cardinale, G. Casoli, F. Perotto, C. Fava, and M. Frascisco (2006). "Bedside lung ultrasound in the assessment of alveolar-interstitial syndrome". In: *Am. J. Emerg. Med.* 24.6, pp. 689–696 (cit. on p. 98).

Gargani, L., V. Lionetti, C. D. Cristofano, G. Bevilacqua, F. Recchia, and E. Picano (2007). "Early detection of acute lung injury uncoupled to hypoxemia in pigs using ultrasound lung comets". In: *Crit Care Med.* 35.12, pp. 2769–2774 (cit. on p. 98).

Gargani, L., F. Frassi, G. Soldati, P. Tesorio, M. Gheorghiade, and E. Picano (2008). "Ultrasound lung comets for the differential diagnosis of acute cardiogenic dyspnoea: A comparison with natriuretic peptides". In: *Eur. J. Heart Failure* 10.1, pp. 70–77 (cit. on p. 98).

Volpicelli, G., L. Cardinale, G. Garofalo, and A. Veltri (2008). "Usefulness of lung ultrasound in the bedside distinction between pulmonary edema and exacerbation of COPD". In: *Am. Soc. Emerg. Radiol.* 15.3, pp. 145–151 (cit. on pp. 99, 107).

Gargani, L. (2011). "Lung ultrasound: A new tool for the cardiologist". In: *Cardiovascular ultrasound* 9.1 (cit. on pp. 98, 99).

Karamalis, A., W. Wein, T. Klein, and N. Navab (2012). "Ultrasound confidence maps using random walks". In: *Med. Image Anal.* 16.6, pp. 1101–1112 (cit. on pp. 100, 101).

Lichtenstein, D. A. (2014). "Lung ultrasound in the critically ill". In: *Ann Intensive Care* 4.1 (cit. on p. 98).

CHAPTER 7

Project Conclusion and Perspectives

Medical US has been a widely used imaging modality to assist medical doctors for examination, diagnostic purposes, and for real-time guidance during surgery (Harvey et al. 2002; OBrien and Holmes 2007). However, despite the recent advances, medical US remains the most operator-dependent imaging modality, as it heavily relies on the user intervention to optimize the scan settings (Baker, Jensen, and Behrens 2013). This explains the huge interest in the subject of this thesis. The thesis has presented the results of the PhD project entitled "AUTOMATIC ULTRASOUND SCANNING". The key goals of this project have been to develop automated techniques to minimize the adjustments done by the users on the scanners to optimize the image quality and to improve the computer-aided diagnosis in US by introducing new quantitative measures. Four major issues concerning automation of the medical US are addressed in this PhD project. They touch upon ATGC, automatic SA image quality optimization, automated vessel segmentation in US, and introducing CAD in LUS.

Chapter 2 Adressed the implications behind current TGC implementations and developed a new automated TGC. In this chapter, the recent implementations of TGC in commercial scanners are reviewed, and their shortcomings are discussed. The main problems with the current implementations are that they rely on the presence of sufficiently large homogeneous soft tissues with uniform distribution of attenuation (Klesenski 1996; Lee, Kim, and Ra 2006; Tang, Luo, and Liu 2009), and that they perform TGC using a 1-D curve, in which the 2-D topology of the image is ignored. This is in fact problematic for scans with large fluid collections. To address the issue, an automated hierarchical TGC (AHTGC) algorithm is proposed. The new technique relies on decay of the power spectral density of the received signal with respect to depth, as well as estimates of scattering strength, focus gain and energy level for gain adjustments. For the first time, 2-D SNR maps are used for distinguishing between the scans with and without large anechoic regions. 2-D tissue characterization profiles are also used to correct the gains after scaling the gains by TGC curves. This ensures that the 2-D topology of the scanned media is taken into account during the gain adjustments. Paper C shows the initial implementation of the AHTGC, evaluated on 44 abdominal scans by two radiologists. The results of the visual evaluations are highly in favor of the proposed algorithm. Paper D equips

the AHTGC with a shadow detection module, which automatically removes the shadow regions from gain compensation. It also adds a dynamic TGC step to the algorithm that benefits from singular spectrum analysis for trend extraction. Paper A expands the automated technique in detail and presents *in-vivo* results. The AHTGC is evaluated by four radiologists on 45 US sequences acquired from diverse population anatomical structures. The Wilcoxon signed-rank test is applied to scores provided by doctors to examine whether radiologists preferred the processed sequences or the unprocessed data. The *p*-value: 2.09×10^{-23} explicitly indicated that the Proposed AHTGC technique is preferred by the doctors. A separate evaluation is also performed on the scans with large anechoic regions. The *p*-value: 3×10^{-5} indicated that in a subset of cine-loops with large fluid collections, the proposed AHTGC is preferred. The proposed technique is automatic, robust, and has a more flexible control over the gains, specially for the anechoic regions. The technique alleviates the problems with 1-D manual and automated TGC methods, reduces the unnecessary and manual gain adjustments on the scanners keyboards, and has the potential to facilitate the use of scanners in point-of-care ultrasound.

Chapter 3 addressed the lack of a generic technique for the optimization of SA image quality, the task of automatically selecting optimal parameters for acquisition of the SA images (based on review in review in Section 3.2). The trade-off between the image quality and frame rate is discussed, and the need for SA image quality optimization is highlighted. This chapter consequently proposed a method for SA image quality optimization using a multi-objective optimization technique based on theory of Pareto optimality. The technique can accommodate several imaging parameters. The optimization technique is performed using simulation. The initial results of the proposed technique are presented in Paper E. Paper A extends the optimization technique and presents *in-vivo* results. The results of the study showed that with only $\alpha_{max} = \pm 22^{\circ}$ and $N = 32$, the image quality is comparable to a high number of emissions. The proposed technique is applied for a $\lambda/2$-pitch transducer, and image quality is compared for simulations, phantom measurements and *in-vivo* scans. The grating lobes are avoided by using a $\lambda/2$-pitch transducer, and therefore fewer emissions are needed to obtain the same image quality. Thus, with a pulse repetition frequency of 5 kHz, more than 156 fps are obtained. The proposed optimization technique is generic and can be applied to any US imaging modality, using any transducer geometry.

Chapter 5 addressed the segmentation of major vessels, in particular the carotid artery, and automating quantitative flow measures using VFI in US. The literature review in Section 5.1 illustrated that the majority of current vessel segmentation techniques uses only B-mode for the segmentation. This limits their segmentation approaches, as the contrast of the vessels might not be high enough for segmentation purposes. However, the information about the blood flow inside the vessel can improve the segmentation.

Recently, contrast enhanced images (CEUS) are used in combination with B-mode images for segmentation of vessels. This is very beneficial, as CEUS images provide information about flow inside the vessel and can act as a marker for the vessel. However, the technique requires injecting contrast agents to the blood stream, which is not achievable for everyday use in a normal scan session. The challenge remains to incorporate a non-invasive and reliable source of flow data for the vessel segmentation. The problem is addressed in this project by using the VFI as a reliable alternative marker for identification of vessels, and for being incorporated into the segmentation of vessels. According to the Chapter 4, VFI enables an angle independent and non-invasive visualization of blood flow in real-time. Chapter 5 thus presents a hybrid segmentation algorithm that fuses B-mode and VFI for robustly detecting and segmenting vessels in ultrasound images. Paper G presented the segmentation algorithm and evaluated the automated segmentation results in comparison with manual segmentations performed by an experienced user on 60 frames (10 frame randomly chosen from 6 sequences). The empirical results showed a dice coefficient of 0.91, indicating a good match between segmentation performed by the algorithm and the expert. The proposed method delineates the vessels in ultrasound scans and enables a better visualization of flow inside the vessel, and provides a firm ground for quantitative flow measures for VFI such as Peak systolic velocity (PSV) and volume flow. Before implementing the VFI measures in a commercial scanner, it must be investigated whether VFI performs better than the already used SDU. Therefore, PSVs measured from VFI and SDU are compared *in-vitro* and *in-vivo*. The results showed that VFI is more precise compared with SDU for PSV estimation in the portal vein. Furthermore, VFI can estimate the same peak velocity in the main portal vein with an insonation angle inapplicable for SDU. Therefore, the proposed method enables a better visualization of VFI as well as the automatic quantitative flow measures using vector velocities. The algorithm can also be used in daily clinical practice as an alternative tool for making a quantitative flow measures.

Chapter 6 investigated the possobility of automating the diagnosis of pulmonary diseases using lung ultrasound. The chapter thus, presented a technique for automated detection of disease correlated reverberation artifacts, more specifically B-lines, in ultrasound lung scans. The proposed method also enables the quantitative measures in bed-side lung ultrasound, thereby exploiting the full potential of this imaging technique.

The goals of this PhD project are achieved for each of the subjects. First, a new automated TGC is proposed that compensates for gains of the images in 2-D, compared with the current 1-D curve compensation in commercial scanners. Second, an automated generic technique for optimization of SA image quality is proposed. Third, for the first time a hybrid segmentation technique that combines both VFI data B-mode images is proposed. The technique enables the wall-to-wall visualization of VFI and automating

the quantification of VFI in state-of-the-art US scanners. Finally, a new technique is introduced to quantify disease-related reverberation artifacts in LUS.

References from Chapter 7

Klesenski, K. (1996). *Automatic gain compensation in an ultrasound imaging system*. US Patent 5,579,768 (cit. on p. 113).

Harvey, C. J., J. M. Pilcher, R. J. Eckersley, M. J. Blomley, and D. O. Cosgrove (2002). "Advances in Ultrasound". In: *Clinical Radiology* 57.3, pp. 157–177 (cit. on p. 113).

Lee, D., Y. Kim, and J. Ra (2006). "Automatic time gain compensation and dynamic range control in ultrasound imaging systems". In: *Proc. SPIE Med. Imag.* 6147, pages (cit. on p. 113).

OBrien, R. T. and S. P. Holmes (2007). "Recent Advances in Ultrasound Technology". In: *Clinical Techniques in Small Animal Practice* 22.3, pp. 93–103 (cit. on p. 113).

Tang, M., F. Luo, and D. Liu (2009). "Automatic Time Gain Compensation in Ultrasound Imaging System". In: *Proc. IEEE Int. Conf. Bioinfo. Biomed. Eng.* Pp. 1–4. DOI: 10.1109/ICBBE.2009.5162432 (cit. on p. 113).

Baker, M., J. Jensen, and C. Behrens (2013). "Inter-operator variability in defining uterine position using three-dimensional ultrasound imaging". In: *2013 IEEE Int. Ultrason. Symp.* Pp. 848–851 (cit. on p. 113).

Papers

To ease the reading of the following publications they have been reformatted to fit the layout of this thesis. No contextual editing of the papers since their publication has taken place.

PAPER A

Advanced gain adjustments for ultrasound imaging

Authors: Ramin Moshavegh[a], Caroline Ewertsen[b], Kristoffer Lindskov Hansen[b], Andreas Hjelm Brandt[b], Thor Bechsgaard[b], Martin Christian Hemmsen[a], Bo Martins[c], Michael Bachmann Nielsen[b] and Jørgen Arendt Jensen[a].

Manuscript submitted to: *Journal of Ultrasound in Medicine and Biology (UMB).*

[a]Center for Fast Ultrasound Imaging, Department of Electrical Engineering, Technical University of Denmark, 2800 Kgs. Lyngby, Denmark

[b]Department of Radiology, Rigshospitalet, Copenhagen University Hospital, Copenhagen, Denmark

[c]BK Ultrasound ApS, Herlev, Denmark

Advanced Gain Adjustments for Ultrasound Imaging

Ramin Moshavegh*, Caroline Ewertsen†, Kristoffer Lindskov Hansen†,
Andreas Hjelm Brandt†, Thor Bechsgaard†, Martin Christian Hemmsen*,
Bo Martins‡, Michael Bachmann Nielsen† and Jørgen Arendt Jensen*
*Center for Fast Ultrasound Imaging, Dept. of Elec. Eng., Technical University of Denmark, Lyngby, Denmark
†Dept. of Radiology, Copenhagen University Hospital, DK-2100 Copenhagen,
Denmark ‡BK Ultrasound ApS, Herlev, Denmark

***Abstract*—Automating the gain adjustments on the ultrasound scanners reduces the number of settings, and therefore, unnecessary user interactions. The growing need for automation is emphasized in portable scanners, which seek the least amount of adjustments to obtain the optimal image quality. The challenge remains to devise an automated time-gain compensation (ATGC) that compensates for the gains in scans with large changes in the attenuation distributions. This paper presents an ATGC algorithm that adapts to the large attenuation variation between different types of tissues and structures. It relies on decay of the received signal power spectral density with respect to depth, as well as estimates of scattering strength, and noise level to gain a more quantitative understanding of the underlying tissue. The proposed algorithm is applied to a set of 45 *in-vivo* movie sequences each containing 50 frames. The scans are acquired by a BK3000 ultrasound scanner (BK Ultrasound, Denmark). Matching pairs of *in-vivo* sequences, unprocessed and processed with the proposed method are shown side by side and evaluated by 4 radiologists for image quality. Wilcoxon signed-rank test is applied to the ratings provided by radiologists. The average VAS score is highly positive** 11.1 **(*p*-value:** 1.09×10^{-13}**) favoring the gain-adjusted scans with the proposed algorithm.**

I. Introduction

Radiofrequency (RF) echoes are strongly attenuated by the tissues scanned [1]. The scattered signals span a wide dynamic range, when they are received by the transducer, and are not suitable to be visualized before gains adjustment. Time gain compensation (TGC) is used to compensate for the acoustic attenuation. TGC compensates for the attenuation of ultrasound echo signals along the depth, so that echoes belonging to deep structures are more amplified compared to echoes of superficial structures. This provides more uniform signals to be displayed on the scanner [1]. Current ultrasound scanners use a TGC curve for time gain compensation. The user adjusts the shape by manually using TGC sliders for different depths, and the image quality is dependent on the adjustments. An automatic adjustment of the TGC (ATGC) without user intervention can address the shortcomings of the manual TGC [2]. To date, several designs of ATGC have been proposed in the literature [1], [2], [3], [4]. However, the majority of these algorithms rely on the presence of sufficiently large homogeneous soft tissue regions with uniform distribution of attenuation [1], [3], [5], and the dependency of the attenuation for several different tissues is ignored in these algorithms. These methods fail to compensate the overall gain, when fluid collections such as the urine bladder or gallbladder are present, which change the uniform distribution of the attenuation drastically. Anechoic segments, surrounded by soft tissue, also present a large variation in attenuation.

This paper proposes a novel automated hierarchical TGC (AHTGC) algorithm with focus on images with large anechoic regions. The algorithm is based on a physical understanding of the underlying tissue based on estimates of the scattering strength, signal-to-noise ratio (SNR), and focusing gain. From these, different constituents of the tissue can be determined. Also, the decay of the received signal power spectral density with respect to depth is used to estimate normalized attenuation profiles and to adapt the AHTGC to large fluid collections. Portions of the proposed technique are presented in two conference papers [6], [7]. This paper expands the automated technique in detail, and presents *in-vivo* results acquired using two different transducers.

The remainder of this article is organized as follows. Section II introduces the proposed algorithm. Section III introduces the measurement setup and image data used in the study. Section IV presents the *in-vivo* results of the proposed AHTGC algorithm and discusses the findings. The conclusion is in Section V.

II. Materials and Methods

The novelty of the proposed technique comes from incorporating several physical estimates of the scanned media as constituents of the compensation strategy. The proposed algorithm contains the five distinct steps shown in Fig. 1.

First, very dark regions (shadow regions) created due to improper connection of transducer to the scanned media were detected and excluded from the gain compensation procedure. Second, the received signals were compensated for the shape of the beam profile to ensure that the entire scanned area receives the same amount of energy. Third, a 2-D SNR map was computed for each frame. A feature (F_1) was computed to decide whether the frame contains large anechoic regions (type 1) or not (type 2). In the fourth step, a TGC curve was computed dynamically for each frame and used to compensate for the gains in that frame. Finally, a 2-D normalized map highlighting the anechoic regions was generated for the frame and used to correct the adjusted gains inside the anechoic

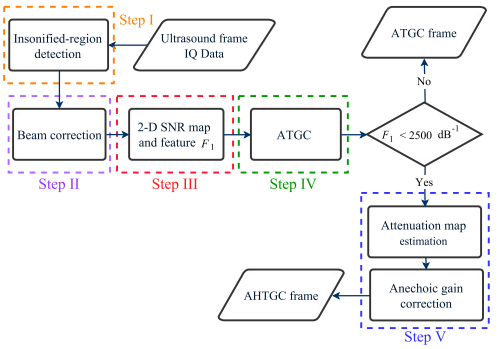

Fig. 1: Block diagram of the proposed algorithm.

regions after applying the TGC curve. The correction was only performed on the scans with large fluid collections (type 1).

A. Insonified-region detection

The purpose of the first step was to identify the insonified region on the ultrasound scans. Long dark shadows sometimes appear in left or right edges of ultrasound images, when the transducer is not perfectly attached to the surface during the scan session. Detection of the shadow region and removing it from the gain adjustment process are necessary. For this purpose, the envelope of the RF data was computed. A binary mask, only including the intensity values lying within lower 10% dynamic range of the envelope data was generated. Each scan-line of the binary mask was treated independently. Scan-lines longer than 90% of the total scan depth were kept on the mask, and shorter scan-lines were excluded. Parts of the binary mask, which were not attached to one of the right or left edges of the screen, were also excluded from the mask. This ensured that only elongated dark shadows touching one or both edges of the screen remained in the mask. The generated mask identified non-sonified parts of the scan, which were excluded from the gain adjustments. Alg. 1 details the shadow detection procedure.

B. Energy equalization

The effects of focusing gains related to the scan sequence were considered in this step. A tissue mimicking speckle phantom was scanned, and 50 frames were acquired. The mean of all 50 frames was computed yielding a mean-frame. The lateral median of the 50 scan lines bracketing the center-line on the mean frame was computed yielding an energy curve as a function of depth. The curve was then inverted, normalized to a maximum of one, and used to scale the energy levels of all scan-lines in every acquired image. This was performed to ensure that the energy was equally distributed throughout the scanned media.

Algorithm 1 Shadow detection

Input: Env envelope of RF-data,
Output: B_{shdw} binary mask outlining the shadow regions.

procedure SHDW
  Let B_{shdw} be a binary mask with the same size as Env.
  Let min_env be the minimum intensity of Env in dB and N be the size of the Env.
  for each $i \in N$ **do**
    if $Env(i) \leq min\_env + 0.1 \times |min\_env|$ **then**
      $B_{shdw}(i) = 1$ # Creating the binary mask by including very dark regions
    end if
  end for
  Let M be the number of columns of the Env.
  for each $i \in M$ **do**
    if $sum(B_{shdw}(i).col) \leq 0.9 \times length(B_{shdw}(i).col)$ **then**
      $B_{shdw}(i).col = 0$ # Excluding scan-lines shorter then 90% of scan depth.
    end if
  end for
  $B_{shdw} = rmv\_obj(B_{shdw})$ # function removing objects that are not attached at least to one side of the B_{shdw}.
end procedure

C. SNR map

Complex IQ data are used to compute the SNR for all frames. The acquired frame from the transducer, is contaminated with noise and can be written as $\mathbf{Y}_i = \mathbf{S}_i + \mathbf{E}_i$, where matrix $\mathbf{S}_i$ is the desired frame signal, $\mathbf{E}_i$ is the noise contribution, and i is the frame number. To estimate the noise contribution in the received signal $\mathbf{E}_i$, a cine-loop of N frames is acquired from a homogeneous tissue mimicking phantom with an attenuation of 0.5 dB/cm $\times$ MHz. The mean of the acquired signal is given by

$$\mathbf{M} = \hat{\mathbf{Y}} = E\{\mathbf{Y}_i\} = E\{\mathbf{S}_i + \mathbf{E}_i\} = \frac{1}{N}\sum_{i=1}^{N}(\mathbf{S}_i + \mathbf{E}_i) \quad (1)$$

in which matrix $\mathbf{M}$ represents the mean of acquired frames. Also, given the assumption that $E\{\mathbf{E}_i\} = 0$, the mean acquired signal by averaging all frames will be equivalent to the mean desired signal and can be written as $\mathbf{M} = \hat{\mathbf{Y}} = \hat{\mathbf{S}}$. The noise contribution for each frame is estimated by subtracting the mean of the all frames from a single frame $\mathbf{E}_i = \mathbf{Y}_i - \hat{\mathbf{Y}}$. Therefore, the noise power for the ultrasound device is expressed as follows:

$$\mathbf{P}_{noise} = \left| \frac{1}{N}\sum_{i=1}^{N}\mathbf{E}_i^2 \right| \quad (2)$$

Finally, the SNR map for an acquired *in-vivo* frame can be determined by dividing the signal power of that frame by the

system noise power computed in (2)

$$\mathbf{P}_{signal}(i) = |\mathbf{Y}_i|^2 \tag{3}$$

$$\mathbf{SNR}_{dB}(i) = 10\log_{10}\left(\frac{\mathbf{P}_{signal}(i)}{\mathbf{P}_{noise}}\right) \tag{4}$$

where $\mathbf{Y}_i$ in (3) is the signal acquired from frame number i in a sequence of *in-vivo* scans. The signal power changes from frame to frame, while the noise power is unchanged.

The essential first step in the proposed time gain compensation algorithm is to determine whether the scans include large fluid collections or not. It is anticipated that fluid collections appear as very low SNR regions in the SNR maps. A feature is specifically designed to characterize this property in SNR maps. For this purpose, a cumulative histogram of the values in the SNR map is computed. A curve is fitted to the counts, and slopes of the fitted curve at 25th and 80th percentiles of the curve are computed. The rates of changes in the slopes at the 25th and 80th percentiles are used to characterize the amount of fluid in the scans, and to distinguish between the two different scans with large fluid collections (type 1) and scans with small or no fluid collections (type 2).

D. Dynamic TGC

A TGC curve was dynamically computed for each frame and used to compensate for the gains. For this purpose, the envelope of the acquired scan was first computed. A cumulative histogram of the intensity values was then generated. The intensity values less than half of the maximum intensities in the envelope were discarded, and a mask of strong signal regions was generated. The mask was applied to the envelope, and the lateral median of the intensities lying inside the mask was computed. The computed curve presented drastic fluctuations and could not be used directly to analyze the axial intensity changes in the envelope. To address this, the curve was smoothed using a Sovitsky-Golay filter [8], [9]. Then, the general trend of the curve was extracted by applying the singular-spectrum analysis (SSA). SSA does not require model of time series, and extracts the trend of time series in the presence of noise and oscillations (see chapter 1 of [10], and [11]). The final curve depicted the trend of intensity change within the envelope and harbored no sudden fluctuations. The curve was finally normalized to its maximum, inverted and applied as a TGC to the envelope to compensate for the gradual changes in the intensities. Alg. 2 details the dynamic TGC curve computation for a frame.

Algorithm 2 Dynamic TGC calculation

Input: Env envelope of RF-data,
Output: TGC Time-gain compensation curve dynamically computed for each frame.

procedure DYNATGC
  Let Env be a discrete gray scale image and let n_i be the number of occurrences of gray level i.
  $p_{_{Env}(i)} = p\,(Env = i) = \frac{n_i}{N}, 0 < i < L$ # probability of an occurrence of a pixel of level i in the Env.
  Let L be the total number of gray levels in the Env (in our case 256), N being the total number of pixels in the image, and $p_{_{Env}(i)}$ be the image's histogram for pixel value i, and normalized to $[0, 1]$.
  for each $i \in L$ **do**
    $cdf_{_{Env}(i)} = \sum_{j=0}^{i} p_{_{Env}(j)}$ # define the cumulative distribution function corresponding to $p_{_{Env}}$.
  end for
  Let th_l be the gray value for which $cdf_{_{Env}=0.5}$ and th_h be the gray value in which $cdf_{_{Env}=1}$.
  Let I_{bright} be a zero gray scale image with the same size as image Env
  for each $ii \in N$ **do** # N is the total number of pixels in the image Env.
    if $th_l \leq Env(ii) \leq th_h$ **then**
      $I_{bright}(ii) = Env(ii)$ # I_{bright} contains parts of the Env lying between the two thresholds of th_l and th_h.
    end if
  end for
  $TGC = lat\_med(I_{bright})$ # computes the lateral median of I_{bright}.
  $TGC = Sovitsky\_Golay(TGC)$ # smoothes the TGC curve using Sovitsky-Golay filter. The window lenght is 5% of the scan depth.
  $TGC = SSA(TGC)$ # performing single-spectrum-snalysis and extracting the trend of TGC. The window lenght is 5% of the scan depth.
  $TGC = \frac{TGC}{max(TGC)}$ # normalizes the TGC curve to its maximum.
  $TGC = \frac{1}{TGC}$ # inverts the curve to be multiplied to each scan line.
end procedure

E. Tissue characterization map

The dynamic adjustment of intensities using the TGC curve can over-gain inside the fluid regions. This section computes normalized tissue characterization maps that can be used to correct the possible miss-adjusted gains inside the fluid regions after applying the TGC curve.

A log spectral difference method adapted from Kuc [12], [13] was used to compute tissue characterization maps highlighting less attenuating regions. The beamformed RF data were used to compute the characterization maps. Each RF line was partitioned into several overlapping segments, in which each RF segment was gated axially by a Tukey function to alleviate the spectral leakage at both boundaries. Each two overlapping segments in the RF line were paired together, where the upper segment was considered as the proximal and the underlying segment was considered as the distal segment. For each pair, the difference between the logarithm of power spectra was computed, a line was fitted to the power spectral difference, and the slope of the resulting line was considered as an attenuation value for the proximal segment (Fig. 2). Both proximal and distal segments were moved down on the

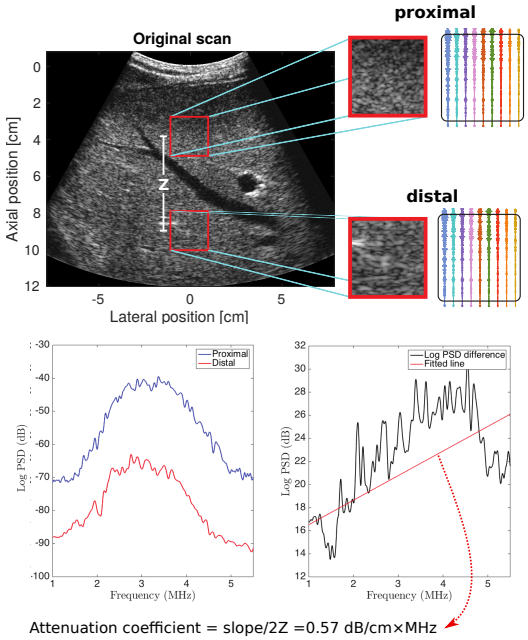

Fig. 2: Illustration of how attenuation coefficients are computed. The scanned plane is subdivided in to several overlapping proximal and distal segments. Each RF segment is gated axially by a Tukey function to alleviate the spectral leakage at both boundaries. The slope of the line fitted to the curve created from subtracting the log spectra of the two segments identifies the attenuation coefficient.

RF line, and several attenuation values were calculated along the RF line by pairing the proximal and distal segments. Blocks were overlapped 50% to increase axial resolution of the characterization maps. The resulting values for RF lines were laterally averaged over scan lines to reduce the high variability of the characterization values in the map. The generated characterization maps were then normalized to a maximum of one, and multiplied to the compensated images by dynamic TGC in Section II-D to correct the gains inside the fluid collections.

III. Measurements

Fifteen healthy volunteers were scanned, and a total of 45 ultrasound sequences each containing 50 frames were acquired. The age of the population was between 25 to 35, with average of 29 years old. The study was approved by the Danish National Committee on Biomedical Research Ethics and the local Ethics Committee, and the volunteers were included into the study after informed consent. The beamformed RF data were acquired using a BK3000 ultrasound scanner (BK Ultrasound, Denmark). Both Linear and convex transducers

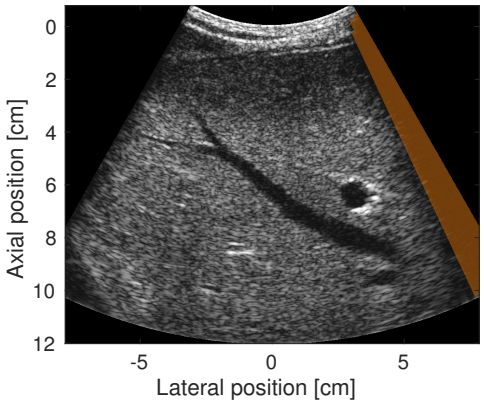

Fig. 3: The figure shows the shadow region detected for an *in-vivo* scan of a human liver. The shadow region was detected using Alg. 1, and overlaid with a brown bar on the B-mode image. The shadow region was then excluded from the gain adjustment.

were used in this study for data acquisition. Convex transducer was a 192-element 3.5 MHz array (9040, BK Ultrasound), and the linear transducer array was a 192-element 5.5 MHz array (9022, BK Ultrasound). The dynamic received focus technique with factory preset TGC was employed to generate the sequences. In addition to the urine bladder and gallbladder scans with large anechoic regions, other anatomical locations such as the liver, kidney, and carotid artery were also included in the dataset. This was done to yield a diverse dataset, for evaluating the performance of the algorithm on images comprising more or less varied attenuation distibutions.

IV. Results and Discussion

The proposed AHTGC algorithm was applied to all 45 *in-vivo* cine-loops, and evaluated in terms of image quality. This section details the results obtained in different steps of the proposed technique, and presents the results of the image quality evaluations.

According to the Section II-A, long dark shadows were usually created on the scan when the transducer was not perfectly attached to the surface. It complicated the gain adjustments, as dark shadows could be mistakenly considered as anechoic regions. Fig. 3 shows a shadow detected and overlaid with a brown bar on top of a B-mode image. The colored area was removed from the gain adjustments.

Fig. 4 illustrates how energy equalization was performed on the acquired sequences. Fig. 4a shows the energy levels of the computed mean-frame, along the center-line as a function of depth. The curve was then inverted and normalized to a maximum of one in Fig. 4b. Finally, the normalized curve was used to scale the energy levels in every acquired image.

Fig. 5 shows an example of a TGC curve dynamically computed for a scan of human liver. The curve was applied to scale all scan-lines of the image. Both Savitsky-Golay

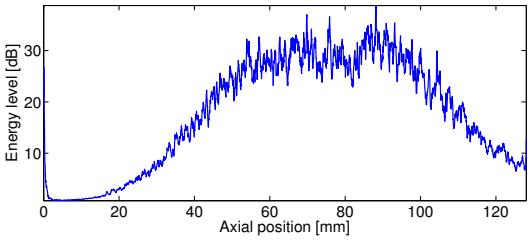

(a) Median of the energy levels of 50 scan lines on the mean-frame.

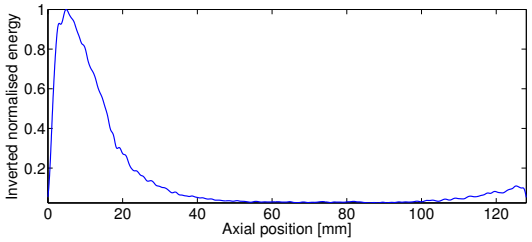

(b) Inverted and normalized energy curve in *(a)* which was applied to scale all scan lines for energy equalization.

Fig. 4: Illustration of the energy equalization procedure using tissue mimicking phantom measurements. 50 frames of a tissue mimicking phantom were acquired. 50 frames were then averaged, and a mean-frame was generated. (a) This curve shows the lateral median of the energy levels of 50 scan lines bracketing the center-line of the mean-frame. (b) The curve in *(a)* was inverted, scaled to a maximum of one and used to scale all scan-lines.

smoothing and the SSA required a window length to operate on the data. A window length equal to 5% of the total penetration depth was chosen empirically. The window length was thus automatically adapted to different scan depths. The computed TGC curve did not harbor drastic fluctuations, which would have appeared as horizontal artifacts when scaling the image intensities.

The variation of noise and SNR with depth for a scan of tissue mimicking phantom along its center-line are depicted in Fig. 6. The black curve shows the noise power of the imaging system as a function of depth. This curve was computed using (1) and (2). The signal power was computed from the received signal by the transducer using (3), and finally, the 2-D SNR maps are generated using (4). Two examples of the 2-D SNR maps computed from scans of a human bladder and liver are shown in Figs. 7a and 7c, respectively.

Figs.7b and 7d illustrate how the feature F_1 was calculated for two scans of the human bladder and liver. These two figures show the cumulative histogram of the SNR images over 100 bins. 100 bins were used to ensure that a high variation of SNR values in each map was captured in the histogram, and also, that the precision of the density estimation was not jeopardized.

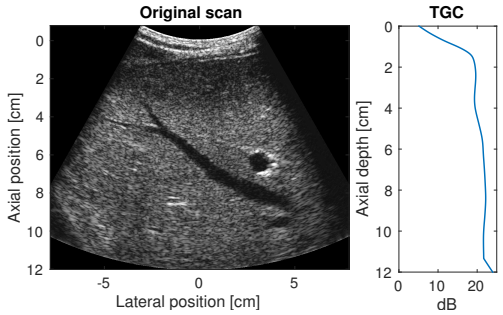

(a) Scan of a human liver from which the TGC curve is computed.

(b) TGC curve computed for *(a)* using AIg. 2.

Fig. 5: Illustration of a TGC curve dynamically computed for an *in-vivo* scan of the human liver. The TGC does not harbor any sudden fluctuations.

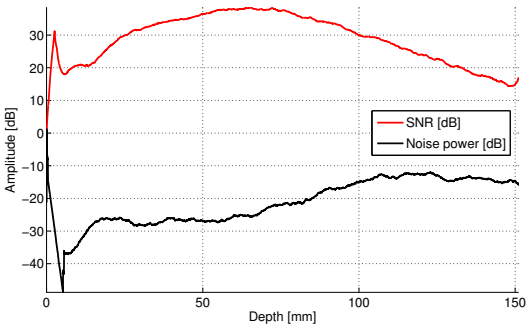

Fig. 6: SNR and noise contribution along to the center-line of scan of a tissue mimicking phantom with an attenuation of $0.5\ \mathrm{dB/cm} \times \mathrm{MHz}$.

The number of counts of low SNR values in the scans with large fluid collections (type 1) was higher compared to that of scans with small or no fluid collections. This yielded a steeper slope of the cumulative histogram at low SNR values (i.e. 25th percentile) for scans with large anechoic regions compared to that of scans with no anechoic regions. The same effect decreased the slope of the cumulative histogram at high SNR values (i.e. 80th percentile) for scans with large anechoic regions compared to that of scans with no anechoic regions. By moving from type 2 scans to type 1 scans, the rate of the decrease in the slope at the 80th percentile was much larger than the increase in the slope at the 25th percentile. Therefore, it was decided to use the slope at the 80th percentile (F_1) to distinguish between the type 1 and the type 2 scans. The value of F_1 was determined empirically using 4 scans additional to the 45 scans used for evaluation of the AHTGC algorithm. $F_1 < 2500\ \mathrm{dB}^{-1}$ characterized a scan with large fluid collection, otherwise, the scan was considered to contain

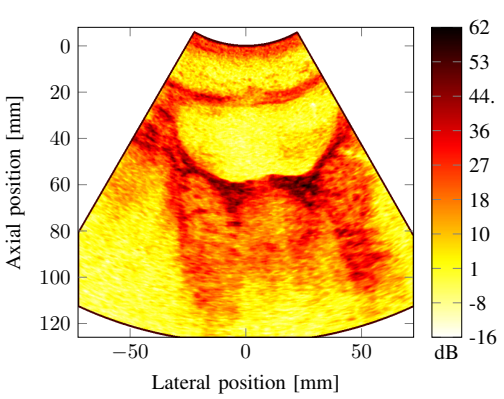

(a) 2-D SNR map calculated from scan of human bladder.

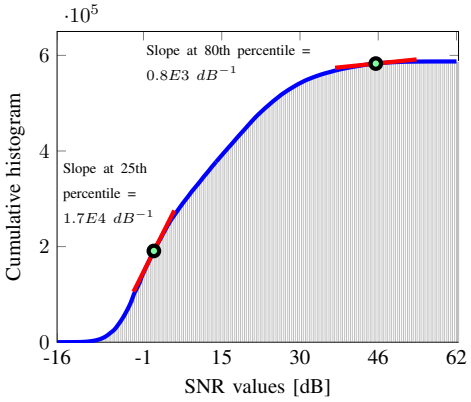

(b) Cumulative histogram of SNR values in map *(a)*.

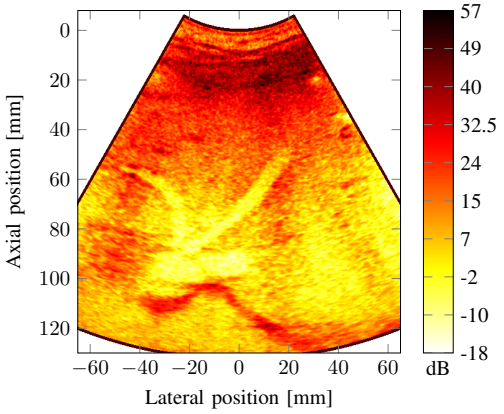

(c) 2-D SNR map calculated from scan of human liver.

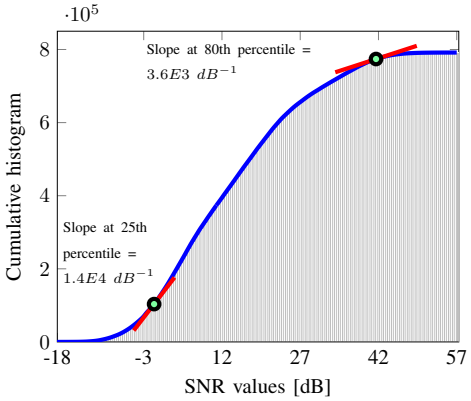

(d) Cumulative histogram of SNR values in map *(c)*.

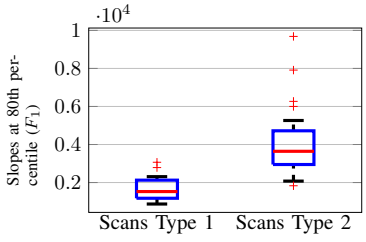

Type 1: Scans with large fluid regions.
Type 2: Scans with small or no fluid regions.

(e) Distribution of 80th percentile slopes (feature F_1)for two types of scans.

Fig. 7: Two examples of 2-D SNR maps computed for scans of a human bladder and liver with illustration of how their corresponding slope features are calculated. (a) 2-D SNR map of the human bladder. (b) Cumulative histogram of all SNR values in map *(a)* and slopes calculated at 25th and 80th percentiles of the fitted curve. (c) 2-D SNR map of the human liver. (d) Cumulative histogram of the values in map *(c)* and slopes calculated at 25th and 80th percentiles of the fitted curve. (e) Boxplots of 80th percentile slopes for two types of scans.

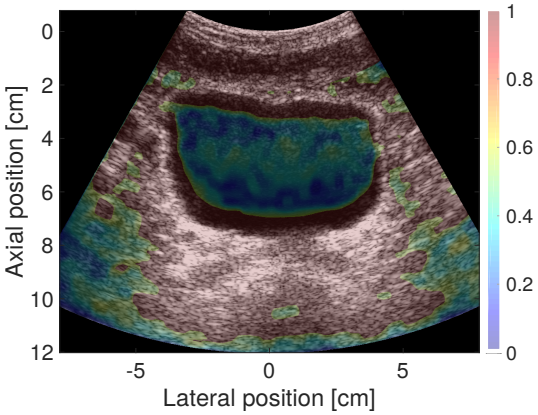

Fig. 8: Normalized tissue characterization map computed for a scan of human bladder. Values close to zero indicate structures attenuating less, and regions with values close to one identify the structures attenuating more.

small or no collections of fluid.

Boxplots in Fig. 7e show the distribution of values of feature F_1 for two types of scans. Scans including large fluid collections were type 1, and scans with small or no collections of fluid were type 2. The interquartile range of the boxplots belonging to two groups had no overlap, indicating that feature F_1 was able to distinguish between the two scans.

Fig. 8 shows an example of a tissue characterization map computed for a scan of the human bladder, overlaid on top of the B-mode image. The length of the RF segments and the number of averaging scan lines determined the axial and lateral resolution of the estimated profiles, respectively. The literature suggests the axial RF segment lengths to be between 1 to 2 cm, and that the number of the averaging lines should be between 8 to 25 RF lines [14]. In this study, anechoic regions adjacent to soft tissue presented a large attenuation variation. To capture this variation, the length of axial segments was set to 1 cm, and the number of averaging RF lines was set to 10 lines.

The proposed AHTGC algorithm was applied to the acquired image sequences off-line. Matching pairs of *in-vivo* sequences, one adjusted by the factory preset TGC with no default gains and the other processed with AHTGC, were evaluated side by side for image quality by four experienced radiologists. The evaluation was double blinded, and each pair was shown twice by randomizing the left and right positioning. This resulted in a total of 360 ($45_{imagepairs} \times 4_{evaluators} \times 2_{random\ displays}$) independent visual evaluations. The radiologists were asked to score the image quality of each pair on a visual analogue scale (VAS) ranging between -50 and +50. This was performed by dragging a slider towards their favored cine loop, where a positive scale favors the processed sequence with the AHTGC algorithm. The ratings provided by the four doctors were shown in Fig. 10. The Wilcoxon signed-rank hypothesis test was applied to the provided ratings

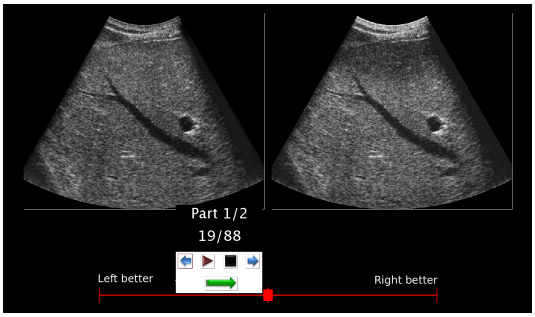

Fig. 9: Evaluation of the image quality performed by randomizing the position of matching pairs of processed and unprocessed data. The image on the left is a AHTGC processed scan of a human liver, and the image on the right is the scan adjusted by the factory preset TGC with no default gains.

by the radiologists to examine whether radiologists preferred the conventional TGC or the AHTGC processed sequences. Visualization and assessment were handled using the program IQap [15] shown in Fig. 9. The computed average VAS score was positive (p-value: 1.09×10^{-13}) and estimated to be 12.16 favoring the compensated data with the AHTGC algorithm. Fig. 10 also shows that even though the distribution of the ratings provided by the doctors were different, they have consistently preferred the proposed AHTGC algorithm. The Wilcoxon signed-rank test was also applied to scores provided by doctors only for scans with large anechoic regions (type 1). The p-value: 3×10^{-5} indicated that in a subset of cine-loops with large fluid collections, the proposed AHTGC was preferred. Fig. 11 shows two examples of the experimental results of the AHTGC algorithm applied to scans of a human gallbladder and carotid artery, obtained with a curved and linear array, respectively.

V. Conclusion

This paper presented an automatic hierarchical TGC that uses estimates such as focus gain and energy level, scatterer strength, and decay of the power spectrum of the received signal for gain adjustments. 2-D SNR maps were used for distinguishing between scans with large anechoic regions (type 1) and scans with small or no anechoic regions (type 2). 2-D tissue characterization profiles were used to correct the gains after compensation by TGC curves. This alleviated the problem with over-gaining the fluid regions in conventional 1-D manual and automated TGC methods. The p-value: 1.09×10^{-13} computed for all 45 cine-loops indicated that the proposed AHTGC was preferred by the radiologist when compared to conventional TGC. The computed p-value: 3×10^{-5} for scans with large anechoic regions indicated that in a subset of cine-loops with large fluid collections, the proposed AHTGC was preferred. The proposed technique is automatic, robust, and has a more flexible control over the gains, especially, for the anechoic regions. The proposed technique reduces the manual gain adjustments on the scanner

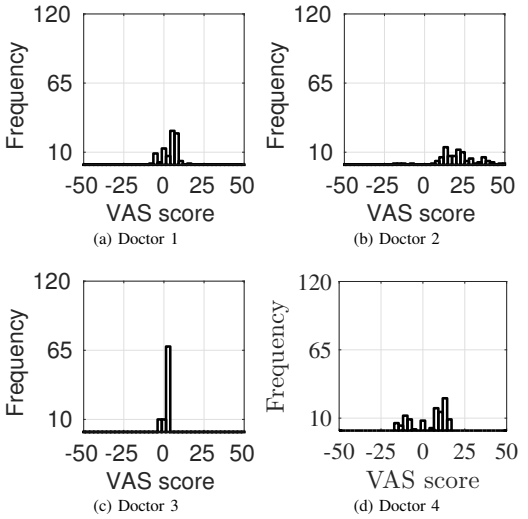

(a) Doctor 1 (b) Doctor 2

(c) Doctor 3 (d) Doctor 4

Fig. 10: Distribution of visual analogue scale (VAS) scores from assessment of overall image quality by four expert radiologists using the tool shown in Fig. 9. Positive values favor AHTGC algorithm.

keyboard, and can potentially facilitate the use of portable scanners in point-of-care ultrasound.

ACKNOWLEDGEMENT

This work is supported by grant 82-2012-4 from the Danish Advanced Technology Foundation and by B-K Ultrasound Aps.

REFERENCES

[1] D. Lee, Y. Kim, and J. Ra, "Automatic time gain compensation and dynamic range control in ultrasound imaging systems," *Proc. SPIE Med. Imag.*, vol. 6147, pp. 614 708–614 708–9, 2006.

[2] S. Pye, S. Wild, and W. McDicken, "Adaptive time gain compensation for ultrasonic imaging," *Ultrasound Med. Biol.*, vol. 18, no. 2, pp. 205–212, 1992.

[3] M. Tang, F. Luo, and D. Liu, "Automatic time gain compensation in ultrasound imaging system," in *Proc. IEEE Int. Conf. Bioinfo. Biomed. Eng.*, June 2009, pp. 1–4.

[4] D. Inbar and M. Delevy, "Time gain compensation for ultrasonic medical imaging systems," aug 1989, uS Patent 4,852,576.

[5] K. Klesenski, "Automatic gain compensation in an ultrasound imaging system," dec 1996, uS Patent 5,579,768.

[6] R. Moshavegh, M. Hemmsen, B. Martins, A. Brandt, K. Hansen, M. Nielsen, and J. Jensen, "Automated hierarchical time gain compensation for in-vivo ultrasound imaging," *Proc. SPIE*, vol. 9419, pp. 941 904–941 904–9, 2015.

[7] R. Moshavegh, M. C. Hemmsen, B. Martins, K. L. Hansen, C. Ewertsen, A. H. Brandt, T. Bechsgaard, M. B. Nielsen, and J. A. Jensen, "Advanced automated gain adjustments for in-vivo ultrasound imaging," in *Proc. IEEE Ultrason. Symp.*, 2015, pp. 1–4.

[8] A. Savitzky and M. J. E. Golay, "Smoothing and differentiation of data by simplified least squares procedures," *Anal. Chem.*, vol. 36, no. 8, pp. 1627–1639, 1964.

[9] S. J. Orfanidis, *Introduction to signal processing*. Pearson Education, Inc., 1996.

[10] N. Golyandina, V. Nekrutkin, and A. A. Zhigljavsky, *Analysis of time series structure: SSA and related techniques*. CRC press, 2001.

[11] T. Alexandrov, "A method of trend extraction using singular spectrum analysis," arXiv preprint arXiv:0804.3367, Tech. Rep., 2008.

[12] R. Kuc and M. Schwartz, "Estimating the acoustic attenuation coefficient slope for liver from reflected ultrasound signals," *IEEE Transactions on Sonics and Ultrasonics*, vol. 26, no. 5, pp. 353–361, 1979.

[13] R. Kuc, "Estimating acoustic attenuation from reflected ultrasound signals: Comparison of spectral-shift and spectral-difference approaches," *IEEE Trans. Acous., Speech, Sig. Pro.*, vol. 32, no. 1, pp. 1–6, 1984.

[14] Z. Klimonda, J. Litniewski, and A. Nowicki, "Spatial resolution of attenuation imaging," *Archives of Acoustics*, vol. 34, no. 4, pp. 461–470, 2009.

[15] M. C. Hemmsen, M. M. Petersen, S. I. Nikolov, M. B., Nielsen, and J. A. Jensen, "Ultrasound image quality assessment: A framework for evaluation of clinical image quality," in *Proc. SPIE Med. Imag.*, vol. 76291. Medical Imaging 2010: Ultrasonic Imaging, Tomography, and Therapy, 2010, pp. 76 290C–12.

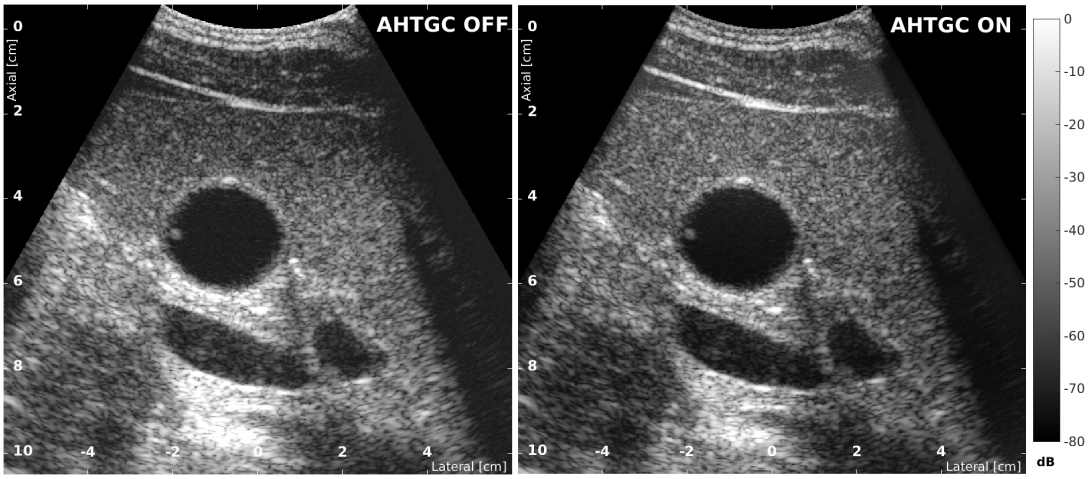

(a) Result of AHTGC applied to an axial view of a human gallbladder. The Image on the left is adjusted by the factory preset TGC with no default gains, and the image on the right is processed with AHTGC.

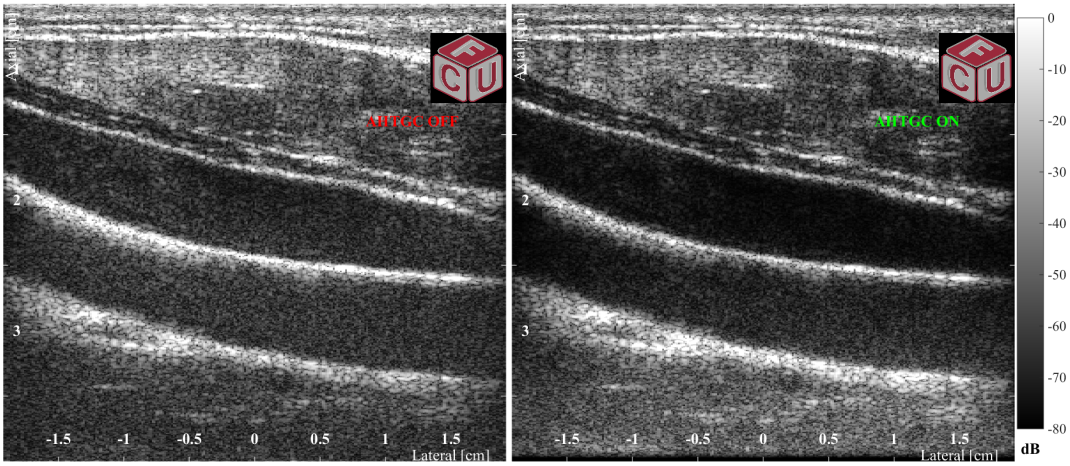

(b) Result of AHTGC applied to a sagittal view of a human carotid and jugular vein. The Image on the left is adjusted by the factory preset TGC with no default gains, and the image on the right is processed with AHTGC.

Fig. 11: *In-vivo* scans adjusted by the factory preset TGC with no default gains ”AHTGC OFF” are compared with the identical scans processed with AHTGC algorithm ”AHTGC ON”.

References from Paper A

Savitzky, A. and M. J. E. Golay (1964). "Smoothing and differentiation of data by simplified least squares procedures". In: *Anal. Chem.* 36.8, pp. 1627–1639 (cit. on p. 121).

Kuc, R. and M. Schwartz (1979). "Estimating the Acoustic Attenuation Coefficient Slope for Liver from Reflected Ultrasound Signals". In: *IEEE Transactions on Sonics and Ultrasonics* 26.5, pp. 353–361 (cit. on p. 121).

Kuc, R. (1984). "Estimating acoustic attenuation from reflected ultrasound signals: Comparison of spectral-shift and spectral-difference approaches". In: *IEEE Trans. Acous., Speech, Sig. Pro.* 32.1, pp. 1–6 (cit. on p. 121).

Inbar, D. and M. Delevy (1989). *Time gain compensation for ultrasonic medical imaging systems*. US Patent 4,852,576 (cit. on p. 121).

Pye, S., S. Wild, and W. McDicken (1992). "Adaptive time gain compensation for ultrasonic imaging". In: *Ultrasound Med. Biol.* 18.2, pp. 205–212 (cit. on p. 121).

Klesenski, K. (1996). *Automatic gain compensation in an ultrasound imaging system*. US Patent 5,579,768 (cit. on p. 121).

Orfanidis, S. J. (1996). *Introduction to signal processing*. Pearson Education, Inc. (cit. on p. 121).

Golyandina, N., V. Nekrutkin, and A. A. Zhigljavsky (2001). *Analysis of time series structure: SSA and related techniques*. CRC press (cit. on p. 121).

Lee, D., Y. Kim, and J. Ra (2006). "Automatic time gain compensation and dynamic range control in ultrasound imaging systems". In: *Proc. SPIE Med. Imag.* 6147, pages (cit. on p. 121).

Alexandrov, T. (2008). *A method of trend extraction using singular spectrum analysis*. Tech. rep. arXiv preprint arXiv:0804.3367 (cit. on p. 121).

Klimonda, Z., J. Litniewski, and A. Nowicki (2009). "Spatial Resolution of Attenuation Imaging". In: *Archives of Acoustics* 34.4, pp. 461–470 (cit. on p. 121).

Tang, M., F. Luo, and D. Liu (2009). "Automatic Time Gain Compensation in Ultrasound Imaging System". In: *Proc. IEEE Int. Conf. Bioinfo. Biomed. Eng.* Pp. 1–4. DOI: 10.1109/ICBBE.2009.5162432 (cit. on p. 121).

Hemmsen, M. C., M. M. Petersen, S. I. Nikolov, M. B., Nielsen, and J. A. Jensen (2010). "Ultrasound image quality assessment: A framework for evaluation of clinical image quality". In: *Proc. SPIE Med. Imag.* Vol. 76291. Medical Imaging 2010: Ultrasonic Imaging, Tomography, and Therapy, pp. 76290C–12 (cit. on p. 121).

Moshavegh, R., M. C. Hemmsen, B. Martins, K. L. Hansen, C. Ewertsen, A. H. Brandt, T. Bechsgaard, M. B. Nielsen, and J. A. Jensen (2015). "Advanced automated gain

adjustments for in-vivo ultrasound imaging". In: *Proc. IEEE Ultrason. Symp.* Pp. 1–4 (cit. on p. 121).

Moshavegh, R., M. Hemmsen, B. Martins, A. Brandt, K. Hansen, M. Nielsen, and J. Jensen (2015). "Automated hierarchical time gain compensation for in-vivo ultrasound imaging". In: *Proc. SPIE* 9419, pages (cit. on p. 121).

PAPER B

Advanced Multi-objective Synthetic Aperture Image Quality Optimization

Authors: Ramin Moshavegh[a], Carlos A. Villagomez-Hoyos[a], Matthias B. Stuart[a], Bo Martins[b], and Jørgen Arendt Jensen[a].

Manuscript submitted to: *IEEE Trans. Ultrasons., Ferroelec., Freq. Contr.*

[a]Center for Fast Ultrasound Imaging, Department of Electrical Engineering, Technical University of Denmark, 2800 Kgs. Lyngby, Denmark

[a]Center for Fast Ultrasound Imaging, Department of Electrical Engineering, Technical University of Denmark, 2800 Kgs. Lyngby, Denmark

[b]BK Ultrasound ApS, Herlev, Denmark

Advanced Multi-objective Synthetic Aperture Image Quality Optimization

Ramin Moshavegh*, Carlos A. Villagomez-Hoyos*, Matthias Bo Stuart*,
Bo Martins†, and Jørgen Arendt Jensen*
*Center for Fast Ultrasound Imaging, Dept. of Elec. Eng., Technical University of Denmark, Lyngby, Denmark
†BK Ultrasound ApS, Herlev, Denmark

***Abstract*—This paper proposes Pareto optimization for selecting the parameters essential for optimal synthetic aperture imaging at high frame rates. Optimization of the image quality is performed using simulations to determine number of emissions N and maximum steering angle (α_{max}). The image quality is quantified in terms of full-width at half maximum (FWHM) and contrast resolution (CTR). Measurements are performed using the experimental SARUS scanner connected to a λ/2-pitch linear array transducer. A wire phantom and a tissue mimicking phantom containing anechoic cysts are scanned using the optimized parameters for the SA sequence. Grating lobes are avoided by using a λ/2-pitch transducer, and therefore fewer emissions were needed to obtain a high image quality. The results show that SA imaging with 32 emissions and maximum sweep angle of $\alpha_{max} = 22^\circ$ yield an image quality comparable with using 256 emissions and $\alpha_{max} = 30^\circ$. The contrast-to-noise ratio (CNR) increases from 1.475 to 1.82 from 8 to 32 emissions, and plateaus after 32 emissions. A frame rate of 156 Hz can be obtained for a pulse repetition of 5 kHz *in-vivo*.**

***Index Terms*—Synthetic aperture, FWHM, contrast resolution, grating lobes, multi-objective optimization, Pareto optimal, ultrasound imaging**

I. Introduction

Synthetic aperture (SA) imaging can significantly improve the frame rate and alleviate the focusing problems of conventional techniques [1], [2], [3]. SA using spherical waves has been studied for multi-element excitation using subapertures by O'Donnell and Thomas [4], Karaman et al. [5], [6], Nikolov et al. [7], and for sparse synthetic aperture systems by Lockwood et al. [8]. Compared to conventional imaging, SA imaging has shown to improve anatomical imaging [9], and flow estimation [10], [11], [12]. In SA spherical waves are emitted in transmit that covers a larger region of intereset. The received signals for all or part of the elements in the aperture are sampled for each transmission. This data is used to generate low resolution images (LRI), which are only focused in the receive (due to the un-focused transmission). The LRIs are then combined to generate a high resolution image (HRI) to synthesize the transmit focusing. The focus is both dynamic in transmit and receive, at every image point. Therefore, SA addresses the problems with low frame rate; when emissions with large areas of sonification can be used, and a complete LRI can be beamformed for each emission. By combining all the LRIs the final HRI is generated [2] as shown in Fig. 1. SA also decouples the pulse repetition time and number of lines. This is possible as only a few set of emissions can create a full image, thus, very fast imaging can be performed.

There is a trade-off between image quality and frame rate in the imaging sequence. Therefore, optimization of the SA and transducer parameters should be performed to obtain the best trade-off between frame rate and image quality. Different scenarios also require different imaging parameters. For the case of B-mode SA imaging, the number of emissions can be kept relatively high, whereas when flow estimates are needed, less emissions and consequently high frame rates are of interest [4], [5], [6], [7]. Recently, a technique for plane wave image quality optimization was proposed, in which the number of emissions and steering angles were optimized to attain the best images at the highest possible frame rate [13]. It was shown that the optimal setup for a simulated 4.1-MHz, λ/2-pitch transducer, used 21 emissions and a maximum steering angle of 20° for imaging depths from 0 to 60 mm.

This paper presents a SA image quality optimization technique based on the performance measures of full-width at half maximum (FWHM) and contrast resolution (CTR). The multi-objective optimization technique proposed in this paper, uses the same analogy as for plane wave [13]. Optimizations are performed using simulation.

Six point scatterers are simulated for a λ/2-pitch linear transducer using the Field II program [14], [15], [16]. The CTR and FWHM are computed for the six scatterers, and for all possible combinations of number of emissions and maximum steering angles. A Pareto optimization procedure [17], [18] is then applied to identify the optimal setups in terms of having a low CTR and a small FWHM. This multi-objective optimization is used, where optimal decisions needed to be taken in the presence of trade-offs between two or more metrics (i.e. CTR and FWHM). The initial results of the proposed technique is presented in a conference paper [19]. This paper extends the optimization technique, and presents *in-vivo* results.

The remainder of this paper is organized as follows. Section II introduces the Principle of SA, investigates how to avoid grating lobes, and presents the concept of steering in SA. Section III proposes the multi-objective optimization used in the paper. Section IV introduces the performance metrics used. Section V explains simulations, as well as phantom and *in-vivo* measurements carried out. The last three sections, present the results, discuss the findings and conclude the paper.

II. Synthetic aperture imaging

The essential first step in optimizing SA image quality is to ensure that the SA emissions are as desired. This implies

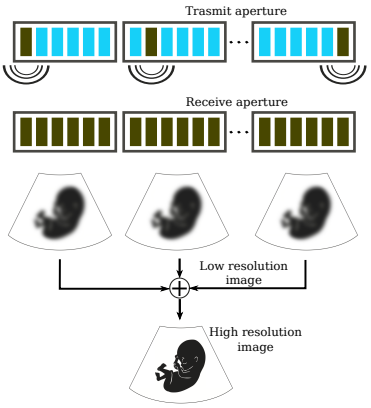

Fig. 1: Illustration of the SA imaging principle. At each transmit event a single element or a sub-aperture is used to generate a spherical wave. The ultrasound pulse propagates in all directions in the medium simultaneously, and, thus, the recorded echoes contain information about every scatterer within the interrogated region. By steering and focusing these signals at every image point, a complete image (LRI) is reconstructed after one emission. This procedure is repeated for all aperture element, and the resulting images are finally summed to produce the displayed ultrasound image (HRI).

having emissions without grating lobes and edge waves by using a $\lambda/2$ transducer. Also, the possibility of the steering the SA emissions by considering the acceptance angle of the transducer elements is considered SA sequence design.

A. Grating Lobes and $\lambda/2$-pitch requirement

Grating lobes exist in transmission and reception, for linear array transducers, if the inter-element pitch is wider than a half wavelength [20], [21]. The angle θ_g of receive grating lobes are at [22], [21]:

$$\theta_g = \sin^{-1}\left(\sin(\theta_s) - \frac{m\lambda}{p}\right), \qquad (m = \pm 1, \pm 2, \pm 3, ...) \quad (1)$$

where p is the transducer pitch, λ is the receive-signal wavelength, θ_s is the steering angle of the main receiving lobe, and m is the grating lobes order. The location of the main receiving lobe corresponds to $m = 0$. The first order grating lobes ($m = \pm 1$), are at:

$$\theta_g = \sin^{-1}\left(\sin(\theta_s) - \frac{\lambda}{p}\right). \quad (2)$$

With a pitch of λ, as for most commercial linear transducers, a steered wave of 15° generates a grating lobe at -48°. This is illustrated in Fig. 2, where the top and middle images show the emitted fields for a fixed time using a 1.5λ-pitch array and a λ-pitch array with Hamming transmit apodization. The energy behind the wave front travels in a direction of -48° off axis. The grating lobe amplitude is around -25 dB relative

(a) 1.5λ-pitch array with Hamming apodization.

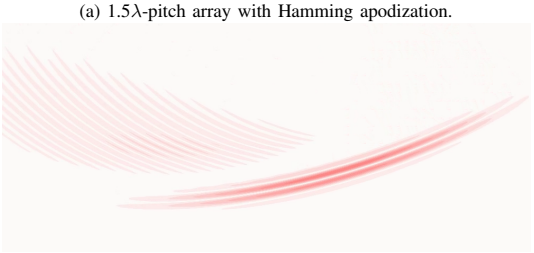

(b) λ-pitch array with Hamming apodization.

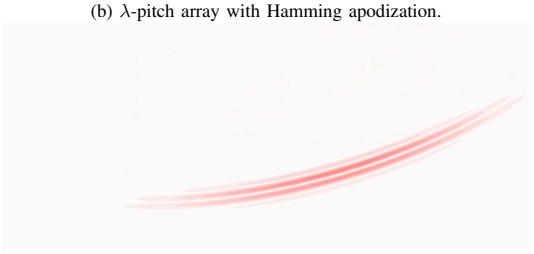

(c) λ/2-pitch array with Hamming apodization.

Fig. 2: Illustration of grating lobes, when a SA emission is emitted at 15°. For a 1.5λ-pitch array (top image), λ-pitch array (middle), and λ/2-pitch array(bottom). A Hamming window was applied as apodization for the three arrays.

to the main lobe, and the large spatial extend of the grating lobe in the near field results in image artifacts. A pitch of $\lambda/2$ moves grating lobes outside the imaging plane even for steered wave fronts as shown in Fig. 2 (bottom image). The spherical edge waves emanate from the transducer edges. They can be suppressed in the emitted field by the use of apodization in transmit, and a Hamming apodization is efficient for this as shown in all three arrays in Fig. 2.

B. SA steered emissions

In addition to subdividing the aperture in small portions during transmit in SA, each emission can also be steered to provide a better insonification of the interesting regions (see Fig. 3). However, every transducer element has a directivity pattern that determines the element's acceptance angle. This angle determines how much an emission can be steered, and to the minimum receive F-number used for beamforming. The first essential step in designing steered emissions prior to image quality optimization, is to investigate the angular response of the transducer elements used in this study. Jensen

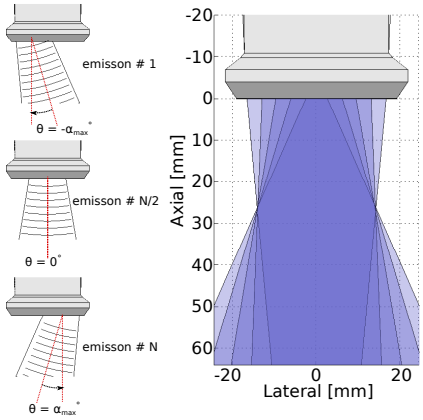

Fig. 3: Illustration of the steered SA emissions principle. At each transmit event a sub-aperture is used. The maximum steering angle is α_{max}, and N is the number of emissions. The figure on the right shows the HRI created by combining all N emissions.

et al. [13] used the same transducer as this study and employed a model proposed by Oddershede and Jensen [23] based on SNR considerations to determine the opening angle of a virtual source. It was done to determine the element acceptance angle. The study for the showed that the acceptance angle for the elements was $\pm 38^\circ$ giving an F-number of 0.64. Therefore, a minimum and maximum thresholds of $\pm 30^\circ$ were used in this paper as the maximum possible steering angle of the SA emissions. Thus, in the imaging setups the maximum steering angle ranges between -30°:0.25°:+30°.

III. Method of Optimization

This section describes the multi-objective optimization (MOP) technique used for optimizing the SA image quality based on the theory of Pareto optimality [18]. The optimization can be defined as finding a vector of decision variables that optimizes a vector function whose components are the objective functions. These functions represent a mathematical description of performance criteria, which are usually in conflict with each other. Thus, optimization means finding such a solution (decision variables) that yield acceptable values for all objective functions [17].

A. Decision variable space

The decision variables are the quantities for which values are to be selected in the optimization. They can be denoted as x_i, where $i = 1, 2, \ldots, n$. The vector $\mathbf{x}$ of n decision variables is $\mathbf{x} = [x_1, x_2, \ldots, x_n]$ (see decision space in Fig 4). In a SA imaging sequence, the decision variables can be parameters affecting the image quality such as number of emissions and steering angles.

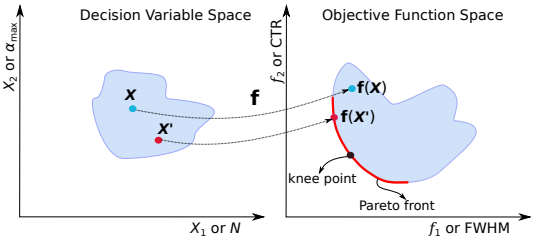

Fig. 4: Illustration of how the Pareto optimization is performed. The axes of decision space are decision variables (i.e. imaging parameters of SA), whereas the axes of objective space are the objective functions (i.e. CTR and FWHM). The set of all Pareto optimal solutions or the Pareto front is shown with the red curve. The knee point of this curve represents the best trade-off between the objective functions, and the best solution of the optimization.

B. Objective function space

Objective functions represent a set MOP's goals to be achieved. Objective function space denotes the space, in which vectors resulting from evaluating MOP's solutions are plotted [17], [18]. The objective functions are given by $f_1(\mathbf{x}), f_2(\mathbf{x}), \ldots, f_k(\mathbf{x})$, where k is the number of objective functions in the MOP. The vector $\mathbf{f}(\mathbf{x}) = [f_1(\mathbf{x}), f_2(\mathbf{x}), \ldots, f_k(\mathbf{x})]$ contains all the k objective functions (see objective space in Fig 4). For designing a SA imaging sequence, the objective functions are the performance metrics used for assessing the imaging quality such as CTR and FWHM.

C. Pareto optimality

Every point in the decision space indicate a solution and gives one point in the objective space, which indicate the quality of this solution in terms of the objective functions. Optimization is used for finding these solutions, and optimal solutions are found that satisfy the Pareto optimality criterion [17], [18]. The Pareto optimality considers a solution to be optimum, only if there are no other solutions better than that with respect to all the objective functions. A solution $\mathbf{x}' = [x_1, x_2]$ is a Pareto optimal solution, if there exists no other solutions like $\mathbf{x}$ for which $\mathbf{f}(\mathbf{x})$ dominates $\mathbf{f}(\mathbf{x}')$. A set of objective functions $\mathbf{f}(\mathbf{x}) = \{f_1, f_2\}$ is dominating another set $\mathbf{f}(\mathbf{x}')$ (mathematically given by $\mathbf{f}(\mathbf{x}) \preceq \mathbf{f}(\mathbf{x}')$), when $\mathbf{f}(\mathbf{x})$ is no worse than $\mathbf{f}(\mathbf{x}')$ in all objective functions, and $\mathbf{f}(\mathbf{x})$ is strictly better than $\mathbf{f}(\mathbf{x}')$ in at least one objective function. The set of all Pareto optimal solutions ($\mathcal{P}^*$) in decision space is given by

$$\mathcal{P}^* := \{\mathbf{x}' | \nexists\, \mathbf{x} : \mathbf{f}(\mathbf{x}) \preceq \mathbf{f}(\mathbf{x}')\}\,, \tag{3}$$

where $\nexists\, \mathbf{x}$ denotes (there exists no other solutions like $\mathbf{x}$. The set of objective functions corresponding to the Pareto optimal solutions ($\mathcal{P}^*$) is called the Pareto front ($\mathcal{PF}^*$), which is given by

$$\mathcal{PF}^* := \{\mathbf{u} = \mathbf{f}(\mathbf{x}) | \mathbf{x} \in \mathcal{P}^*\}\,. \tag{4}$$

The Pareto front is shown with a red curve in Fig. 4. The shape of the Pareto front manifests the nature of trade-off between different objective functions. The Pareto front is particularly interesting, because it contains the solutions that their objective vector components cannot be all simultaneously improved [17]. Thus, in this study only the Pareto optimal solutions are considered. Special attention must be paid to the knee-point solution on the Pareto front. It represents the best (among other points in the Pareto front) trade-off between the objective functions (see knee-point in Fig. 4).

IV. Imaging performance measures

The metrics used for evaluating the ultrasound imaging quality are contrast resolution (CTR) [24], [25], and detail resolution or full-width at half maximum (FWHM) [21]. In this study the Pareto optimization is applied to a two-objective problem, in which two metrics of CTR and FWHM are used. Optimization is performed based on the rate of changes in these features, while considering all the possible setups. The contrast-to-noise ratio (CNR) [26] is used as an alternative and independent measure for quantifying anechoic regions in measurements.

A. Contrast resolution (CTR)

The CTR measures the contrast resolution and determines the ability of the imaging system to differentiate between an anechoic region bracketed within a uniform scattering medium. CTR is the ratio between the energy outside of a circular area surrounding the point spread function (PSF) with radius of r to the total energy of the PSF [24]. It gives a measure of clutter energy outside the main lobe of the PSF. The CTR is related to the radius r and is given as

$$CTR(r) = \sqrt{\frac{E_{out}(r)}{E_{total}}}, \tag{5}$$

where $E_{out}(r)$ is the PSF energy outside a circular region with radius r centered at the peak of the PSF and E_{total} is the total energy. CTR can be calculated for either a fixed radius to get a contrast measure, or by fixing the CTR to determine resolution as the required radius for a fixed relative energy. In this study the radius r is kept fixed, and CTR is determined as the relative energy for a fixed radius of 2.5λ ($r_{2.5\lambda}$).

B. Detail resolution

The detail resolution is the -6 dB width of the main lobe of the point-spread-function (PSF), i.e., the full width at half maximum (FWHM) in the lateral direction [21].

C. Contrast-to-Noise Ratio (CNR)

The Contrast-to-Noise Ratio (CNR) is also used to quantify cyst contrast as [26]:

$$CNR = \frac{\mu_s - \mu_c}{\sqrt{\delta_s^2 + \delta_c^2}}, \tag{6}$$

where μ_c and μ_s are the mean intensities of envelope-detected signals from a region inside a cyst and a region of image speckle, and δ_c^2 and δ_s^2 are the corresponding variances. The cyst and speckle regions are of the same size and at the same depth.

V. Methods of simulations and measurements

The following section explains how the optimization technique was performed using simulations. The section then explains how the technique was implemented on the experimental scanner SARUS, and details the setups for phantom and *in-vivo* measurements.

A. Simulations

To avoid grating lobes, a λ/2-pitch array was modeled and six different point scatterers were simulated independently along the center-line of the transducer located at depths of 10, 20, 30, 40, 50, and 60 mm. Simulations were performed using the Field II program [14], [15], [16] (see Table I for details of the parameters used). A Hamming apodization on the active transmit aperture was used to reduce the edge waves.

The decision variables were number of emissions N and the maximum steering angle α_{max}. The evaluation of the image quality was performed with respect to the CTR and FWHM, which were thus, the objectives functions. An automated technique is developed in MATLAB to generate a Pareto plot and it's Pareto front, for each of the six point targets. Several combinations of N and α_{max} ($\mathbf{x}$ in the decision space) are used for generating a HRI of each of point scatterers, and calculating the corresponding objective functions of FWHM and CTR.

Based on Section II-B, α_{max} were set to vary from -30° to +30° with 0.25° separation between emissions. This was performed to ensure that emissions were not outside the transducer element's acceptance angle. The number of emissions varied between 1 to 256. Received signals from all elements were stored for each emission and beamformation were performed using the BFT3 toolbox [27]. The beamformed LRIs were subsequently combined to HRIs. Several HRIs were generated by considering several combinations of maximum beam steered angle (α_{max}) and the number of emissions (N). The image quality of the HRIs were then evaluated by computing both CTR and the lateral FWHM for simulated point scatterers.

For each simulated scatterer, two plots were generated. First one, quantifying the CTR as a function of α_{max} and N, and the second, quantifying the FWHM as a function of α_{max} and N. Each of these plots represented a decision space for the simulated point scatterer (see the decision space in Fig. 4).

Two constraints based on the rate of improvement in CTR and FWHM, when increasing the α_{max} and N. First, at least an improvement of 1% was required in FWHM, when steering 2° more and using 2 more emissions. Second, at least an improvement of 2.5% was required in CTR, when steering 2° more and using 2 more emissions. The two constrains must be both satisfied, and those combinations, for which the constraints are no longer satisfied, were excluded from the decision spaces. The remaining of the decision spaces were used to create a objective function space (see objective space in Fig. 4). It must

TABLE I: Parameters used for simulation and measurements.

Parameters	λ/2-pitch transducer
Number of elements	192
Trans. center frequency f_0	4.1 MHz
Wavelength λ	0.376 mm
Element pitch	0.2 mm (0.56λ)
Element height	6 mm
Elevation focus	38 mm
Cycles in emitted pulse	1
Transmit apodization	Hamming
Receive apodization	Hamming
Transmit F-number	0.8
Receive F-number	1
Emission steering angles	-30°:0.25°:+30°
Trans. sub aperture size (elements)	48

be pointed out that several other constraints could have been used, such as weighting either CTR or FWHM and cut-off at a specified CTR or FWHM, yielding specified HRI quality. The knee-point solution of the Pareto front represents the best trade-off between CTR and FWHM for each point scatterer. The center of gravity of all the knee-point solutions, belonging to all six point scatterers, is used as an optimal solution for the SA imaging system. This is done to include depth-dependency and to achieve a setup that yields good quality images for depths less than 60 mm.

B. Measurements

Phantom measurements were made using the SARUS experimental ultrasound scanner [28] driving a 192-element 4.1 MHz λ/2-pitch linear transducer (BK Ultrasound). A SA B-mode imaging sequence using the virtual sources behind the transducer was used to perform the imaging. Parameters used in the imaging sequence are depicted in the Table I. First, a geometry wire phantom including two wires was scanned. A multi-purpose, multi-tissue phantom containing three anechoic cysts located at 17 mm, 48 mm, and 75 mm (Model 040GSE, CIRS inc., Virginia, USA) with acoustic attenuation of 0.5 dB/(cm$\times$MHz) was also scanned. The *in-vivo* measurements were also performed using the same equipment as for the phantom measurements. A SA imaging sequence, similar to phantom measurements, with the optimal values of α_{max} and N (computed in section VI-A) is used. Longitudinal scans of the right common carotid artery, and common carotid with bulbous were acquired from a 29 year-old male volunteer.

VI. Results

This section presents the results of the simulations performed for the optimization procedure, phantom measurements, and

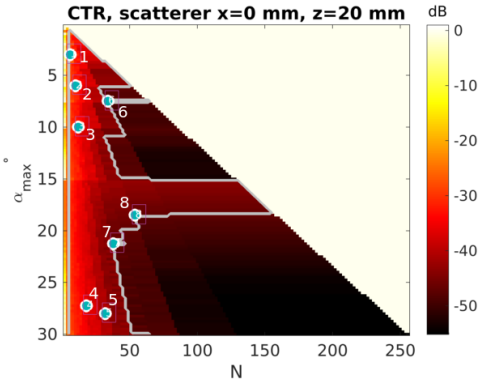

(a) CTR decision space, computed as a function of α_{max} and N for scatterer at 20 mm.

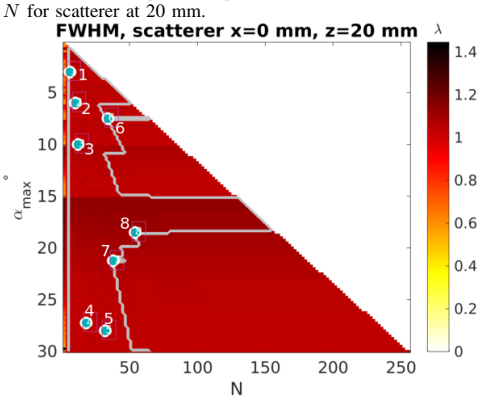

(b) FWHM decision space as a function of α_{max} and N for scatterer at 20 mm.

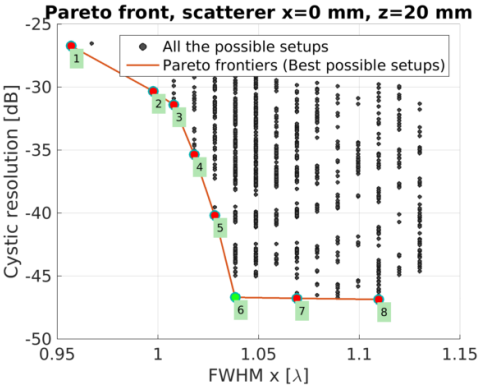

(c) Pareto plot (Objective space) created by merging the CTR and FWHM decision spaces for scatterer at 20 mm.

Fig. 5: Optimization procedure demonstrated for the scatterer at 20 mm. (a) shows the CTR decision space. (b) shows the FWHM decision space. White lines on *(a)* and *(b)* are the border lines. The enumerated points are the Pareto front optimal solutions. The green point (number 6) is the knee-point solution shown in *(c)*.

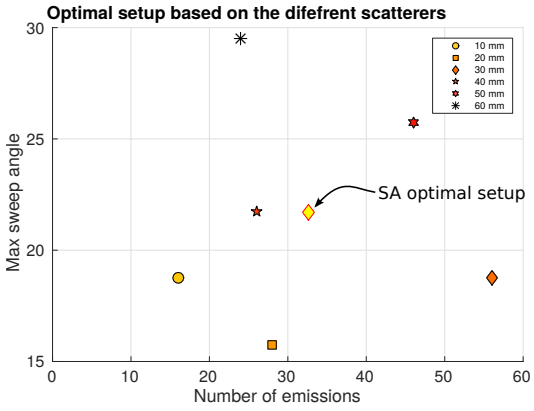

Fig. 6: Illustrates the α_{max} and N corresponding to the knee-points computed for six scatterers. The yellow diamond ($\alpha_{max} = 22°$ and $N = 32$) is the center of the gravity of all knee-points and considered to be the optimal setup for SA imaging.

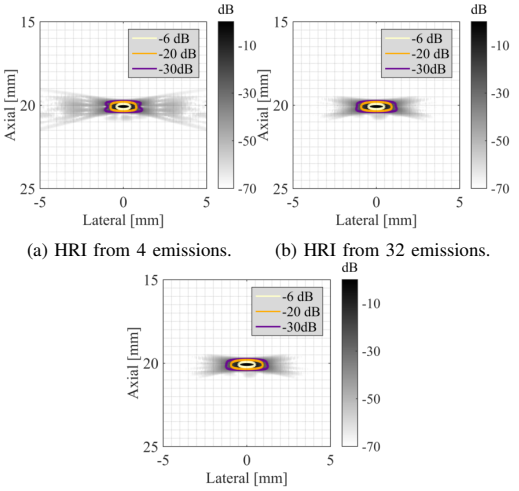

(a) HRI from 4 emissions. (b) HRI from 32 emissions.

(c) HRI from 256 emissions.

Fig. 7: Simulation results of a point scatterer located at 20 mm. HRIs reconstructed from low, optimal and high number of emissions.

in-vivo measurements performed with the optimized sequence.

A. Simulation results

The automated optimization technique is applied to six scatterers. The simulation results shown in this paper, belong to one of the six scatterers (located at 20 mm), which exemplifies the optimization performed. The CTR and Lateral FWHM of HRIs for the scatterer 20 mm, for all combinations of α_{max} and N, is shown in the Figs. 5a and 5b. The white lines on the figures show the areas of the plots satisfying the two constraints put on rates of changes of CTR and FWHM (mentioned in section V). The axial FWHM is not considered, as the simulations showed that it was very close to λ, for all the combinations. The areas satisfying the two constraints created a Pareto plot shown in Fig. 5c. It represented the objective function space of CTR and FWHM for the point scatterer located at 20 mm.

The Pareto plots, alone, do not yield the optimal setup for the SA imaging sequence. That is why, Pareto fronts are more interesting, because they decrease the number of optimal solutions to be considered for imaging. The Pareto fronts for all six scatterers are computed. Fig. 5c shows the Pareto plot belonging to the scatterer at 20 mm. The enumerated points on the Pareto front, show the optimal solutions (set of α_{max} and N) that yield the optimal solutions for the 20 mm scatterer. The eight frontier points in Fig. 5c are shown with blue points on the CTR and FWHM decision spaces in Figs. 5a and 5b. The knee-point of the pareto-front is also shown with green circle on the Pareto front in Fig. 5c. The α_{max} and N corresponding to the knee-points computed for six scatterers are shown in Fig. 6. The yellow diamond ($\alpha_{max} = 22°$ and $N = 32$) is the center of the gravity of all points and the optimal setup for SA imaging. This optimal setup requires 32 emissions and 22° maximum sweeping angle. Fig. 7 shows the point scatterer simulated at 20 mm. HRIs of the scatterer were reconstructed using three different number of emissions (N = 4, 32, 256). The FWHM and CTRs are depicted in the Table II.

TABLE II: Simulated scatterer at 20 mm quality metrics.

Scatterers	20 mm
N = 4	FWHM = 1.40λ CTR = -25.41 dB
N = 32 (optimal)	FWHM = 1.49λ CTR = -30.25 dB
N = 256	FWHM = 1.50λ CTR = -30.31 dB

B. Phantom measurement results

1) Wire phantom results: A phantom containing two wires located at 32.5 mm, and 57.5 mm were imaged using a SA sequence using varying number of emissions. Fig. 8 shows the HRIs belonging to two wires located at 32.5 mm (left column), and 57.5 mm (right column). Each HRI was reconstructed with 4, 32 and 256 emissions, where the 32 emissions is the optimized sequence. The FWHM and CTR corresponding to each of the reconstructions is depicted in the Table III.

The results show that the FWHM increases 0.41λ from 4 emissions to 32 emissions for the wire at 32.5 mm, but it only changes 0.07λ from 32 emissions to 256 emissions. For the same wire, the CTR improves 3.63 dB from 4 emissions to 32 emissions for the wire at 32.5 mm, while it does not change from 32 emissions to 256 emissions. For the wire at 57.5 mm, the FWHM increases 0.04λ from 4 emissions to 32 emissions for the wire at 32.5 mm, but it only changes 0.02λ from 32 emissions to 256 emissions. The CTR changes are not noticeable for this wire. The point wires reconstructed with 32 emissions represent similar CTR and FWHM compared with

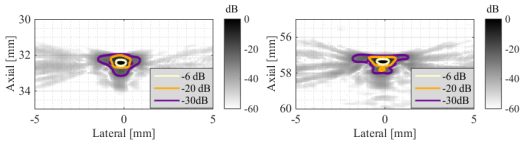

(a) HRI from 4 emissions.

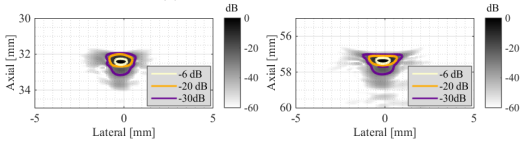

(b) HRI from 32 emissions (optimal).

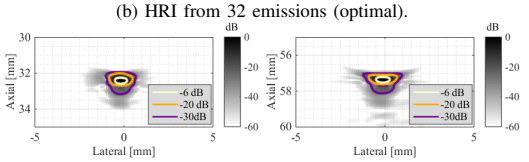

(c) HRI from 256 emissions.

Fig. 8: Phantom measurement results of wires located at 32.5 mm and 57.5 mm. HRIs reconstructed from low, optimal and high number of emissions.

TABLE III: Wire phantom measurements quality metrics.

Scatterers	32.5 mm	57.5 mm
N = 4	FWHM = 1.09λ CTR = -19.62 dB	FWHM = 1.38λ CTR = -10.19 dB
N = 32 (optimal)	FWHM = 1.5λ CTR = -23.25 dB	FWHM = 1.44λ CTR = -10.39 dB
N = 256	FWHM = 1.43λ CTR = -23.2 dB	FWHM = 1.46λ CTR = -10.3 dB

wires reconstructed with 256 emissions. This suggests that for the same image quality, number of emissions can be lowered from 256 to 32.

2) Cyst phantom results: Fig. 10 shows the cyst phantom measured and HRIs reconstructed with $N = 4$, the optimized sequence ($\alpha_{max} = 22°$ and $N = 32$), and also $N = 256$. To evaluate the quality of the HRIs, the CNR is used to quantify cysts contrast. The mean CNRs of the two cysts located at 17 mm and 48 mm, were computed for the HRIs reconstructed with increasing number of emissions. This was done to evaluate the performance of the sequence for small parts imaging, and scanning superficial tissues located above 60 mm in depth. Fig. 10 shows that the CNR increases from 1.475 to 1.82 by reaching to 32 emissions, and plateaus after 32 emissions. This coincides with the simulation and wire phantom measurement results, and indicates that for achieving a specific image quality, the number of emissions does not have to be increased to more than the optimal value computed for the SA.

C. In-vivo results

A healthy 29 male was scanned using the optimized SA sequence with ($\alpha_{max} = 22°$ and $N = 32$), in two longitudinal views of the common carotid, and carotid with bulbous. The results are shown in Fig. 11.

VII. Discussion

As discussed in the Section II-A, having a good control over the emissions wave front is crucial, and a $\lambda/2$-pitch transducer ensures avoiding the grating lobes behind the wave front. The optimization performed in this study was a 2-objective optimization, in which two SA imaging parameters of α_{max} and N was optimized only. The technique can be more advanced and the number of parameters to be optimized can be increased. For SA, the optimization can be 4-objective, by optimizing the α_{max}, N, F-number, and aperture size (the transmit sub-aperture). If the number of objective functions does not change (only CTR and FWHM are considered), then the technique yields two 4-D decision spaces (one for the CTR, and one for the FWHM). The final objective space would still be 2-D, because of considering CTR and FWHM only.

A higher dimension decision space requires a higher dimension objective space. For a 4-objective optimization (4-D decision spaces), a 3-D objective space can be a good alternative, since the solutions in 4-D decision spaces can be distributed in 3-D objective space, and do not squeeze in a 2-D space that might not be quantitatively representative. The "curse of dimensionality" has to be considered, when increasing the number of parameters to be optimized (see chapter 2 of [29]). This refers to how certain optimization techniques or machine learning algorithms may perform poorly in high-dimensional data. Increasing the number of parameters will not necessarily yield a correct optimization.

Another challenge in high quality SA, is the inter-emission tissue motions. They are more obvious, when number of emissions used for recunstructing HRI is very high. The issue is addressed by [30], [31], and can be compensated for. The clutter behind the wire in Fig. 8 can be due to a long impulse response of the transducer. It can also be related to artifacts arising from quantization of the transmit delay profile at 70 MHz [32].

SA image quality was investigated using a $\lambda/2$-pitch transducer, and slightly improved contrast was obtained for the same number of emissions when using $\lambda/2$-pitch rather than λ-pitch [33]. Other techniques exist for lowering the grating lobes in SA and plane wave, which are mainly based on sparse-aperture methods [8], special apodizations of the array [34], or modulating receive beams [35]. The common problem with these techniques is mainly the reduced transmitted energy. The other problem with these methods is that transmit grating lobes are not always avoided. However, the grating lobes can be completely avoided by using a $\lambda/2$-pitch transducer, as suggested in this paper.

VIII. Conclusion

This paper presented a hierarchical and automated optimization technique for characterizing the optimal setup in SA imaging. The optimization technique is performed using simulation. The results of the simulation showed that with only $\alpha_{max} = \pm 22°$ and $N = 32$, the image quality is comparable with a high number of emissions. Phantom measurement results also indicated that CNR increases from 1.475 to 1.82 by reaching to 32 emissions, and plateaus after 32 emissions.

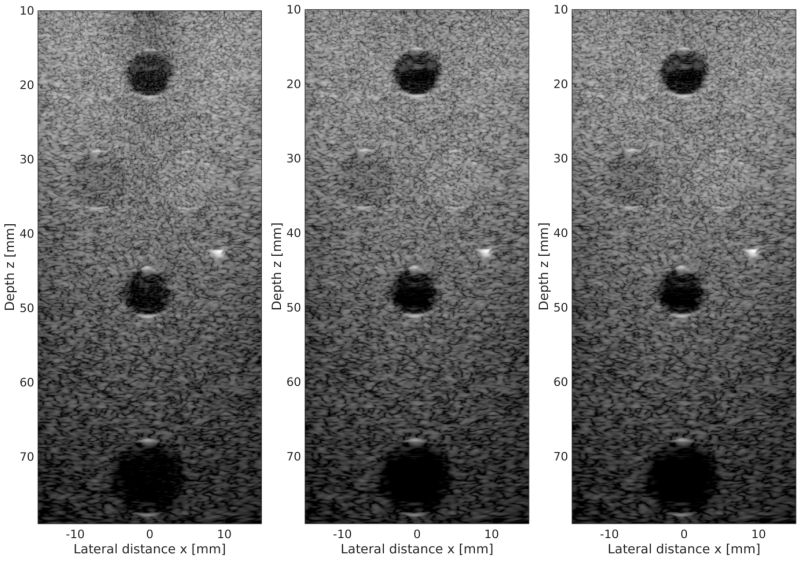

(a) HRI from 8 emissions. (b) HRI from 32 emissions. (c) HRI from 256 emissions.

Fig. 9: Measured cyst phantom and reconstructed from low, optimal, and high number of emissions. All three images are shown using a 60 dB dynamic range.

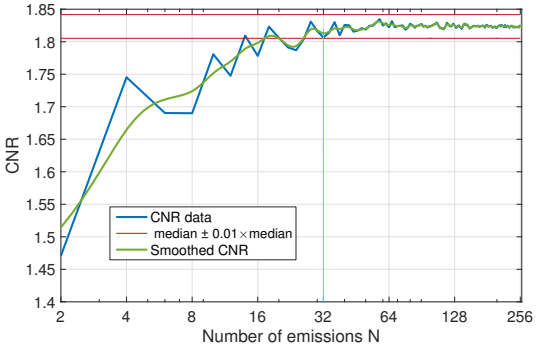

Fig. 10: CNR computed for measured cyst phantom images and reconstructed with increasing number of emissions.

Wire phantom measurement results indicated that for achieving a specific image quality, the number of emissions does not have to be increased to more than the optimal value. Improvements in frame rate is also achievable by using less number of emissions. This can be highlighted when high frame rate is needed for velocity estimation, and when the standard deviation of the velocity estimates are related to the frame rate. The technique was applied for a $\lambda/2$-pitch transducer, and image quality was compared for simulations and phantom measurements. The grating lobes were avoided by using a $\lambda/2$-pitch transducer, and therefore fewer emissions were needed to obtain the same image quality. The *in-vivo* results of the optimized sequence for carotid of a healthy subject are presented, in which with a pulse repetition frequency of 5 kHz more than 156 fps are obtained. The generic technique used in this study can be applied to any ultrasound imaging modality, using any transducer geometry.

REFERENCES

[1] M. H. Bae and M. K. Jeong, "A study of synthetic-aperture imaging with virtual source elements in B-mode ultrasound imaging systems," in *IEEE Trans. Ultrason., Ferroelec., Freq. Contr.*, vol. 47, 2000, pp. 1510–1519.

[2] J. A. Jensen, S. Nikolov, K. L. Gammelmark, and M. H. Pedersen, "Synthetic aperture ultrasound imaging," *Ultrasonics*, vol. 44, pp. e5–e15, 2006.

[3] M. H. Pedersen, K. L. Gammelmark, and J. A. Jensen, "In-vivo evaluation of convex array synthetic aperture imaging," *Ultrasound Med. Biol.*, vol. 33, pp. 37–47, 2007.

[4] M. O'Donnell and L. J. Thomas, "Efficient synthetic aperture imaging from a circular aperture with possible application to catheter-based imaging," *IEEE Trans. Ultrason., Ferroelec., Freq. Contr.*, vol. 39, pp. 366–380, 1992.

[5] M. Karaman, P. C. Li, and M. O'Donnell, "Synthetic aperture imaging for small scale systems," *IEEE Trans. Ultrason., Ferroelec., Freq. Contr.*, vol. 42, pp. 429–442, 1995.

[6] M. Karaman and M. O'Donnell, "Subaperture processing for ultrasonic imaging," *IEEE Trans. Ultrason., Ferroelec., Freq. Contr.*, vol. 45, pp. 126–135, 1998.

[7] S. I. Nikolov, K. Gammelmark, and J. A. Jensen, "Recursive ultrasound imaging," in *Proc. IEEE Ultrason. Symp.*, vol. 2, 1999, pp. 1621–1625.

[8] G. R. Lockwood, J. R. Talman, and S. S. Brunke, "Real-time 3-D ultrasound imaging using sparse synthetic aperture beamforming," *IEEE Trans. Ultrason., Ferroelec., Freq. Contr.*, vol. 45, pp. 980–988, 1998.

[9] K. L. Gammelmark and J. A. Jensen, "Multielement synthetic transmit aperture imaging using temporal encoding," *IEEE Trans. Med. Imag.*, vol. 22, no. 4, pp. 552–563, 2003.

[10] S. I. Nikolov and J. A. Jensen, "In-vivo synthetic aperture flow imaging in medical ultrasound," *IEEE Trans. Ultrason., Ferroelec., Freq. Contr.*, vol. 50, no. 7, pp. 848–856, 2003.

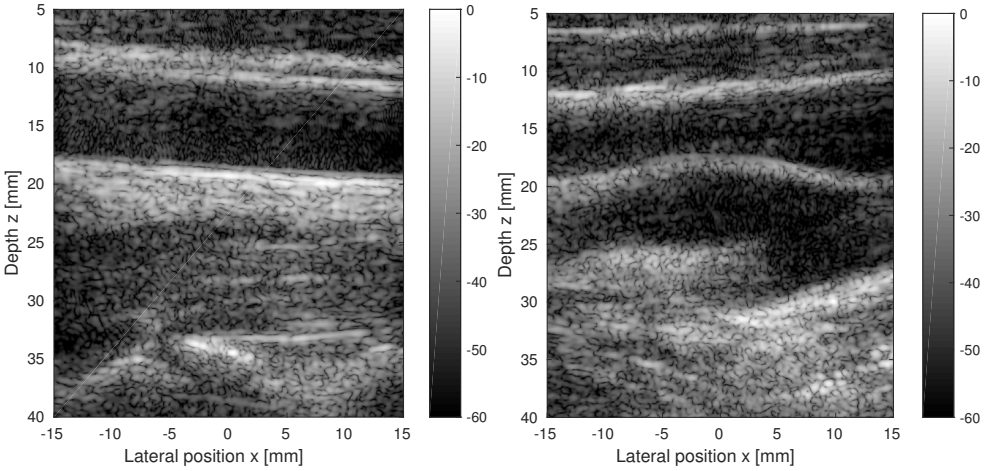

(a) (b)

Fig. 11: Measurements performed on a 28 years old healthy male using the optimized sequence. (a) shows the common carotid of the subject measured and reconstructed from 32 emissions. (b) shows the common carotid with bulbous of the subject measured and reconstructed from 32 emissions.

[11] J. A. Jensen and S. I. Nikolov, "Directional synthetic aperture flow imaging," *IEEE Trans. Ultrason., Ferroelec., Freq. Contr.*, vol. 51, pp. 1107–1118, 2004.

[12] B. Y. Yiu, S. S. Lai, and A. C. Yu, "Vector projectile imaging: time-resolved dynamic visualization of complex flow patterns." *Ultrasound Med. Biol.*, vol. 40, no. 9, pp. 2295–2309, sept 2014.

[13] J. Jensen, M. B. Stuart, and J. A. Jensen, "Optimized plane wave imaging for fast and high-quality ultrasound imaging," *IEEE Trans. Ultrason., Ferroelec., Freq. Contr.*, vol. 63, no. 11, pp. 1922–1934, 2016.

[14] J. A. Jensen and N. B. Svendsen, "Calculation of pressure fields from arbitrarily shaped, apodized, and excited ultrasound transducers," *IEEE Trans. Ultrason., Ferroelec., Freq. Contr.*, vol. 39, pp. 262–267, 1992.

[15] J. A. Jensen, "Field: A program for simulating ultrasound systems," *Med. Biol. Eng. Comp.*, vol. 10th Nordic-Baltic Conference on Biomedical Imaging, Vol. 4, Supplement 1, Part 1, pp. 351–353, 1996.

[16] ——, "A multi-threaded version of Field II," in *Proc. IEEE Ultrason. Symp.* IEEE, 2014, pp. 2229–2232.

[17] C. A. C. Coello, G. B. Lamont, and D. A. V. Veldhuizen, "Basic concepts," in *Evolutionary Algorithms for Solving Multi-Objective Problems*. Springer, 2007.

[18] K. Deb, "Multi-objective optimization," in *Search methodologies*. Springer, 2005.

[19] R. Moshavegh, J. Jensen, C. A. Villagomez-Hoyos, M. B. Stuart, M. C. Hemmsen, and J. A. Jensen, "Optimization of synthetic aperture image quality," in *Proc. SPIE Med. Imag.*, vol. 9790, 2016, pp. 97 900Z–97 900Z–9.

[20] P. Y. Barthez, R. Léveillé, and P. V. Scrivani, "Side lobes and grating lobes artifacts in ultrasound imaging," *Veterinary Radiology & Ultrasound*, vol. 38, no. 5, pp. 387–393, 1997.

[21] T. L. Szabo, *Diagnostic ultrasound imaging: Inside out*, 2nd ed. Elsevier (Oxford, UK), 2014.

[22] J. Huang, P. W. Que, and J. H. Jin, "A parametric study of beam steering for ultrasonic linear phased array transducer," *Russ. J. Nondestr. Test.*, vol. 40, no. 4, pp. 254–259, 2004.

[23] N. Oddershede and J. A. Jensen, "Effects influencing focusing in synthetic aperture vector flow imaging," *IEEE Trans. Ultrason., Ferroelec., Freq. Contr.*, vol. 54, no. 9, pp. 1811–1825, 2007.

[24] K. Ranganathan and W. F. Walker, "Cystic resolution: A performance metric for ultrasound imaging systems," *IEEE Trans. Ultrason., Ferroelec., Freq. Contr.*, vol. 54, no. 4, pp. 782–792, 2007.

[25] D. A. Guenther and W. F. Walker, "Generalized cystic resolution: a metric for assessing the fundamental limits on beamformer performance," *IEEE Trans. Ultrason., Ferroelec., Freq. Contr.*, vol. 56, no. 1, pp. 77–90, January 2009.

[26] M. A. Lediju, G. E. Trahey, B. C. Byram, and J. J. Dahl, "Short-lag spatial coherence of backscattered echoes: imaging characteristics," *IEEE Trans. Ultrason., Ferroelec., Freq. Contr.*, vol. 58, no. 7, pp. 1377–1388, 2011.

[27] J. M. Hansen, M. C. Hemmsen, and J. A. Jensen, "An object-oriented multi-threaded software beamformation toolbox," in *Proc. SPIE Med. Imag.*, vol. 7968, March 2011, pp. 79 680Y–1–79 680Y–9.

[28] J. A. Jensen, H. Holten-Lund, R. T. Nilsson, M. Hansen, U. D. Larsen, R. P. Domsten, B. G. Tomov, M. B. Stuart, S. I. Nikolov, M. J. Pihl, Y. Du, J. H. Rasmussen, and M. F. Rasmussen, "SARUS: A synthetic aperture real-time ultrasound system," *IEEE Trans. Ultrason., Ferroelec., Freq. Contr.*, vol. 60, no. 9, pp. 1838–1852, 2013.

[29] T. Hastie, R. Tibshirani, and J. Friedman, *The Elements of Statistical Learning Data Mining, Inference, and Prediction*, second edition ed. Springer Series in Statistics, 2009.

[30] B. Denarie, T. A. Tangen, I. K. Ekroll, N. Rolim, H. H. Torp, T. Bjastad, and L. Løvstakken, "Coherent plane wave compounding for very high frame rate ultrasonography of rapidly moving targets," *IEEE Trans. Ultrason., Ferroelec., Freq. Contr.*, vol. 32, no. 7, pp. 1265–1276, 2013.

[31] K. L. Gammelmark and J. A. Jensen, "2-D tissue motion compensation of synthetic transmit aperture images," *IEEE Trans. Ultrason., Ferroelec., Freq. Contr.*, pp. 594–610, April 2014.

[32] M. B. Stuart, J. Jensen, T. Di Ianni, and J. A. Jensen, "Image quality degradation from transmit delay profile quantization," in *Proc. IEEE Ultrason. Symp.*, 2015, pp. 1–4.

[33] H. Hasegawa and C. L. de Korte, "Impact of element pitch on synthetic aperture ultrasound imaging," *J. Med. Ultrason.*, pp. 1–9, 2016.

[34] C. R. Cooley and B. S. Robinson, "Synthetic aperture imaging using partial datasets," in *Proc. IEEE Ultrason. Symp.*, 1994, pp. 1539–1542.

[35] A. Ponnle, H. Hasegawa, and H. Kanai, "Suppression of grating lobe artifacts in ultrasound images formed from diverging transmitting beams by modulation of receiving beams," *Ultrasound Med. Biol.*, vol. 39, no. 4, pp. 681–691, 2013.

References from Paper B

Jensen, J. A. and N. B. Svendsen (1992). "Calculation of Pressure Fields from Arbitrarily Shaped, Apodized, and Excited Ultrasound Transducers". In: *IEEE Trans. Ultrason., Ferroelec., Freq. Contr.* 39, pp. 262–267 (cit. on p. 135).

O'Donnell, M. and L. J. Thomas (1992). "Efficient synthetic aperture imaging from a circular aperture with possible application to catheter-based imaging". In: *IEEE Trans. Ultrason., Ferroelec., Freq. Contr.* 39, pp. 366–380 (cit. on p. 135).

Cooley, C. R. and B. S. Robinson (1994). "Synthetic aperture imaging using partial datasets". In: *Proc. IEEE Ultrason. Symp.* Pp. 1539–1542. DOI: 10.1109/ULTSYM.1994.401884 (cit. on p. 135).

Karaman, M., P. C. Li, and M. O'Donnell (1995). "Synthetic aperture imaging for small scale systems". In: *IEEE Trans. Ultrason., Ferroelec., Freq. Contr.* 42, pp. 429–442 (cit. on p. 135).

Jensen, J. A. (1996). "Field: A Program for Simulating Ultrasound Systems". In: *Med. Biol. Eng. Comp.* 10th Nordic-Baltic Conference on Biomedical Imaging, Vol. 4, Supplement 1, Part 1, pp. 351–353 (cit. on p. 135).

Barthez, P. Y., R. Léveillé, and P. V. Scrivani (1997). "Side lobes and grating lobes artifacts in ultrasound imaging". In: *Veterinary Radiology & Ultrasound* 38.5, pp. 387–393 (cit. on p. 135).

Karaman, M. and M. O'Donnell (1998). "Subaperture processing for ultrasonic imaging". In: *IEEE Trans. Ultrason., Ferroelec., Freq. Contr.* 45, pp. 126–135 (cit. on p. 135).

Lockwood, G. R., J. R. Talman, and S. S. Brunke (1998). "Real-time 3-D ultrasound imaging using sparse synthetic aperture beamforming". In: *IEEE Trans. Ultrason., Ferroelec., Freq. Contr.* 45, pp. 980–988 (cit. on p. 135).

Nikolov, S. I., K. Gammelmark, and J. A. Jensen (1999). "Recursive ultrasound imaging". In: *Proc. IEEE Ultrason. Symp.* Vol. 2, pp. 1621–1625 (cit. on p. 135).

Bae, M. H. and M. K. Jeong (2000). "A study of synthetic-aperture imaging with virtual source elements in B-mode ultrasound imaging systems". In: *IEEE Trans. Ultrason., Ferroelec., Freq. Contr.* Vol. 47, pp. 1510–1519 (cit. on p. 135).

Gammelmark, K. L. and J. A. Jensen (2003). "Multielement Synthetic Transmit Aperture Imaging using Temporal Encoding". In: *IEEE Trans. Med. Imag.* 22.4, pp. 552–563 (cit. on p. 135).

Nikolov, S. I. and J. A. Jensen (2003). "In-vivo Synthetic Aperture Flow Imaging in Medical Ultrasound". In: *IEEE Trans. Ultrason., Ferroelec., Freq. Contr.* 50.7, pp. 848–856 (cit. on p. 135).

Huang, J., P. W. Que, and J. H. Jin (2004). “A Parametric Study of Beam Steering for Ultrasonic Linear Phased Array Transducer”. In: *Russ. J. Nondestr. Test.* 40.4, pp. 254–259 (cit. on p. 135).

Jensen, J. A. and S. I. Nikolov (2004). “Directional Synthetic Aperture Flow Imaging”. In: *IEEE Trans. Ultrason., Ferroelec., Freq. Contr.* 51, pp. 1107–1118 (cit. on p. 135).

Deb, K. (2005). “Multi-objective optimization”. In: *Search methodologies*. Springer (cit. on p. 135).

Jensen, J. A., S. Nikolov, K. L. Gammelmark, and M. H. Pedersen (2006). “Synthetic Aperture Ultrasound Imaging”. In: *Ultrasonics* 44, e5–e15 (cit. on p. 135).

Coello, C. A. C., G. B. Lamont, and D. A. V. Veldhuizen (2007). “Basic Concepts”. In: *Evolutionary Algorithms for Solving Multi-Objective Problems*. Springer (cit. on p. 135).

Oddershede, N. and J. A. Jensen (2007). “Effects influencing focusing in synthetic aperture vector flow imaging”. In: *IEEE Trans. Ultrason., Ferroelec., Freq. Contr.* 54.9, pp. 1811–1825 (cit. on p. 135).

Pedersen, M. H., K. L. Gammelmark, and J. A. Jensen (2007). “In-vivo evaluation of convex array synthetic aperture imaging”. In: *Ultrasound Med. Biol.* 33, pp. 37–47 (cit. on p. 135).

Ranganathan, K. and W. F. Walker (2007). “Cystic Resolution: A Performance Metric for Ultrasound Imaging Systems”. In: *IEEE Trans. Ultrason., Ferroelec., Freq. Contr.* 54.4, pp. 782–792. DOI: 10.1109/TUFFC.2007.311 (cit. on p. 135).

Guenther, D. A. and W. F. Walker (2009). “Generalized cystic resolution: a metric for assessing the fundamental limits on beamformer performance”. In: *IEEE Trans. Ultrason., Ferroelec., Freq. Contr.* 56.1, pp. 77–90 (cit. on p. 135).

Hastie, T., R. Tibshirani, and J. Friedman (2009). *The Elements of Statistical Learning Data Mining, Inference, and Prediction*. Second edition. Springer Series in Statistics (cit. on p. 135).

Hansen, J. M., M. C. Hemmsen, and J. A. Jensen (2011). “An object-oriented multi-threaded software beamformation toolbox”. In: *Proc. SPIE Med. Imag.* Vol. 7968, pages. DOI: 10.1117/12.878178 (cit. on p. 135).

Lediju, M. A., G. E. Trahey, B. C. Byram, and J. J. Dahl (2011). “Short-lag spatial coherence of backscattered echoes: imaging characteristics”. In: *IEEE Trans. Ultrason., Ferroelec., Freq. Contr.* 58.7, pp. 1377–1388. DOI: 10.1109/TUFFC.2011.1957 (cit. on p. 135).

Denarie, B., T. A. Tangen, I. K. Ekroll, N. Rolim, H. H. Torp, T. Bjastad, and L. Løvstakken (2013). “Coherent Plane Wave Compounding for Very High Frame Rate Ultrasonography of Rapidly Moving Targets”. In: *IEEE Trans. Ultrason., Ferroelec., Freq. Contr.* 32.7, pp. 1265–1276 (cit. on p. 135).

Jensen, J. A., H. Holten-Lund, R. T. Nilsson, M. Hansen, U. D. Larsen, R. P. Domsten, B. G. Tomov, M. B. Stuart, S. I. Nikolov, M. J. Pihl, Y. Du, J. H. Rasmussen, and M. F. Rasmussen (2013). "SARUS: A Synthetic Aperture Real-time Ultrasound System". In: *IEEE Trans. Ultrason., Ferroelec., Freq. Contr.* 60.9, pp. 1838–1852 (cit. on p. 135).

Ponnle, A., H. Hasegawa, and H. Kanai (2013). "Suppression of grating lobe artifacts in ultrasound images formed from diverging transmitting beams by modulation of receiving beams". In: *Ultrasound Med. Biol.* 39.4, pp. 681–691. DOI: 10.1016/j.ultrasmedbio.2012.10.019 (cit. on p. 135).

Gammelmark, K. L. and J. A. Jensen (2014). "2-D Tissue Motion Compensation of Synthetic Transmit Aperture Images". In: *IEEE Trans. Ultrason., Ferroelec., Freq. Contr.* Pp. 594–610. DOI: http://dx.doi.org/10.1109/TUFFC.2014.2948 (cit. on p. 135).

Jensen, J. A. (2014). "A Multi-threaded Version of Field II". In: *Proc. IEEE Ultrason. Symp.* IEEE, pp. 2229–2232 (cit. on p. 135).

Szabo, T. L. (2014). *Diagnostic ultrasound imaging: Inside out*. 2nd ed. Elsevier (Oxford, UK) (cit. on p. 135).

Yiu, B. Y., S. S. Lai, and A. C. Yu (2014). "Vector projectile imaging: time-resolved dynamic visualization of complex flow patterns." In: *Ultrasound Med. Biol.* 40.9, pp. 2295–2309 (cit. on p. 135).

Stuart, M. B., J. Jensen, T. Di Ianni, and J. A. Jensen (2015). "Image quality degradation from transmit delay profile quantization". In: *Proc. IEEE Ultrason. Symp.* Pp. 1–4. DOI: 10.1109/ULTSYM.2015.0126 (cit. on p. 135).

Hasegawa, H. and C. L. de Korte (2016). "Impact of element pitch on synthetic aperture ultrasound imaging". In: *J. Med. Ultrason.* Pp. 1–9. DOI: 10.1007/s10396-016-0700-6 (cit. on p. 135).

Jensen, J., M. B. Stuart, and J. A. Jensen (2016). "Optimized Plane Wave Imaging for Fast and High-Quality Ultrasound Imaging". In: *IEEE Trans. Ultrason., Ferroelec., Freq. Contr.* 63.11, pp. 1922–1934. DOI: 10.1109/TUFFC.2016.2591980 (cit. on p. 135).

Moshavegh, R., J. Jensen, C. A. Villagomez-Hoyos, M. B. Stuart, M. C. Hemmsen, and J. A. Jensen (2016). "Optimization of synthetic aperture image quality". In: *Proc. SPIE Med. Imag.* Vol. 9790, pages (cit. on p. 135).

PAPER C

Automated Hierarchical Time Gain Compensation for *In-Vivo* Ultrasound Imaging

Authors: Ramin Moshavegh[a], Martin Christian Hemmsen[a], Bo Martins[c], Andreas Hjelm Brandt[b], Kristoffer Lindskov Hansen[b], Michael Bachmann Nielsen[b] and Jørgen Arendt Jensen[a].

Manuscript published: *Proceedings of SPIE Medical Imaging*, (2015).

Abstract

Time gain compensation (TGC) is essential to ensure the optimal image quality of the clinical ultrasound scans. When large fluid collections are present within the scan plane, the attenuation distribution is changed drastically and TGC compensation becomes challenging. This paper presents an automated hierarchical TGC (AHTGC) algorithm that accurately adapts to the large attenuation variation between different types of tissues and structures. The algorithm relies on estimates of tissue attenuation, scattering strength, and noise level to gain a more quantitative understanding of the underlying tissue and the ultrasound signal strength. The proposed algorithm was applied to a set of 44 *in-vivo* abdominal movie sequences each containing 15 frames. Matching pairs of *in-vivo* sequences, unprocessed and processed with the proposed AHTGC were visualized side by side and evaluated by two radiologists in terms of image quality. Wilcoxon signed-rank test was used to evaluate whether radiologists

[a]Center for Fast Ultrasound Imaging, Department of Electrical Engineering, Technical University of Denmark, 2800 Kgs. Lyngby, Denmark

[b]Department of Radiology, Rigshospitalet, Copenhagen University Hospital, Copenhagen, Denmark

[c]BK Ultrasound ApS, Herlev, Denmark

"F"urther author information: Send correspondence to Ramin Moshavegh E-mail: ramosh@elektro.dtu.dk

preferred the processed sequences or the unprocessed data. The results indicate that the average visual analogue scale (VAS) is positive (p-value: 2.34×10^{-13}) and estimated to be 1.01 (95% CI: 0.85; 1.16) favoring the processed data with the proposed AHTGC algorithm.

C.1 Introduction

Radiofrequency (RF) echoes are strongly attenuated by the tissues scanned (Lee, Kim, and Ra 2006). These RF signals span a wide dynamic range, when they are received by the transducer, and are not suitable to be visualized before the gains are adjusted. Time gain compensation (TGC) is usually utilized to compensate for the acoustic attenuation. TGC offsets the attenuation of ultrasound echo signals along the depth, so that echoes belonging to deep structures are more amplified compared to superficial echoes. This provides more uniform image to be displayed on the scanner (Lee, Kim, and Ra 2006).

Current ultrasound scanners use a TGC curve for time gain compensation. The user adjusts the shape by manually using TGC sliders for different depths. However, this is cumbersome and the image quality is highly dependent on the adjustments. An automatic adjustment of the TGC (ATGC) without user intervention can address the shortcomings of the manual TGC (Pye, Wild, and McDicken 1992). To date, several designs of ATGC are proposed in the literature (Pye, Wild, and McDicken 1992; Lee, Kim, and Ra 2006; Tang, Luo, and Liu 2009). However, the majority of these algorithms rely on the presence of sufficiently large homogeneous soft tissues with an uniform distribution of attenuation (Klesenski 1996; Lee, Kim, and Ra 2006; Tang, Luo, and Liu 2009). In other words, the dependency of the attenuation for several different tissues is ignored in these algorithms. These methods fail to compensate the overall gain when large fluid collections such as the urine bladder or gallbladder exist that change the uniform distribution of the attenuation drastically. Large anechoic segments, surrounded by soft tissue, present a large variation in attenuation.

This paper extends the adaptive ATGC algorithm developed by Hemmsen et al. (Hemmsen, Hansen, et al. 2012), and propose an automated hierarchical TGC (AHTGC) algorithm with focus on images with large anechoic regions. The algorithm is based on a physical understanding of the underlying tissue based on the scattering strength, signal-to-noise ratio, focusing gain, and tissue attenuation. From these, different constituents of the tissue can be determined. For this purpose, the decay of the power spectrum frequency components of the received signal with respect to depth is considered to estimate the attenuation and to adapt the ATGC to the large attenuation variations. The remainder of this paper is organized as follows. Section G.2 introduces the proposed algorithm. Section 3 presents the *in-vivo* results of the proposed AHTGC algorithm and discusses

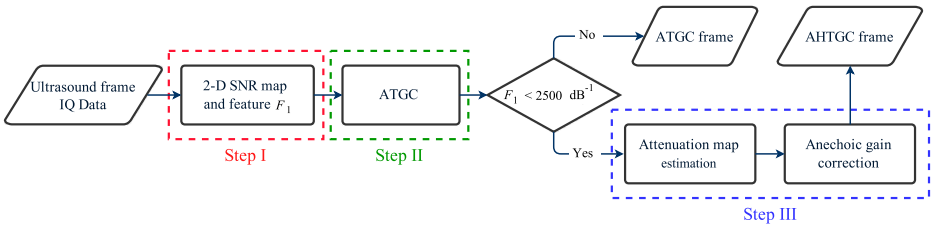

Step I: A 2-D SNR map for each frame is computed and the slope at 80th percentile of its cumulative histogram (i.e. feature F_1) is determined.
Step II: A TGC curve is automatically determined for each frame and used to compensate the gains in that frame. the input to this step is the envelope of RF-data. The output of this step is called ATGC frame.
Step III: A normalized 2-D attenuation map is generated for scans with large fluid collections, and used to correct the gains inside the fluid regions. The input to this step is the RF-data, and the output of this step is called AHTGC frame.

Figure C.1: Block diagram of the AHTGC algorithm.

the findings. Finally section 4 is the conclusion and the perspectives.

C.2 Materials and methods

It is common practice to assume that the attenuation has a linear relation with the frequency of the acoustic wave (Kuc 1984). In this paper, the spectral difference method adapted from Kuc (Kuc 1984) is used to generate 2-D attenuation maps. These maps are then used to correct the mis-adjusted gains by the ATGC algorithm inside the anechoic regions.

The proposed algorithm contains three distinct steps. First, a 2-D signal-to-noise ratio (SNR) map for each frame is computed. Based on the SNR map it was decided if the frame contained large anechoic regions or not. Then, a TGC curve is computed using the algorithm of Hemmsen et al. (Hemmsen, Hansen, et al. 2012). This TGC curve is applied to the original ultrasound frame. A 2-D attenuation map is then generated from the original image and is used to correct the adjusted gains inside the anechoic regions after applying the TGC curve. This correction is done only on the scans including large fluid regions. The block diagram of the proposed AHTGC is shown in the Fig. F.1. Three main steps of the algorithm are shown on the diagram and discussed in detail in this section.

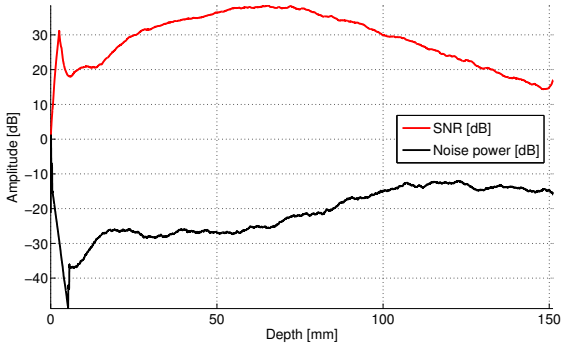

Figure C.2: SNR and noise contribution belonging to the center line of scan of a tissue mimicking phantom with an attenuation of $0.5\ \mathrm{dB/cm} \times \mathrm{MHz}$.

C.2.1 Step I. SNR map computation

Complex IQ data is used to compute the signal to noise ratio (SNR) for all the frames. The acquired frame from the transducer, is contaminated with noise and can be written as

$$\mathbf{Y}_i = \mathbf{S}_i + \mathbf{E}_i \tag{C.1}$$

where matrix $\mathbf{S}_i$ is the desired frame signal, $\mathbf{E}_i$ is the noise contribution, and i is the frame number. The measurement is performed on a tissue mimicking phantom with an attenuation of $0.5\ \mathrm{dB/cm} \times \mathrm{MHz}$ and N frames acquired, the mean acquired signal is given by

$$\mathbf{M} = \hat{\mathbf{Y}} = E\left\{\mathbf{Y}_i\right\} = E\left\{\mathbf{S}_i + \mathbf{E}_i\right\} = \frac{1}{N}\sum_{i=1}^{N}(\mathbf{S}_i + \mathbf{E}_i) \tag{C.2}$$

in which matrix $\mathbf{M}$ represents the mean of acquired frames. Also given the assumption that $E\left\{\mathbf{E}_i\right\} = 0$, the mean acquired signal by averaging all the frames will be equivalent to the mean desired signal and can be written as

$$\mathbf{M} = \hat{\mathbf{Y}} = \hat{\mathbf{S}} \tag{C.3}$$

The noise contribution for each frame is estimated by subtracting the mean of the all frames from a single frame

$$\mathbf{E}_i = \mathbf{Y}_i - \hat{\mathbf{Y}} \tag{C.4}$$

Therefore, The noise power for the ultrasound device is expressed as follows:

$$\mathbf{P}_{noise} = \left| \frac{1}{N} \sum_{i=1}^{N} \mathbf{E}_i^2 \right| \tag{C.5}$$

Finally, the SNR map for an acquired *in-vivo* frame is determined by dividing the signal power of that frame by the system noise power computed from (C.5)

$$\mathbf{P}_{signal}(i) = |\mathbf{Y}_i|^2 \tag{C.6}$$

$$\mathbf{SNR}_{dB}(i) = 10 \log_{10} \left(\frac{\mathbf{P}_{signal}(i)}{\mathbf{P}_{noise}} \right) \tag{C.7}$$

where $\mathbf{Y}_i$ in (C.6) is the signal acquired from frame number i in a sequence of *in-vivo* scans. The power of signal changes from frame to frame, while the noise power is unchanged. The variation of noise and SNR with depth for a scan of tissue mimicking phantom along its center line is depicted in Fig. C.2. Also two examples of the 2-D SNR maps computed from scans of the human bladder and liver are shown in Figs. 2.5(a) and 2.5(c) respectively. The essential first step in the proposed time gain compensation algorithm was to determine whether the scans included large fluid collections or not. As it is anticipated, fluid collections appear as very low SNR regions in the SNR maps. A feature is specifically designed to characterise this property in SNR maps. First, cumulative histogram of the values inside the SNR map is computed. Then, a curve is fitted to the counts and the slope of the fitted curve at 25th and 80th percentiles of the curve was used to characterise the amount of fluid in the scans.

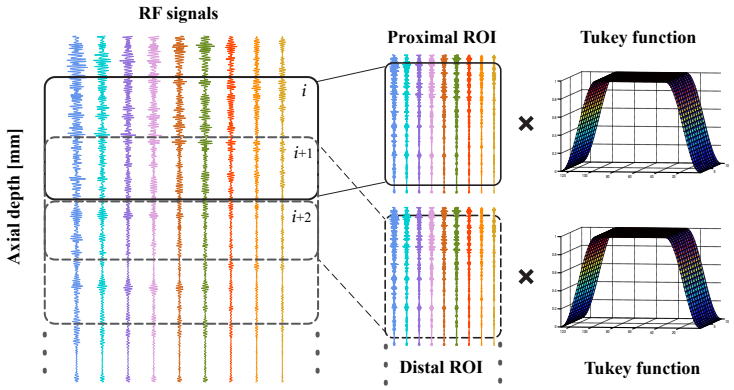

Figure C.3: Illustration of how RF data is subdivided into sets of different proximal and distal windows.

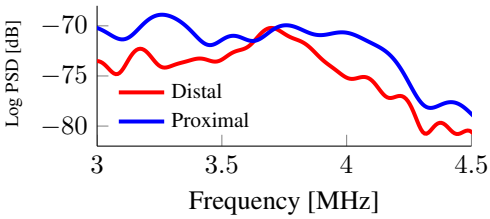

(a) Example Log PSD of a paired proximal and distal segments, where the $f_0 = 3.75$ MHz.

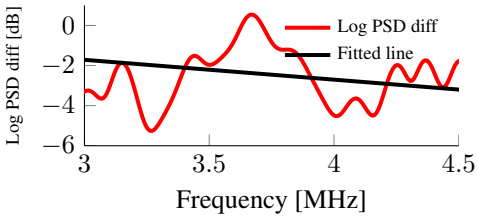

(b) Log PSD difference, and fitted line with slope $= -0.502$ dB/cm $\times$ MHz.

Figure C.4: Illustration of how the attenuation value for a pair of proximal and distal segments is computed.

The idea behind using these two features was to benefit from changes in distribution of SNR values in SNR maps to distinguish between different scans. Number of counts of low SNR values in scans with large fluid collections is higher compared to that of scans with small or no fluid collections. This yielded a bigger slope of cumulative histogram at low SNR values (i.e. 25th percentile) for scans with large anechoic regions compare to that of scans with no anechoic regions. The same effect decreased the slope of cumulative histogram at high SNR values (i.e. 80th percentile) for scans with large anechoic regions compared to that of scans with no anechoic regions. The rate of decrease in the slope at 80th percentile is much bigger than the increase in the slope at 25 percentile. Therefore, it was decided to use the slope at 80th percentile (F_1) to distinguish between the two different scans with large fluid collections and small or no fluid collections. The value of F_1 was determined empirically using 4 scans additional to the 44 scans used for evaluation of the AHTGC algorithm. $F_1 < 2500$ dB^{-1} characterised a scan with large

fluid collection, otherwise, the scan was considered to contain small or no collections of fluid.

Figures 2.5(b) and 2.5(d) illustrate how this feature is calculated for two scans of the human bladder and liver. These two figures show the cumulative histogram of the SNR images over 100 bins. 100 bins are used to ensure that high variation of SNR values in each map is captured in the histogram and also precision of the density estimation is not jeopardized. In the next step of the algorithm, each scan is dynamically compensated for the attenuated gain using a TGC curve.

C.2.2 Step II. TGC compensation by ATGC

Gains were corrected for all depths for each frame to obtain homogeneous images. The automatic TGC correction in this section simulated the TGC adjustments performed by a physician, eliminating the possible mistakes due to user intervention (Hemmsen, Hansen, et al. 2012). The algorithm used envelope of RF-data as input. The correction was performed by calculating a mask to filter out strong and weak specular regions inside the envelope data. The mask was then applied to each envelope detected data and the median value of all scan-lines for all depths in the recorded frame was found. The resulting curve was normalized to a maximum of one, inverted and used to normalize all scan-lines in that frame. The compensation is finally performed by dividing the values in every column by the TGC curve. Next step of the proposed hierarchical algorithm is to compute 2-D attenuation maps for those scans including large fluid collections. This is done by using a spectral difference method described in the next section.

C.2.3 Step III. Attenuation map estimation and gain correction

An attenuation map is calculated for those scans characterised to have large fluid regions in step I. This map is used to correct the over-gained regions inside the fluid collections after they compensated with a the TGC curve in step II.

Beamformed RF data was used to compute the attenuation maps. Each RF line was partitioned into several overlapping segments, in which each RF segment was gated axially by a Tukey window to alleviate the spectral leakage at both boundaries. Each two overlapping segments in the RF line were paired together, where the upper segment was considered as proximal and the underlying segment was considered as distal segment. For each pair the difference between the logarithm of power spectra computed, a line fitted to the power spectral difference, and the slope of the resulting line considered as an attenuation value for the proximal segment (see Fig. C.4). Both proximal and distal segments were moved down on the RF line and several attenuation values were calculated along the RF line by pairing the proximal and distal segments. Blocks were overlapped by

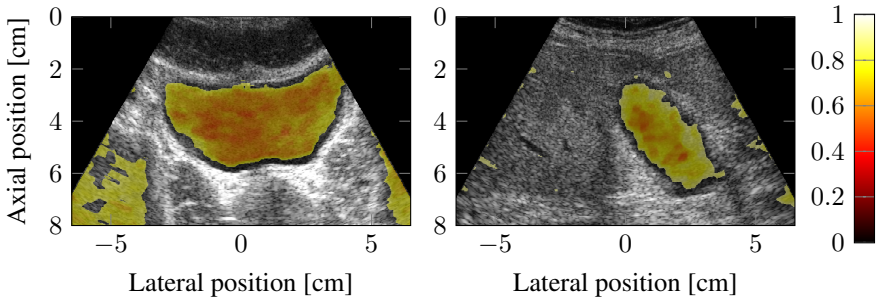

(a) Normalized attenuation map of a human bladder.

(b) Normalized attenuation map of a scan of human gallbladder.

Figure C.5: Examples of normalized attenuation maps overlaying on B-mode images

50% to increase axial resolution of the attenuation maps. Figure C.3 shows how the RF data is subdivided into pairs of proximal and distal windows and overlapped to increase the axial and lateral resolutions. The resulted attenuation values for RF lines are laterally averaged over scan lines to reduce the high variability of the attenuation values in the map.

Figure C.5 shows examples of computed and normalized attenuation maps overlaying on B-mode images. The length of the RF segments and the number of averaging scan lines determine the axial and lateral resolution of the estimated attenuation maps respectively. Literature suggests the axial RF segment lengths to be between 1 to 2 cm (Klimonda, Litniewski, and Nowicki 2009). It also suggests that the number of the averaging lines should be between 8 to 25 RF lines. In this study, anechoic regions adjacent to soft tissues presented large attenuation variation. To capture this variation, the length of axial segments was set to 1 cm, and the number of averaging RF lines was set to 10 lines. The generated attenuation maps were then normalized and multiplied to the compensated images by ATGC (Hemmsen, Hansen, et al. 2012), to correct the gains inside the anechoic regions.

C.3 Results and discussion

The proposed AHTGC algorithm was applied to *in-vivo* abdominal scans. Fifteen subjects were scanned and a total of 44 abdominal sequences each containing 15 frames were

acquired. In addition to the urine bladder and gallbladder scans that have large anechoic regions, other anatomical locations such as the liver and kidney were also included in the dataset. This was done to evaluate the performance of the algorithm on images with less-variable attenuation distribution. The beamformed RF data were acquired using a 2202 ProFocus ultrasound scanner (BK Medical, Denmark) connected to a 192-element 3.5 MHz convex array transducer (8820e, BK Medical). The dynamic received focus technique with factory preset TGC was employed to generate the sequences. A research interface connected to the scanner simultaneously recorded the real-time beamformed RF data from the scanner (Hemmsen, Nikolov, et al. 2012).

The proposed AHTGC algorithm was applied to the acquired image sequences off-line in Matlab(2013b). Figure C.6 shows an example of the experimental results of the AHTGC algorithm applied to a axial scan of the human bladder. The figure illustrates how the gains were first compensated by ATGC, and then corrected using a 2-D attenuation profile. Figure C.6(a) shows the original image in which gains were only adjusted by the factory preset TGC with no default gains. Figure C.6(b) shows the calculated TGC curve using the ATGC method discussed in the Section C.2.2. Figure C.6(c) shows the the compensated image using the ATGC. Whilst the resulting image is more homogeneous, the area inside the bladder is highly over-gained. The normalized 2-D attenuation profile (see Fig. C.6(d)) computed using the method introduced in Section C.2.3 was then multiplied with the ATGC compensated image to correct the mis-adjusted high gains inside the bladder. The result is shown in the Fig. C.6(e). It can be observed that inside of the bladder is not over-gained and the uniformity of the result is comparable to the ATGC corrected image shown in Fig. C.6(c).

A double blinded study was conducted to evaluate the performance of the AHTGC algorithm. Matching pairs of *in-vivo* sequences, unprocessed and processed with AHTGC, were evaluated side by side by two experienced radiologists. Each pair was shown twice by randomizing the left and right positioning. This yielded a total of 176 independent visual evaluations. The radiologists were then asked to score the image quality of each pair on a visual analogue scale (VAS) ranging between -50 and +50. This is performed by dragging a slider towards their favored movie sequence, where a positive scale favors the processed sequence with the AHTGC algorithm. The distribution of ratings from the individual doctors are shown in Fig. C.7. Wilcoxon signed-rank test was applied to assess whether radiologists preferred the processed sequences or the unprocessed data. The computed average VAS score is positive (p-value: 2.34×10^{-13}) and estimated to be 1.01 (95% CI: 0.85; 1.16) favoring the compensated data with the AHTGC algorithm. Although the average VAS scores is not significantly positive, doctors consistently chose the processed images with AHTGC to be better than the unprocessed images.

A secondary evaluation was conducted to assess the discrimination power of the

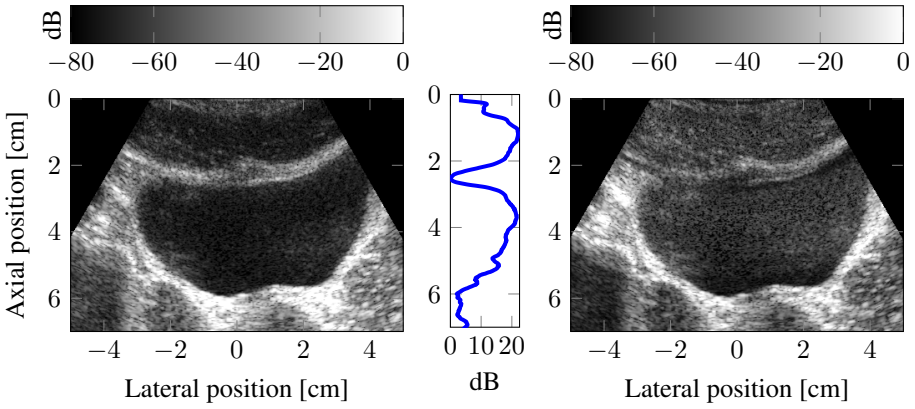

(a) Un-processed axial scan of human bladder.

(b) TGC

(c) ATGC compensated Image *(a)* with curve *(b)*.

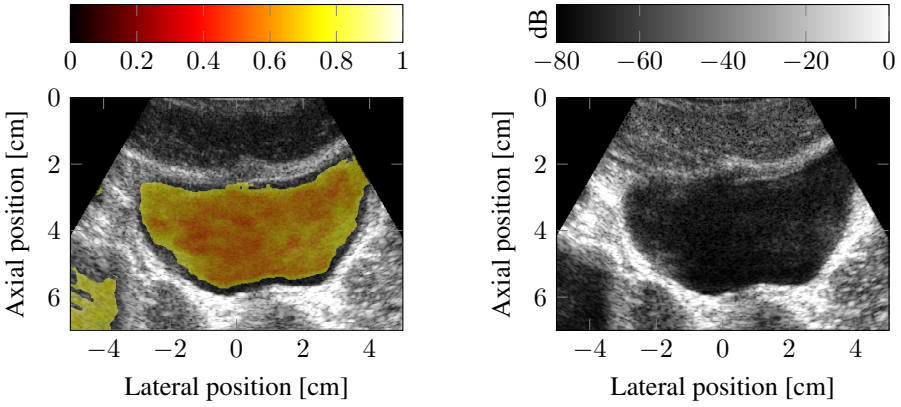

(d) Normalized attenuation map computed from image *(a)*.

(e) AHTGC corrected image *(c)* with 2-D map *(d)*.

Figure C.6: Illustration of how the proposed AHTGC algorithm is applied to a axial scan of the human bladder. (a) Un-processesed scan. (b) TGC curve computed by the ATGC method in section C.2.2. (c) ATGC compensated image *(a)* with curve *(b)*. (d) 2-D attenuation map computed from image *(a)*. (e) Attenuation corrected image *(c)* with map *(d)*.

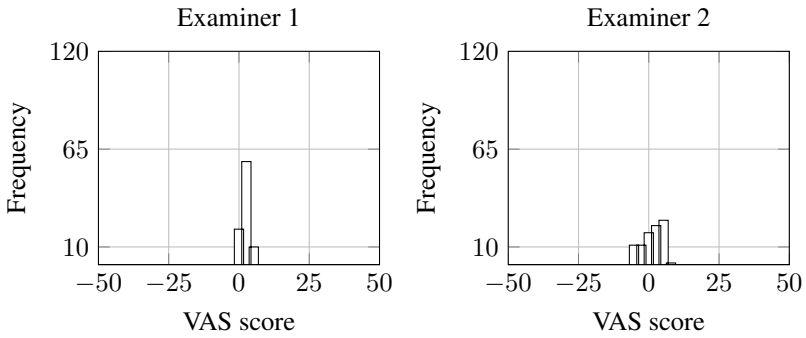

Figure C.7: Distribution of pooled answers from assessment of overall image quality by two expert radiologists. Positive values favor AHTGC algorithm.

feature F_1 to differentiate between two types of the scans. 44 scans used in this study were visually divided into two categories, 11 scans including large fluid collections (type 1) and 33 scans with small or no collections of fluid (type 2). Feature F_1 was computed for all scans and boxplots illustrating the distribution of F_1 for two types of scans were generated and shown in Fig. 2.5(e). No overlap between interquartile interval of the two boxplots indicated that feature F_1 was able to discriminate between two types of scans.

C.4 Conclusion

This paper presented a hierarchical ATGC (AHTGC) algorithm, where estimates of SNR and attenuation profiles used to correct the gains after applying the ATGC. The new algorithm presents a robust and more flexible control over gain especially inside the large anechoic regions. In addition, the proposed method adjusts the gains automatically, which increases the clinical throughput by avoiding unnecessary user manual adjustments of TGC on the scanner. Furthermore, the 2-D attenuation profiles provide solid foundation for other processes like segmentation of the tissues and structures.

ACKNOWLEDGMENTS

This work was financially supported by grant 82-2012-4 from the Danish Advanced Technology Foundation and from BK Medical ApS, Herlev, Denmark.

References from Paper C

Kuc, R. (1984). "Estimating acoustic attenuation from reflected ultrasound signals: Comparison of spectral-shift and spectral-difference approaches". In: *IEEE Trans. Acous., Speech, Sig. Pro.* 32.1, pp. 1–6 (cit. on p. 151).

Pye, S., S. Wild, and W. McDicken (1992). "Adaptive time gain compensation for ultrasonic imaging". In: *Ultrasound Med. Biol.* 18.2, pp. 205–212 (cit. on p. 150).

Klesenski, K. (1996). "Automatic gain compensation in an ultrasound imaging system". In: *US Patent*, pp. 5, 579, 768. URL: http://www.google.com/patents/US5579768 (cit. on p. 150).

Lee, D., Y. Kim, and J. Ra (2006). "Automatic time gain compensation and dynamic range control in ultrasound imaging systems". In: *Proc. SPIE Med. Imag.* 6147, pages (cit. on p. 150).

Klimonda, Z., J. Litniewski, and A. Nowicki (2009). "Spatial Resolution of Attenuation Imaging". In: *Archives of Acoustics* 34.4, pp. 461–470 (cit. on p. 156).

Tang, M., F. Luo, and D. Liu (2009). "Automatic Time Gain Compensation in Ultrasound Imaging System". In: *Proc. IEEE Int. Conf. Bioinfo. Biomed. Eng.* Pp. 1–4. DOI: 10.1109/ICBBE.2009.5162432 (cit. on p. 150).

Hemmsen, M. C., S. I. Nikolov, M. M. Pedersen, M. J. Pihl, M. S. Enevoldsen, J. M. Hansen, and J. A. Jensen (2012). "Implementation of a versatile research data acquisition system using a commercially available medical ultrasound scanner". In: *IEEE Trans. Ultrason., Ferroelec., Freq. Contr.* 59.7, pp. 1487–1499 (cit. on p. 157).

Hemmsen, M. C., P. M. Hansen, T. Lange, J. M. Hansen, K. L. Hansen, M. B. Nielsen, and J. A. Jensen (2012). "In Vivo Evaluation of Synthetic Aperture Sequential Beamforming". In: *Ultrasound Med. Biol.* 38.4, pp. 708–716. DOI: http://dx.doi.org/10.1016/j.ultrasmedbio.2011.12.017. URL: http://www.sciencedirect.com/science/article/pii/S0301562911015729 (cit. on pp. 150, 151, 155, 156).

PAPER D

Advanced Automated Gain Adjustments for *In-Vivo* Ultrasound Imaging

Authors: Ramin Moshavegh[a], Martin Christian Hemmsen[a], Bo Martins[c], Kristoffer Lindskov Hansen[b], Caroline Ewertsen[b], Andreas Hjelm Brandt[b], Thor Bechsgaard[b], Michael Bachmann Nielsen[b] and Jørgen Arendt Jensen[a].

Manuscript published: *Proceedings of IEEE Ultrasonic Symposium*, (2015).

Abstract

Automatic gain adjustments are necessary on the state-of-the-art ultrasound scanners to obtain optimal scan quality while reducing the unnecessary user interactions with the scanner. However, when large anechoic regions exist in the scan plane, the sudden and drastic variation of attenuations in the scanned media complicates the gain compensation. This paper presents an advanced and automated gain adjustment method that precisely compensate for the gains on scans and dynamically adapts to the drastic attenuation variations between different media. The proposed algorithm makes use of several ultrasonic physical estimates such as scattering strength, focus gain, acoustic attenuation, and noise level to gain a more quantitative understanding of the scanned media and to provide an intuitive adjustment of gains on the scan. The proposed algorithm was applied to a set of 45 *in-vivo* movie sequences each containing 50 frames. The scans are acquired by a recently commercialized BK3000 ultrasound scanner (BK Ultrasound, Denmark). Matching pairs of *in-vivo* sequences,

[a]Center for Fast Ultrasound Imaging, Department of Electrical Engineering, Technical University of Denmark, 2800 Kgs. Lyngby, Denmark

[b]Department of Radiology, Rigshospitalet, Copenhagen University Hospital, Copenhagen, Denmark

[c]BK Ultrasound ApS, Herlev, Denmark

unprocessed and processed with the proposed method were visualized side by side and evaluated by 4 radiologists for image quality. Wilcoxon signed-rank test was then applied to the ratings provided by radiologists. The average VAS score was highly positive 12.16 (p-value: 2.09×10^{-23}) favoring the gain-adjusted scans with the proposed algorithm.

D.1 Introduction

In ultrasound imaging the scanned media strongly attenuate the RF signals and therefore, they span a wide dynamic range when they are received by the transducer. Time gain compensation (TGC) is usually used to compensate for the acoustic attenuation before received echoes are visualised on the scanner. TGC offsets the attenuation of the RF signals along the depth, so those echoes belonging to the deep structures are more amplified compared to the echoes from superficial structures. The result is a more uniform image to be displayed on the scanner (Lee, Kim, and Ra 2006). A simple curve is usually used in the current scanners for the TGC. The user manually adjusts the shape of this curve using sliders corresponding to different depths. However, the image quality is highly dependent on the adjustments, and they are rarely used by the users. An automatic adjustment of the gains (ATGC) without user intervention obviates the shortcomings of the manual TGC (Pye, Wild, and McDicken 1992). However, few designs are proposed in the literature (Pye, Wild, and McDicken 1992; Lee, Kim, and Ra 2006; Tang, Luo, and Liu 2009). Despite their advantage of reducing the interaction, such methods have an inherent draw-back. These methods consider that large and homogeneous media exist while scanning, and as a consequence, the dependency of the acoustic attenuation in the presence of different tissues and structures is not highlighted. Therefore, they fail to adjust the TGC and overall gain when large fluid collections such as urine bladder or gallbladder exist (Lee, Kim, and Ra 2006; Tang, Luo, and Liu 2009; Litniewski, Klimonda, and Nowicki 2012). To address the issue, a solution that integrates several measures based on a physical understanding of the scanned media must be implemented.

The objective of this paper is to propose an advanced automated gain adjustment algorithm based on the scattering strength, signal-to-noise ratio, focusing gain, and the acoustic attenuation. From these parameters, different structures in the scanned media are determined automatically, and gains are precisely adjusted in the scanned media. The remainder of this paper is organized as follows. Section 2 introduces the proposed algorithm. Section 3 presents the measurement setups of the proposed algorithm and discusses the findings. Finally Section 4 gives the discussion and conclusion.

D.2 Advanced Automated Gain Adjustments

The Advanced Automated Gain Adjustment (ADGA) contains five distinct steps. The steps are discussed accordingly in the following sections.

D.2.1 Insonified-region detection

The purpose of the first step was to determine the insonified-region on the ultrasound scans. Long dark shadows sometimes appear on one or both sides of ultrasound scans, when transducer is not perfectly attached to the surface during the normal scan session. Therefore, detection of insonified region and removing the dark shadows from the gain adjustment process is necessary. For this purpose, the envelope of the RF data was computed. A binary mask, only including the intensity values lying within lower 10% dynamic range of the envelope data was generated . B-lines longer than 90% of the total scan depth were kept on that binary mask and the shorter B-lines were excluded. Objects that were not attached to one of the right or left borders were also excluded from the mask. This made sure that only elongated and very dark regions on one side or both sides of the scan remained. Those regions were considered as areas that were not insonified and were excluded from the gain adjustments.

D.2.2 Energy equalization

The main purpose of the second step was to make sure that the energy is equally distributed throughout the scanned media and its evenly highlighted. An experiment was conducted in which a tissue mimicking speckle phantom was scanned, and 50 frames were acquired. The mean of all 50 frames computed yielded a mean frame. The lateral median of the 50 scan lines bracketing the center line on the mean frame was computed yielded an energy curve as a function of depth. This is shown in Fig. D.1(a). The curve was then inverted, normalized to a maximum of one, and used to scale the energy levels of all the lines in the image (Fig. D.1(b)).

D.2.3 2-D SNR map computation

2-D signal to noise ratio (SNR) maps of the acquired frames were computed from the complex IQ data with the method previously introduced by authors (Moshavegh et al. 2015). The noise power of the ultrasound device is first computed. Then, the SNR map for an acquired *in-vivo* ultrasound frame is computed by dividing the signal power of the frame by the noise power of the system. An example of the 2-D SNR map computed from scan of the human liver is shown in Fig. D.2(a). Fluid collections depict very low SNR values in the SNR maps. Two features are then used to characterize this property. First,

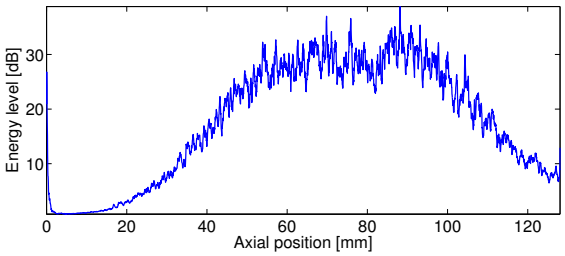

(a) Median of the energy levels of 50 scan lines.

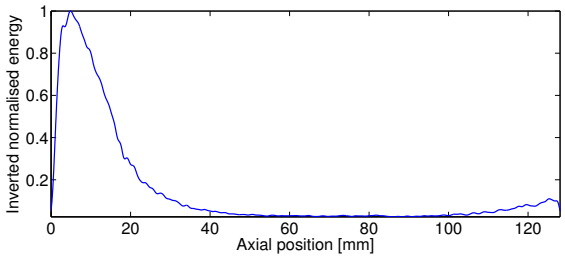

(b) Inverted and normalized energy curve in *(a)*.

Figure D.1: Energy equalization step.

the cumulative frequency histogram of all SNR values inside the SNR map is generated. A curve is fitted to the histogram values. The amount of fluid in the scan was then characterized by slopes of the curve at 25th and 80th percentiles (Fig. D.2(b)).

D.2.4 Dynamic TGC

A TGC curve is dynamically computed for each frame and used to compensate the signal levels. For this purpose, the envelope of the acquired scan is first computed. A cumulative histogram of the intensity values is then generated. The intensity values less than half of the maximum intensities in the envelope are disregarded, and a mask of strong signal regions is generated. The mask is applied to the envelope, and the lateral median of the intensities lying inside the mask is computed. The computed curve presents drastic fluctuations and can not be used directly to analyse the axial intensity changes in the envelope. To address this, the curve is smoothed using a Sovitsky-Golay filter. Then

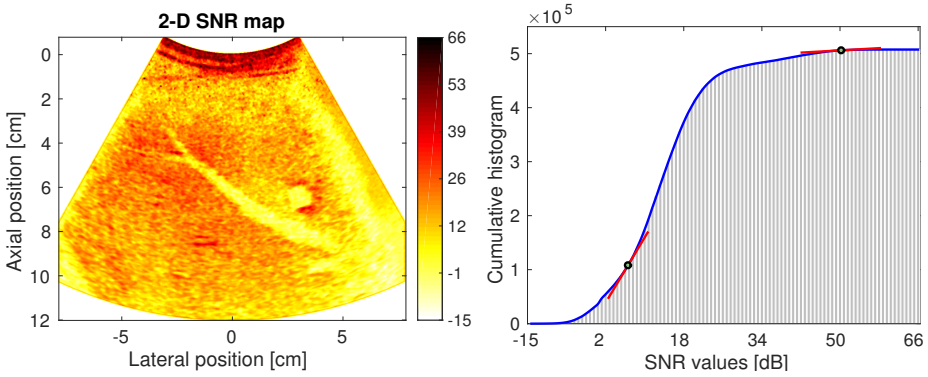

(a) 2-D SNR map computed for a scan of human liver.

(b) Slope of the histogram at 25th (feature f_1)and the 80th (feature f_2) percentiles.

Figure D.2: 2-D SNR maps for a scan of human liver and the slope of histogram at 25th (feature f_1)and the 80th (feature f_2) percentiles.

the general trend of the curve is extracted by applying the singular-spectrum analysis (SSA). SSA does not require model of time series, and extracts the trend of time series in the presence of noise and oscillations (Golyandina, Nekrutkin, and Zhigljavsky 2001). The final curve depicts the trend of intensity change within the envelope and no sudden fluctuations (Fig. D.3(b)). The curve is finally normalized to it's maximum, inverted, and applied as a TGC to the envelope to compensate for the gradual changes in the intensities. The dynamic adjustment of intensities using this curve might over-gain inside the fluid regions. Therefore, the next step computes an attenuation map that can be used to correct the possible miss-adjusted gains inside the fluid regions after applying the TGC curve.

D.2.5 2-D attenuation map

2-D attenuation maps of the acquired scans were determined by a spectral difference method adapted from Kuc (Kuc 1984). The attenuation maps were computed from the beamformed RF data. RF lines were segmented to overlapping blocks. For each two overlapping blocks, slope of a line fitted to the power spectral difference of the two blocks was computed (Fig. D.4). That slope was considered as the attenuation value for the top block. The overlapping blocks were moved on the RF data, several attenuation coefficients were then calculated, and finally a 2-D attenuation map was determined. The method is

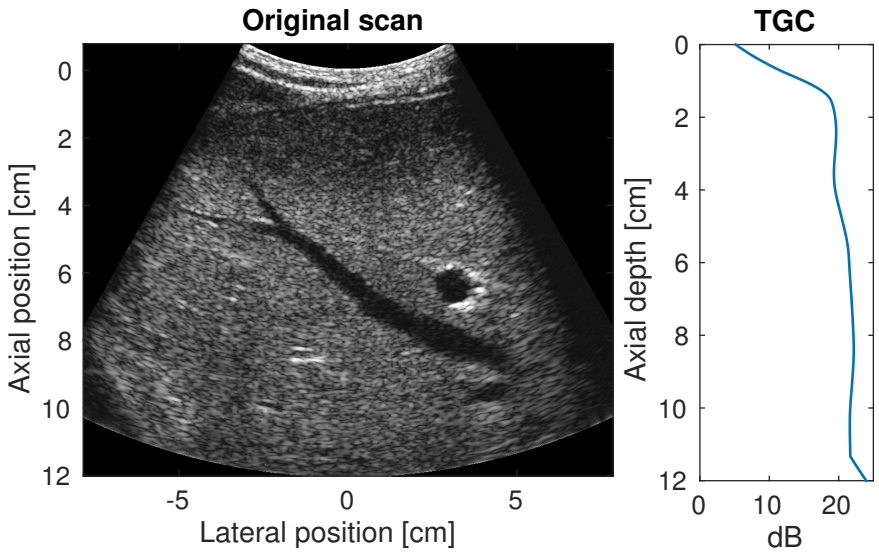

(a) Scan for which the TGC curve is computed.

(b) TGC curve computed for *(a)*.

Figure D.3: Illustration of a TGC curve dynamically computed for a frame of human liver scan.

discussed in (Moshavegh et al. 2015). The attenuation map was normalized to a maximum of one and multiplied to the gain-adjusted frame by the dynamic TGC in Section D.2.4. This was performed to correct the gains inside the fluid collections.

D.3 Measurement setup

The proposed ADGA algorithm was applied to 45 *in-vivo* ultrasound sequences. Nine subjects were scanned, and a total of 45 sequences, each containing 50 frames were acquired. A collection of different anatomical locations such as urine bladder, gallbladder, kidney, liver, and carotid artery was acquired and included in the dataset. This was done to evaluate the performance of the ADGA on the scans including large fluid collections and those horboring less-variable attenuation distribution.

The beamformed RF data were acquired using a recently commercialized BK3000 scanner (BK Ultrasound, Denmark) connected to a 192-element 3.5 MHz convex array

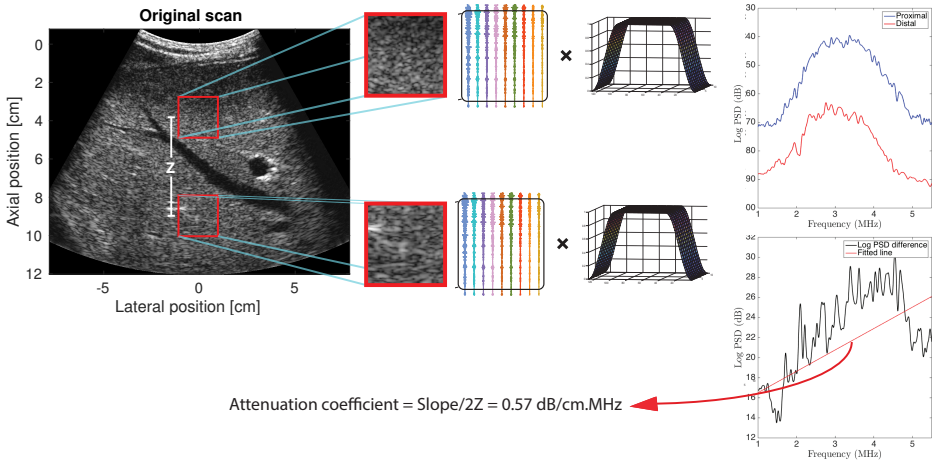

Figure D.4: Illustration of how attenuation coefficients are computed.

transducer (9040, BK Ultrasound). The acquired sequences were generated by the dynamic receive focusing technique with factory preset TGC. The beamformed RF data were simultaneously recorded by a research interface on the scanner, and processed with the proposed algorithm off-line. Fig. D.5 shows an *in-vivo* result of the algorithm applied to scans of a human gallbladder and inferior vena cava.

To empirically evaluate the performance of the algorithm, matching Pairs of *in-vivo* sequences, unprocessed and processed with the proposed algorithm, were evaluated side by side by four experienced radiologists. The evaluation was double blinded, and each pair was shown twice by randomizing the left and right positioning. This resulted in a total of 360 independent visual evaluations. During the evaluation, each radiologist was asked to rate the image quality of the pairs on a visual analogue scale (VAS) ranging between -50 and +50. The rating was performed by moving a slider towards their favored movie sequence. A positive scale favored the gain-adjusted sequence with the proposed algorithm. Wilcoxon signed-rank hypothesis test was applied to the provided ratings by the radiologists to check whether radiologists preferred the sequence with or without the proposed algorithm. Visualization and assessment were handled using the program IQap(Hemmsen et al. 2010).

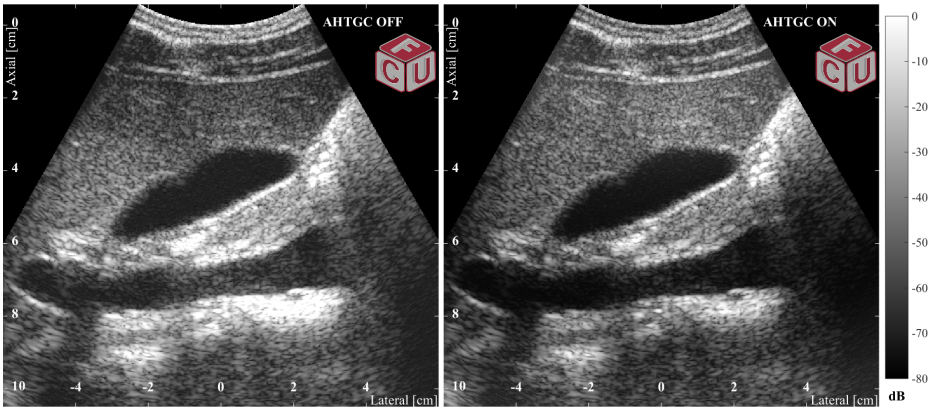

Figure D.5: Sagittal view of a human gallbladder and inferior vena cava.

D.4 Discussion and Conclusion

The average VAS score computed from the provided ratings was highly positive (p-value: 2.09×10^{-23}) and estimated to be 12.16 favoring the gain-adjusted data with the proposed algorithm. This paper presented an advanced automated gain adjustment algorithm that utilises the estimates of attenuation, SNR , and focus gain to adjust the gains on the ultrasound scans. The proposed method is automatic, robust, and demonstrates reliable gain adjustments especially inside the large fluid collections. Also, the automatic adjustment of gains on the scans significantly reduces the unnecessary and manual gain adjustments on the ultrasound scanner. This highly increases the performance of the clinical staff during the scan session.

Acknowledgment

This work was financially supported by grant 82-2012-4 from the Danish Advanced Technology Foundation and from BK Medical ApS, Herlev, Denmark.

References from Paper D

Kuc, R. (1984). “Estimating acoustic attenuation from reflected ultrasound signals: Comparison of spectral-shift and spectral-difference approaches”. In: *IEEE Trans. Acous., Speech, Sig. Pro.* 32.1, pp. 1–6 (cit. on p. 165).

Pye, S., S. Wild, and W. McDicken (1992). “Adaptive time gain compensation for ultrasonic imaging”. In: *Ultrasound Med. Biol.* 18.2, pp. 205–212 (cit. on p. 162).

Golyandina, N., V. Nekrutkin, and A. A. Zhigljavsky (2001). *Analysis of time series structure: SSA and related techniques*. CRC press (cit. on p. 165).

Lee, D., Y. Kim, and J. Ra (2006). “Automatic time gain compensation and dynamic range control in ultrasound imaging systems”. In: *Proc. SPIE Med. Imag.* 6147, pages (cit. on p. 162).

Tang, M., F. Luo, and D. Liu (2009). “Automatic Time Gain Compensation in Ultrasound Imaging System”. In: *Proc. IEEE Int. Conf. Bioinfo. Biomed. Eng.* Pp. 1–4. DOI: 10.1109/ICBBE.2009.5162432 (cit. on p. 162).

Hemmsen, M. C., M. M. Petersen, S. I. Nikolov, M. B., Nielsen, and J. A. Jensen (2010). “Ultrasound image quality assessment: A framework for evaluation of clinical image quality”. In: *Proc. SPIE Med. Imag.* Vol. 76291. Medical Imaging 2010: Ultrasonic Imaging, Tomography, and Therapy, pp. 76290C–12 (cit. on p. 167).

Litniewski, J., Z. Klimonda, and A. Nowicki (2012). “Parametric sonographic imaging-application of synthetic aperture technique to imaging attenuation of ultrasound in tissue structures”. In: *Hydroacoustics* 15, pp. 99–110 (cit. on p. 162).

Moshavegh, R., M. Hemmsen, B. Martins, A. Brandt, K. Hansen, M. Nielsen, and J. Jensen (2015). “Automated hierarchical time gain compensation for in-vivo ultrasound imaging”. In: *Proc. SPIE* 9419, pages (cit. on pp. 163, 166).

PAPER E

Optimization of Synthetic Aperture Image Quality

Authors: Ramin Moshavegh[a], Jonas Jensen[a], Carlos A. Villagomez-Hoyos[a], Matthias B. Stuart[a], Martin Christian Hemmsen[a], and Jørgen Arendt Jensen[a].

Manuscript published: *Proceedings of SPIE Medical Imaging*, (2016).

Abstract

Synthetic Aperture (SA) imaging produces high-quality images and velocity estimates of both slow and fast flow at high frame rates. However, grating lobe artifacts can appear both in transmission and reception. These affect the image quality and the frame rate. Therefore optimization of parameters effecting the image quality of SA is of great importance, and this paper proposes an advanced procedure for optimizing the parameters essential for acquiring an optimal image quality, while generating high resolution SA images. Optimization of the image quality is mainly performed based on measures such as F-number, number of emissions and the aperture size. They are considered to be the most contributing acquisition factors in the quality of the high resolution images in SA. Therefore, the performance of image quality is quantified in terms of full-width at half maximum (FWHM) and the cystic resolution (CTR). The results of the study showed that SA imaging with only 32 emissions and maximum sweep angle of 22 degrees yields a very good image quality compared with using 256 emissions and the full aperture size. Therefore the number of emissions and the maximum sweep angle in the SA can be optimized to reach a reasonably

[a]Center for Fast Ultrasound Imaging, Department of Electrical Engineering, Technical University of Denmark, 2800 Kgs. Lyngby, Denmark

"F"urther author information: Send correspondence to Ramin Moshavegh E-mail: ramosh@elektro.dtu.dk

good performance, and to increase the frame rate by lowering the required number of emissions. All the measurements are performed using the experimental SARUS scanner connected to a λ/2-pitch transducer. A wire phantom and a tissue mimicking phantom containing anechoic cysts are scanned using the optimized parameters for the transducer. Measurements coincide with simulations.

Keywords: Synthetic aperture, FWHM, cystic resolution, grating lobes, Multi objective optimization, Pareto optimal, ultrasound imaging

E.1 Introduction

Synthetic aperture imaging (SA) addresses the problems with low frame rate in conventional ultrasound imaging, where one line at a time is beamformed for generating the final ultrasound image. In SA emissions with large areas of sonification can be used and a complete resolution image can be beamformed for each emission. By combining all the low resolution images the final high resolution image is generated (Jensen, S. Nikolov, et al. 2006).

Number of emissions and aperture size are two parameters strongly effecting the quality of the high resolution images in SA imaging. Different scenarios also require different values of these parameters. For the case of B-mode SA imaging, the number of emissions can be kept quite high, whereas when flow estimates are needed, less emissions and consequently high frame rates are interesting (O'Donnell and Thomas 1992; Karaman, Li, and O'Donnell 1995; Karaman and O'Donnell 1998; S. I. Nikolov, Gammelmark, and Jensen 1999).

This paper presents a pilot study of image quality optimization for SA based on the performance measures of full-width at half maximum (FWHM) and the cystic resolution (CTR). All the possible imaging setups for different number of emissions and aperture sizes are considered for a λ/2-pitch linear transducer. Six point scatterers located underneath the transducer are simulated using the Field II program (Jensen and Svendsen 1992; Jensen 1996, 2014). For each possible combination of number of emissions N and the aperture size α_{max}, the CTR and FWHM are computed for all scatterers and the values recorded. Third, two independent plots featuring the CTR and FWHM as a function of α_{max} and N are generated. The information of the two plots are then merged and scatter-plotted as all possible setups. A Pareto optimization procedure (Deb 2005; Coello, Lamont, and Veldhuizen 2007) is then applied to the scatterer plot to identify the optimal setups in terms of having low CTR and also relatively small FWHM. The remainder of this paper is organized as follows. Section G.2 introduces the proposed algorithm. Section

TABLE E.1: PARAMETERS USED FOR SIMULATION.

Parameters	λ/2-pitch transducer
Number of elements	192
Transducer center frequency f_0	4.1 MHz
Wavelength λ	0.376 mm
Element pitch	0.2 mm (0.56λ)
Element height	6 mm
Elevation focus	38 mm
Cycles in emitted pulse	1
Transmit apodization	Hamming
Receive apodization	Hamming
Receive F-number	1
Emission steering angles	-30°:0.25°:+30°

3 presents the results of the proposed method and discusses the findings. Finally section 4 is the conclusion and the perspectives.

E.2 Materials and methods

This section first presents the quality metrics used in the study for optimization of SA image quality, and then details the optimization procedure.

E.2.1 Imaging performance measures

Two of the main quality metrics used in the literature for evaluating the performance of the ultrasound imaging quality are cystic resolution (CTR) and full-width in half maximum (FWHM). This paper uses these two features and all the optimizations are performed based on the rate of the changes in these features while moving between setups by changing the sweep angle (corresponding to the aperture size) α_{max} and the number of emissions N.

The CTR measures the contrast resolution and determines the ability of the imaging system to differentiate between an anechoic region bracketed within a uniform scattering medium. Ranganathan and Walker (Ranganathan and Walker 2007) quantified CTR as the ratio between the energy outside of a circular area surrounding the point spread function

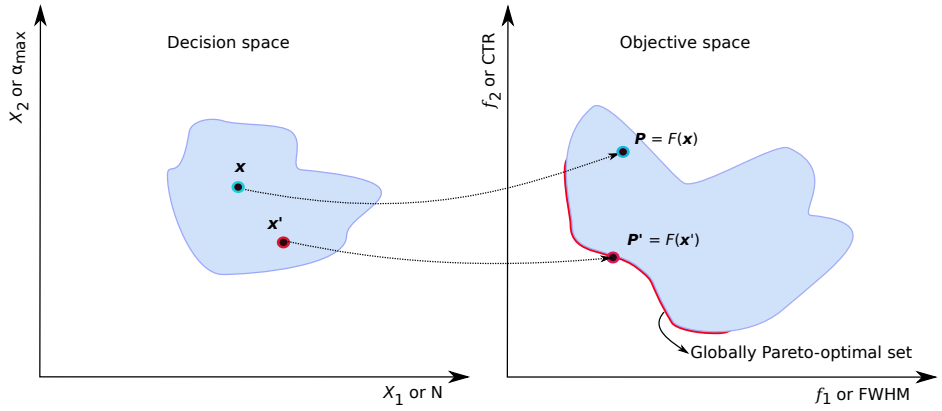

Figure E.1: Illustration of how the Pareto optimization is performed.The decision space contains independent variables whereas the objective space contains the dependent variables. The set of all Pareto optimal solutions or Pareto front is shown with the red curve.

(PSF) with radius of R to the total energy of the PSF. Therefore it gives a measure of clutter energy outside the main lobe of the PSF.

The FWHM on the other hand measures the detail resolution. It is a measure of the width of the main lobe of the PSF. The FWHM is usually measured both axially and laterally and those are both influenced by the bandwidth of the imaging system. The lateral FWHM is also dependent on the pulse wavelength, size of the aperture (F number), and the maximum steering angle of the emissions.

E.2.2 Method of optimization

This section describes the method of multi-objective optimization used in this study for optimizing the SA image quality based on the theory of Pareto optimality (Deb 2005). In many circumstances, solutions in the presence of the conflicting objectives are needed. In such cases, solutions are chosen such that sensible trade-offs exist among different objectives. Pareto optimization is used for finding these solutions. In this multi-objective optimality theory, many solutions are found that satisfy the Pareto optimality

criterion (Coello, Lamont, and Veldhuizen 2007). This criterion considers a solution to be optimum only if there are no other solutions better than that with respect to all the objectives. A solution $\mathbf{x}' = \{x_1, x_2\}$ is a Pareto optimal solution if there exists no other solutions like $\mathbf{x}$ for which $\mathbf{P}$ dominates $\mathbf{P}'$. Notice, F is the objective function. A point $\mathbf{P}$ is dominating another point $\mathbf{P}'$ (mathematically given by $\mathbf{P} \preceq \mathbf{P}'$), when $\mathbf{P}$ is no worse than $\mathbf{P}'$ in all objectives, and $\mathbf{P}$ is strictly better than $\mathbf{P}'$ in at least one objective. Therefore a pareto optimal solution is given by

$$\mathcal{P}^* := \left\{ \mathbf{x}' \mid \nexists\, \mathbf{x} :\ \mathbf{P} \preceq \mathbf{P}' \right\}. \tag{E.1}$$

The set of all optimal solutions is called Pareto front or curve or surface (see red curve in Fig. E.1). The shape of the Pareto front manifests the nature of trade-off between different objectives. In this study the pareto optimization is applied to a two-objective problem, in which two conflicting parameters are required to be optimized. The Pareto front is particularly interesting because it contains the solutions where improvement in one variable is not possible without jeopardizing the other. Hence, in this study only the Pareto optimal solutions are considered while optimizing the SA image quality. Section E.2.4 describes how the Pareto optimization is applied in the study.

E.2.3 Simulations

A λ/2-pitch transducer pitch transducer was modelled and six different point scatterers were simulated axially located underneath the transducer and positioned 10 mm apart from each other. Simulations were performed using the Field II program (Jensen and Svendsen 1992; Jensen 1996, 2014) (see Table E.1 for details of the parameters used). A Hamming apodization on the active transmit aperture was used to reduce the edge waves. In SA emissions were set to steer from -30° to +30° with 0.25° separation between emissions. Received signals from all elements were stored for each emission and beamformation were performed using the BFT3 toolbox (Hansen, Hemmsen, and Jensen 2011). The beamformed low-resolution images were subsequently combined to high-resolution images. Several high-resolution images were generated by varying maximum beam steered angle (α_{max}) and the number of emissions (N). The image quality of the high-resolution images were then evaluated by computing both CTR and the lateral FWHM for simulated point scatterers. For each simulated scatterer two plots were generated. First one quantifying the CTR as a function of α_{max} and N, and the second quantifying the FWHM as a function of α_{max} and N. These images are used in the Section E.2.4 to construct the objective space plots to optimize the two dependent variables of maximum beam steered angle (α_{max}) and the number of emissions (N)

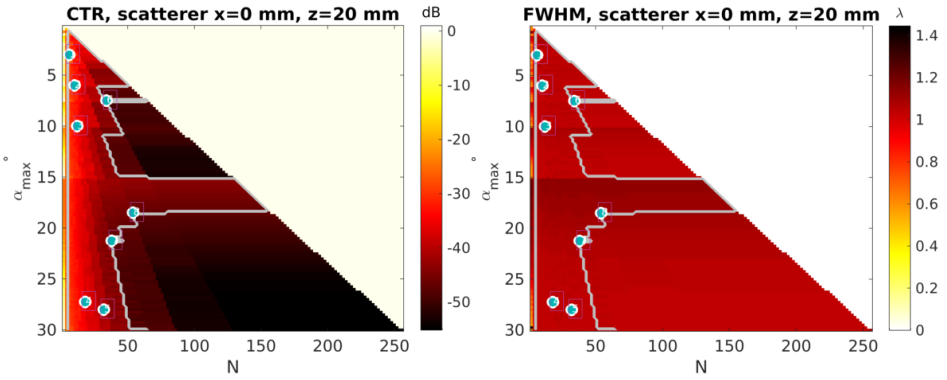

(a) CTR computed as a function of α_{max} and N for scatterer at 20 mm.

(b) FWHM as a function of α_{max} and N for scatterer at 20 mm.

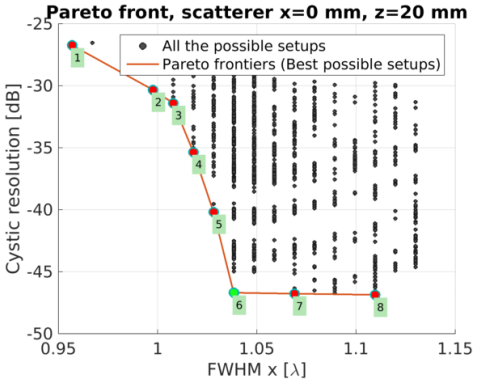

(c) Pareto made by merging the CTR and FWHM for scatterer at 20 mm.

Figure E.2: Optimization procedure demonstrated for the scatterer at 20 mm from the surface of the transducer.

E.2.4 Optimization of the setup

This section discusses the optimization performed to find the optimal setup for the SA image quality in terms of α_{max} and N. The information regarding the CTR and FWHM in two plots generated for each scatterer in Section E.2.3 were merged and and a Pareto plot (scatterer plot of all possible setups) was generated for each scatterer. On the Pareto plot, the Pareto front or all the optimal setups in terms of CTR and FWHM were computed, whereby any improvement with respect to CTR comes at the expense of FWHM and vice-versa. The Pareto front in a sense characterise the setups in which the FWHM and CTR values are optimal. The optimal Pareto setups (Pareto fronts) for all scatterers were then combined in one plot and the center of the gravity for all the optimal setups was considered to be the optimal setup for the SA imaging.

E.2.5 Phantom measurements

Phantom measurements were made using the SARUS experimental ultrasound scanner(Jensen, Holten-Lund, et al. 2013) driving a 192-element 4.1 MHz λ/2-pitch linear transducer (8L2, BK Ultrasound). A synthetic aperture B-mode imaging sequence using the virtual sources behind transducer was used to perform the imaging. Parameters used in the imaging sequence are depicted in the Table E.1. First, A geometry wire phantom including three wires was scanned. A multi purpose, multi-yissue phantom containing three anechoic cysts located at 17 mm, 48 mm, and 75 mm (Model 040GSE, CIRS inc., Virgina, USA) with acoustic attenuation of 0.5 dB/(cm.MHz) was also scanned.

E.3 Results and discussion

The results of CTR, FWHM and Pareto optimizations for one of the scatterers located 20 mm underneath the transducer is shown in the Fig. E.2. Fig. E.3 also shows all the optimal setups corresponding to the Pareto fronts of all 6 different scatterers combined in one plot. The yellow diamond ($\alpha_{max} = 22°$ and $N = 32$) is the center of the gravity of all points and the optimal setup for the SA. This optimal setup requires 32 emissions and 22° maximum sweeping angle. The other observation was made in the Fig. E.4, in which a point scatterer at 20 mm was simulated and the high resolution images of the scatterer were reconstructed using three different number of emissions. The PSFs for high-resolution images made of 32 and 256 emissions are quite identical. The same observation was also made on the measured wire phantom using varying number of emissions. Fig. E.5 shows the measured PSFs belonging to two point scatterers located at 32.5 mm and 57.5 mm. Each PSF was reconstructed with 4, 32 and 256 emissions, where the 32 emissions is the optimized sequence. The point PSFs reconstructed with 32

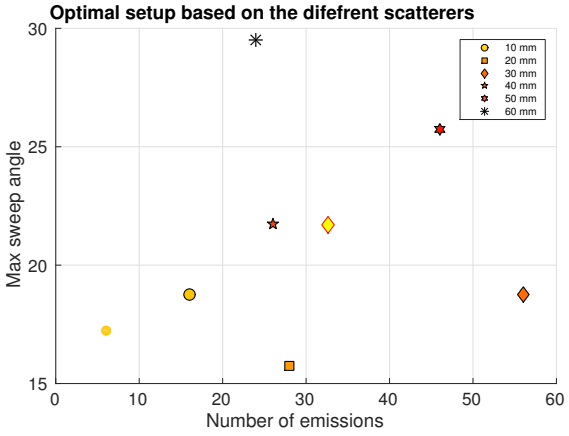

Figure E.3: Combination of all the optimal setups (Pareto fronts) belonging to all scatterers in one plot.

emissions are quite similar to the one reconstructed with 256 emissions. Fig. E.6 shows two phantoms measured with $N = 4$, the optimized sequence ($\alpha_{max} = 22°$ and $N = 32$), and also $N = 256$. This set of measurements also indicated that the quality of the image does not improve by increasing the emissions to more than 32. A set of this indicates that for achieving a reasonably good image quality the number of emissions does not have to be increased to more than the optimal value computed for the SA.

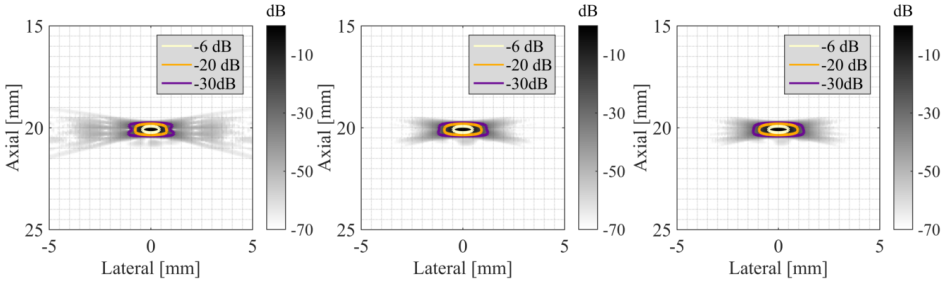

(a) Reconstructed from 4 emissions. (b) Reconstructed from 32 emissions. (c) Reconstructed from 256 emissions.

Figure E.4: Comparison of the high-resolution image of the scatterer at 20mm reconstructed from low, optimal and high number of emissions.

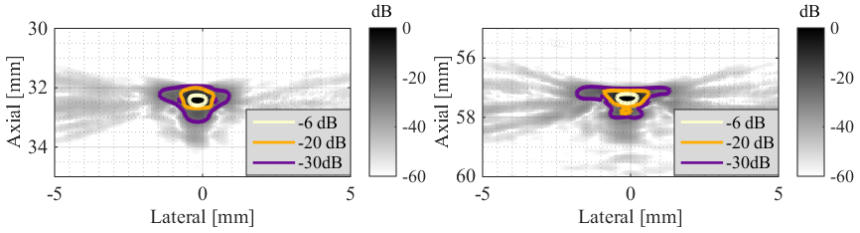

(a) Reconstructed from 4 emissions.

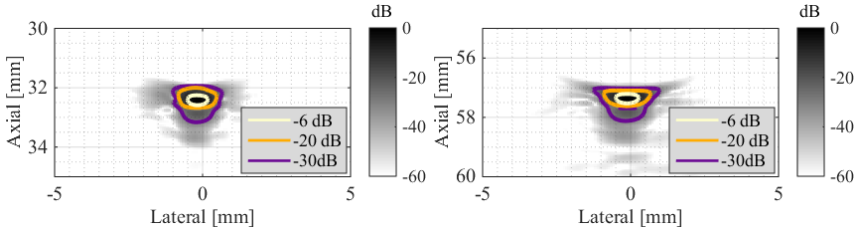

(b) Reconstructed from 32 emissions.

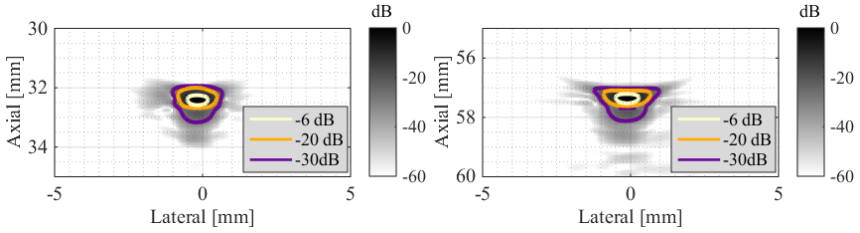

(c) Reconstructed from 256 emissions.

Figure E.5: Comparison of the high-resolution image of the scatterer at 20mm reconstructed from low, optimal and high number of emissions.

E.4 Conclusion

This paper presented a hierarchical method for characterising the optimal setup in SA imaging. The results showed that with only $\alpha_{max} = 22°$ and $N = 32$, the image quality is reasonably good and comparable with high number of emissions. Improvements in frame rate is also achievable by using less number of emissions. This can more highlighted when high frame rate is needed for velocity estimation, and when the standard deviation of the velocity estimates are related to the frame rate. The optimized sequence also enables fast acuisition of SA images without degrading the quality. This is rather crucial when the real-time automatic segmentation of vessels are performed.

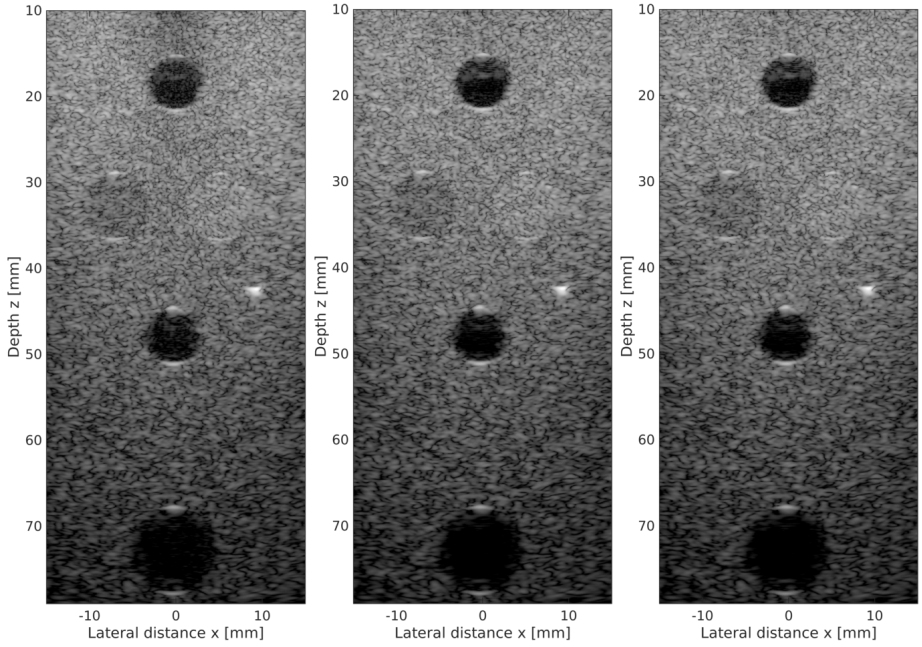

(a) Reconstructed from 8 emissions.

(b) Reconstructed from 32 emissions.

(c) Reconstructed from 256 emissions.

Figure E.6: Measured cyst phantom and reconstructed from low, optimal and high number of emissions. All three images are shown in 60 dB dynamic range.

References from Paper E

Jensen, J. A. and N. B. Svendsen (1992). "Calculation of Pressure Fields from Arbitrarily Shaped, Apodized, and Excited Ultrasound Transducers". In: *IEEE Trans. Ultrason., Ferroelec., Freq. Contr.* 39, pp. 262–267 (cit. on pp. 172, 175).

O'Donnell, M. and L. J. Thomas (1992). "Efficient synthetic aperture imaging from a circular aperture with possible application to catheter-based imaging". In: *IEEE Trans. Ultrason., Ferroelec., Freq. Contr.* 39, pp. 366–380 (cit. on p. 172).

Karaman, M., P. C. Li, and M. O'Donnell (1995). "Synthetic aperture imaging for small scale systems". In: *IEEE Trans. Ultrason., Ferroelec., Freq. Contr.* 42, pp. 429–442 (cit. on p. 172).

Jensen, J. A. (1996). "Field: A Program for Simulating Ultrasound Systems". In: *Med. Biol. Eng. Comp.* 10th Nordic-Baltic Conference on Biomedical Imaging, Vol. 4, Supplement 1, Part 1, pp. 351–353 (cit. on pp. 172, 175).

Karaman, M. and M. O'Donnell (1998). "Subaperture processing for ultrasonic imaging". In: *IEEE Trans. Ultrason., Ferroelec., Freq. Contr.* 45, pp. 126–135 (cit. on p. 172).

Nikolov, S. I., K. Gammelmark, and J. A. Jensen (1999). "Recursive ultrasound imaging". In: *Proc. IEEE Ultrason. Symp.* Vol. 2, pp. 1621–1625 (cit. on p. 172).

Deb, K. (2005). "Multi-objective optimization". In: *Search methodologies*. Springer (cit. on pp. 172, 174).

Jensen, J. A., S. Nikolov, K. L. Gammelmark, and M. H. Pedersen (2006). "Synthetic Aperture Ultrasound Imaging". In: *Ultrasonics* 44, e5–e15 (cit. on p. 172).

Coello, C. A. C., G. B. Lamont, and D. A. V. Veldhuizen (2007). "Basic Concepts". In: *Evolutionary Algorithms for Solving Multi-Objective Problems*. Springer (cit. on pp. 172, 175).

Ranganathan, K. and W. F. Walker (2007). "Cystic Resolution: A Performance Metric for Ultrasound Imaging Systems". In: *IEEE Trans. Ultrason., Ferroelec., Freq. Contr.* 54.4, pp. 782–792. DOI: 10.1109/TUFFC.2007.311 (cit. on p. 173).

Hansen, J. M., M. C. Hemmsen, and J. A. Jensen (2011). "An object-oriented multi-threaded software beamformation toolbox". In: *Proc. SPIE Med. Imag.* Vol. 7968, pages. DOI: 10.1117/12.878178 (cit. on p. 175).

Jensen, J. A., H. Holten-Lund, R. T. Nilsson, M. Hansen, U. D. Larsen, R. P. Domsten, B. G. Tomov, M. B. Stuart, S. I. Nikolov, M. J. Pihl, Y. Du, J. H. Rasmussen, and M. F. Rasmussen (2013). "SARUS: A Synthetic Aperture Real-time Ultrasound System". In: *IEEE Trans. Ultrason., Ferroelec., Freq. Contr.* 60.9, pp. 1838–1852 (cit. on p. 177).

Jensen, J. A. (2014). "A Multi-threaded Version of Field II". In: *Proc. IEEE Ultrason. Symp.* IEEE, pp. 2229–2232 (cit. on pp. 172, 175).

PAPER F

Novel Automatic Detection of Pleura and B-lines (Comet-Tail Artifacts) on *In-Vivo* Lung Ultrasound Scans

Authors: Ramin Moshavegh[a], Kristoffer Lindskov Hansen[b], Hasse Møller Sørensen[c], Martin Christian Hemmsen[a], Caroline Ewertsen[b], Michael Bachmann Nielsen[b] and Jørgen Arendt Jensen[a].

Manuscript published: *Proceedings of SPIE Medical Imaging*, (2016).

Abstract

This paper presents a novel automatic method for detection of B-lines (comet-tail artifacts) in lung ultrasound scans. B-lines are the most commonly used artifacts for analyzing the pulmonary edema. They appear as laser-like vertical beams, which arise from the pleural line and spread down without fading to the edge of the screen. An increase in their number is associated with presence of edema. All the scans used in this study were acquired using a BK3000 ultrasound scanner (BK Ultrasound, Denmark) driving a 192-element 5.5 MHz wide linear transducer (10L2W, BK

[a]Center for Fast Ultrasound Imaging, Department of Electrical Engineering, Technical University of Denmark, 2800 Kgs. Lyngby, Denmark

[b]Dept. of Radiology, Copenhagen University Hospital, DK-2100 Copenhagen, Denmark

[c]Dept. of Thoracic anestesiologic, Copenhagen University Hospital, DK-2100 Copenhagen, Denmark

"F"urther author information: Send correspondence to Ramin Moshavegh E-mail: ramosh@elektro.dtu.dk

Ultrasound). The dynamic received focus technique was employed to generate the sequences. Six subjects, among those three patients after major surgery and three normal subjects, were scanned once and Six ultrasound sequences each containing 50 frames were acquired. The proposed algorithm was applied to all 300 *in-vivo* lung ultrasound images. The pleural line is first segmented on each image and then the B-line artifacts spreading down from the pleural line are detected and overlayed on the image. The resulting 300 images showed that the mean lateral distance between B-lines detected on images acquired from patients decreased by 20% in compare with that of normal subjects. Therefore, the method can be used as the basis of a method of automatically and qualitatively characterizing the distribution of B-lines.

Keywords: B-lines, comet-tail artifacts, segmentation, lung disease, pulmonary edema, ultrasound imaging

F.1 Introduction

In ultrasound an intimate mixture of air and water can characterize the lung. The change in their balance can be the sign of the pulmonary diseases. Interactions of water and air in lung ultrasound scans generate a variety of artifacts, and therefore, the lung ultrasound of pulmonary disease is rather based on analyzing these artifacts than pure visualization of the structures. B-lines are laser-like vertical artifacts, which start from the pleura and spread down to the edge of the screen. B-line detection is an essential parameter in the assessment of lung-edema in lung ultrasound imaging, which is often present in patients with heart and lung problems as well as patients after major surgery (Volpicelli et al. 2006; Gargani 2011; Lichtenstein 2014). B-line detection is also used in detection of pneumothorax as B-lines disappear, when a pneumothorax is present. The condition where air is found within the pleural cavity can result in collapsed lung, and if untreated be fatal. In daily clinical practice, patients suspected for lung edema or pneumothorax are imaged with X-ray, and often repeatedly imaged with short intervals to monitor the effect of the applied treatment. Lung ultrasound is an emerging ultrasound modality, but is often bypassed, as the medical staff handling these patients are not familiar with ultrasound. If ultrasound is used for evaluation of the lungs, the common practice for diagnosing pulmonary edema is based on visual analysis and interpretation of B-lines on still lung ultrasound images. For the detection of pneumothorax, the detection of a single B-line excludes pneumothorax in the imaged lung segment. Fig. F.1 illustrates how B-lines are generated. They are reverberation artifacts that originate from water-thickened pulmonary interlobular septa (Gargani 2011).

Based on the authors' knowledge, there are no computerized and automated model for characterizing the B-line artifacts in the literature. This paper proposes a novel algorithm

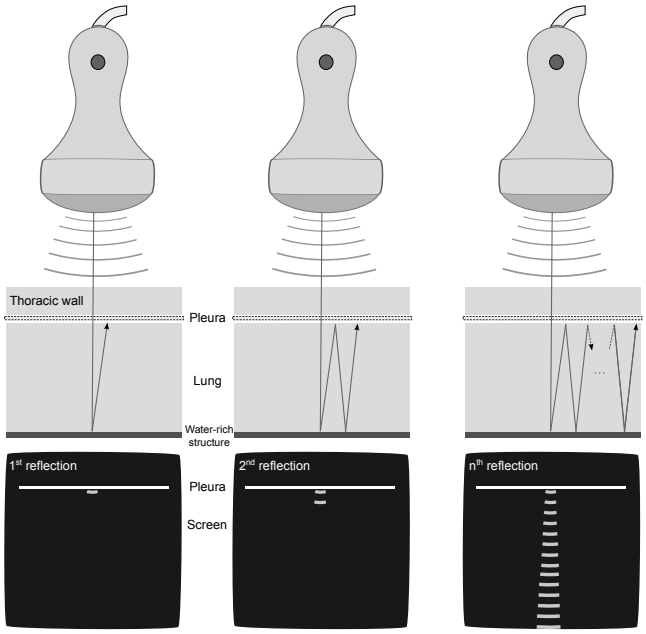

Figure F.1: Illustration of how the comet-tail artifacts are generated. They are hyperechoic reverberation artifacts arising from the pleural line and spreading down towards the lower edge of the screen.

as the first possible solution for monitoring of lung edema and detection of pneumothorax. The remainder of this paper is organized as follows. Section G.2 introduces the proposed algorithm. Section 3 presents the *in-vivo* results and discusses the findings. Finally section 4 is the conclusion and the perspectives.

F.2 Materials and methods

This paper introduces an automatic real-time method for detection of pleura and the B-lines in lung ultrasound scans. The method first delineates the pleural line on the image and then detects the B-lines, as they originate from the pleural line and extend to the edge of the display. The proposed algorithm contains four distinct steps. First, the pleural line is delineated using a random walks method (Grady 2006). Second, the upper-pleural region is excluded from the scan, the Hilbert transform of the remaining region is computed, a cumulative frequency histogram is generated, a zone of influence of strong signals in the

image is calculated, and the B-line artifacts are identified on the scan plane. Third, an alternate sequential filtering is applied to the results of step 2. Finally, the result of step 3 is top-hat filtered and the B-lines are extracted and overlaid on the B-mode scan. Four main steps of the algorithm are discussed in detail in this section.

F.2.1 Step I. Confidence map estimation and delineation of the pleural line

The first step in detection of the B-lines is to delineate the pleural line on the lung scans. For this purpose a graph based approach that computes a per-pixel uncertainty map based on the information depicted by ultrasound image is used (Karamalis et al. 2012). This rather specifically measures the uncertainty in attenuated and/or shadow regions. To identify the map for each ultrasound frame, a random walks framework by taking into account ultrasound specific constraints is used (Karamalis et al. 2012). The solution to the random walks equilibrium problem is global and takes the entire content of the RF data into account. The required starting points are automatically placed at the beginning of each scan-line to represent the transducer elements. Thus, a problem is formulated by computing the probability of a random walk starting from a pixel to reach the transducer elements. The domain specific knowledge for ultrasound is integrated with a simple modelling of the ultrasound image formation process. The ultrasound specific constraints obtained from physics of acquired RF data by the transducer must be integrated to ensure the accuracy of the confidence map. One of the fundamental properties of ultrasound is the attenuation of the signal by increasing depth. The Beer–Lambert Law is used to express the depth dependent attenuation, and the attenuated signal I could be given by $I = I_0 \exp(-\alpha d)$, where I_0 is the initial intensity, α the attenuation coefficient, and d the distance from the source. This property is included into the confidence map in a way that the further away a random walk starts from the transducer is, the more unlikely it will be able to reach one of the transducer elements. The computed confidence map is used to determine the upper-pleural region and exclude that from the Rf-data prior to detecting the B-lines (see Fig. F.2). The pleural line is delineated on the confidence map by thresholding the confidence map to be higher than the global threshold of the entire map. The region with values higher than the threshold is considered the upper pleura, and the rest is lower pleural region. In the next step the B-lines starting from the pleura and appearing inside the lower pleural region are detected.

In the next step of the algorithm, after delineating the pleural line in each scan, the B-lines are characterized from the Hilbert transform of the gradient of the RF-data.

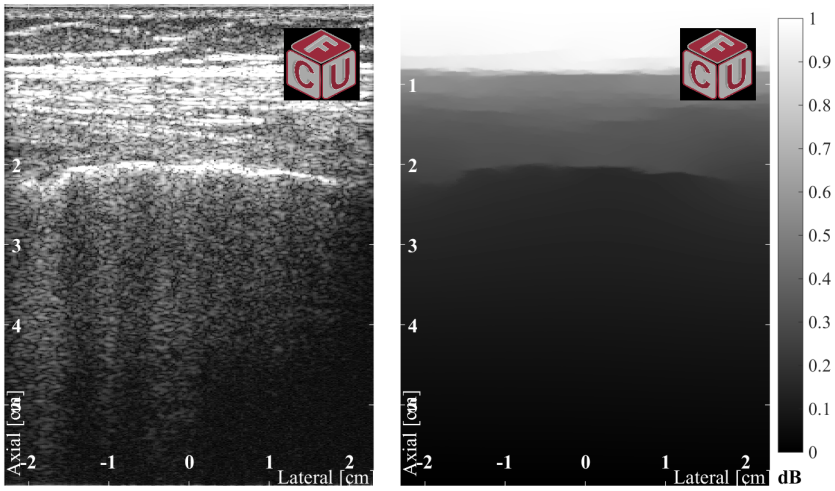

Figure F.2: Example of a confidence map computed for a human lung scan. This map is then thresholded to delineate the pleural line.

F.2.2 Step II. B-line detection

The RF-data corresponding to the region above the pleural line are excluded, and only the RF-data belonging to the lower pleural region is used for B-line detection. This is performed knowing that the artifacts arise from the pleural line and spreads down in the scan. The axial gradient of RF-data is then computed. The Hilbert transform of the axial gradient components is calculated, the absolute value of the complex data is computed and data is compressed by taking the logarithm transform. Finally, a binary mask including the strong specular regions inside the compressed envelope data is computed. This binary mask also outlines the most prominent B-lines in the envelope data (see Fig. F.3(a)). The mask is later manipulated in the sections F.2.3 and F.2.4 to extract the position of the B-lines.

F.2.3 Step III. Alternate sequential filtering

An alternate sequential filtering (ASF) procedure using a repeated sequential morphological opening and closing is applied to the mask and the ASF mask is generated (see Fig. F.3(b)). The procedure is depicted in the Alg. 5. The structuring element used in this process is considered to be an axial line-structuring element. The line structuring element along the ultrasound beem is used to ensure that only elongated and axial information (B-line artifacts) in the compressed data is preserved and highlighted.

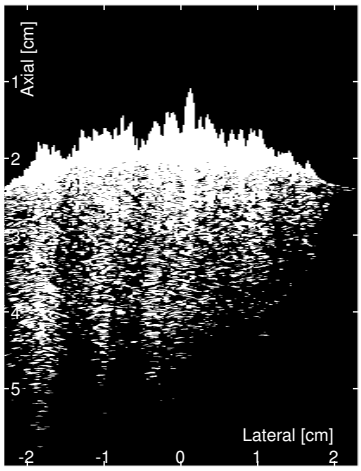

(a) Mask outlining the most prominent B-lines in the compressed data is then computed from the RF-data.

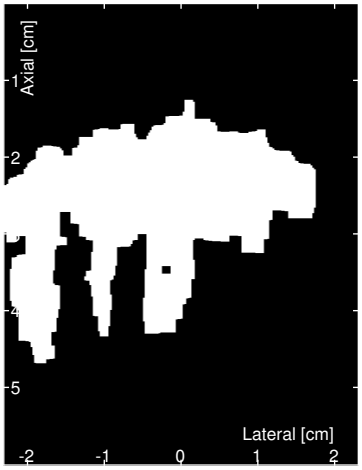

(b) Alternate sequential filtering applied to the mask *(a)*. B-lines are better identified.

Figure F.3: Illustration of how B-lines are detected from the RF-data.

Algorithm 5 Alternate sequential filtering

Input: Binary mask (B_{in}) outlining the most prominent edges computed in Section F.2.2, and parameter N indicating the maximum size of the structuring element to be used in ASF.

Output: Binary mask (B_{ASF}) in which the strong axial B-lines are highlighted.

procedure ASF
    $B_{ASF} = B_{in}$
    for each $i \in N$ **do**
        Let S_{lin} be a line structuring element of length N.
        $B_{ASF} = (B_{ASF} \ominus S_{lin}) \oplus S_{lin}$ # performing the morphological opening.
        $B_{ASF} = (B_{ASF} \oplus S_{lin}) \ominus S_{lin}$ # performing the morphological closing.
    end for
end procedure

Note: $\oplus$ and $\ominus$ denote morphological dilation and erosion respectively.

F.2.4 Step IV. Top-hat filtering

The generated mask in the previous step contains prominent axially elongated and adjacent tails locating the B-lines. However, the tails can be laterally connected and that makes the clean separation of them (B-lines) quite difficult. To separate and extract the B-lines automatically, a top-hat filtering procedure is used. The top-hat transform originally proposed by Mayer (Meyer 1977) is a mathematical morphology operator that uses morphological opening or closing for extracting bright (respectively dark) objects from an uneven background in a 2D grey-scale image. Top-hat transformation can be formulated in two ways: White Top-hat (WTH) and Black Top-hat (BTH). White Top-hat can also be used to identify prominent peaks in a 1D signal, and the BTH as the dual of the WTH can be used to identify the prominent minima in a 1D signal. In this paper a White Top-hat (WTH) with a flat disk structuring element is used to extract the very the B-lines. The WTH transformation of a 1D signal f with a flat structuring element B is defined as:

$$T_{white}(f) = f - (f \circ B) \tag{F.1}$$

First, A curve is generated by computing the axial summation of all pixel values inside mask from Section F.2.2. The peaks of the resulting curve are corresponding to the tails locating the B-lines in the mask (see Fig. F.4. To identify the peaks of the curve, the Top-hat transform is applied using a flat structuring element (B) that is somewhat larger than the size of the connected regions. The $\circ$ is the opening operator and is basically a min operation that removes the regions smaller than the size of structuring element. Subtracting this signal from the original signal produces a signal that only contains the desired strong peaks. Fig. F.4 shows the B-lines detected after alternate sequential filtering and top-hat filtering for a lung scan of a patient with lung edema. The B-lines are overlaid on the corresponding B-mode image in Fig. F.5(a).

F.3 Results and discussion

The proposed algorithm was applied to *in-vivo* lung scans. Three healthy subjects and three patients with different levels of lung edema were scanned after having major open-chest surgery. A total of 6 lung sequences each containing 50 frames were acquired. The study was approved by the Danish National Committee on Biomedical Research Ethics and the local Ethics Committee, and the volunteers were included into the study after informed consent. Anatomical locations included in the dataset have been analysed first to make sure B-lines exist. The beamformed RF data were acquired using a BK3000 ultrasound scanner (BK Medical, Denmark). A research interface connected to the scanner

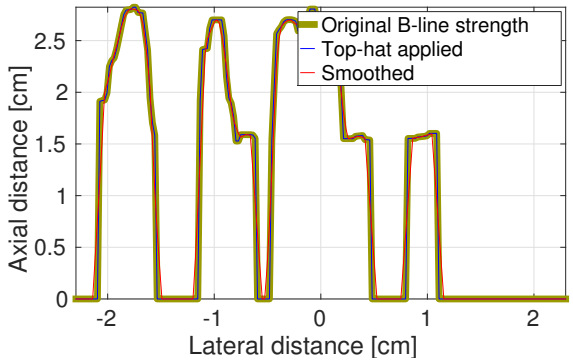

Figure F.4: Alternate sequential filtering and the result of the top-hat filtering.

simultaneously recorded the real-time beamformed RF data from the scanner (Hemmsen et al. 2012). The proposed B-line detection algorithm was applied to the acquired image sequences in MATLAB (2015b). Fig. F.5 shows two examples of the detected pleura and B-lines on lung scans of a patient and a normal subject, respectively. The mean lateral distance between neighbouring B-lines in the 150 images belonging to the patient is (0.93 cm) which is decreased by 20% in compared with that of 150 images belonging normal subjects (1.17 cm).

F.4 Conclusion

This paper presented a novel advanced B-line detection algorithm. The novely of the algorithm stems from proposing the first automatic real-time technique for characterization of the B-lines (comet tail artifacts) in lung ultrasound scans as a crucial measure for diagnosing pulmonary edema. The results showed a 20% decrease in the mean lateral distance between B-lines in patients with lung edema in compare with the normal subjects. Therefore, the proposed method enables the automatic quantitative estimation of edema and have a tremendous clinical impact. The algorithm can also be an aid for the sonographer and a tool for making a quantitative estimation of lung edema and detection of pneumothorax. Furthermore, the algorithm can be an aid for the untrained personnel performing the ultrasound scan, as well as providing a quantitative measure for B-lines presence.

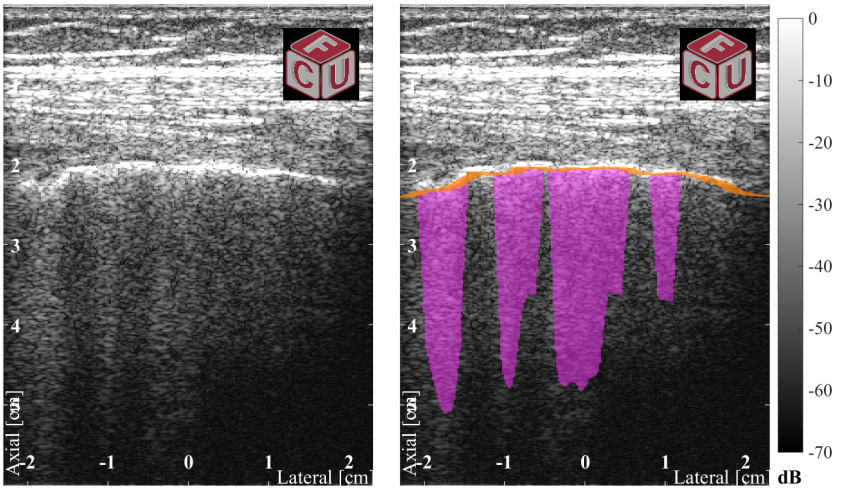

(a) The pleural line outlined and B-lines are overlaid on the lung scan of a patient after surgery.

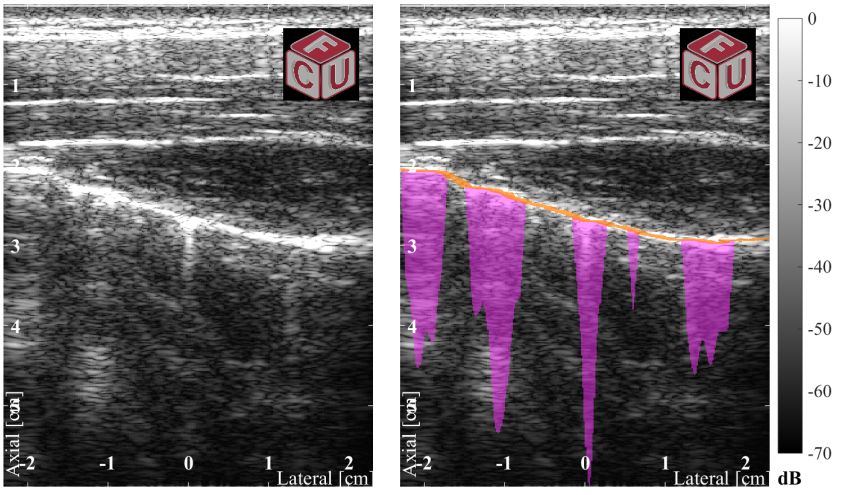

(b) The pleural line outlined and B-lines are overlaid on the lung scan of a normal subject.

Figure F.5: Two examples of ultrasound lung scans, on top of which the pleural lines are outlined and B-lines overlaid.

References from Paper F

Meyer, F. (1977). "Contrast features extraction, Special Issues of Practical Metallography". In: *Quant. Anal. Microstruct. Mat. Sc. Bio. Med.* Vol. 8 (cit. on p. 189).

Grady, L. (2006). "Random Walks for Image Segmentation". In: *IEEE. Trans Patt. Ana. Mach. Int.* 28.11, pp. 1768–1783 (cit. on p. 185).

Volpicelli, G., A. Mussa, G. Garofalo, L. Cardinale, G. Casoli, F. Perotto, C. Fava, and M. Frascisco (2006). "Bedside lung ultrasound in the assessment of alveolar-interstitial syndrome". In: *Am. J. Emerg. Med.* 24.6, pp. 689–696 (cit. on p. 184).

Gargani, L. (2011). "Lung ultrasound: A new tool for the cardiologist". In: *Cardiovascular ultrasound* 9.1 (cit. on p. 184).

Hemmsen, M. C., S. I. Nikolov, M. M. Pedersen, M. J. Pihl, M. S. Enevoldsen, J. M. Hansen, and J. A. Jensen (2012). "Implementation of a versatile research data acquisition system using a commercially available medical ultrasound scanner". In: *IEEE Trans. Ultrason., Ferroelec., Freq. Contr.* 59.7, pp. 1487–1499 (cit. on p. 190).

Karamalis, A., W. Wein, T. Klein, and N. Navab (2012). "Ultrasound confidence maps using random walks". In: *Med. Image Anal.* 16.6, pp. 1101–1112 (cit. on p. 186).

Lichtenstein, D. A. (2014). "Lung ultrasound in the critically ill". In: *Ann Intensive Care* 4.1 (cit. on p. 184).

PAPER G

Hybrid Segmentation of Vessels and Automated Flow Measures in *In-Vivo* Ultrasound Imaging

Authors: Ramin Moshavegh[a], Bo Martins[c], Kristoffer Lindskov Hansen[b], Thor Bechsgaard[b], Michael Bachmann Nielsen[b] and Jørgen Arendt Jensen[a].

Manuscript published: *Proceedings of IEEE Ultrasonic Symposium*, (2016).

Abstract

Vector Flow Imaging (VFI) has received an increasing attention in the scientific field of ultrasound, as it enables angle independent visualization of blood flow. VFI can be used in volume flow estimation, but a vessel segmentation is needed to make it fully automatic. A novel vessel segmentation procedure is crucial for wall-to-wall visualization, automation of adjustments, and quantification of flow in state-of-the-art ultrasound scanners. We propose and discuss a method for accurate vessel segmentation that fuses VFI data and B-mode for robustly detecting and delineating vessels. The proposed method implements automated VFI flow measures such as peak systolic velocity (PSV) and volume flow. An evaluation of the performance of the segmentation algorithm relative to expert manual segmentation of 60 frames randomly chosen from 6 ultrasound sequences (10 frame randomly chosen from each sequence) is also presented. Dice coefficient denoting the similarity between segmentations is used for the evaluation. The coefficient ranges between 0 and 1, where 1 indicates perfect agreement and 0 indicates no agreement. The Dice coefficient was 0.91

[a]Center for Fast Ultrasound Imaging, Department of Electrical Engineering, Technical University of Denmark, 2800 Kgs. Lyngby, Denmark

[b]Department of Radiology, Rigshospitalet, Copenhagen University Hospital, Copenhagen, Denmark

[c]BK Ultrasound ApS, Herlev, Denmark

indicating to a very agreement between automated and manual expert segmentations. The flowrig results also demonstrated that the PSVs measured from VFI had a mean relative error of 14.5% in comparison with the actual PSVs. The error for the PSVs measured from spectral Doppler was 29.5%, indicating that VFI is 15% more precise than spectral Doppler in PSV measurement.

G.1 Introduction

Accurate delineation of vessels is crucial for visualization and quantification of flow in state-of-the-art ultrasound scanners. Available segmentation procedures are mainly based on either B-mode images or flow estimates only. However, the main challenge in devising an accurate vessel segmentation procedure is to incorporate both B-mode image and flow data for better identifying the vessels. This paper presents a hybrid segmentation algorithm that fuses B-mode and vector velocity estimations (VFI) for robustly detecting and segmenting vessels in ultrasound images. VFI enables angle independent visualization of blood flow, and allows doctors to see and estimate the direction and velocity of blood flow in all directions and at any angle. This provides an angle independent visualization of blood hemodynamics for the cardiovascular system in real time (Pedersen et al. 2012). Today's commercial ultrasound scanners are not able to present a perfect wall-to-wall delineation of vessels, while displaying the VFI images. Of particular interest is the extraction of new features that can express several desired properties of a vessel (i.e. constriction in carotid artery) in a single feature such as peak systolic velocity (PSV) (Grant et al. 2003; Reutern et al. 2012) using VFI. The volume flow is also a very interesting measure when inspecting the VFI, which quantifies the flow and characterizes the vessel (Hansen, Heerwagen, et al. 2013; Hansen, Olesen, et al. 2014; Jensen, Olesen, Hansen, et al. 2014; Brandt et al. 2016). However, this measure is very susceptible to the vessel diameter, which makes the accurate delineation of the vessel very essential (Jensen, Olesen, Hansen, et al. 2014; Jensen, Olesen, Stuart, et al. 2016). The proposed method delineates the vessel walls and enables the correct estimation of the volume flow. In the current implementation of VFI in ultrasound scanners, the correct volume flow estimation is not possible. The reason is that the VFI does not perfectly attach to the vessel walls, and therefore the VFI data is not available for regions very close to the vessel walls. This paper proposes a novel hybrid vessel segmentation in ultrasound that also enables the automated flow quantification. The proposed method delineates the vessels in ultrasound scans and enables a better visualization of flow inside the vessel, as well as providing the firm ground for quantitative flow measures for VFI such as PSV and volume flow. These are done without manual adjustments by users and without compromising on the accuracy of VFI. The remainder of this paper is organized

as follows. Section G.2 introduces the algorithm. Section G.3 presents the measurement setup. Section G.4 presents the results and discusses the findings. Finally section G.5 is the conclusion.

G.2 Materials and methods

The method has two distinct steps. First, it automatically segments the vessel boundaries using a combination of VFI data and B-mode. Second, it automates the VFI flow measures such as PSV, and volume flow.

G.2.1 Novel hybrid segmentation of vessels

The segmentation has four distinct steps. First, a marker image is generated from both VFI data and B-mode. An example of a marker image computed for a carotid phantom scan with bifurcation is shown in Fig. G.1(f). Second, the marker image is used in a subsequent marker-controlled region growing procedure to delineate the vessel boundaries. The third step implements artifact rejection based on size, shape, and amount of flow to ensure that only vessels are retained. Fourth step implements an inter-frame co-registration of consequent segmented frames to make sure that vessels segmented in each frame are in correspondence with the same vessels segmented in the neighboring frames of the sequence.

G.2.1.1 Generating the marker image

Extraction of inner-markers: Detection of inner markers are achieved by skeletonization that extracts the center-line of the VFI data. The absolute value of VFI estimates were used in segmentation procedure. The process extracted the center-line of the flow data that also indicated the locations inside the vessel boundary. The skeletonization started by computing the distance transform of the inverted binary mask of VFI data (see Fig. G.1(b) and G.1(c)). Then the ridge lines on the distance transform are considered as the center-line of the flow data (see Fig. G.1(d)).

Extraction of outer-marker mask: The detection of outer markers are achieved using the B-mode image. Strong specular regions are extracted from the B-mode and used as an indication of regions outside the vessels. For this purpose, the envelope of the acquired scan is first computed. A cumulative histogram of the intensity values is then generated. The intensity values less than half of the maximum intensities in the envelope are disregarded, and a mask of strong signal regions is generated. The mask is then multiplied to a dilated version of the VFI mask and yielded the outer marker mask as

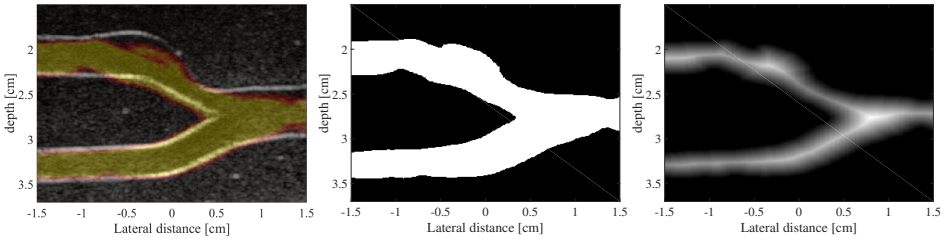

(a) Absolute value of VFI overlaid on B-mode.

(b) Binary mask of VFI data.

(c) Distance transform of inverted mask in *(b)*.

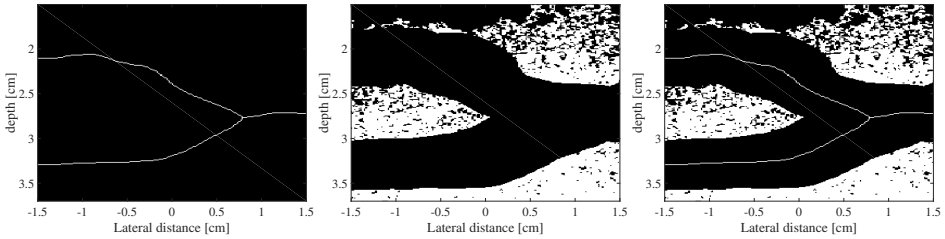

(d) Center-line of image in *(c)* (inner markers).

(e) Outer markers generated from B-mode.

(f) Marker image –combination of *(d)* and *(e)*.

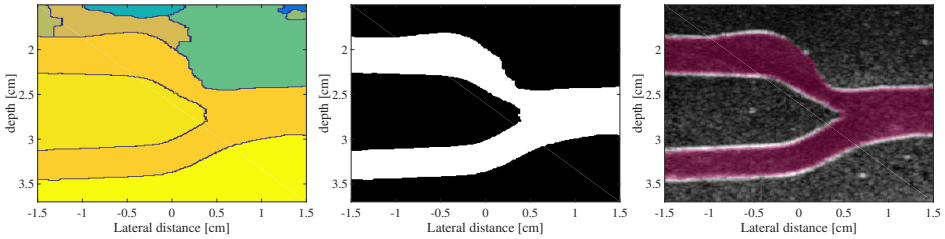

(g) Result of watershed segmentation.

(h) Artifacts rejected from image *(g)*.

(i) Inter-frame co-registration and refinement.

Figure G.1: Illustration of segmentation performed on a sequence from a carotid phantom with a bifurcation.

shown in Fig. G.1(e). The inner and outer markers are combined in one marker-image binary mask (see Fig. G.1(f)), and used to initialize the region growing algorithm on the B-mode image.

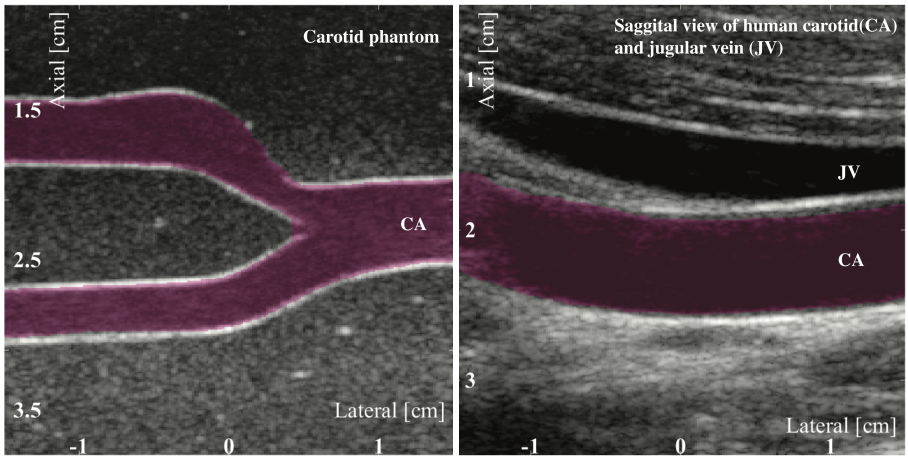

(a) Carotid artery segmented on carotid phantom.

(b) Carotid artery segmentation *In-Vivo*.

Figure G.2: Results of carotid segmentations performed on phantom and *In-Vivo* scans.

G.2.1.2 Marker-controlled region growing

Marker-controlled watershed is used to delineate the boundaries of the vessel-like structures bracketed by the marker image. The B-mode image is median filtered, and a watershed segmentation of this filtered image with respect to the Marker image yielded the segmentation of the vessel-like structures (see Fig. G.1(g)). However, segmentation results contain non-vessel structures that should be excluded.

G.2.1.3 Artifact rejection

The region growing resulted in over-segmented regions, which are not vessels. This step implements artifact rejection based on size, shape and amount of flow to ensure that only the vessels are retained(see Fig.G.1(h)). Basically, elongated objects containing flow data are kept in segmentation results and the rest are excluded. Even though, the retained

structures in this step are vessel-like objects, the boundaries of the vessels might have some discrepancies with respect to the actual vessel boundaries.

G.2.1.4 Inter-frame co-registration of segmentations

To refine the segmentation, so that it follows the exact vessel boundaries, an inter-frame co-registration of segmentations is performed. To deform parts of the segmentation that does not follow the actual vessel boundaries, 10 to 25 frames (according to the frame rate) neighboring in time are considered. Segmentations performed on all the neighboring frames are co-registered and regions matching in at least 80% of the frames are considered to be the actual vessels (See Fig. G.1(i)).

G.2.2 Enabling VFI automated measures

In this section the possibility of automating the two crucial flow measures such as PSV and volume flow using VFI are introduced.

G.2.2.1 Automated Peak systolic velocity (PSV) measurement using VFI

Using the proposed method, the vessel walls are accurately delineated. Fig. G.5 shows an example of segmentation of a human carotid. The red lines indicate the location of the vessel walls delineated by the proposed method. Two points are set across the vessel on the delineated vessel boundaries. Then, PSV along the line connecting the two points, through the vessel, across a cardiac cycle is calculated (see Fig. G.5). The red horizontal line indicates the position as well as the average peak velocity angle throughout the cycle. The green horizontal line indicates the center and the circular cross section found inside the vessel for measuring the volume flow.

G.2.2.2 Automated volume flow measurement using VFI

First, the vessel walls are automatically delineated, and VFI is refined so that it covers the whole vessel region. This enables the correct estimation of volume flow. Second, the volume flow can be computed without user manual intervention of a user. This is performed by automatically selecting vessel cross-sections between the segmented walls for computing the volume flow in VFI (see yellow circular cross section in Fig. G.5). The volume flow is implemented using the method proposed in (Jensen, Olesen, Stuart, et al. 2016).

G.3 Measurement setup

The proposed segmentation algorithm was applied to 5 carotid artery sequences. Five healthy subjects were scanned, and a total of 5 carotid artery sequences each containing 500 frames were acquired. Also a phantom including a carotid with a bifurcation was scanned and used in this study. The beamformed RF data were acquired using a BK3000 scanner (BK Ultrasound, Denmark) connected to a 192-element 4.1 MHz linear array transducer (9032, BK Ultrasound). The beamformed RF data were simultaneously recorded by a research interface on the scanner, and processed with the proposed algorithm off-line. For in-vitro flowrig validation of VFI, a flow system (CompuFlow 1000, Shelley Medical Imaging Technologies, Toronto, Canada) circulating a blood-mimicking fluid (BMF-US, Shelley Medical Imaging Technologies, Toronto, Canada) in a closed loop circuit was used. The linear transducer was fixed at a distance of 1.5 cm from the vessel of 12 mm in diameter with a beam-to-flow angle of 60 degrees. For increasing constant flowrig peak velocities of 5-60 cm/s, Spectral Doppler and VFI data were recorded. For precision analysis, each velocity setting was recorded twice.

All the measures are implemented in a in-house application specialized for VFI visualization and quantitative flow measures. All the PSV and volume flow measurements are performed using this application. The distribution of peak velocity amplitudes and angles during one cardiac cycle are also automatically computed and reported in the tool.

G.4 Results and discussion

Automated segmentation results were compared with manual segmentations performed by an experienced user on 60 frames (10 frame randomly chosen from each sequence). Dice coefficient denoting the similarity between segmentations was then computed. The coefficient ranges between 0 and 1. A value of 1 indicates perfect agreement and a value of 0 indicates no agreement. The Dice coefficient was 0.91, indicating that vessel boundaries obtained using the algorithm are highly accurate and consistent with the experts' visual perception of vessel boundaries. Two examples of segmentations performed by the proposed hybrid method on scans acquired from a carotid phantom with a bifurcation and carotid of a normal male subject are shown in Figs. G.2(a) and G.2(b) respectively.

Fig. G.3 shows the results of in-vitro flowrig validation of VFI for measuring PSV. Relative errors of the PSVs measured from VFI and spectral Doppler comparing to the actual PSVs were 14.5% and 29.5% respectively (see Fig. G.4). The figure shows that VFI offers a more precise and reliable alternative for velocity estimation of PSV in comparison with the current clinical standard using spectral Doppler. Fig. G.5 shows a screen shot of the CFU visualization application, in which a carotid artery belonging to a 29 years old

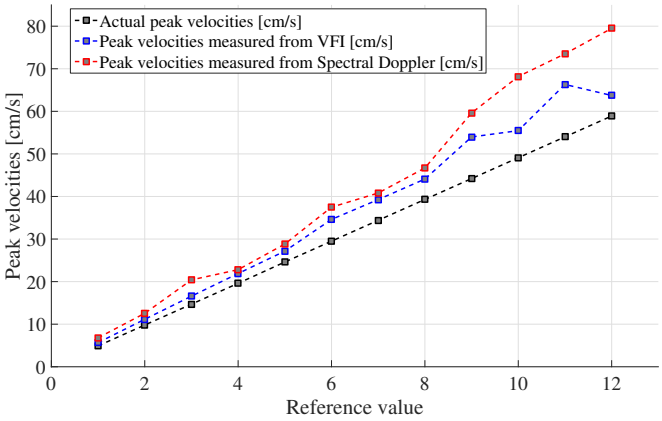

Figure G.3: Comparison of flowrig PSV measured by VFI and spectral Doppler.

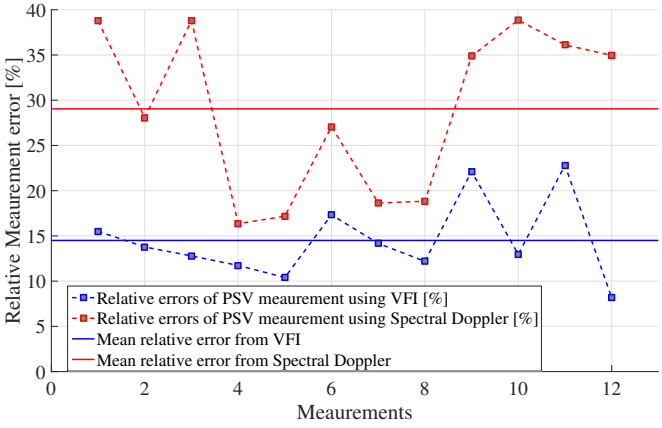

Figure G.4: Relative errors of measurements with VFI and spectral Doppler.

healthy male subject is segmented and VFI is visualized. The PSV and volume flow are also measured using the application and reported. PSV was 52.66 cm/s and the volume flow was 9 cm^3/s. The distribution of angle during one cardiac cycle was 89.54 ± 1.46 degrees.

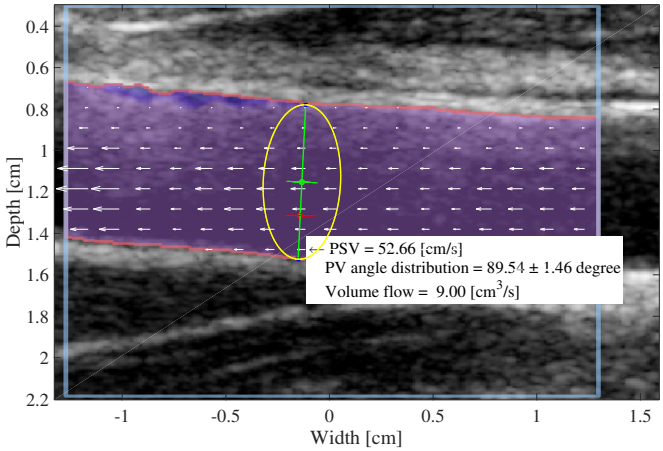

Figure G.5: Carotid artery segmented, The VFI is visualized, and a cross-section is automatically selected to compute the PSV and volume flow.

G.5 Conclusion

This paper presented a novel hybrid segmentation algorithm that combines VFI and B-mode to delineate the vessel boundaries. The algorithm also implemented PSV and volume flow for VFI. The empirical results showed a dice coefficient of 0.91, indicating a good match between segmentation performed by the algorithm and the expert. The results of the flowrig measurements also showed that VFI was 15% more precise than spectral Doppler for PSV measurement. Therefore, the proposed method enables a better visualization of VFI as well as the automatic quantitative flow measures using vector velocities. The algorithm can also be used in daily clinical practice as an alternative tool for making a quantitative flow measures.

References from Paper G

Grant, E. G., C. B. Benson, G. L. Moneta, A. V. Alexandrov, J. D. Baker, E. I. Bluth, B. A. Carroll, and et al. (2003). “Carotid artery stenosis: gray-scale and Doppler US

diagnosis - Society of radiologists in ultrasound consensus conference". In: *Radiology* 229.2. M. Eliasziw and J. Gocke and B. S. Hertzberg, pp. 340–346. DOI: 10.1148/radiol.2292030516 (cit. on p. 194).

Pedersen, M. M., M. J. Pihl, P. Haugaard, J. M. Hansen, K. L. Hansen, M. B. Nielsen, and J. A. Jensen (2012). "Comparison of Real-Time In Vivo Spectral and Vector Velocity Estimation". In: *Ultrasound Med. Biol.* 38.1, pp. 145–151 (cit. on p. 194).

Reutern, G. M. von, M. W. Goertler, N. M. Bornstein, M. D. Sette, D. H. Evans, A. Hetzel, M. Kaps, F. Perren, and et al. (2012). "Grading Carotid Stenosis Using Ultrasonic Methods". In: *Stroke* 43.3, pp. 916–921. DOI: 10.1161/STROKEAHA.111.636084 (cit. on p. 194).

Hansen, P. M., S. Heerwagen, M. M. Pedersen, M. Rix, L. Lønn, M. B. Nielsen, J. B. Olesen, M. J. Pihl, and J. A. Jensen (2013). "Vector Volume Flow in Arteriovenous Fistulas". In: *Proc. IEEE Ultrason. Symp.* Pp. 2026–2029 (cit. on p. 194).

Hansen, P. M., J. B. Olesen, M. J. Pihl, T. Lange, S. Heerwagen, M. M. Pedersen, M. Rix, L. Lønn, J. A. Jensen, and M. B. Nielsen (2014). "Volume Flow in Arteriovenous Fistulas using Vector Velocity Ultrasound". In: *Ultrasound Med. Biol.* 40.11, pp. 2707–2714 (cit. on p. 194).

Jensen, J., J. B. Olesen, P. M. Hansen, M. B. Nielsen, and J. A. Jensen (2014). "Accuracy and Sources of Error for an Angle Independent Volume Flow Estimator". In: *Proc. IEEE Ultrason. Symp.* Pp. 1714–1717 (cit. on p. 194).

Brandt, A. H., J. Jensen, K. L. Hansen, P. M. Hansen, T. Lange, M. Rix, J. A. Jensen, L. Lönn, and M. B. Nielsen (2016). "Surveillance for Hemodialysis Access Stenosis: Usefulness of Ultrasound Vector Volume Flow". In: *J. Vascul. Access.* Accepted for publication (cit. on p. 194).

Jensen, J., J. B. Olesen, M. B. Stuart, P. M. Hansen, M. B. Nielsen, and J. A. Jensen (2016). "Vector velocity volume flow estimation: Sources of error and corrections applied for arteriovenous fistulas". In: *Ultrasonics* 70, pp. 136–146. DOI: http://dx.doi.org/10.1016/j.ultras.2016.04.023 (cit. on pp. 194, 198).

Patent Applications

PATENT APPLICATION A

Wall-to-wall vessel segmentation in US imaging using a combination of VFI data and US imaging data

Authors Ramin Moshavegh, Bo Martins, and Jørgen Arendt Jensen.

File date September 09, 2016

Number ANA1311-US; PD08509

A.1 Technical Field

The following generally relates to ultrasound (US) imaging and more particularly to segmenting a vessel, wall-to-wall, in an ultrasound B-mode image/volume using a combination of 2-D/3-D velocity flow imaging (VFI) data and the ultrasound B-mode image/volume.

A.2 Background

Velocity flow imaging enables angle independent visualization of blood flow, allowing clinicians to visualize and estimate direction and velocity of blood flow in all directions and at any angle. However, today's commercial ultrasound scanners are not able to produce a wall-to-wall delineation of a vessel and present it simultaneously with VFI data superimposed within the entire vessel. FIGURE 1 shows a prior art example in which VFI data 102 (the region approximately between dotted straight lines) for a region of interest 104 does not extend to the true walls 106 and 108 (approximated through the dashed straight lines) of a sub-portion 110 of a vessel 112 represented in a B-mode image 114. In this example, regions 116 and 118 between the dashed and dotted lines represent regions in the vessel sub-portion 110 without VFI data.

Furthermore, to obtain the full view of the velocities in the cardiac cycle, clinicians have to manually change parameters such as the pulse repetition frequency (PRF) when examining different magnitudes of velocities. For example, during systole, when higher velocities are present, a higher PRF is needed in order to estimate the right velocities. If the PRF is set too low, aliasing will occur as the blood scatterers are moving too fast to be detected. Unfortunately, it can be a troublesome maneuver to change back and forth between different PRF's at least since the full velocity range cannot be displayed simultaneously. As a consequence, clinicians typically select a static range. However, blood flow outside of the range can contain artifact and/or not even be detected. Unfortunately, this can lead to a misdiagnosis.

Furthermore, the clinician has to manually approximate, e.g., through visual inspection of the B-mode image 114, the location of the vessel walls to place a flow measurement line 120 along a cross-section of the vessel sub-portion 110 from one wall to the other wall for velocity flow measurements. However, this process can be tedious at least since the vessel walls 106 and 108 of the vessel sub-portion 110 are not clearly defined in the B-mode image 114. As a result, the velocity flow measurements may be taken using a part of the vessel sub-portion 110, where no VFI data is present (e.g., regions 116 and/or 118), and/or part of the anatomy outside of the vessel sub-portion 110 (e.g., non-vessel anatomy). Unfortunately, this may lead to erroneous and/or inaccurate flow measurements.

A.3 Summay

Aspects of the application address the above matters, and others. In one aspect, an ultrasound imaging system includes an image processor configured to process beamformed ultrasound data representing structure flowing through a tubular object and generate an image indicative of the tubular object based thereon. The ultrasound imaging system further includes a velocity processor configured to process the beamformed ultrasound data and generate vector flow imaging data indicative of the structure flowing through the tubular object based thereon. The vector flow imaging data includes at least an axial velocity component signal and one or more transverse velocity components indicating a direction and a speed of the structure flowing through the tubular object. The ultrasound imaging system further includes a segmentation processor configured to segment the tubular object from the image based on a combination of both the vector flow imaging data and the image, wherein a resulting segmentation extends from wall-to-wall of the tubular object. The ultrasound imaging system further includes a display configured to display the image with the segmentation and the vector flow imaging data superimposed thereover, with the vector flow imaging data extending from wall-to-wall within the tubular object. In another aspect, a method includes generating an image indicative of a

tubular object from beamformed ultrasound data representing structure flowing through the tubular object. The method further includes generating vector flow imaging data indicative of the structure flowing through the tubular object from beamformed ultrasound. The vector flow imaging data includes at least an axial velocity component signal and one or more transverse velocity components indicating a direction and a speed of the structure flowing through the tubular object. The method further includes generating a wall-to-wall segmentation of the tubular object from the image with a combination of the vector flow imaging data and the image. The method further includes visually presenting the image with the segmentation and the vector flow imaging data superimposed thereover, with the vector flow imaging data extending from wall-to-wall within the tubular object. In another aspect, a computer readable storage medium is encoded with computer readable instructions. The computer readable instructions, when executed by a processor, causes the processor to: construct an image indicative of a tubular object from beamformed ultrasound data representing structure flowing through the tubular object, estimate vector flow imaging data indicative of the structure flowing through the tubular object from beamformed ultrasound, wherein the vector flow imaging data includes at least an axial velocity component signal and one or more transverse velocity components indicating a direction and a speed of the structure flowing through the tubular object, compute a wall-to-wall segmentation of the tubular object from the image with a combination of the vector flow imaging data and the image, and display the image with the segmentation and the vector flow imaging data superimposed thereover, with the vector flow imaging data extending from wall-to-wall within the tubular object. Those skilled in the art will recognize still other aspects of the present application upon reading and understanding the attached description.

A.4 Brief Description of the Drawings

The application is illustrated by way of example and not limited by the figures of the accompanying drawings, in which like references indicate similar elements and in which:

FIGURE 1 illustrates an example prior art B-mode image with VFI data superimposed thereover;

FIGURE 2 schematically illustrates an example ultrasound imaging system in accordance with an embodiment described herein;

FIGURE 3 illustrates an example B-mode image with segmented vessel walls, wall-to-wall, (segmented based on a combination VFI data and the B-mode image) and VFI data superimposed thereover;

FIGURE 4 illustrates another example B-mode image with segmented vessel walls, wall-to-wall, (segmented based on a combination VFI data and the B-mode image)

superimposed thereover;

FIGURE 5 illustrates another example B-mode with segmented vessel walls, wall-to-wall, (segmented based on a combination VFI data and the B-mode image) superimposed thereover;

FIGURE 6 illustrates an example segmentation algorithm based on a combination VFI data and a B-mode image;

FIGURES 7-10 illustrate examples of the segmentation for a first step of the segmentation algorithm of FIGURE 6;

FIGURES 11 and 12 illustrate examples of the segmentation for a second step of the segmentation algorithm of FIGURE 6;

FIGURE 13 illustrates an example of the segmentation for a third step of the segmentation algorithm of FIGURE 6; and

FIGURE 14 illustrates an example segmentation method in accordance with an embodiment described herein.

A.5 Detailed Description

The following describes an approach that combines VFI data and B-mode imaging to create a wall-to-wall segmentation of walls of a blood vessel represented in a B-mode image or volume. The segmentation can be utilized at least for adaptively adjusting/optimizing a PRF and/or echo cancelling during imaging based on the flow rate determined with the VFI data and the wall-to-wall segmentation and/or determine flow measurements such as peak systolic velocity (PSV), a largest vessel diameter (Dmax), volume flow, etc. based on the VFI data and the wall-to-wall segmentation. For sake of brevity and clarity, the terms “image” and “region” also encompasses the term “volume” herein.

Figure 2 schematically illustrates an example ultrasound imaging system 200. A transducer array 202 includes one or more transducer elements 204, which are configured to transmit ultrasound signals. The one or more transducer elements 204 are also configured to receive echo signals and generate electrical signals indicative thereof. The echo signals are produced in response to an interaction between the ultrasound signals and the structure (e.g., flowing blood cells, organ cells, etc.).

The transducer array 202 can be a one or two-dimensional (1-D or 2-D) array. Examples of 1-D arrays include arrays with 8, 16, 32, 64, 96, 128, 512, and/or other number of elements. Examples of 2-D arrays include square, rectangular, circular, row-column, irregular, and/or other arrays. The transducer array 202 can be linear, curved, phased, and/or other array. The transducer array 202 can be fully populated or sparse and/or a combination thereof.

Transmit circuitry 206 generates a set of pulses that are conveyed to the transducer array 202. The set of pulses excites a set of the transducer elements 204, which causes the elements 204 to emit ultrasound signals, optionally with an adaptively determined PRF, which is estimated from a wall-to-wall segmentation of a vessel. Receive circuitry 208 receives the electrical signals. The receive circuitry 208 may amplify, filter, convert analog signals to digital signals, etc. The transducer array 202 may have separate transmit and receive elements, and/or a switch may switch between the transmit and receive circuitry 206 and 208.

A beamformer 210 beamforms the signals by applying time delays to signals, weighting signals, summing delayed and weighted signals, and/or otherwise beamforming received signals, creating a beam of RF data. For VFI, the beamformer 210 produces ultrasound data to estimate an axial velocity component, which extends along a direction of a propagating beam, and at least one transverse velocity component, which extends transverse to the axial velocity component. This may include applying echo cancelation to the beamformed data, where the echo cancelation is optionally optimized based on a wall-to-wall segmentation of a vessel.

An image processor 212 processes the beamformed data and generates an image/volume. For B-mode imaging, this may include, e.g., envelope detection, log-compression, and/or other processing. The image processor 210 may also process scan-lines to lower speckle and/or improve specular reflector delineation, and/or perform other processing such as FIR and/or IIR filtering, etc.

A velocity processor 214 processes the pre-processed data and generates VFI data. This includes generating the axial and the one or more transverse velocity components. These velocity components indicate a direction and a speed of flowing structure. Example of determining such components are described in U.S. 6,859,659 B1, filed on November 9, 2001, and entitled "Estimation of Vector Velocity," and application serial number 14/350,500, publication number US 2014/0257103 A1, filed on April 8, 2014, and entitled "Three Dimensional (3D) Transverse Oscillation Vector Velocity Ultrasound Imaging," both of which are incorporated herein by reference in their entireties. Other approaches are also contemplated herein.

A segmentation processor 216 receives both the VFI data and B-mode image/volume. The segmentation processor 216 creates an accurate wall-to-wall segmentation of walls of a blood vessel represented in the B-mode image/volume. As described in greater detail below, this includes generating a marker image/volume from 2-D/3-D VFI information, using the marker image/volume with a marker-controlled region/volume growing algorithm to delineate the vessel boundaries in the B-mode image/volume, rejecting non-vessel structure, and implementing an inter-frame co-registration of segmentations to make sure that vessels segmented in each frame are in correspondence with the same vessels

segmented in neighboring frames in the sequence.

Briefly turning to FIGURE 3, a B-mode image 302 with a user identified region of interest 304 within which VFI data 306 is superimposed over a sub-portion 308 of a vessel 310, within the sub-portion 308 between vessel walls 312 and 314, is illustrated. Using the segmentation approach described herein, the vessel walls 312 and 314 are accurately segmented, wall-to-wall, based on the combination of the VFI data and B-mode image. In the prior art approach in FIGURE 1, without the wall-to-wall delineation described herein, the user has to visually estimate where the vessel walls are, and the superimposed VFI data does not track well to the actual vessel walls 106 and 108 and thus is not available for regions close to the vessel walls for measurement purposes such that velocities are not displayed for those regions.

Returning to FIGURE 2, an operating parameter processor 218 receives the segmented vessel walls as an input. In one instance, the operating parameter processor 218 estimates a PRF based on the segmented vessel walls. The operating PRF can then be adaptively adjusted to the estimated PRF for further imaging. In general, the operating PRF is adapted based on the vessel delineation without need for manual adjustment by the user, although the user can manually adjust the PRF if desired. The auto adjustment includes a PRF optimized for full visualization of the velocities in the cardiac cycle. For example, the estimated PRF ensures that during systole, when higher velocities are present, a higher PRF is utilized, and during diastole, a lower PRF is utilized. By using the estimated PRF, the generated VFI mask (discussed below) will have the closest boundaries relative to the automated segmentation. In another instance, echo cancelling can be automatically tuned so that it yields the biggest correlation with the segmentation. The optimal echo cancelling occurs when the VFI mask is the closest match to the mask generated from the segmentation procedure.

A measurement processor 220 also receives the segmented vessel walls as an input. The measurement processor 220 processes the segmented vessel walls to extract certain features, and then determines one or more measurements from these features. For an automated PSV measurement, the measurement processor 220 determines PSV along a line along a cross section of the vessel based on the delineated vessel of the segmentation. In FIGURE 3, with the accurate identification of the vessel walls 310 and 312, the measurement processor 220 can identify a path 316 from wall to wall, perpendicular to each wall, and compute a PSV 318 along the path 316. In FIGURE 1, without the vessel delineation from the segmentation, the user has to manually place the path 120 without the segmentation, which may lead to a less accurate PSV measurement.

Returning to FIGURE 2, for an automated largest vessel diameter measurement for abdominal aortic aneurysms assessment, the measurement processor 220 computes a maximum diameter of the vessel during a cardiac cycle using the accurate vessel wall

delineation of the segmentation. For example, in FIGURE 3, the measurement processor 220 can determine a diameter for the wall-to-wall path 316 by a length of the path 316. In one instance, this enables clinicians to use VFI to automatically diagnose the aneurysms while scanning the vessel, without performing manual measurement on the scans. For abdominal aortic aneurysms assessment, a focal dilatation in an artery, with at least a 50% increase of its normal diameter, is defined as an aneurysm. An enlargement larger than three centimeters (3 cm) of the abdominal aorta, even if asymptomatic, has been considered in the literature to be an abdominal aortic aneurysm.

Returning to FIGURE 2, the measurement processor 220 is also configured to estimate volume flow using the vessel wall delineation of the segmentation by automatically selecting vessel cross-sections (316, 320, 322, etc.) between the segmented walls for computing the volume flow in VFI. Volume flow quantifies the flow and characterizes the vessel, and the reliability of this measure depends on the estimated vessel diameter. In FIGURE 3, with the accurate identification of the vessel walls 310 and 312, the VFI data extends from wall-to-wall (the entire vessel region), and velocities can be computed for the entire vessel sub-portion 308. As such, the approach described herein enables correct estimation of the volume flow, and computes volume flow without manual intervention of user.

Returning to FIGURE 2, a rendering engine 222 receives the B-mode image/volume, the VFI data, the segmentation, and, if take, the measurement(s) and displays, via a display 324 and/or other display, one or more of the B-mode image/volume, the VFI data, the segmentation, and/or the measurement(s). For example, the rendering engine 120 can display only the B-mode image/volume, the B-mode image/volume with the VFI data superimposed thereover, the B-mode image/volume with the segmented vessel wall superimposed thereover the B-mode image/volume with the VFI data and segmented vessel wall superimposed thereover, the B-mode image/volume with the VFI data, segmented vessel wall, and measurement superimposed thereover, etc. FIGURES 4 and 5 show examples of B-mode images 402 and 502 with wall-to-wall segmentation of vessels 404 and 504 superimposed thereover.

Returning to FIGURE 2, a user interface 226 includes one or more input devices (e.g., a button, a knob, a slider, a touch pad, a mouse, a trackball, a touch screen, etc.) and/or one or more output devices (e.g., a display screen, a light, an audio generator, etc.), which allow for interaction between a user and the ultrasound imaging system 200. A controller 228 controls one or more of the components 102-122, e.g., based on one or more modes of operation (e.g., VFI + B-mode, measurement mode, auto PRF, echo cancelation, etc.). In one instance, this includes adjusting the operating PRF based on the PRF estimated by the operating parameter processor 218 and/or a signal from the user interface 226 adjusting the PRF, optimizing echo cancelling based on the segmentation, etc.

One or more of the beamformer 210, the image processor 212, the velocity processor 214, the segmentation processor 216, the operating parameter processor 218, the measurement processor 220 and/or other component(s) can be implemented via one or more processors (e.g., a central processing unit CPU, a microprocessor, a controller, a graphics processing unit GPU, etc.) executing one or more computer readable instructions encoded or embedded on computer readable storage medium (which excludes transitory medium) such as physical memory or other non-transitory medium. Additionally or alternatively, at least one of the instructions can be carried by a carrier wave, a signal, or other transitory medium.

It is to be understood that the ultrasound imaging system 200 can be part of a portable system on a stand with wheels, a system residing on a tabletop, and/or other system in which the transducer array 202 is housed and mechanically supported in a probe or the like and one or more of the other components (e.g., one or more of the components 206-230) are housed and mechanically supported in a console, which is separate from the probe. The display 224 may or may not be part of the console. In another instance, the transducer array 202 and one or more of the other components are housed and/or mechanically supported within a single enclosure hand-held ultrasound scanning device.

In a variation, at least one of the operating parameter processor 218 or the measurement processor 220 is omitted.

As briefly discussed above, the segmentation processor 216 processes the VFI flow data and the B-mode image/volume and creates a wall-to-wall segmentation for a blood vessel. FIGURE 6 illustrates an example segmentation algorithm in connection with 2-D VFI data and a 2-D B-mode image. However, it is to be understood that one skilled in the art would know how to adjust the algorithm without undue experimentation for 3-D VFI data and a 3-D B-mode volume to generate a marker volume and use this maker volume in a volume growing algorithm with respect to the B-mode volume to delineate vessel boundaries in 3-D. Generally, the segmentation of FIGURE 6 can be divided into the below described four distinct steps.

1) Step I (602): Generating a marker-image. With reference to FIGURES 2 and 6-10, the segmentation processor 216 detects inner markers and outer markers. The segmentation processor 216 detects inner markers using gray scale skeletonization of the VFI data. In one instance, the flow data are absolute velocities of VFI estimates. The skeletonization process extracts a center-line of the flow data that also indicates locations inside the vessel boundary. The skeletonization starts by computing a distance transform 800 (FIGURE 8) of an inverted binary mask of VFI data 700 (FIGURE 7). Ridge lines 900 on the distance transform 80 are extracted as a centerline 902 of the flow data (FIGURE 9). The centerline 902 is the inner marker

The segmentation processor 216 detects outer markers using the B-mode image.

Strong specular regions are extracted from the B-mode image and used as an indication of regions outside the vessels. For this purpose, the envelope of the acquired scan is first computed. A cumulative histogram of the intensity values is then generated. The intensity values less than half of the maximum intensities in the envelope are disregarded, and a mask of strong signal regions is generated. The mask is then multiplied to a dilated version of the VFI mask and yields an outer marker mask 1000 (FIGURE 10). FIGURE 11 shows a marker-image 1100 including the outer marker mask 1000 with the centerline 902.

2) Step II (604): Marker-controlled region growing. With reference to FIGURES 2, 6, 11, and 12, the segmentation processor 216 employs a marker-controlled watershed image processing approach to delineate or segment boundaries of vessel-like structures bracketed by the marker-image 1100. The B-mode image is median filtered, and a watershed segmentation of this filtered image with respect to the marker-image yields a segmentation 1200 of the vessel-like structures. (FIGURE 12)

3) Step III (606): Artifact rejection. With reference to FIGURES 2, 6 and 13, the segmentation processor 216 reduces over-segmented regions (resulting from the region growing), which do not belong to the vessel regions. For this, in one instance, the segmentation processor 216 employs artifact rejection based on size, shape and/or vascularity (e.g., using a vesselness filter such as a Frangi filter or the like to ensure that only vessels are retained). Basically elongated objects containing flow data are kept in segmentation results and the rest are excluded. Even though, the retained structures in this step are vessel-like objects, the boundaries of vessels might have some discrepancies to the actual vessel boundaries. FIGURE 13 shows an example image 1300 in which in which artifacts are rejected and vessel-like structures are retained.

4) Step IV (608): Inter-frame co-registration of segmentations. Returning to FIGURE 2, the segmentation processor 216 corrects the segmentation so that it follows the vessel boundaries using an inter-frame co-registration of the segmentations. To refine parts of the segmentation that does not follow the actual vessel boundaries, a few neighboring frames in time are considered. Segmentations of those frames are co-registered and regions matching in at least a sub-portion (e.g., 50% to 100%, such as 80%, 85%, etc.) of frames are considered to be the actual vessel.

Figure 14 illustrates an example method.

It is to be understood that the following acts are provided for explanatory purposes and are not limiting. As such, one or more of the acts may be omitted, one or more acts may be added, one or more acts may occur in a different order (including simultaneously with another act), etc.

At 1402, VFI + B-mode imaging is activated for the system 200.

At 1404, the transducer 202 is employed to scan a subject and acquire ultrasound data

of a blood vessel(s) of interest.

At 1406, VFI data is generated with the acquired ultrasound data.

At 1408, a B-mode image is generated with the acquired ultrasound data.

At 1410, a sub-portion of a blood vessel(s) in a region of interest is segmented wall-to-wall using a combination of the VFI data and the B-mode image, as described herein and/or otherwise.

At 1412, the B-mode image is displayed with the segmentation and the VFI data superimposed thereover within the entirety of the sub-portion of the blood vessel between the walls.

At 1414, at least one of the PRF or echo cancellation is optimized based on the wall-to-wall vessel segmentation, as described herein and/or otherwise.

At 1416, at least one measurement it made based on the wall-to-wall vessel segmentation, as described herein and/or otherwise.

In a variation, at least one of act 1414 or 1416 is omitted.

The methods described herein may be implemented via one or more processors executing one or more computer readable instructions encoded or embodied on computer readable storage medium such as physical memory, which causes the one or more processors to carry out the various acts and/or other functions and/or acts. Additionally or alternatively, the one or more processors can execute instructions carried by transitory medium such as a signal or carrier wave.

The application has been described with reference to various embodiments. Modifications and alterations will occur to others upon reading the application. It is intended that the invention be construed as including all such modifications and alterations, including insofar as they come within the scope of the appended claims and the equivalents thereof.

A.6 Claims

What is claimed is:

1. An ultrasound system, comprising: an image processor configured to process beamformed ultrasound data representing structure flowing through a tubular object and generate an image indicative of the tubular object based thereon; a velocity processor configured to process the beamformed ultrasound data and generate vector flow imaging data indicative of the structure flowing through the tubular object based thereon, wherein the vector flow imaging data includes at least an axial velocity component signal and one or more transverse velocity components indicating a direction and a speed of the structure flowing through the tubular object; a segmentation processor configured to segment the tubular object from

the image based on a combination of both the vector flow imaging data and the image, wherein a resulting segmentation extends from wall-to-wall of the tubular object; and a display configured to display the image with the segmentation and the vector flow imaging data superimposed thereover, with the vector flow imaging data extending from wall-to-wall within the tubular object.

2. The system of claim 1, wherein the segmentation processor segments the tubular object by: generating a marker image from velocity flow data and the image; using the marker image with a marker-controlled region growing algorithm to delineate tubular object boundaries in the image; rejecting non-tubular object structure; and employing an inter-frame co-registration of segmentations across to ensure a tubular object segmented in each frame are in correspondence with a same tubular object segmented in neighboring frames in a sequence, wherein tubular objects matching in all frames are considered to be the actual tubular structure.

3. The system of claim 2, wherein the segmentation processor determines an inner marker from the vector flow imaging data, an outer marker from only the image and the vector flow imaging data, and combines the inner and outer markers to produce the marker image.

4. The system of claim 3, wherein the segmentation processor determines the inner marker by employing a gray scale skeletonization of the vector flow imaging data, wherein the skeletonization includes extracting a center line of the vector flow imaging data, which indicates locations inside the tubular object boundary.

5. The system of claim 4, wherein the segmentation processor extracts the center line by generating a distance map of an inverse of a velocity flow imaging binary mask, determining ridge lines on the distance map as an initial skeleton of the velocity flow imaging mask, and generating a final skeleton using only velocity flow imaging data pixels lying inside the initial skeleton and larger than a predetermined percent of the velocity flow imaging data.

6. The system of claim 3, wherein the segmentation processor determines the outer marker by extracting strong specular regions from the image, which are considered outside of the tubular structure.

7. The system of claim 2, wherein the segmentation processor employs a marker-controlled watershed image processing approach, using the marker image, to segment boundaries of tubular-like structures located by the marker image.

8. The system of claim 7, wherein the segmentation processor generates a binary mask containing strong specular regions, and multiplies the binary mask by an inverted and dilated version of a velocity flow information mask, which generates an outer marker mask that highlights the strong specular regions and ensures the mask does not cover an area with flow.

9. The system of claim 2, wherein the segmentation processor rejects non-tubular object structure based on at least one of a size, a shape, an amount of flow, and/or a vascularity to ensure only tubular structure is retained.

10. The system of claim 1, further comprising: an operating system processor configured to adaptively adjust a pulse repetition frequency during imaging based on the wall-to-wall segmentation.

11. The system of claim 1, further comprising: an operating parameter processor configured to tune echo cancelling during imaging based on the wall-to-wall segmentation.

12. The system of claim 1, further comprising: a measurement processor configured to estimate a peak systolic velocity based on the wall-to-wall segmentation.

13. The system of claim 1, further comprising: a measurement processor configured to estimate a largest vessel diameter based on the wall-to-wall segmentation.

14. The system of claim 1, further comprising: a measurement processor configured to estimate a volume flow based on the wall-to-wall segmentation.

15. A method, comprising: generating an image indicative of a tubular object from beamformed ultrasound data representing structure flowing through the tubular object; generating vector flow imaging data indicative of the structure flowing through the tubular object from beamformed ultrasound, wherein the vector flow imaging data includes at least an axial velocity component signal and one or more transverse velocity components indicating a direction and a speed of the structure flowing through the tubular object; generating a wall-to-wall segmentation of the tubular object from the image with a combination of the vector flow imaging data and the image; and visually presenting the image with the segmentation and the vector flow imaging data superimposed thereover, with the vector flow imaging data extending from wall-to-wall within the tubular object.

16. The method of claim 15, wherein generating a wall-to-wall segmentation includes: generating a marker image from velocity flow data and the image; using the marker image with a marker-controlled region growing algorithm to delineate tubular object

boundaries in the image; rejecting non-tubular object structure; and employing an inter-frame co-registration of segmentations across to make sure that a tubular object segmented in each frame are in correspondence with a same tubular object segmented in neighboring frames in a sequence.

17. The method of claim 16, wherein the generating the marker image includes: determining an inner marker by employing gray scale skeletonization of the velocity flow imaging data, which extracts a center-line of flow data, which indicates locations inside the tubular object boundary; determining an outer marker by extracting strong specular regions from the image, which are considered outside of the tubular structure; and combining the inner and outer markers to produce the marker image.

18. The method of claim 17, wherein using the marker image with a marker-controlled region growing algorithm includes: generating a binary mask containing strong specular regions; and multiplying the binary mask by an inverted and dilated version of a velocity flow information mask, which generates an outer marker mask that highlights the strong specular regions and ensures the mask does not cover an area with flow.

19. The method of claim 18, wherein non-tubular object structure is rejected based on at least one of a size, a shape, an amount of flow, and/or a vascularity to ensure only tubular structure is retained.

20. The method of claim 19, wherein employing the inter-frame co-registration includes identifying only regions matching in at least 80

21. The method of claim 16, further comprising: at least one of adaptively adjusting a pulse repetition frequency during imaging based on the segmentation or tuning echo cancelling during imaging based on the segmentation.

22. The method of claim 16, further comprising: at least one of estimating a peak systolic velocity based on the segmentation, estimating a largest vessel diameter based on the segmentation, or estimating a volume flow based on the segmentation.

23. A computer readable storage medium encoded with computer readable instructions, which, when executed by a processer, causes the processor to: construct an image indicative of a tubular object from beamformed ultrasound data representing structure flowing through the tubular object; estimate vector flow imaging data indicative of the structure flowing through the tubular object from beamformed ultrasound, wherein the vector flow imaging data includes at least an axial velocity component signal and one or more transverse velocity components indicating a direction and a

speed of the structure flowing through the tubular object; compute a wall-to-wall segmentation of the tubular object from the image with a combination of the vector flow imaging data and the image; and display the image with the segmentation and the vector flow imaging data superimposed thereover, with the vector flow imaging data extending from wall-to-wall within the tubular object.

A.7 Abstract

An ultrasound imaging system includes an image processor and a velocity processor configured to process beamformed ultrasound data representing structure flowing through a tubular object and generate, respectively, an image indicative of the tubular object and vector flow imaging data indicative of the structure flowing through the tubular object. The system further includes a segmentation processor configured to segment the tubular object from the image based on a combination of both the vector flow imaging data and the image, wherein a resulting segmentation extends from wall-to-wall of the tubular object. The system further includes a display configured to display the image with the segmentation and the vector flow imaging data superimposed thereover, with the vector flow imaging data extending from wall-to-wall within the tubular object. The system further includes the automatic computation of largest vessel diameter (Dmax), and/or quantitative flow measures such as Peak systolic velocity (PSV) and/or volume flow.

A.8 Drawings

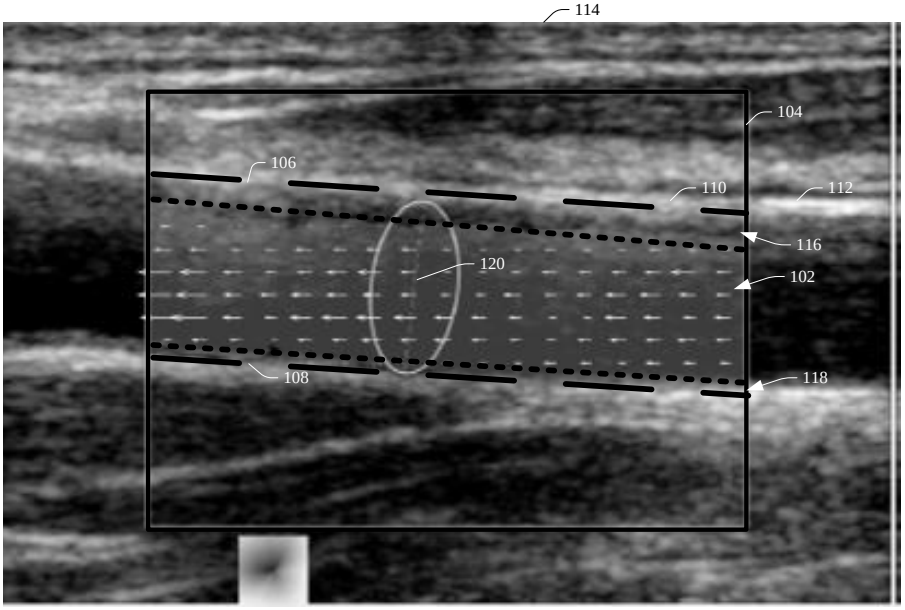

FIGURE 1
(PRIOR ART)

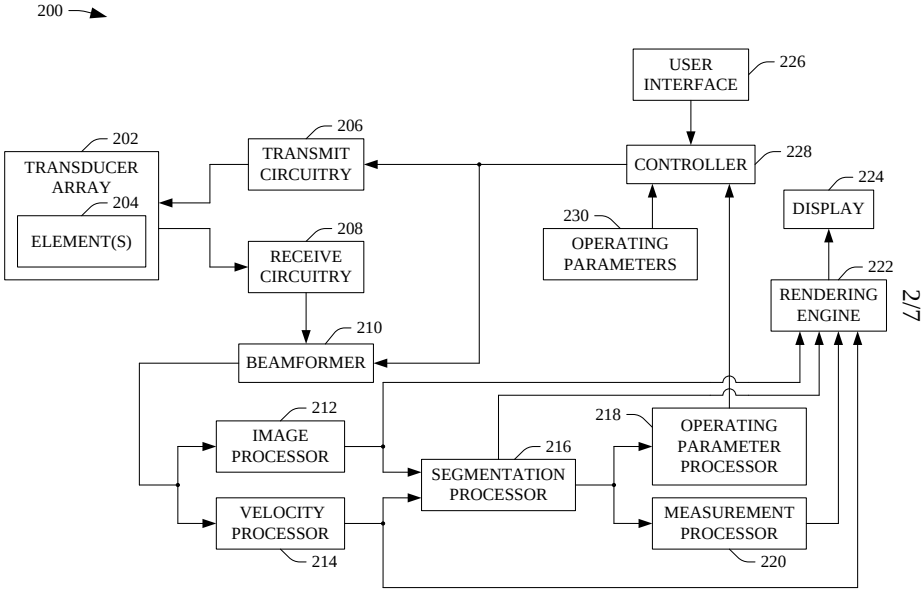
200
USER INTERFACE
226
TRANSDUCER ARRAY
202
ELEMENT(S)
204
TRANSMIT CIRCUITRY
206
RECEIVE CIRCUITRY
208
CONTROLLER
228
OPERATING PARAMETERS
230
DISPLAY
224
RENDERING ENGINE
222
BEAMFORMER
210
IMAGE PROCESSOR
212
VELOCITY PROCESSOR
214
SEGMENTATION PROCESSOR
216
OPERATING PARAMETER PROCESSOR
218
MEASUREMENT PROCESSOR
220

FIGURE 2

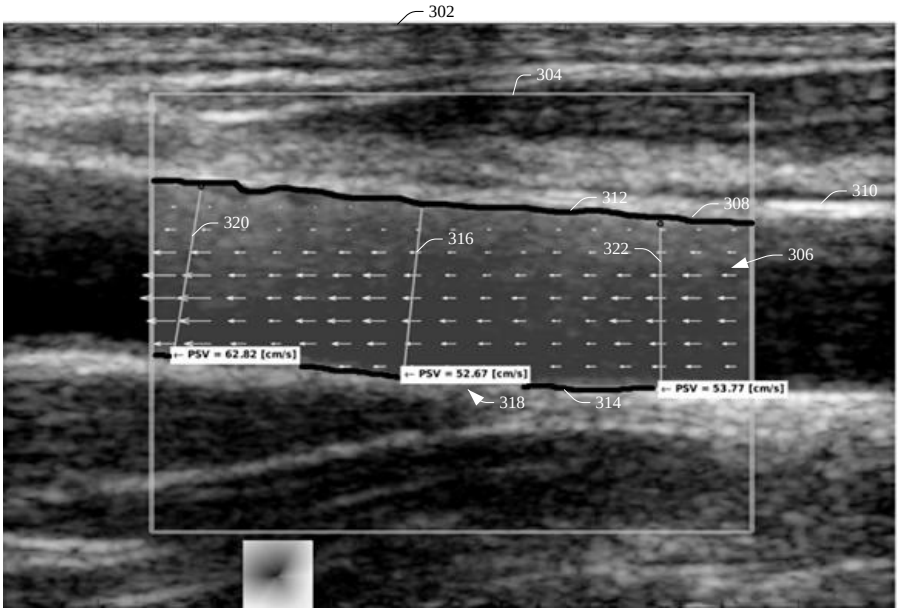
302
304
312
308
310
320
316
322
306
← PSV = 62.82 [cm/s]
← PSV = 52.67 [cm/s]
← PSV = 53.77 [cm/s]
318
314

FIGURE 3

4/7

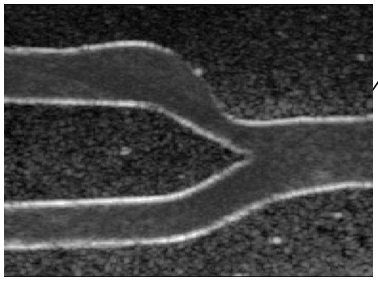

FIGURE 4

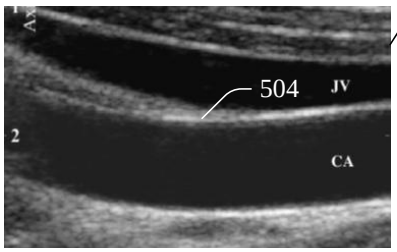

FIGURE 5

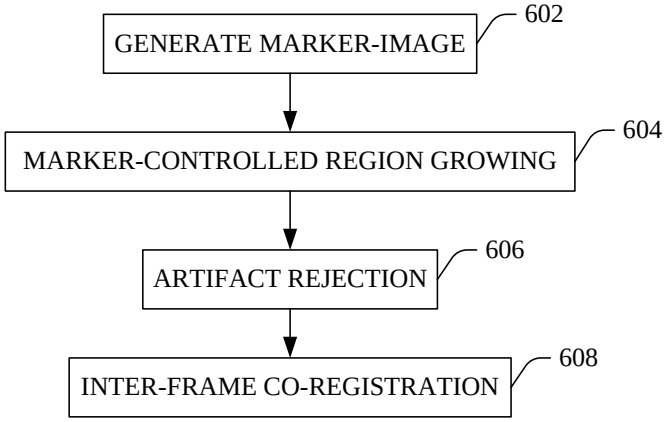

FIGURE 6

5/7

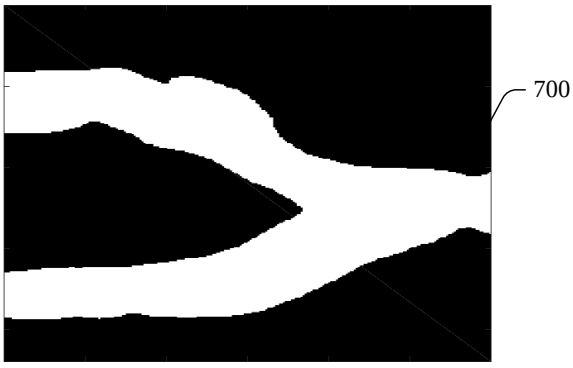

FIGURE 7

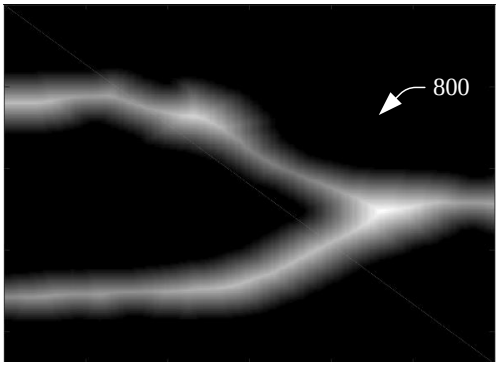

FIGURE 8

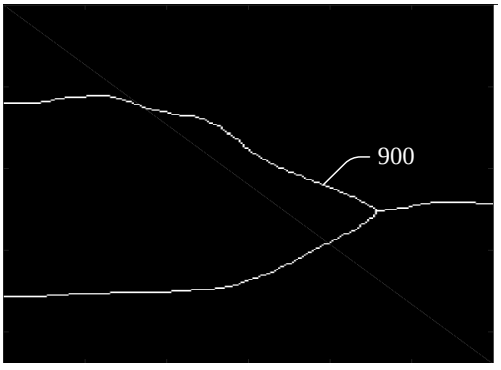

FIGURE 9

6/7

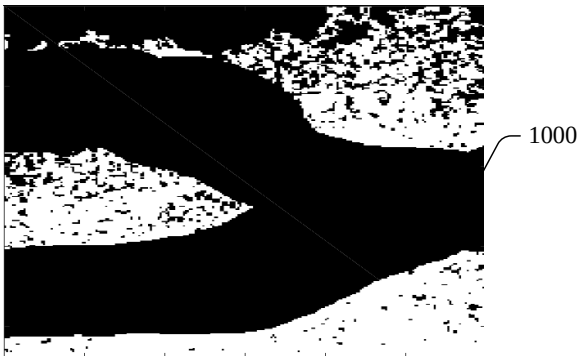

FIGURE 10

FIGURE 11

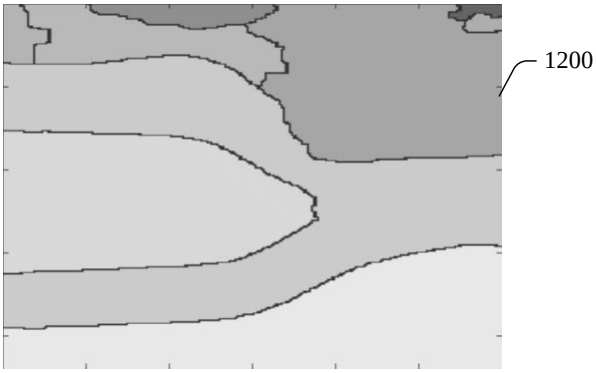

FIGURE 12

7/7

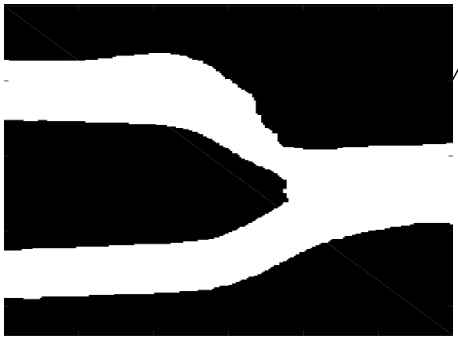

FIGURE 13

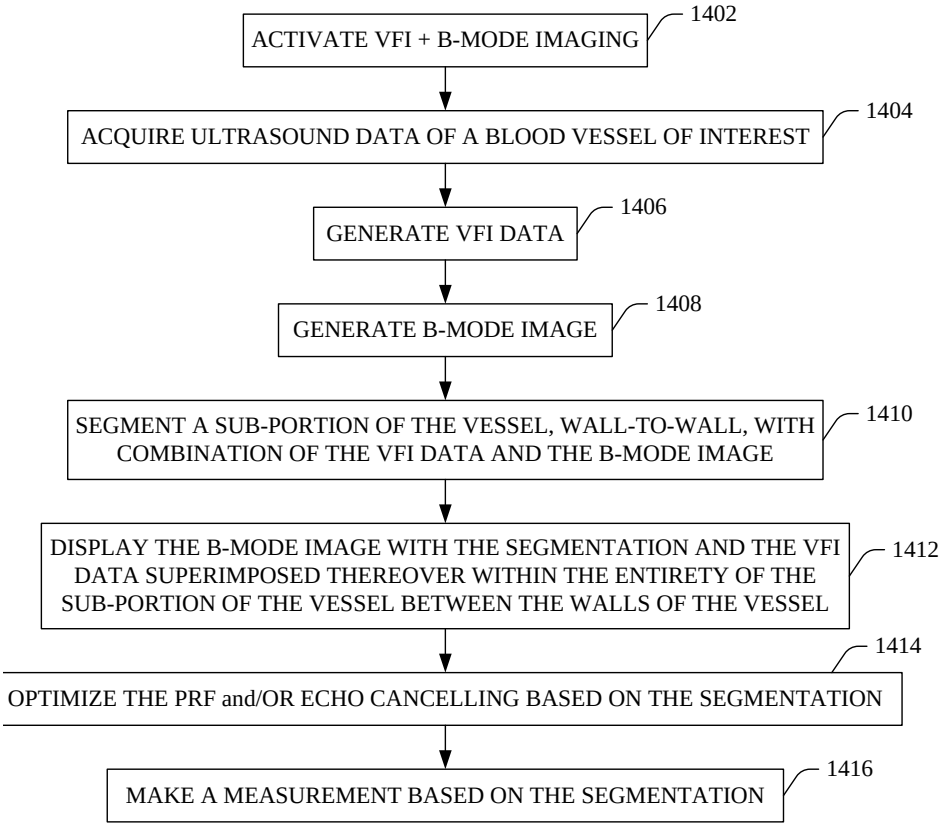

FIGURE 14

Combined Bibliography

References from Chapter 1

Thompson, R. S., B. J. Trudinger, and C. M. Cook (1985). "Doppler ultrasound waveforms in the fetal umbilical artery; Quantitative analysis technique". In: *Ultrasound Med. Biol.* 11, pp. 707–718 (cit. on p. 1).

Tjøtta, J. N., S. Tjøtta, and E. H. Verfring (1991). "Effects of focusing on the nonlinear interaction between two collinear finite amplitude sound beams". In: *J. Acoust. Soc. Am.* 89, pp. 1017–1027 (cit. on p. 2).

Pye, S., S. Wild, and W. McDicken (1992). "Adaptive time gain compensation for ultrasonic imaging". In: *Ultrasound Med. Biol.* 18.2, pp. 205–212 (cit. on pp. 1, 3).

Klesenski, K. (1996). "Automatic gain compensation in an ultrasound imaging system". In: *US Patent*, pp. 5, 579, 768. URL: http://www.google.com/patents/US5579768 (cit. on p. 3).

Mao, F., J. Gill, D. Downey, and A. Fenster (2000). "Segmentation of carotid artery in ultrasound images: Method development and evaluation technique". In: *Medical physics* 27.8, pp. 1961–1970 (cit. on p. 4).

Meire, H. B., D. O. Cosgrove, K. C. Dewbury, and P. Farrant (2001). *Abdominal and General Ultrasound*. Vol. 2. Churchill Livingstone (cit. on p. 1).

Nikolov, S. I. (2001). "Synthetic Aperture Tissue and Flow Ultrasound Imaging". PhD thesis. 2800, Lyngby, Denmark: Ørsted•DTU, Technical University of Denmark (cit. on p. 3).

Stewart, S. F. C. (2001). "Effects of transducer, velocity, Doppler angle, and instrument settings on the accuracy of color Doppler ultrasound". In: *Ultrasound Med. Biol.* 27.4, pp. 551–564. DOI: 10.1016/s0301-5629(01)00357-x (cit. on pp. 1, 2).

Harvey, C. J., J. M. Pilcher, R. J. Eckersley, M. J. Blomley, and D. O. Cosgrove (2002). "Advances in Ultrasound". In: *Clinical Radiology* 57.3, pp. 157–177 (cit. on p. 1).

Gammelmark, K. L. and J. A. Jensen (2003). "Multielement Synthetic Transmit Aperture Imaging using Temporal Encoding". In: *IEEE Trans. Med. Imag.* 22.4, pp. 552–563 (cit. on p. 3).

Schlaikjer, M., S. Torp-Pedersen, and J. A. Jensen (2003). "Simulation of RF data with tissue motion for optimizing stationary echo canceling filters". In: *Ultrasonics* 41, pp. 415–419 (cit. on p. 2).

Willadsen, J. (2004). "Investigation of Synthetic Aperture Ultrasound Cardiac Imaging". MA thesis. Lyngby, Denmark: Ørsted•DTU, Technical University of Denmark (cit. on p. 1).

Lee, D., Y. Kim, and J. Ra (2006). "Automatic time gain compensation and dynamic range control in ultrasound imaging systems". In: *Proc. SPIE Med. Imag.* 6147, pages (cit. on pp. 1, 3).

Volpicelli, G., A. Mussa, G. Garofalo, L. Cardinale, G. Casoli, F. Perotto, C. Fava, and M. Frascisco (2006). "Bedside lung ultrasound in the assessment of alveolar-interstitial syndrome". In: *Am. J. Emerg. Med.* 24.6, pp. 689–696 (cit. on p. 4).

Wardlaw, J. M., F. M. Chappell, J. J. K. Best, K. Wartolowska, and E. Berry (2006). "Non-invasive imaging compared with intra-arterial angiography in the diagnosis of symptomatic carotid stenosis: a meta-analysis". In: *Lancet* 367.9521, pp. 1503–1512 (cit. on p. 1).

Golemati, S., J. Stoitsis, E. G. Sifakis, T. Balkizas, and K. S. Nikita (2007). "Using the Hough transform to segment ultrasound images of longitudinal and transverse sections of the carotid artery". In: *Ultrasound Med. Biol.* 33.12, pp. 1918–1932 (cit. on p. 4).

OBrien, R. T. and S. P. Holmes (2007). "Recent Advances in Ultrasound Technology". In: *Clinical Techniques in Small Animal Practice* 22.3, pp. 93–103 (cit. on p. 1).

Moore, C. L., R. S. Holliday, J. Q. Hwang, and M. R. Osborne (2008). "Screening for abdominal aortic aneurysm in asymptomatic at-risk patients using emergency ultrasound". In: *The American Journal of Emergency Medicine* 26.8, pp. 883–887 (cit. on p. 1).

Volpicelli, G., L. Cardinale, G. Garofalo, and A. Veltri (2008). "Usefulness of lung ultrasound in the bedside distinction between pulmonary edema and exacerbation of COPD". In: *Am. Soc. Emerg. Radiol.* 15.3, pp. 145–151 (cit. on p. 1).

Tang, M., F. Luo, and D. Liu (2009). "Automatic Time Gain Compensation in Ultrasound Imaging System". In: *Proc. IEEE Int. Conf. Bioinfo. Biomed. Eng.* Pp. 1–4. DOI: 10.1109/ICBBE.2009.5162432 (cit. on pp. 1, 3).

Gargani, L. (2011). "Lung ultrasound: A new tool for the cardiologist". In: *Cardiovascular ultrasound* 9.1 (cit. on pp. 1, 4).

Moore, C. L. and J. A. Copel (2011). "Point-of-Care Ultrasonography". In: *New England Journal of Medicine* 364.8, pp. 749–757 (cit. on p. 1).

Santhiyakumari, N., P. Rajendran, M. Madheswaran, and S. Suresh (2011). "Detection of the intima and media layer thickness of ultrasound common carotid artery image

using efficient active contour segmentation technique". In: *Med. Biol. Eng. Comp.* 49.11, pp. 1299–1310 (cit. on p. 4).

Baker, M., J. Jensen, and C. Behrens (2013). "Inter-operator variability in defining uterine position using three-dimensional ultrasound imaging". In: *2013 IEEE Int. Ultrason. Symp.* Pp. 848–851 (cit. on p. 1).

Terkawi, A. S., D. Karakitsos, M. Elbarbary, M. Blaivas, and M. E. Durieux (2013). "Ultrasound for the anesthesiologists: present and future". In: *The scientific world journal* 2013, pp. 1–15 (cit. on p. 1).

Tong, L., A. Ortega, H. Gao, and J. D'hooge (2013). "Fast Three-Dimensional Ultrasound Cardiac Imaging Using Multi-Transmit Beam Forming: A Simulation Study". In: *Proc. IEEE Ultrason. Symp.* Pp. 1448–1451. DOI: 10.1109/ULTSYM.2013.0369 (cit. on p. 1).

Lichtenstein, D. A. (2014). "Lung ultrasound in the critically ill". In: *Ann Intensive Care* 4.1 (cit. on pp. 1, 4).

Loizou, C. P. (2014). "A review of ultrasound common carotid artery image and video segmentation techniques". In: *Med. Biol. Eng. Comp.* 52.12, pp. 1073–1093 (cit. on p. 4).

Carvalho, D. D. B., Z. Akkus, S. C. H. van den Oord, A. F. L. Schinkel, A. F. W. van der Steen, W. J. Niessen, J. G. Bosch, and S. Klein (2015). "Lumen Segmentation and Motion Estimation in B-Mode and Contrast-Enhanced Ultrasound Images of the Carotid Artery in Patients With Atherosclerotic Plaque". In: *IEEE Trans. Med. Imag.* 34.4, pp. 983–993 (cit. on p. 4).

Jensen, J. A., S. I. Nikolov, A. Yu, and D. Garcia (2016a). "Ultrasound Vector Flow Imaging I: Sequential Systems". In: *IEEE Trans. Ultrason., Ferroelec., Freq. Contr.* 63.11, pp. 1704–1721. DOI: 10.1109/TUFFC.2016.2600763 (cit. on p. 4).

— (2016b). "Ultrasound Vector Flow Imaging II: Parallel Systems". In: *IEEE Trans. Ultrason., Ferroelec., Freq. Contr.* 63.11, pp. 1722–1732. DOI: 10.1109/TUFFC.2016.2598180 (cit. on p. 4).

References from Chapter 2

Savitzky, A. and M. J. E. Golay (1964). "Smoothing and differentiation of data by simplified least squares procedures". In: *Anal. Chem.* 36.8, pp. 1627–1639 (cit. on p. 24).

Kuc, R., M. Schwartz, and L. Micsky (1976). "Parametric Estimation of the Acoustic Attenuation Coefficient Slope for Soft Tissue". In: *Proc. IEEE Ultrason. Symp.* Pp. 44–47 (cit. on p. 26).

Kuc, R. (1984). “Estimating acoustic attenuation from reflected ultrasound signals: Comparison of spectral-shift and spectral-difference approaches”. In: *IEEE Trans. Acous., Speech, Sig. Pro.* 32.1, pp. 1–6 (cit. on p. 26).

Inbar, D. and M. Delevy (1989). *Time gain compensation for ultrasonic medical imaging systems*. US Patent 4,852,576 (cit. on p. 16).

Pye, S., S. Wild, and W. McDicken (1992). “Adaptive time gain compensation for ultrasonic imaging”. In: *Ultrasound Med. Biol.* 18.2, pp. 205–212 (cit. on p. 16).

Jensen, J. A. (1996). *Estimation of Blood Velocities Using Ultrasound: A Signal Processing Approach*. New York: Cambridge University Press (cit. on pp. 13, 14).

Klesenski, K. (1996). *Automatic gain compensation in an ultrasound imaging system*. US Patent 5,579,768 (cit. on p. 16).

Orfanidis, S. J. (1996). *Introduction to signal processing*. Pearson Education, Inc. (cit. on p. 24).

Golyandina, N., V. Nekrutkin, and A. A. Zhigljavsky (2001). *Analysis of time series structure: SSA and related techniques*. CRC press (cit. on pp. 24, 25).

Lee, D., Y. Kim, and J. Ra (2006). “Automatic time gain compensation and dynamic range control in ultrasound imaging systems”. In: *Proc. SPIE Med. Imag.* 6147, pages (cit. on pp. 15, 16).

Alexandrov, T. (2008). *A method of trend extraction using singular spectrum analysis*. Tech. rep. arXiv preprint arXiv:0804.3367 (cit. on p. 25).

Klimonda, Z., J. Litniewski, and A. Nowicki (2009). “Spatial Resolution of Attenuation Imaging”. In: *Archives of Acoustics* 34.4, pp. 461–470 (cit. on p. 28).

Tang, M., F. Luo, and D. Liu (2009). “Automatic Time Gain Compensation in Ultrasound Imaging System”. In: *Proc. IEEE Int. Conf. Bioinfo. Biomed. Eng.* Pp. 1–4. DOI: 10.1109/ICBBE.2009.5162432 (cit. on p. 16).

Hemmsen, M. C., M. M. Petersen, S. I. Nikolov, M. B., Nielsen, and J. A. Jensen (2010). “Ultrasound image quality assessment: A framework for evaluation of clinical image quality”. In: *Proc. SPIE Med. Imag.* Vol. 76291. Medical Imaging 2010: Ultrasonic Imaging, Tomography, and Therapy, pp. 76290C–12 (cit. on p. 30).

Szabo, T. L. (2014). *Diagnostic ultrasound imaging: Inside out*. 2nd ed. Elsevier (Oxford, UK) (cit. on p. 13).

References from Chapter 3

Burckhardt, C. B., P.-A. Grandchamp, and H. Hoffmann (1974). “An Experimental 2 MHz Synthetic Aperture Sonar System Intended for Medical Use”. In: *IEEE Trans. Son. Ultrason.* 21.1, pp. 1–6 (cit. on pp. 40, 41).

Bennett, S., D. K. Peterson, D. Corl, and G. S. Kino (1982). “A real-time synthetic aperture digital acoustic imaging system”. In: *Acoust. Imaging*. Ed. by P. Alais and A. F. Metherell. Vol. 10, pp. 669–692 (cit. on p. 42).

Mayer, K., R. Marklein, K. J. Langenberg, and T. Kreutter (1990). “Three-dimensional imaging system based on Fourier transform synthetic aperture focusing technique”. In: *Ultrasonics* 28, pp. 241–255 (cit. on p. 41).

Busse, L. J. (1992). “Three-dimensional imaging using a frequency-domain synthetic aperture focusing technique”. In: *IEEE Trans. Ultrason., Ferroelec., Freq. Contr.* 39, pp. 174–179 (cit. on p. 41).

Jensen, J. A. and N. B. Svendsen (1992). “Calculation of Pressure Fields from Arbitrarily Shaped, Apodized, and Excited Ultrasound Transducers”. In: *IEEE Trans. Ultrason., Ferroelec., Freq. Contr.* 39, pp. 262–267 (cit. on p. 48).

O’Donnell, M. and L. J. Thomas (1992). “Efficient synthetic aperture imaging from a circular aperture with possible application to catheter-based imaging”. In: *IEEE Trans. Ultrason., Ferroelec., Freq. Contr.* 39, pp. 366–380 (cit. on p. 42).

Cooley, C. R. and B. S. Robinson (1994). “Synthetic aperture imaging using partial datasets”. In: *Proc. IEEE Ultrason. Symp.* Pp. 1539–1542. DOI: 10.1109/ULTSYM.1994.401884 (cit. on p. 58).

Ylitalo, J. T. (1994). “In-vitro study of computed ultrasound imaging method”. In: *Proc. IEEE Ultrason. Symp.* Pp. 1577–1580 (cit. on p. 42).

Ylitalo, J. T. and H. Ermert (1994). “Ultrasound synthetic aperture imaging: Monostatic approach”. In: *IEEE Trans. Ultrason., Ferroelec., Freq. Contr.* 41, pp. 333–339 (cit. on p. 42).

Karaman, M., P. C. Li, and M. O’Donnell (1995). “Synthetic aperture imaging for small scale systems”. In: *IEEE Trans. Ultrason., Ferroelec., Freq. Contr.* 42, pp. 429–442 (cit. on p. 42).

Ylitalo, J. T. (1995). “Synthetic aperture ultrasound imaging using a convex array”. In: *Proc. IEEE Ultrason. Symp.* Pp. 1337–1340 (cit. on p. 42).

Goodman, J. W. (1996). *Introduction to Fourier optics*. Second. New York: McGraw Hill Inc. (cit. on p. 41).

Jensen, J. A. (1996). “Field: A Program for Simulating Ultrasound Systems”. In: *Med. Biol. Eng. Comp.* 10th Nordic-Baltic Conference on Biomedical Imaging, Vol. 4, Supplement 1, Part 1, pp. 351–353 (cit. on p. 48).

Ylitalo, J. T. (1996a). “A fast ultrasonic synthetic aperture imaging method: application to NDT”. In: *Ultrasonics*, pp. 331–333 (cit. on p. 42).

— (1996b). “On the signal-to-noise ratio of a synthetic aperture ultrasound imaging method”. In: *Eur. J. Ultrasound* 3, pp. 277–281 (cit. on p. 42).

Barthez, P. Y., R. Léveillé, and P. V. Scrivani (1997). "Side lobes and grating lobes artifacts in ultrasound imaging". In: *Veterinary Radiology & Ultrasound* 38.5, pp. 387–393 (cit. on p. 43).

Vray, D., T. Rastello, F. Schoofs, and P. Delachartre (1997). "Improving the spatial resolution of intravascular ultrasound imaging with synthetic aperture Fourier-based methods". In: *Proc. IEEE Ultrason. Symp.* Pp. 1531–1534 (cit. on p. 42).

Karaman, M. and M. O'Donnell (1998). "Subaperture processing for ultrasonic imaging". In: *IEEE Trans. Ultrason., Ferroelec., Freq. Contr.* 45, pp. 126–135 (cit. on p. 42).

Lockwood, G. R., J. R. Talman, and S. S. Brunke (1998). "Real-time 3-D ultrasound imaging using sparse synthetic aperture beamforming". In: *IEEE Trans. Ultrason., Ferroelec., Freq. Contr.* 45, pp. 980–988 (cit. on pp. 42, 58).

Nikolov, S. I., K. Gammelmark, and J. A. Jensen (1999). "Recursive ultrasound imaging". In: *Proc. IEEE Ultrason. Symp.* Vol. 2, pp. 1621–1625 (cit. on p. 42).

Soumekh, M. (1999). *Synthetic aperture radar. Signal processing with MATLAB algorithms*. New York: John Wiley & Sons, Inc. (cit. on p. 42).

Gammelmark, K. L. and J. A. Jensen (2003). "Multielement Synthetic Transmit Aperture Imaging using Temporal Encoding". In: *IEEE Trans. Med. Imag.* 22.4, pp. 552–563 (cit. on p. 42).

Nikolov, S. I. and J. A. Jensen (2003). "In-vivo Synthetic Aperture Flow Imaging in Medical Ultrasound". In: *IEEE Trans. Ultrason., Ferroelec., Freq. Contr.* 50.7, pp. 848–856 (cit. on p. 42).

Huang, J., P. W. Que, and J. H. Jin (2004). "A Parametric Study of Beam Steering for Ultrasonic Linear Phased Array Transducer". In: *Russ. J. Nondestr. Test.* 40.4, pp. 254–259 (cit. on p. 43).

Jensen, J. A. and S. I. Nikolov (2004). "Directional Synthetic Aperture Flow Imaging". In: *IEEE Trans. Ultrason., Ferroelec., Freq. Contr.* 51, pp. 1107–1118 (cit. on p. 42).

Deb, K. (2005). "Multi-objective optimization". In: *Search methodologies*. Springer (cit. on p. 47).

Jensen, J. A. (2006). "Spectral velocity estimation in ultrasound using sparse data sets". In: *J. Acoust. Soc. Am.* vol 120(1), pp. 211–220 (cit. on p. 41).

Jensen, J. A., S. Nikolov, K. L. Gammelmark, and M. H. Pedersen (2006). "Synthetic Aperture Ultrasound Imaging". In: *Ultrasonics* 44, e5–e15 (cit. on p. 41).

Coello, C. A. C., G. B. Lamont, and D. A. V. Veldhuizen (2007). "Basic Concepts". In: *Evolutionary Algorithms for Solving Multi-Objective Problems*. Springer (cit. on p. 47).

Oddershede, N. and J. A. Jensen (2007). "Effects influencing focusing in synthetic aperture vector flow imaging". In: *IEEE Trans. Ultrason., Ferroelec., Freq. Contr.* 54.9, pp. 1811–1825 (cit. on p. 43).

Ranganathan, K. and W. F. Walker (2007). "Cystic Resolution: A Performance Metric for Ultrasound Imaging Systems". In: *IEEE Trans. Ultrason., Ferroelec., Freq. Contr.* 54.4, pp. 782–792. DOI: 10.1109/TUFFC.2007.311 (cit. on pp. 45, 46).

Guenther, D. A. and W. F. Walker (2009). "Generalized cystic resolution: a metric for assessing the fundamental limits on beamformer performance". In: *IEEE Trans. Ultrason., Ferroelec., Freq. Contr.* 56.1, pp. 77–90 (cit. on p. 45).

Hastie, T., R. Tibshirani, and J. Friedman (2009). *The Elements of Statistical Learning Data Mining, Inference, and Prediction*. Second edition. Springer Series in Statistics (cit. on p. 58).

Hansen, J. M., M. C. Hemmsen, and J. A. Jensen (2011). "An object-oriented multi-threaded software beamformation toolbox". In: *Proc. SPIE Med. Imag.* Vol. 7968, pages. DOI: 10.1117/12.878178 (cit. on p. 49).

Lediju, M. A., G. E. Trahey, B. C. Byram, and J. J. Dahl (2011). "Short-lag spatial coherence of backscattered echoes: imaging characteristics". In: *IEEE Trans. Ultrason., Ferroelec., Freq. Contr.* 58.7, pp. 1377–1388. DOI: 10.1109/TUFFC.2011.1957 (cit. on pp. 45, 46).

Denarie, B., T. A. Tangen, I. K. Ekroll, N. Rolim, H. H. Torp, T. Bjastad, and L. Løvstakken (2013). "Coherent Plane Wave Compounding for Very High Frame Rate Ultrasonography of Rapidly Moving Targets". In: *IEEE Trans. Ultrason., Ferroelec., Freq. Contr.* 32.7, pp. 1265–1276 (cit. on p. 58).

Jensen, J. A., H. Holten-Lund, R. T. Nilsson, M. Hansen, U. D. Larsen, R. P. Domsten, B. G. Tomov, M. B. Stuart, S. I. Nikolov, M. J. Pihl, Y. Du, J. H. Rasmussen, and M. F. Rasmussen (2013). "SARUS: A Synthetic Aperture Real-time Ultrasound System". In: *IEEE Trans. Ultrason., Ferroelec., Freq. Contr.* 60.9, pp. 1838–1852 (cit. on p. 50).

Ponnle, A., H. Hasegawa, and H. Kanai (2013). "Suppression of grating lobe artifacts in ultrasound images formed from diverging transmitting beams by modulation of receiving beams". In: *Ultrasound Med. Biol.* 39.4, pp. 681–691. DOI: 10.1016/j.ultrasmedbio.2012.10.019 (cit. on p. 58).

Gammelmark, K. L. and J. A. Jensen (2014). "2-D Tissue Motion Compensation of Synthetic Transmit Aperture Images". In: *IEEE Trans. Ultrason., Ferroelec., Freq. Contr.* Pp. 594–610. DOI: http://dx.doi.org/10.1109/TUFFC.2014.2948 (cit. on p. 58).

Jensen, J. A. (2014). "A Multi-threaded Version of Field II". In: *Proc. IEEE Ultrason. Symp.* IEEE, pp. 2229–2232 (cit. on p. 48).

Szabo, T. L. (2014). *Diagnostic ultrasound imaging: Inside out*. 2nd ed. Elsevier (Oxford, UK) (cit. on pp. 43, 45, 46).

Yiu, B. Y., S. S. Lai, and A. C. Yu (2014). "Vector projectile imaging: time-resolved dynamic visualization of complex flow patterns." In: *Ultrasound Med. Biol.* 40.9, pp. 2295–2309 (cit. on p. 42).

Stuart, M. B., J. Jensen, T. Di Ianni, and J. A. Jensen (2015). "Image quality degradation from transmit delay profile quantization". In: *Proc. IEEE Ultrason. Symp.* Pp. 1–4. DOI: 10.1109/ULTSYM.2015.0126 (cit. on p. 58).

Hasegawa, H. and C. L. de Korte (2016). "Impact of element pitch on synthetic aperture ultrasound imaging". In: *J. Med. Ultrason.* Pp. 1–9. DOI: 10.1007/s10396-016-0700-6 (cit. on p. 58).

Jensen, J., M. B. Stuart, and J. A. Jensen (2016). "Optimized Plane Wave Imaging for Fast and High-Quality Ultrasound Imaging". In: *IEEE Trans. Ultrason., Ferroelec., Freq. Contr.* 63.11, pp. 1922–1934. DOI: 10.1109/TUFFC.2016.2591980 (cit. on p. 43).

References from Chapter 4

Trahey, G. E., J. W. Allison, and O. T. von Ramm (1987). "Angle independent ultrasonic detection of blood flow". In: *IEEE Trans. Biomed. Eng.* BME-34, pp. 965–967 (cit. on p. 66).

Picot, P. A. and P. M. Embree (1994). "Quantitative volume flow estimation using velocity profiles". In: *IEEE Trans. Ultrason., Ferroelec., Freq. Contr.* 41, pp. 340–345 (cit. on p. 66).

Jensen, J. A. (1996a). *Apparatus and method for determining movements and velocities of moving objects*. International patent PCT/DK97/00287 (cit. on p. 66).

— (1996b). *Estimation of Blood Velocities Using Ultrasound: A Signal Processing Approach*. New York: Cambridge University Press (cit. on p. 69).

Anderson, M. E. (1998). "Multi-dimensional velocity estimation with ultrasound using spatial quadrature". In: *IEEE Trans. Ultrason., Ferroelec., Freq. Contr.* 45, pp. 852–861 (cit. on p. 67).

Jensen, J. A. and P. Munk (1998). "A New Method for Estimation of Velocity Vectors". In: *IEEE Trans. Ultrason., Ferroelec., Freq. Contr.* 45, pp. 837–851 (cit. on pp. 66–68, 70).

Jensen, J. A. (2000). *Estimation of vector velocity*. International patent PCT/DK00/00243 (cit. on p. 66).

— (2001). "A New Estimator for Vector Velocity Estimation". In: *IEEE Trans. Ultrason., Ferroelec., Freq. Contr.* 48.4, pp. 886–894 (cit. on p. 69).

Nikolov, S. I. (2001). "Synthetic Aperture Tissue and Flow Ultrasound Imaging". PhD thesis. 2800, Lyngby, Denmark: Ørsted•DTU, Technical University of Denmark (cit. on p. 71).

Nikolov, S. I. and J. A. Jensen (2001). "Velocity estimation using synthetic aperture imaging". In: *Proc. IEEE Ultrason. Symp.* Pp. 1409–1412 (cit. on p. 66).

Jensen, J. A. and S. I. Nikolov (2002). "Transverse flow imaging using synthetic aperture directional beamforming". In: *Proc. IEEE Ultrason. Symp.* Pp. 1488–1492 (cit. on p. 66).

— (2004). "Directional Synthetic Aperture Flow Imaging". In: *IEEE Trans. Ultrason., Ferroelec., Freq. Contr.* 51, pp. 1107–1118 (cit. on p. 66).

Kruskal, J. B., P. A. Newman, L. G. Sammons, and R. A. Kane (2004). "Optimizing Doppler and Color Flow US: Application to Hepatic Sonography". In: *Radiographics* 24.3, pp. 657–675 (cit. on p. 66).

Jensen, J. A., S. Nikolov, K. L. Gammelmark, and M. H. Pedersen (2006). "Synthetic Aperture Ultrasound Imaging". In: *Ultrasonics* 44, e5–e15 (cit. on p. 66).

Udesen, J. and J. A. Jensen (2006). "Investigation of Transverse Oscillation Method". In: *IEEE Trans. Ultrason., Ferroelec., Freq. Contr.* 53, pp. 959–971 (cit. on pp. 66, 68).

Hansen, P. M., M. M. Pedersen, K. L. Hansen, M. B. Nielsen, and J. A. Jensen (2011). "Demonstration of a vector velocity technique". In: *Ultraschall in Med.* 32, pp. 213–215 (cit. on p. 66).

BK Medical (2015). *http://bkultrasound.com/bk-medical/VectorFlow* (cit. on p. 67).

Jensen, J. A., S. I. Nikolov, A. Yu, and D. Garcia (2016a). "Ultrasound Vector Flow Imaging I: Sequential Systems". In: *IEEE Trans. Ultrason., Ferroelec., Freq. Contr.* 63.11, pp. 1704–1721. DOI: 10.1109/TUFFC.2016.2600763 (cit. on p. 66).

— (2016b). "Ultrasound Vector Flow Imaging II: Parallel Systems". In: *IEEE Trans. Ultrason., Ferroelec., Freq. Contr.* 63.11, pp. 1722–1732. DOI: 10.1109/TUFFC.2016.2598180 (cit. on p. 66).

Villagomez-Hoyos, C. A., M. B. Stuart, K. L. Hansen, M. B. Nielsen, and J. A. Jensen (2016). "Accurate Angle Estimator for High Frame Rate 2-D Vector Flow Imaging". In: *IEEE Trans. Ultrason., Ferroelec., Freq. Contr.* 63.6, pp. 842–853 (cit. on pp. 66, 72).

References from Chapter 5

Smeulders, A., C. Cornelisse, A. Vossepoel, and J. Ploem (1978). "An image segmentation approach to the analysis of nuclear texture of cervical cells". In: *Acta histochemica. Supplement band* 20, pp. 217–222 (cit. on p. 78).

Beucher, S. and C. Lantuejoul (1979). “Use of watersheds in contour detection”. In: (cit. on p. 79).

Borgefors, G. (1986). “Distance Transformations in Digital Images”. In: *Comput. Vision Graph. Image Process.* 34.3, pp. 344–371 (cit. on p. 81).

Kondo, A. and K. Taniguchi (1986). “Evaluation of the chromatin for cell images”. In: *Systems and Computers in Japan* 17.9, pp. 11–19 (cit. on p. 78).

Meyer, F. and S. Beucher (1990). “Morphological segmentation”. In: *Journal of Visual Communication and Image Representation* 1.1, pp. 21–46 (cit. on pp. 80, 81).

Adams, R. and L. Bischof (1994). “Seeded Region Growing”. In: *IEEE Trans. Pattern Anal. Mach. Intell.* 16.6, pp. 641–647 (cit. on p. 79).

Jensen, J. A. (1996). *Estimation of Blood Velocities Using Ultrasound: A Signal Processing Approach*. New York: Cambridge University Press (cit. on p. 83).

Mojsilovic, A., M. Popovic, N. Amodaj, R. Babic, and M. Ostojic (1997). “Automatic segmentation of intravascular ultrasound images: a texture-based approach”. In: *Annals of biomedical engineering* 25.6, pp. 1059–1071 (cit. on p. 76).

Wendelhag, I., Q. Liang, T. Gustavsson, and J. Wikstrand (1997). “A new automated computerized analyzing system simplifies readings and reduces the variability in ultrasound measurement of intima-media thickness”. In: *Stroke* 28.11, pp. 2195–2200 (cit. on p. 76).

Jensen, J. A. and P. Munk (1998). “A New Method for Estimation of Velocity Vectors”. In: *IEEE Trans. Ultrason., Ferroelec., Freq. Contr.* 45, pp. 837–851 (cit. on pp. 83, 86).

Evans, D. H. and W. N. McDicken (2000). *Doppler Ultrasound, Physics, Instrumentation, and Signal Processing*. New York: John Wiley & Sons (cit. on p. 83).

Mao, F., J. Gill, D. Downey, and A. Fenster (2000). “Segmentation of carotid artery in ultrasound images: Method development and evaluation technique”. In: *Medical physics* 27.8, pp. 1961–1970 (cit. on p. 76).

Kamgar-Parsi, B. and B. Kamgar-Parsi (2001). “Improved image thresholding for object extraction in IR images”. In: *Int. Conf. Image Processing*. Vol. 1, pp. 758–761 (cit. on p. 81).

Selzer, R. H., W. J. Mack, P. L. Lee, H. Kwong-Fu, and H. N. Hodis (2001). “Improved common carotid elasticity and intima-media thickness measurements from computer analysis of sequential ultrasound frames”. In: *Atherosclerosis* 154.1, pp. 185–193 (cit. on p. 76).

Cheng, D., A. Schmidt-Trucksaess, K. Cheng, and H. Burkhardt (2002). “Using snakes to detect the intimal and adventitial layers of the common carotid artery wall in sonographic images”. In: *Computer methods and programs in biomedicine* 67.1, pp. 27–37 (cit. on p. 76).

Gutierrez, M., P. Pilon, S. Lage, L. Kopel, R. Carvalho, and S. Furuie (2002). "Automatic measurement of carotid diameter and wall thickness in ultrasound images". In: *Computers in Cardiology*. IEEE, pp. 359–362 (cit. on p. 76).

Xiao, G., M. Brady, J. A. Noble, and Y. Zhang (2002). "Segmentation of ultrasound B-mode images with intensity inhomogeneity correction". In: *IEEE Trans. Med. Imag.* 21.1, pp. 48–57 (cit. on p. 76).

Grant, E. G., C. B. Benson, G. L. Moneta, A. V. Alexandrov, J. D. Baker, E. I. Bluth, B. A. Carroll, and et al. (2003). "Carotid artery stenosis: gray-scale and Doppler US diagnosis - Society of radiologists in ultrasound consensus conference". In: *Radiology* 229.2. M. Eliasziw and J. Gocke and B. S. Hertzberg, pp. 340–346. DOI: 10.1148/radiol.2292030516 (cit. on p. 82).

Steel, R., K. V. Ramnarine, F. Davidson, P. J. Fish, and P. R. Hoskins (2003). "Angle-independent estimation of maximum velocity through stenoses using vector Doppler ultrasound". In: *Ultrasound Med. Biol.* 29.4, pp. 575–584. DOI: http://dx.doi.org/10.1016/S0301-5629(02)00736-6 (cit. on p. 83).

Bengtsson, E., C. Wahlby, and J. Lindblad (2004). "Robust cell image segmentation methods". In: *Patt. Recog. Im. anal.* 14.2, pp. 157–167 (cit. on p. 81).

Stein, J. H., C. E. Korcarz, M. E. Mays, P. S. Douglas, M. Palta, H. Zhang, T. LeCaire, D. Paine, D. Gustafson, and L. Fan (2005). "A semiautomated ultrasound border detection program that facilitates clinical measurement of ultrasound carotid intima-media thickness". In: *J. Am. Soc. Echocardiog.* 18.3, pp. 244–251 (cit. on p. 76).

Delsanto, S., F. Molinari, P. Giustetto, W. Liboni, S. Badalamenti, and J. S. Suri (2007). "Characterization of a completely user-independent algorithm for carotid artery segmentation in 2-D ultrasound images". In: *IEEE Transactions on Instrumentation and Measurement* 56.4, pp. 1265–1274 (cit. on p. 76).

Golemati, S., J. Stoitsis, E. G. Sifakis, T. Balkizas, and K. S. Nikita (2007). "Using the Hough transform to segment ultrasound images of longitudinal and transverse sections of the carotid artery". In: *Ultrasound Med. Biol.* 33.12, pp. 1918–1932 (cit. on p. 76).

Loizou, C., C. Pattichis, M. Pantziaris, T. Tyllis, and A. Nicolaides (2007). "Snakes based segmentation of the common carotid artery intima media". In: *Medical & Biological Engineering & Computing* 45.1, pp. 35–49. DOI: 10.1007/s11517-006-0140-3. URL: http://dx.doi.org/10.1007/s11517-006-0140-3 (cit. on p. 76).

Faita, F., V. Gemignani, E. Bianchini, C. Giannarelli, L. Ghiadoni, and M. Demi (2008). "Real-time measurement system for evaluation of the carotid intima-media thickness with a robust edge operator". In: *Journal of Ultrasound in Medicine* 27.9, pp. 1353–1361 (cit. on p. 76).

Destrempes, F., J. Meunier, M. Giroux, G. Soulez, and G. Cloutier (2009). “Segmentation in ultrasonic B-mode images of healthy carotid arteries using mixtures of Nakagami distributions and stochastic optimization”. In: *IEEE Trans. Med. Imag.* 28.2, pp. 215–229 (cit. on p. 76).

Rossi, A. C., P. J. Brands, and A. P. Hoeks (2010). “Automatic localization of intimal and adventitial carotid artery layers with noninvasive ultrasound: a novel algorithm providing scan quality control”. In: *Ultrasound Med. Biol.* 36.3, pp. 467–479 (cit. on p. 76).

Santhiyakumari, N., P. Rajendran, M. Madheswaran, and S. Suresh (2011). “Detection of the intima and media layer thickness of ultrasound common carotid artery image using efficient active contour segmentation technique”. In: *Med. Biol. Eng. Comp.* 49.11, pp. 1299–1310 (cit. on p. 76).

Molinari, F., C. S. Pattichis, G. Zeng, L. Saba, U. R. Acharya, R. Sanfilippo, A. Nicolaides, and J. S. Suri (2012). “Completely automated multiresolution edge snappera new technique for an accurate carotid ultrasound IMT measurement: clinical validation and benchmarking on a multi-institutional database”. In: *IEEE Transactions on Image Processing* 21.3, pp. 1211–1222 (cit. on p. 76).

Pedersen, M. M., M. J. Pihl, P. Haugaard, J. M. Hansen, K. L. Hansen, M. B. Nielsen, and J. A. Jensen (2012). “Comparison of Real-Time In Vivo Spectral and Vector Velocity Estimation”. In: *Ultrasound Med. Biol.* 38.1, pp. 145–151 (cit. on p. 77).

Petroudi, S., C. Loizou, M. Pantziaris, and C. Pattichis (2012). “Segmentation of the common carotid intima-media complex in ultrasound images using active contours”. In: *IEEE Trans. Biomed. Eng.* 59.11, pp. 3060–3069 (cit. on p. 76).

Reutern, G. M. von, M. W. Goertler, N. M. Bornstein, M. D. Sette, D. H. Evans, A. Hetzel, M. Kaps, F. Perren, and et al. (2012). “Grading Carotid Stenosis Using Ultrasonic Methods”. In: *Stroke* 43.3, pp. 916–921. DOI: 10.1161/STROKEAHA.111.636084 (cit. on p. 82).

Xu, X., Y. Zhou, X. Cheng, E. Song, and G. Li (2012). “Ultrasound intima–media segmentation using Hough transform and dual snake model”. In: *Computerized Medical Imaging and Graphics* 36.3, pp. 248–258 (cit. on p. 76).

Hansen, P. M., S. Heerwagen, M. M. Pedersen, M. Rix, L. Lønn, M. B. Nielsen, J. B. Olesen, M. J. Pihl, and J. A. Jensen (2013). “Vector Volume Flow in Arteriovenous Fistulas”. In: *Proc. IEEE Ultrason. Symp.* Pp. 2026–2029 (cit. on p. 82).

Yang, X., W. He, K. Li, J. Jin, X. Zhang, M. Yuchi, and M. Ding (2013). “Ultrasound common carotid artery segmentation based on active shape model”. In: *Computational and mathematical methods in medicine*, pp. 1–11 (cit. on p. 76).

Hansen, P. M., J. B. Olesen, M. J. Pihl, T. Lange, S. Heerwagen, M. M. Pedersen, M. Rix, L. Lønn, J. A. Jensen, and M. B. Nielsen (2014). “Volume Flow in Arteriovenous

Fistulas using Vector Velocity Ultrasound". In: *Ultrasound Med. Biol.* 40.11, pp. 2707–2714 (cit. on p. 82).

Jensen, J., J. B. Olesen, P. M. Hansen, M. B. Nielsen, and J. A. Jensen (2014). "Accuracy and Sources of Error for an Angle Independent Volume Flow Estimator". In: *Proc. IEEE Ultrason. Symp.* Pp. 1714–1717 (cit. on pp. 82, 83).

Menchon-Lara, R., M. C. Bastida-Jumilla, J. Morales-Sanchez, and J. Sancho-Gomez (2014). "Automatic detection of the intima-media thickness in ultrasound images of the common carotid artery using neural networks". In: *Medical biological engineering computing* 52.2, pp. 169–181 (cit. on p. 76).

Carvalho, D. D. B., Z. Akkus, S. C. H. van den Oord, A. F. L. Schinkel, A. F. W. van der Steen, W. J. Niessen, J. G. Bosch, and S. Klein (2015). "Lumen Segmentation and Motion Estimation in B-Mode and Contrast-Enhanced Ultrasound Images of the Carotid Artery in Patients With Atherosclerotic Plaque". In: *IEEE Trans. Med. Imag.* 34.4, pp. 983–993 (cit. on p. 76).

Brandt, A. H., J. Jensen, K. L. Hansen, P. M. Hansen, T. Lange, M. Rix, J. A. Jensen, L. Lönn, and M. B. Nielsen (2016). "Surveillance for Hemodialysis Access Stenosis: Usefulness of Ultrasound Vector Volume Flow". In: *J. Vascul. Access.* Accepted for publication (cit. on p. 82).

Jensen, J. A. (2016). "Quantitative Measurements using Ultrasound Vector Flow Imaging". In: *Proc. IEEE Ultrason. Symp.* Pp. 1–4 (cit. on p. 83).

Jensen, J., J. B. Olesen, M. B. Stuart, P. M. Hansen, M. B. Nielsen, and J. A. Jensen (2016). "Vector velocity volume flow estimation: Sources of error and corrections applied for arteriovenous fistulas". In: *Ultrasonics* 70, pp. 136–146. DOI: http://dx.doi.org/10.1016/j.ultras.2016.04.023 (cit. on pp. 83, 84).

References from Chapter 6

Meyer, F. (1977). "Contrast features extraction, Special Issues of Practical Metallography". In: *Quant. Anal. Microstruct. Mat. Sc. Bio. Med.* Vol. 8 (cit. on p. 102).

Lichtenstein, D., G. Mézière, P. Biderman, A. Gepner, and O. Barré (1997). "The Comet-tail Artifact. An ultrasound sign of alveolar-interstitial syndrome". In: *Am. J. Respir. Crit. Care. Med.* 156.5, pp. 1640–1646 (cit. on p. 98).

Lichtenstein, D., G. Meziere, P. Biderman, and A. Gepner (1999). "The comet-tail artifact: An ultrasound sign ruling out pneumothorax". In: *Intensive Care Medicine* 25.4, pp. 383–388 (cit. on p. 98).

Jambrik, Z., S. Monti, V. Coppola, E. Agricola, G. Mottola, M. Miniati, and E. Picano (2004). "Usefulness of ultrasound lung comets as a nonradiologic sign of extravascular lung water". In: *Am. J. Cardiology* 93.10, pp. 1265–1270 (cit. on p. 98).

E.Agricola, T. Bove, M. Oppizzi, G. Marino, A. Zangrillo, A. Margonato, and E. Picano (2005). "Ultrasound Comet-Tail Images: A Marker Of Pulmonary Edema: A Comparative Study With Wedge Pressure And Extravascular Lung Water". In: *Chest* 127.5, pp. 1690–1695 (cit. on p. 98).

Grady, L. (2006). "Random Walks for Image Segmentation". In: *IEEE. Trans Patt. Ana. Mach. Int.* 28.11, pp. 1768–1783 (cit. on p. 100).

Volpicelli, G., A. Mussa, G. Garofalo, L. Cardinale, G. Casoli, F. Perotto, C. Fava, and M. Frascisco (2006). "Bedside lung ultrasound in the assessment of alveolar-interstitial syndrome". In: *Am. J. Emerg. Med.* 24.6, pp. 689–696 (cit. on p. 98).

Gargani, L., V. Lionetti, C. D. Cristofano, G. Bevilacqua, F. Recchia, and E. Picano (2007). "Early detection of acute lung injury uncoupled to hypoxemia in pigs using ultrasound lung comets". In: *Crit Care Med.* 35.12, pp. 2769–2774 (cit. on p. 98).

Gargani, L., F. Frassi, G. Soldati, P. Tesorio, M. Gheorghiade, and E. Picano (2008). "Ultrasound lung comets for the differential diagnosis of acute cardiogenic dyspnoea: A comparison with natriuretic peptides". In: *Eur. J. Heart Failure* 10.1, pp. 70–77 (cit. on p. 98).

Volpicelli, G., L. Cardinale, G. Garofalo, and A. Veltri (2008). "Usefulness of lung ultrasound in the bedside distinction between pulmonary edema and exacerbation of COPD". In: *Am. Soc. Emerg. Radiol.* 15.3, pp. 145–151 (cit. on pp. 99, 107).

Gargani, L. (2011). "Lung ultrasound: A new tool for the cardiologist". In: *Cardiovascular ultrasound* 9.1 (cit. on pp. 98, 99).

Karamalis, A., W. Wein, T. Klein, and N. Navab (2012). "Ultrasound confidence maps using random walks". In: *Med. Image Anal.* 16.6, pp. 1101–1112 (cit. on pp. 100, 101).

Lichtenstein, D. A. (2014). "Lung ultrasound in the critically ill". In: *Ann Intensive Care* 4.1 (cit. on p. 98).

References from Chapter 7

Klesenski, K. (1996). *Automatic gain compensation in an ultrasound imaging system*. US Patent 5,579,768 (cit. on p. 113).

Harvey, C. J., J. M. Pilcher, R. J. Eckersley, M. J. Blomley, and D. O. Cosgrove (2002). "Advances in Ultrasound". In: *Clinical Radiology* 57.3, pp. 157–177 (cit. on p. 113).

Lee, D., Y. Kim, and J. Ra (2006). “Automatic time gain compensation and dynamic range control in ultrasound imaging systems”. In: *Proc. SPIE Med. Imag.* 6147, pages (cit. on p. 113).

OBrien, R. T. and S. P. Holmes (2007). “Recent Advances in Ultrasound Technology”. In: *Clinical Techniques in Small Animal Practice* 22.3, pp. 93–103 (cit. on p. 113).

Tang, M., F. Luo, and D. Liu (2009). “Automatic Time Gain Compensation in Ultrasound Imaging System”. In: *Proc. IEEE Int. Conf. Bioinfo. Biomed. Eng.* Pp. 1–4. DOI: 10.1109/ICBBE.2009.5162432 (cit. on p. 113).

Baker, M., J. Jensen, and C. Behrens (2013). “Inter-operator variability in defining uterine position using three-dimensional ultrasound imaging”. In: *2013 IEEE Int. Ultrason. Symp.* Pp. 848–851 (cit. on p. 113).

References from Paper A

Savitzky, A. and M. J. E. Golay (1964). “Smoothing and differentiation of data by simplified least squares procedures”. In: *Anal. Chem.* 36.8, pp. 1627–1639 (cit. on p. 121).

Kuc, R. and M. Schwartz (1979). “Estimating the Acoustic Attenuation Coefficient Slope for Liver from Reflected Ultrasound Signals”. In: *IEEE Transactions on Sonics and Ultrasonics* 26.5, pp. 353–361 (cit. on p. 121).

Kuc, R. (1984). “Estimating acoustic attenuation from reflected ultrasound signals: Comparison of spectral-shift and spectral-difference approaches”. In: *IEEE Trans. Acous., Speech, Sig. Pro.* 32.1, pp. 1–6 (cit. on p. 121).

Inbar, D. and M. Delevy (1989). *Time gain compensation for ultrasonic medical imaging systems*. US Patent 4,852,576 (cit. on p. 121).

Pye, S., S. Wild, and W. McDicken (1992). “Adaptive time gain compensation for ultrasonic imaging”. In: *Ultrasound Med. Biol.* 18.2, pp. 205–212 (cit. on p. 121).

Klesenski, K. (1996). *Automatic gain compensation in an ultrasound imaging system*. US Patent 5,579,768 (cit. on p. 121).

Orfanidis, S. J. (1996). *Introduction to signal processing*. Pearson Education, Inc. (cit. on p. 121).

Golyandina, N., V. Nekrutkin, and A. A. Zhigljavsky (2001). *Analysis of time series structure: SSA and related techniques*. CRC press (cit. on p. 121).

Lee, D., Y. Kim, and J. Ra (2006). “Automatic time gain compensation and dynamic range control in ultrasound imaging systems”. In: *Proc. SPIE Med. Imag.* 6147, pages (cit. on p. 121).

Alexandrov, T. (2008). *A method of trend extraction using singular spectrum analysis*. Tech. rep. arXiv preprint arXiv:0804.3367 (cit. on p. 121).

Klimonda, Z., J. Litniewski, and A. Nowicki (2009). “Spatial Resolution of Attenuation Imaging”. In: *Archives of Acoustics* 34.4, pp. 461–470 (cit. on p. 121).

Tang, M., F. Luo, and D. Liu (2009). “Automatic Time Gain Compensation in Ultrasound Imaging System”. In: *Proc. IEEE Int. Conf. Bioinfo. Biomed. Eng.* Pp. 1–4. DOI: 10.1109/ICBBE.2009.5162432 (cit. on p. 121).

Hemmsen, M. C., M. M. Petersen, S. I. Nikolov, M. B., Nielsen, and J. A. Jensen (2010). “Ultrasound image quality assessment: A framework for evaluation of clinical image quality”. In: *Proc. SPIE Med. Imag.* Vol. 76291. Medical Imaging 2010: Ultrasonic Imaging, Tomography, and Therapy, pp. 76290C–12 (cit. on p. 121).

Moshavegh, R., M. C. Hemmsen, B. Martins, K. L. Hansen, C. Ewertsen, A. H. Brandt, T. Bechsgaard, M. B. Nielsen, and J. A. Jensen (2015). “Advanced automated gain adjustments for in-vivo ultrasound imaging”. In: *Proc. IEEE Ultrason. Symp.* Pp. 1–4 (cit. on p. 121).

Moshavegh, R., M. Hemmsen, B. Martins, A. Brandt, K. Hansen, M. Nielsen, and J. Jensen (2015). “Automated hierarchical time gain compensation for in-vivo ultrasound imaging”. In: *Proc. SPIE* 9419, pages (cit. on p. 121).

References from Paper B

Jensen, J. A. and N. B. Svendsen (1992). “Calculation of Pressure Fields from Arbitrarily Shaped, Apodized, and Excited Ultrasound Transducers”. In: *IEEE Trans. Ultrason., Ferroelec., Freq. Contr.* 39, pp. 262–267 (cit. on p. 135).

O’Donnell, M. and L. J. Thomas (1992). “Efficient synthetic aperture imaging from a circular aperture with possible application to catheter-based imaging”. In: *IEEE Trans. Ultrason., Ferroelec., Freq. Contr.* 39, pp. 366–380 (cit. on p. 135).

Cooley, C. R. and B. S. Robinson (1994). “Synthetic aperture imaging using partial datasets”. In: *Proc. IEEE Ultrason. Symp.* Pp. 1539–1542. DOI: 10.1109/ULTSYM.1994.401884 (cit. on p. 135).

Karaman, M., P. C. Li, and M. O’Donnell (1995). “Synthetic aperture imaging for small scale systems”. In: *IEEE Trans. Ultrason., Ferroelec., Freq. Contr.* 42, pp. 429–442 (cit. on p. 135).

Jensen, J. A. (1996). “Field: A Program for Simulating Ultrasound Systems”. In: *Med. Biol. Eng. Comp.* 10th Nordic-Baltic Conference on Biomedical Imaging, Vol. 4, Supplement 1, Part 1, pp. 351–353 (cit. on p. 135).

Barthez, P. Y., R. Léveillé, and P. V. Scrivani (1997). “Side lobes and grating lobes artifacts in ultrasound imaging”. In: *Veterinary Radiology & Ultrasound* 38.5, pp. 387–393 (cit. on p. 135).

Karaman, M. and M. O'Donnell (1998). "Subaperture processing for ultrasonic imaging". In: *IEEE Trans. Ultrason., Ferroelec., Freq. Contr.* 45, pp. 126–135 (cit. on p. 135).

Lockwood, G. R., J. R. Talman, and S. S. Brunke (1998). "Real-time 3-D ultrasound imaging using sparse synthetic aperture beamforming". In: *IEEE Trans. Ultrason., Ferroelec., Freq. Contr.* 45, pp. 980–988 (cit. on p. 135).

Nikolov, S. I., K. Gammelmark, and J. A. Jensen (1999). "Recursive ultrasound imaging". In: *Proc. IEEE Ultrason. Symp.* Vol. 2, pp. 1621–1625 (cit. on p. 135).

Bae, M. H. and M. K. Jeong (2000). "A study of synthetic-aperture imaging with virtual source elements in B-mode ultrasound imaging systems". In: *IEEE Trans. Ultrason., Ferroelec., Freq. Contr.* Vol. 47, pp. 1510–1519 (cit. on p. 135).

Gammelmark, K. L. and J. A. Jensen (2003). "Multielement Synthetic Transmit Aperture Imaging using Temporal Encoding". In: *IEEE Trans. Med. Imag.* 22.4, pp. 552–563 (cit. on p. 135).

Nikolov, S. I. and J. A. Jensen (2003). "In-vivo Synthetic Aperture Flow Imaging in Medical Ultrasound". In: *IEEE Trans. Ultrason., Ferroelec., Freq. Contr.* 50.7, pp. 848–856 (cit. on p. 135).

Huang, J., P. W. Que, and J. H. Jin (2004). "A Parametric Study of Beam Steering for Ultrasonic Linear Phased Array Transducer". In: *Russ. J. Nondestr. Test.* 40.4, pp. 254–259 (cit. on p. 135).

Jensen, J. A. and S. I. Nikolov (2004). "Directional Synthetic Aperture Flow Imaging". In: *IEEE Trans. Ultrason., Ferroelec., Freq. Contr.* 51, pp. 1107–1118 (cit. on p. 135).

Deb, K. (2005). "Multi-objective optimization". In: *Search methodologies*. Springer (cit. on p. 135).

Jensen, J. A., S. Nikolov, K. L. Gammelmark, and M. H. Pedersen (2006). "Synthetic Aperture Ultrasound Imaging". In: *Ultrasonics* 44, e5–e15 (cit. on p. 135).

Coello, C. A. C., G. B. Lamont, and D. A. V. Veldhuizen (2007). "Basic Concepts". In: *Evolutionary Algorithms for Solving Multi-Objective Problems*. Springer (cit. on p. 135).

Oddershede, N. and J. A. Jensen (2007). "Effects influencing focusing in synthetic aperture vector flow imaging". In: *IEEE Trans. Ultrason., Ferroelec., Freq. Contr.* 54.9, pp. 1811–1825 (cit. on p. 135).

Pedersen, M. H., K. L. Gammelmark, and J. A. Jensen (2007). "In-vivo evaluation of convex array synthetic aperture imaging". In: *Ultrasound Med. Biol.* 33, pp. 37–47 (cit. on p. 135).

Ranganathan, K. and W. F. Walker (2007). "Cystic Resolution: A Performance Metric for Ultrasound Imaging Systems". In: *IEEE Trans. Ultrason., Ferroelec., Freq. Contr.* 54.4, pp. 782–792. DOI: 10.1109/TUFFC.2007.311 (cit. on p. 135).

Guenther, D. A. and W. F. Walker (2009). "Generalized cystic resolution: a metric for assessing the fundamental limits on beamformer performance". In: *IEEE Trans. Ultrason., Ferroelec., Freq. Contr.* 56.1, pp. 77–90 (cit. on p. 135).

Hastie, T., R. Tibshirani, and J. Friedman (2009). *The Elements of Statistical Learning Data Mining, Inference, and Prediction*. Second edition. Springer Series in Statistics (cit. on p. 135).

Hansen, J. M., M. C. Hemmsen, and J. A. Jensen (2011). "An object-oriented multi-threaded software beamformation toolbox". In: *Proc. SPIE Med. Imag.* Vol. 7968, pages. DOI: 10.1117/12.878178 (cit. on p. 135).

Lediju, M. A., G. E. Trahey, B. C. Byram, and J. J. Dahl (2011). "Short-lag spatial coherence of backscattered echoes: imaging characteristics". In: *IEEE Trans. Ultrason., Ferroelec., Freq. Contr.* 58.7, pp. 1377–1388. DOI: 10.1109/TUFFC.2011.1957 (cit. on p. 135).

Denarie, B., T. A. Tangen, I. K. Ekroll, N. Rolim, H. H. Torp, T. Bjastad, and L. Løvstakken (2013). "Coherent Plane Wave Compounding for Very High Frame Rate Ultrasonography of Rapidly Moving Targets". In: *IEEE Trans. Ultrason., Ferroelec., Freq. Contr.* 32.7, pp. 1265–1276 (cit. on p. 135).

Jensen, J. A., H. Holten-Lund, R. T. Nilsson, M. Hansen, U. D. Larsen, R. P. Domsten, B. G. Tomov, M. B. Stuart, S. I. Nikolov, M. J. Pihl, Y. Du, J. H. Rasmussen, and M. F. Rasmussen (2013). "SARUS: A Synthetic Aperture Real-time Ultrasound System". In: *IEEE Trans. Ultrason., Ferroelec., Freq. Contr.* 60.9, pp. 1838–1852 (cit. on p. 135).

Ponnle, A., H. Hasegawa, and H. Kanai (2013). "Suppression of grating lobe artifacts in ultrasound images formed from diverging transmitting beams by modulation of receiving beams". In: *Ultrasound Med. Biol.* 39.4, pp. 681–691. DOI: 10.1016/j.ultrasmedbio.2012.10.019 (cit. on p. 135).

Gammelmark, K. L. and J. A. Jensen (2014). "2-D Tissue Motion Compensation of Synthetic Transmit Aperture Images". In: *IEEE Trans. Ultrason., Ferroelec., Freq. Contr.* Pp. 594–610. DOI: http://dx.doi.org/10.1109/TUFFC.2014.2948 (cit. on p. 135).

Jensen, J. A. (2014). "A Multi-threaded Version of Field II". In: *Proc. IEEE Ultrason. Symp.* IEEE, pp. 2229–2232 (cit. on p. 135).

Szabo, T. L. (2014). *Diagnostic ultrasound imaging: Inside out*. 2nd ed. Elsevier (Oxford, UK) (cit. on p. 135).

Yiu, B. Y., S. S. Lai, and A. C. Yu (2014). "Vector projectile imaging: time-resolved dynamic visualization of complex flow patterns." In: *Ultrasound Med. Biol.* 40.9, pp. 2295–2309 (cit. on p. 135).

Stuart, M. B., J. Jensen, T. Di Ianni, and J. A. Jensen (2015). "Image quality degradation from transmit delay profile quantization". In: *Proc. IEEE Ultrason. Symp.* Pp. 1–4. DOI: 10.1109/ULTSYM.2015.0126 (cit. on p. 135).

Hasegawa, H. and C. L. de Korte (2016). "Impact of element pitch on synthetic aperture ultrasound imaging". In: *J. Med. Ultrason.* Pp. 1–9. DOI: 10.1007/s10396-016-0700-6 (cit. on p. 135).

Jensen, J., M. B. Stuart, and J. A. Jensen (2016). "Optimized Plane Wave Imaging for Fast and High-Quality Ultrasound Imaging". In: *IEEE Trans. Ultrason., Ferroelec., Freq. Contr.* 63.11, pp. 1922–1934. DOI: 10.1109/TUFFC.2016.2591980 (cit. on p. 135).

Moshavegh, R., J. Jensen, C. A. Villagomez-Hoyos, M. B. Stuart, M. C. Hemmsen, and J. A. Jensen (2016). "Optimization of synthetic aperture image quality". In: *Proc. SPIE Med. Imag.* Vol. 9790, pages (cit. on p. 135).

References from Paper C

Kuc, R. (1984). "Estimating acoustic attenuation from reflected ultrasound signals: Comparison of spectral-shift and spectral-difference approaches". In: *IEEE Trans. Acous., Speech, Sig. Pro.* 32.1, pp. 1–6 (cit. on p. 151).

Pye, S., S. Wild, and W. McDicken (1992). "Adaptive time gain compensation for ultrasonic imaging". In: *Ultrasound Med. Biol.* 18.2, pp. 205–212 (cit. on p. 150).

Klesenski, K. (1996). "Automatic gain compensation in an ultrasound imaging system". In: *US Patent*, pp. 5, 579, 768. URL: http://www.google.com/patents/US5579768 (cit. on p. 150).

Lee, D., Y. Kim, and J. Ra (2006). "Automatic time gain compensation and dynamic range control in ultrasound imaging systems". In: *Proc. SPIE Med. Imag.* 6147, pages (cit. on p. 150).

Klimonda, Z., J. Litniewski, and A. Nowicki (2009). "Spatial Resolution of Attenuation Imaging". In: *Archives of Acoustics* 34.4, pp. 461–470 (cit. on p. 156).

Tang, M., F. Luo, and D. Liu (2009). "Automatic Time Gain Compensation in Ultrasound Imaging System". In: *Proc. IEEE Int. Conf. Bioinfo. Biomed. Eng.* Pp. 1–4. DOI: 10.1109/ICBBE.2009.5162432 (cit. on p. 150).

Hemmsen, M. C., S. I. Nikolov, M. M. Pedersen, M. J. Pihl, M. S. Enevoldsen, J. M. Hansen, and J. A. Jensen (2012). "Implementation of a versatile research data acquisition system using a commercially available medical ultrasound scanner". In: *IEEE Trans. Ultrason., Ferroelec., Freq. Contr.* 59.7, pp. 1487–1499 (cit. on p. 157).

Hemmsen, M. C., P. M. Hansen, T. Lange, J. M. Hansen, K. L. Hansen, M. B. Nielsen, and J. A. Jensen (2012). "In Vivo Evaluation of Synthetic Aperture Sequential Beam-

forming". In: *Ultrasound Med. Biol.* 38.4, pp. 708–716. DOI: http://dx.doi.org/10.1016/j.ultrasmedbio.2011.12.017. URL: http://www.sciencedirect.com/science/article/pii/S0301562911015729 (cit. on pp. 150, 151, 155, 156).

References from Paper D

Kuc, R. (1984). "Estimating acoustic attenuation from reflected ultrasound signals: Comparison of spectral-shift and spectral-difference approaches". In: *IEEE Trans. Acous., Speech, Sig. Pro.* 32.1, pp. 1–6 (cit. on p. 165).

Pye, S., S. Wild, and W. McDicken (1992). "Adaptive time gain compensation for ultrasonic imaging". In: *Ultrasound Med. Biol.* 18.2, pp. 205–212 (cit. on p. 162).

Golyandina, N., V. Nekrutkin, and A. A. Zhigljavsky (2001). *Analysis of time series structure: SSA and related techniques*. CRC press (cit. on p. 165).

Lee, D., Y. Kim, and J. Ra (2006). "Automatic time gain compensation and dynamic range control in ultrasound imaging systems". In: *Proc. SPIE Med. Imag.* 6147, pages (cit. on p. 162).

Tang, M., F. Luo, and D. Liu (2009). "Automatic Time Gain Compensation in Ultrasound Imaging System". In: *Proc. IEEE Int. Conf. Bioinfo. Biomed. Eng.* Pp. 1–4. DOI: 10.1109/ICBBE.2009.5162432 (cit. on p. 162).

Hemmsen, M. C., M. M. Petersen, S. I. Nikolov, M. B., Nielsen, and J. A. Jensen (2010). "Ultrasound image quality assessment: A framework for evaluation of clinical image quality". In: *Proc. SPIE Med. Imag.* Vol. 76291. Medical Imaging 2010: Ultrasonic Imaging, Tomography, and Therapy, pp. 76290C–12 (cit. on p. 167).

Litniewski, J., Z. Klimonda, and A. Nowicki (2012). "Parametric sonographic imaging-application of synthetic aperture technique to imaging attenuation of ultrasound in tissue structures". In: *Hydroacoustics* 15, pp. 99–110 (cit. on p. 162).

Moshavegh, R., M. Hemmsen, B. Martins, A. Brandt, K. Hansen, M. Nielsen, and J. Jensen (2015). "Automated hierarchical time gain compensation for in-vivo ultrasound imaging". In: *Proc. SPIE* 9419, pages (cit. on pp. 163, 166).

References from Paper E

Jensen, J. A. and N. B. Svendsen (1992). "Calculation of Pressure Fields from Arbitrarily Shaped, Apodized, and Excited Ultrasound Transducers". In: *IEEE Trans. Ultrason., Ferroelec., Freq. Contr.* 39, pp. 262–267 (cit. on pp. 172, 175).

O'Donnell, M. and L. J. Thomas (1992). "Efficient synthetic aperture imaging from a circular aperture with possible application to catheter-based imaging". In: *IEEE Trans. Ultrason., Ferroelec., Freq. Contr.* 39, pp. 366–380 (cit. on p. 172).

Karaman, M., P. C. Li, and M. O'Donnell (1995). "Synthetic aperture imaging for small scale systems". In: *IEEE Trans. Ultrason., Ferroelec., Freq. Contr.* 42, pp. 429–442 (cit. on p. 172).

Jensen, J. A. (1996). "Field: A Program for Simulating Ultrasound Systems". In: *Med. Biol. Eng. Comp.* 10th Nordic-Baltic Conference on Biomedical Imaging, Vol. 4, Supplement 1, Part 1, pp. 351–353 (cit. on pp. 172, 175).

Karaman, M. and M. O'Donnell (1998). "Subaperture processing for ultrasonic imaging". In: *IEEE Trans. Ultrason., Ferroelec., Freq. Contr.* 45, pp. 126–135 (cit. on p. 172).

Nikolov, S. I., K. Gammelmark, and J. A. Jensen (1999). "Recursive ultrasound imaging". In: *Proc. IEEE Ultrason. Symp.* Vol. 2, pp. 1621–1625 (cit. on p. 172).

Deb, K. (2005). "Multi-objective optimization". In: *Search methodologies*. Springer (cit. on pp. 172, 174).

Jensen, J. A., S. Nikolov, K. L. Gammelmark, and M. H. Pedersen (2006). "Synthetic Aperture Ultrasound Imaging". In: *Ultrasonics* 44, e5–e15 (cit. on p. 172).

Coello, C. A. C., G. B. Lamont, and D. A. V. Veldhuizen (2007). "Basic Concepts". In: *Evolutionary Algorithms for Solving Multi-Objective Problems*. Springer (cit. on pp. 172, 175).

Ranganathan, K. and W. F. Walker (2007). "Cystic Resolution: A Performance Metric for Ultrasound Imaging Systems". In: *IEEE Trans. Ultrason., Ferroelec., Freq. Contr.* 54.4, pp. 782–792. DOI: 10.1109/TUFFC.2007.311 (cit. on p. 173).

Hansen, J. M., M. C. Hemmsen, and J. A. Jensen (2011). "An object-oriented multi-threaded software beamformation toolbox". In: *Proc. SPIE Med. Imag.* Vol. 7968, pages. DOI: 10.1117/12.878178 (cit. on p. 175).

Jensen, J. A., H. Holten-Lund, R. T. Nilsson, M. Hansen, U. D. Larsen, R. P. Domsten, B. G. Tomov, M. B. Stuart, S. I. Nikolov, M. J. Pihl, Y. Du, J. H. Rasmussen, and M. F. Rasmussen (2013). "SARUS: A Synthetic Aperture Real-time Ultrasound System". In: *IEEE Trans. Ultrason., Ferroelec., Freq. Contr.* 60.9, pp. 1838–1852 (cit. on p. 177).

Jensen, J. A. (2014). "A Multi-threaded Version of Field II". In: *Proc. IEEE Ultrason. Symp.* IEEE, pp. 2229–2232 (cit. on pp. 172, 175).

References from Paper F

Meyer, F. (1977). "Contrast features extraction, Special Issues of Practical Metallography". In: *Quant. Anal. Microstruct. Mat. Sc. Bio. Med.* Vol. 8 (cit. on p. 189).

Grady, L. (2006). “Random Walks for Image Segmentation”. In: *IEEE. Trans Patt. Ana. Mach. Int.* 28.11, pp. 1768–1783 (cit. on p. 185).

Volpicelli, G., A. Mussa, G. Garofalo, L. Cardinale, G. Casoli, F. Perotto, C. Fava, and M. Frascisco (2006). “Bedside lung ultrasound in the assessment of alveolar-interstitial syndrome”. In: *Am. J. Emerg. Med.* 24.6, pp. 689–696 (cit. on p. 184).

Gargani, L. (2011). “Lung ultrasound: A new tool for the cardiologist”. In: *Cardiovascular ultrasound* 9.1 (cit. on p. 184).

Hemmsen, M. C., S. I. Nikolov, M. M. Pedersen, M. J. Pihl, M. S. Enevoldsen, J. M. Hansen, and J. A. Jensen (2012). “Implementation of a versatile research data acquisition system using a commercially available medical ultrasound scanner”. In: *IEEE Trans. Ultrason., Ferroelec., Freq. Contr.* 59.7, pp. 1487–1499 (cit. on p. 190).

Karamalis, A., W. Wein, T. Klein, and N. Navab (2012). “Ultrasound confidence maps using random walks”. In: *Med. Image Anal.* 16.6, pp. 1101–1112 (cit. on p. 186).

Lichtenstein, D. A. (2014). “Lung ultrasound in the critically ill”. In: *Ann Intensive Care* 4.1 (cit. on p. 184).

References from Paper G

Grant, E. G., C. B. Benson, G. L. Moneta, A. V. Alexandrov, J. D. Baker, E. I. Bluth, B. A. Carroll, and et al. (2003). “Carotid artery stenosis: gray-scale and Doppler US diagnosis - Society of radiologists in ultrasound consensus conference”. In: *Radiology* 229.2. M. Eliasziw and J. Gocke and B. S. Hertzberg, pp. 340–346. DOI: 10.1148/radiol.2292030516 (cit. on p. 194).

Pedersen, M. M., M. J. Pihl, P. Haugaard, J. M. Hansen, K. L. Hansen, M. B. Nielsen, and J. A. Jensen (2012). “Comparison of Real-Time In Vivo Spectral and Vector Velocity Estimation”. In: *Ultrasound Med. Biol.* 38.1, pp. 145–151 (cit. on p. 194).

Reutern, G. M. von, M. W. Goertler, N. M. Bornstein, M. D. Sette, D. H. Evans, A. Hetzel, M. Kaps, F. Perren, and et al. (2012). “Grading Carotid Stenosis Using Ultrasonic Methods”. In: *Stroke* 43.3, pp. 916–921. DOI: 10.1161/STROKEAHA.111.636084 (cit. on p. 194).

Hansen, P. M., S. Heerwagen, M. M. Pedersen, M. Rix, L. Lønn, M. B. Nielsen, J. B. Olesen, M. J. Pihl, and J. A. Jensen (2013). “Vector Volume Flow in Arteriovenous Fistulas”. In: *Proc. IEEE Ultrason. Symp.* Pp. 2026–2029 (cit. on p. 194).

Hansen, P. M., J. B. Olesen, M. J. Pihl, T. Lange, S. Heerwagen, M. M. Pedersen, M. Rix, L. Lønn, J. A. Jensen, and M. B. Nielsen (2014). “Volume Flow in Arteriovenous Fistulas using Vector Velocity Ultrasound”. In: *Ultrasound Med. Biol.* 40.11, pp. 2707–2714 (cit. on p. 194).

Jensen, J., J. B. Olesen, P. M. Hansen, M. B. Nielsen, and J. A. Jensen (2014). "Accuracy and Sources of Error for an Angle Independent Volume Flow Estimator". In: *Proc. IEEE Ultrason. Symp.* Pp. 1714–1717 (cit. on p. 194).

Brandt, A. H., J. Jensen, K. L. Hansen, P. M. Hansen, T. Lange, M. Rix, J. A. Jensen, L. Lönn, and M. B. Nielsen (2016). "Surveillance for Hemodialysis Access Stenosis: Usefulness of Ultrasound Vector Volume Flow". In: *J. Vascul. Access.* Accepted for publication (cit. on p. 194).

Jensen, J., J. B. Olesen, M. B. Stuart, P. M. Hansen, M. B. Nielsen, and J. A. Jensen (2016). "Vector velocity volume flow estimation: Sources of error and corrections applied for arteriovenous fistulas". In: *Ultrasonics* 70, pp. 136–146. DOI: http://dx.doi.org/10.1016/j.ultras.2016.04.023 (cit. on pp. 194, 198).